THEORETICAL AND COMPUTATIONAL INVESTIGATIONS OF FLAME-VORTEX AND DROPLET-SURFACE DYNAMICS

TAO YANG

PhD

The Hong Kong Polytechnic University

2025

The Hong Kong Polytechnic University
Department of Mechanical Engineering

Theoretical and Computational Investigations of Flame-Vortex and Droplet-Surface Dynamics

Tao Yang

A thesis submitted in partial fulfilment of the requirements for the degree of Doctor of Philosophy

July 2024

CERTIFICATE OF ORIGINALITY

I hereby declare that this thesis is my own work and that, to the best of my knowledge and belief, it reproduces no material previously published or written, nor material that has been accepted for the award of any other degree or diploma, except where due acknowledgement has been made in the text.

Signature: _____

Name of Student: Tao Yang

Abstract

The thesis consists of two parts, with Part I on flame-vortex dynamics and Part II on droplet-surface impact dynamics. Specifically, the vortex-dynamics interactions and synchronization modes of single-, dual-, triple-, and octa-flickering diffusion flames were investigated computationally and theoretically in Part 1, while the splash and complete rebound of droplets impacting on the surface was modelled theoretically based on the previous experimental findings in Part 2. These works are conducive to studying spray flames.

Flickering flames are bridges between flame dynamics and vortex dynamics, which is a powerful analysis approach in fluid mechanics and deserves more attention from the combustion community. Turbulence characterizes multi-scale vortex interaction and is hardly bypassed to deeply understand turbulent flames, in which multi-scale chemical reactions are coupled with vortices. Flickering flames facilitate the experimental, numerical, and theoretical studies of unsteady flames, as they retain the intrinsically unsteady nature of turbulent flames but contain richer physics than laminar flames. In the thesis, the main studies and achievements of flickering flame are summarized as follows:

1. Flickering buoyant diffusion methane flames in weakly rotatory flows were computationally and theoretically investigated. One notable computational discovery is the nonlinear increase in flicker frequency with the nondimensional rotational intensity R (up to 0.24), correlating with the nondimensional circumferential circulation. This finding aligns with prior experimental evidence suggesting that rotatory flows can amplify flame flickering to a certain degree. Drawing on a vortex-dynamical comprehension of flickering flames, where flame flickering results from the periodic shedding of buoyancy-induced toroidal vortices, a scaling theory was developed for

flickering buoyant diffusion flames in weakly rotatory flows. This theory posits that the rise in flicker frequency f follows the scaling relation $(f - f_0) \propto R^2$, a proposition that closely mirrors the computational findings. Moreover, the presence of external rotatory flow in physics augments the radial pressure gradient around the flame, with the significant baroclinic effect of $\nabla p \times \nabla \rho$ serving as an additional factor fueling the growth of toroidal vortices, thereby accelerating their periodic shedding.

2. Small-scale flickering buoyant diffusion flames in externally swirling flows were computationally investigated, with emphasis on identifying and characterizing various distinct dynamical behaviours of the flames. A one-step reaction mechanism is utilized to explore the impact of finite rate chemistry on flame flicker. By adjusting the external swirling flow conditions (the intensity R and the inlet angle α), six flame modes, including flickering flame, oscillating flame, steady flame, lifted flame, spiral flame, and flame with a vortex bubble, were computationally identified in both physical and phase spaces. Observing the phase portraits and their differences in distinct modes could help identify the dynamical behaviours of flames and understand complex phenomena.

3. Anti-phase and in-phase flickering modes of dual buoyant diffusion flames were numerically investigated and theoretically analyzed. The mode transition was found to rely on the inner-side shear layers between two flames, of which the crucial role resembles the von Karman vortex street in the wake of a bluff body. A unified regime nomogram in the parameter space of the normalized frequency and the newly defined flame Reynolds number was obtained and verified by present simulations and the previous experiments.

4. Triple flickering buoyant diffusion flames of methane gas in an equilateral triangle arrangement, regarded as a nonlinear dynamical system of interconnected

oscillators, were computationally investigated. For the first time, the study successfully replicated four distinct dynamical modes: in-phase, death, rotation, and partially in-phase, which were interpreted through the perspective of vortex interaction, with a specific emphasis on vorticity reconnection and vortex-induced flow. This work well establishes a connection between vortex dynamics and the nonlinear dynamics of the triple-flame system, which could be essential in comprehending more extensive dynamic systems involving multiple flickering flames.

5. A series of circular arrays of octuple flickering laminar buoyant diffusion flames were investigated in computational and modelling manners to understand their collective behaviours. In the work, five distinct dynamical modes, such as the merged, in-phase mode, rotation, flickering death, partially flickering death, and anti-phase modes, were identified and interpreted from the perspective of vortex dynamics. A unified regime diagram was obtained in terms of f/f_0 and of a combined Reynolds-number-like parameter $\alpha Gr^{1/2}$. The bifurcation transition from the in-phase mode and the anti-phase mode to the totally or partially flickering death occurs at $\alpha Gr^{1/2} = 655 \pm 55$. In addition, a toy model of identical Stuart-Landau oscillators with time-delay coupling was utilized to mimic the collective dynamics of multiple flame systems, bringing out a great capability of reproducing the general features and collective modes. The physical model based on vortex-dynamics mechanisms and the toy model of Stuart-Landau oscillators both provide valuable insights into the behaviour of complex coupled oscillatory systems.

Modelling droplet-surface impact plays an important role in the numerical simulation of many industrial devices, such as inkjet printing, spray coating, nuclear installation, and bipropellant rocket engines. The droplet impact on a solid surface involves rich phenomena of gas-liquid-solid three-phase interplays, of which

understanding is crucial for optimizing processes in various applications. Droplet impact facilitates the experimental, numerical, and theoretical studies of fluid dynamics. In the thesis, the main studies and achievements of droplet impact are summarized as follows:

6. The splash in low-Oh region and the receding breakup in high-Oh region were analyzed qualitatively based on the unbalanced forces acting on the rim of the spreading or receding liquid film. A semi-empirical correlation of splash threshold is proposed and well fits the experimental results from previous and present studies over a wide range of liquid viscosity. When the surface is high temperature (T_{W}), three sub-patterns of thin-sheet splash were unified in the three-dimensional phase diagram of $Oh - We - T_{\mathrm{W}}$. For the transition surface temperature $T_{\mathrm{W,cr}}$ from thin-sheet splash to deposition, a scaling correlation of $T_{\mathrm{W,cr}}/T_0 \sim We^{3/2}$ is derived based on the analysis of the temperature-dependent destabilizing force on the levitated lamella and agrees well with the experimental data.

7. A practically useful model of droplet splashing on a smooth solid surface was established by unifying many previous experimental data for different liquids, droplet sizes, droplet velocities, and ambient pressures. Specifically, a scaling law of the splash threshold comprising the physical properties of the impacting liquid and the surrounding gas was derived from the instabilities of the spreading liquid sheet and the entrapping air film. The resulting correlation between two combinations of non-dimensional parameters $\Pi_L = Re^{1/2}Oh^2$ and $\Pi_G = \eta Kn^{-1}$ (Re, Oh, Kn, and η are the Reynolds, Ohnesorge, and Knudsen numbers and the gas-to-liquid viscosity ratio) agrees well with the previous splashing criteria that are either limited to narrow parametric ranges or expressed by piecewise fitting formulas.

8. The fluctuating recovery coefficient of oscillating droplets rebounding

completely from non-superhydrophobic surfaces was theoretically interpreted and modelled. A physical understanding is that the inevitable oscillation of a large droplet in freely falling makes the impacting droplet shape slightly deviate from being spherical and in turn affects the interaction between the droplet and the surface. A theoretical model of oscillating droplet rebound is proposed and well fits the present experiments over a wide range of We.

In the concluding chapter, potential research directions are suggested to extend those addressed in the thesis.

Publications Arising from the Thesis

Journal Publications

1. **Yang, T.**, Ma Y., and Zhang, P. (2024) Computational Identification and Stuart-Landau Modeling of Collective Dynamical Behaviours of Octuple Laminar Diffusion Flame Oscillators, *Combustion and Flame*, (under review)
2. **Yang, T.**, Ma Y., and Zhang, P. (2024) Dynamical Behaviours of Small-scale Buoyant Diffusion Flames in Externally Swirling Flows, *Symmetry*, 16(3), 292.
3. **Yang, T.** and Zhang, P. (2023) Flickering Buoyant Diffusion Flames in Weakly Rotatory Flows. *Theoretical and Computational Fluid Dynamics*, 37 (6), 781-798.
4. **Yang, T.**, Chi, Y., and Zhang, P. (2022). Vortex Interaction in Triple Flickering Buoyant Diffusion Flames. *Proceedings of the Combustion Institute*, 39 (2), 1893-1903
5. **Yang, T.,** Xia, X., and Zhang, P. (2019). Vortex-dynamical Interpretation of Anti-phase and In-phase Flickering of Dual Buoyant Diffusion Flames. *Physical Review Fluids*, 4(5), 053202.
6. **Yang, T.** and Zhang, P. (2024) A Unified Model of Droplet Splashing on a Smooth Solid Surface under Variable Ambient Pressures, *Physical Review Fluids*, (to be submitted)
7. Yang L., Liu, X., **Yang, T.**, and Zhang, P. (2024). Rebound of Oscillating Droplets on Non-superhydrophobic Surfaces, *International Journal of Multiphase Flow*, 178, 104901.
8. Qin, M., **Yang, T.**, Song, Y., Tang, C., and Zhang, P. (2021). Sub-patterns of Thin-Sheet Splash of a Droplet Impact on a Heated Surface. *Langmuir*, 38(2), 810-817.
9. Yang, L., Li, Z., **Yang, T.**, Chi, Y., and Zhang, P. (2021). Experimental study on droplet splash and receding breakup on a smooth surface at atmospheric pressure. *Langmuir*, 37(36), 10838-10848.

Conference Publications

1. **Yang, T.**, Ma, Yuan and Zhang, P., Dynamical Behaviors of Circular Flickering Flames: Computational Identification and Stuart-Landau Modeling, Oral presentation at the *China National Symposium on Combustion*, October 2024.
2. **Yang, T.**, Xu, W. and Zhang, P., Circular Flame Systems Using Deep Learning Approach: Dimensionality Reduction and Dynamical Mode Recognition, Oral presentation at the *1st National Conference on Intelligent Fluid Mechanics*, October 2024.
3. **Yang, T.** and Zhang, P., A New Scaling Law of Splashing Threshold for Droplets Impacting on a Smooth Solid Surface, Oral presentation at the *16th International Conference on Liquid Atomization and Spray Systems (ICLASS 2024)*, June 2024.
4. **Yang, T.**, Ma, Y., and Zhang, P., Numerical Investigations on the Dynamical Behaviours of Flickering Buoyant Diffusion Flames in Externally Rotating Flows, Oral presentation at the *International Technical Conference of Global Power and Propulsion Society (GPPS Hong Kong23)*, October 2023.
5. **Yang, T.**, Ma, Y., and Zhang, P., Dynamical Behaviours of Small-scale Flickering Buoyant Diffusion Flames in Externally Swirling Flows, Oral presentation at the *15th International Conference on Combustion and Energy Utilization (ICCEU)*, August 2023.
6. **Yang, T.** and Zhang, P., Flickering Buoyant Diffusion Flames in Rotatory Flows, Oral presentation at the *14th Asia-Pacific Conference on Combustion*, May 2023.
7. **Yang, T.**, Chi, Y., and Zhang, P., Vortex Interaction in Triple Flickering Buoyant Diffusion Flames, Oral presentation at the *39th International Symposium on Combustion*, July 2022.
8. **Yang, T.** and Zhang, P., Flickering Buoyant Diffusion Flames in Rotatory Flows, Oral presentation at *China National Symposium on Combustion*, December 2022. (Best Paper Award)

Other Publications

1. Chi, Y., Hu Z., **Yang, T.**, and Zhang, P. (2024) Synchronization Modes of Triple Flickering Buoyant Diffusion Flames: Experimental Identification and Model Interpretation. *Physical Review E*, 109(2), 024211.
2. Chi, Y., **Yang, T.**, and Zhang, P. (2023) Dynamical Mode Recognition of Triple Flickering Buoyant Diffusion Flames in Wasserstein Space. *Combustion and Flame*, 248, 112526. (First and second authors equally contributed to the work)

Acknowledgements

First and foremost, I would like to express my deepest gratitude to my supervisor, Prof. Yuan Ma, for giving his great help and support to my PhD study, and my co-supervisor, Prof. Peng Zhang, for the interesting research topics and professional guidance on my research. Throughout my PhD journey, their unwavering support, guidance, and encouragement have been a cornerstone of my academic success.

I am grateful to the examiners, Prof. Huangwei Zhang and Prof. Fengquan Zhong, for their thoughtful questions and constructive suggestions on the thesis. Then, special thanks should also be given to the group members of Prof. Yuan Ma and Prof. Peng Zhang, who helped me during my PhD study period. Particularly, Dr. Xi Xia helped me with my first paper, and I acquired many skills from him in analyzing and writing. I would like also to thank many coworkers, such as Prof. Lei Yang, Prof. Chenglong Tang, Dr Yicheng Chi, Dr Mengxiao Qin, Dr Jiayue Han, Mr Weiming Xu, Ms Ximiao Liu, and others, for our cooperation works.

Last, I would like to express my great gratitude to my family for their long-term support. Particularly, Dr Ling Li, Miya, Xinba, and Moka, gave me a great understanding in pursuit of my PhD.

Nomenclature

A	control mass
∂A	material contour of A
$B(t)$	time-dependent control volume enclosing the toroidal vortex
C	constant threshold for vortex shedding
C_j	constant prefactor relating to the initial fuel jet
C_r	constant prefactor relating to rotational flow
C_{jr}	$C_j + C_r$
C_θ	constant prefactor relating to azimuthal velocity within the vortex core
C_h	constant prefactor relating to the vertical motion of toroidal vortex
C_ρ	ρ_∞/ρ_f ranging from 4 to 8
D	diameter of fuel inlet, fixed at 10 mm
D_α	diffusion coefficient of species α
f	flickering frequency
Δf	$f(R) - f(R = 0)$
g	gravitational constant
h_s	sensible enthalpy under low Mach number approximation
$h(t)$	height of the upper boundary of $B(t)$
$\overline{H}$	time-averaged height of growing toroidal vortex, $\overline{H} = \hat{\tau}^{-1} \int_0^{\hat{\tau}} \hat{h}(t)dt$
l	gap distance
$\dot{m}_\alpha'''$	mass production rate per unit volume of species α by chemical reactions
$\dot{m}_F'''$	mass production rate per unit volume of fuel by evaporation
$\dot{q}'''$	heat release per unit volume
$\dot{\boldsymbol{q}}''$	heat flux vector

Q	total heat release rate
R	rotational intensity number
r_a	the radius of the vortex core
r_c	radial position of the vortex layer
$r(t)$	width of the right boundary of $B(t)$
$\bar{R}$	time-averaged width of growing toroidal vortex, $\bar{R} = \hat{\tau}^{-1} \int_0^{\hat{\tau}} \hat{r}(t)dt$
t	time
$\hat{t}$	dimensionless time, $t\sqrt{g/D}$
t^*	normalized time, tf_0
U_0	inlet velocity of fuel jet, fixed at 0.165 m/s
U	magnitude of inlet airflow, $\|\boldsymbol{U}\|$
u	velocity magnitude
h	helicity density, $\boldsymbol{u} \cdot \boldsymbol{\omega}$
p	pressure
Fr	Froude number, U_0^2/gD
Re	Reynold number, $U_0 D/\nu_F$
Ri	Richardson number, $(C_\rho - 1)gD/U_0^2$
$\boldsymbol{a}$	acceleration
$\boldsymbol{r}$	unit radial vector
$\boldsymbol{s}$	unit tangential vector along the contour ∂A
$\boldsymbol{z}$	unit normal vector
$\boldsymbol{u}$	velocity vector

$\boldsymbol{U}$	inlet velocity of airflow on the wind wall
$\boldsymbol{U}_{\perp}$	the normal component of $\boldsymbol{U}$
$\boldsymbol{U}_{\parallel}$	the tangential component of $\boldsymbol{U}$
$\widehat{\ }$	dimensionless quantity

Greek symbols

α	angle between the $\boldsymbol{U}_{\perp}$ and $\boldsymbol{U}_{\parallel}$, fixed at 45 degrees
ν	viscosity
ρ	density
τ	periodic time, $1/f$
ω	vorticity magnitude
$\boldsymbol{\omega}$	vorticity vector

Subscripts

A	airflow
0	quiescent environment ($R = 0$)
x, y, z	components in Cartesian coordinates
r, θ, z	components in cylindrical coordinates
f	flame
F	fuel
∞	environment condition at the far field

Table of Contents

List of Figures

List of Tables

Chapter 1. Introduction

Spray combustion is widely used in many practical applications, such as internal combustion engines, gas turbines, and industrial burners. However, spray combustion is a complex process of atomization, evaporation, mixing, droplet burning, and flame [1-3]. Usually, liquid fuel injected into a combustion chamber needs to be atomized into fine droplets, evaporated into the gas phase, and mixed with air to form an ignitable mixture, as shown in Fig. 1.1(a), Therefore, the droplet distribution of fuel spray and the mixing of gaseous fuel and air play a crucial role in improving combustion efficiency, controlling combustion stability, and reducing pollutant emission.

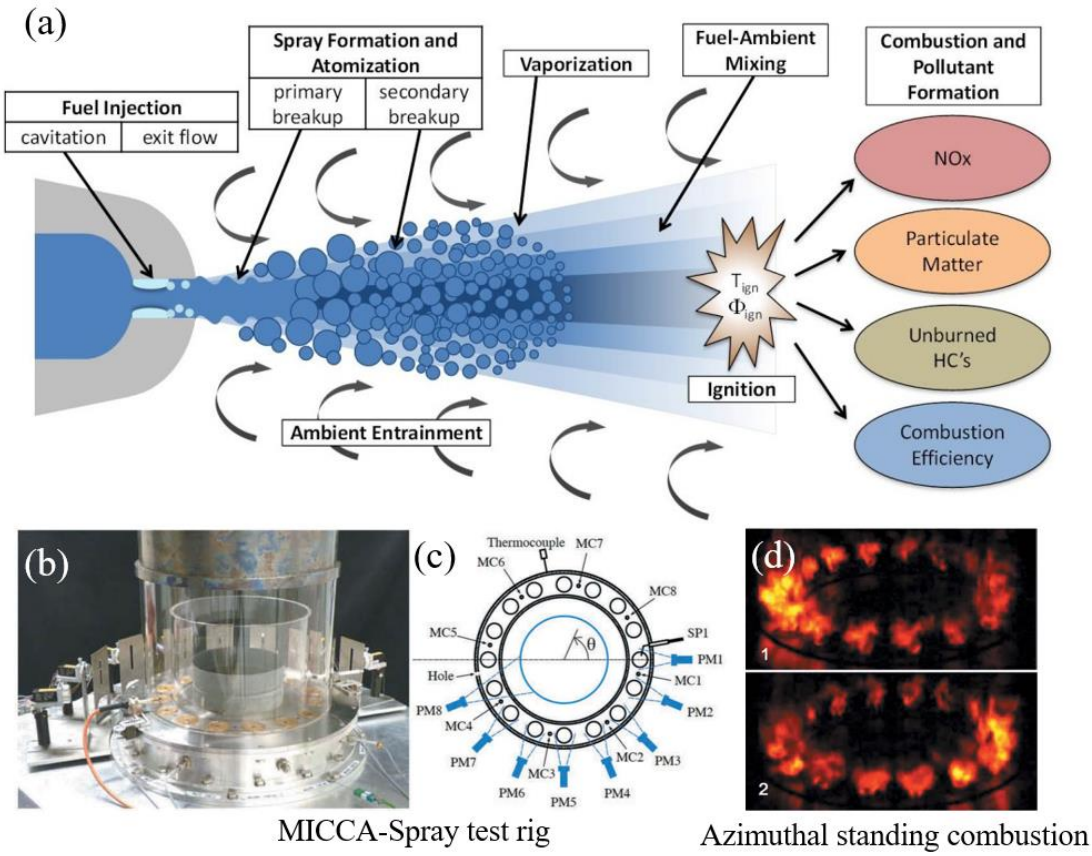

Figure 1- 1 (a) Schematic illustration of spray combustion [4]; (b-c) MICCA-Spray and (d) azimuthal standing combustion [5].

Spray flames are usually studied to understand, evaluate, and optimize the various processes in spray combustion, for example, canonical flames in the series of workshops on Turbulent Non-premixed Flames (TNF) [6] and Networks (ECN) [7]. Particularly, the MICCA-Spray configuration is designed to investigate ignition dynamics and instability modes of annular spray combustion systems, as shown in Fig .1.1 (b-c). Instabilities in spray flames are a complex and significant challenge [8], in which the nature and causes result from thermoacoustic instabilities (interactions between heat release and acoustic waves), hydrodynamic instabilities (unstable flows of air and fuel), and chemical-kinetic instabilities (variations in the chemical reaction rates). These instabilities in the combustion chamber can lead to issues such as reduced efficiency, increased emissions, and even damage to the combustion system [8].

In addition, the spray impingement is a fundamental issue [9] as it can affect mixture preparation prior to combustion and finally determine engine performance and pollutant emissions. Although many experimental studies have attempted to understand the underlying physics of spray impact in or close to the practical engine conditions, the fluid dynamic phenomena of a single droplet impinging onto a solid surface merit further work as the process is complicated and depends on many parameters associated with the interface and the impact conditions.

Simulating spray combustion in a combustor is a complex task due to several inherent challenges, such as diverse mechanisms of droplet-droplet, droplet-flow, flame-flow, and droplet-surface interactions and their models. Although this type of simulation is critical in designing efficient engines, there are some difficulties in physical modelling limitations and computational constraints. It is worth noting that understanding flame dynamics and droplet impact is significantly helpful in improving the physical models, as simplified and effective models can largely reduce

computational costs. Currently, simulating a spray flame needs a high cost and the accuracy of computational results is still up for debate. As a fundamental study, this thesis mainly focused on diffusion flames and the droplet impact on smooth and dry surfaces, as they are not only common in many everyday situations and industrial applications, but also classical physical problems. Those two problems are in a close relationship with the spray flame modelling.

In diffusion flame, the fuel and oxidizer are initially separate and mixed through the process of diffusion so that combustion occurs at the interface between the fuel and the oxidizer. To facilitate the modelling studies, diffusion flames are small scale and the fuel flows are at low Reynolds number. In many practical applications, low Reynolds number diffusion flames are widely found in scenarios, such as micro-combustion systems for portable power generation and various micro-scale chemical processes, fundamental combustion processes for flame structure, soot formation, and emission characteristics, and chemical synthesis for coatings, thin films, or composite materials.

Therefore, this thesis concerns flame-vortex interactions and dynamical modes of multiple coupled flames as well as splash and complete rebound of droplets impacting on the surface, which have obtained many great recently but remain insufficiently studied.

1.1 Flickering Buoyant Diffusion Flames

Diffusion flames [10, 11], also often referred to as non-premixed flames, are ubiquitous, such as wildfire, candle flame, gas stoves, gas-turbine, and rocket engines. The diffusion flame could be unstable under buoyancy [12-29]. The first study on the unstable flame is that Chamberlin and Rose [12] observed the flame flicker in Bunsen

diffusion flames, while some later works referred it to as “fire puffing" [14, 20]. Interestingly, they discovered many times of vibratory motion within one second, as shown in Fig. 1.2(a). The flame is pinched off periodically and separated into two parts.

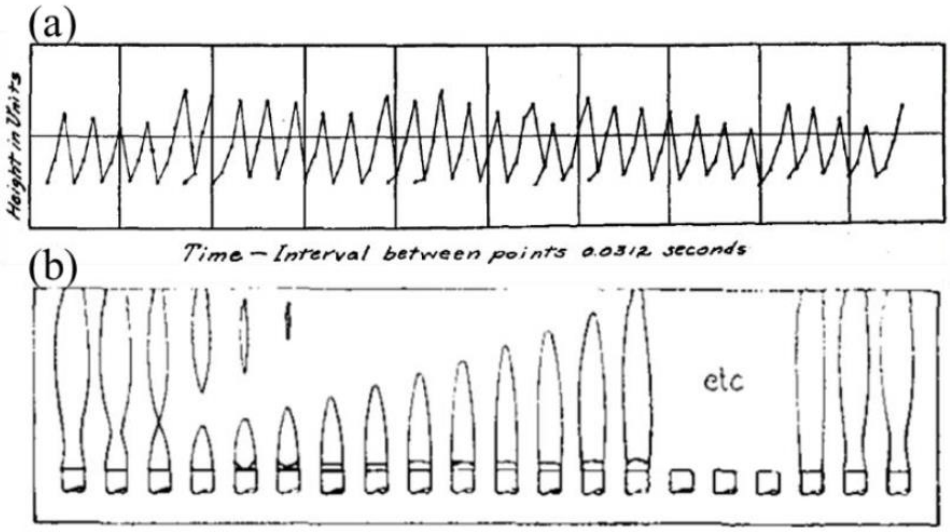

Figure 1- 2 (a) Vibratory motion of Bunsen diffusion flame [12]; (b) Flickering Burke-Schumann flame [13].

Subsequently, a similar vibratory pattern was discovered by Barr [13] in a butane diffusion flame. As illustrated in Fig. 1.2(b), the flame varies up and down about 20 cycles per second, and flame vibration involves progressive necking, potentially forming a detached, self-extinguishing bubble. It should be noted that recent works found that the flame flicker is observed in the oscillatory behavior of buoyant jets and plumes [30-33], in the wakes of droplets and porous spheres [25, 26, 34, 35], in low-density periodic flows of plume and jet [32]. Therefore, the flame flicker is ubiquitous in various flow problems.

1.2 Vortex Dynamics and Scaling Laws of Flickering Flames

Many studies have attempted to understand the physics of flickering diffusion flames. They pointed to a striking feature of the flames that the flicker is not caused by

an externally forced vibration or by the alternate flame extinction and re-ignition. Instead, the flicker of diffusion flames is a self-exciting flow oscillation.

As shown in Fig. 1.3(a), a prominent substantiation of the feature was owing to Chen et al.'s [15] experimental visualization of flickering flame, where the small vortices within the luminous flame are attributed to the Kelvin-Helmholtz instability of the fuel jet, while the larger toroidal vortices outside the luminous flame result from buoyancy-induced Kelvin-Helmholtz instability. Papadopouos et al.'s experiments [36] found that the outside large vortices become sufficiently powerful under certain conditions, therefore the flame early starts to pinch off, leading to a big individual pocket in Fig. 1.2 (b-c).

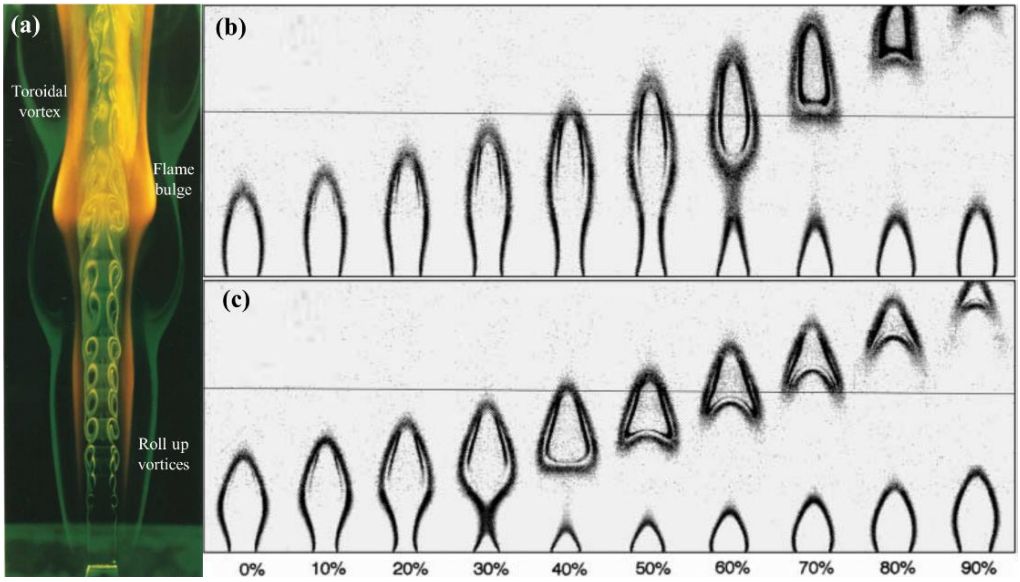

Figure 1- 3 (a) Visualizations of a methane jet diffusion flame for Re = 2,390 [15]; Fluorescence images of moderately (b) and strongly (c) flickering flames with different pinch-off [36].

In the early years, researchers attempted to predict the flickering frequency due to the flame instability. Early experimental studies [14, 37-41] showed that the flicker frequency f is proportional to $(g/D)^{1/2}$, where g is the gravitational constant and D

the fuel inlet diameter. Cetegen and Ahmed [16] experimentally investigated the periodic instability of buoyant plumes and pool fires and plotted the function between flickering frequency and diameter in Fig. 1.4(a).

Then, the flickering frequency was found to well correlate with the periodic shed-off of the toroidal vortices. Buckmaster and Peters [42] conducted a linear stability analysis of a self-similar solution of an annular burner diffusion flame and confirmed that the Kelvin-Helmholtz instability of the buoyancy-induced flow is responsible for the flicker. The quantitatively poor predictions of the stability analysis based on the quasi-parallel approximation were remedied by Moreno-Boza et al. [43] using the global linear stability analysis. Previous work [44] indicated that flame oscillation phenomena, such as flame pinch-off and flickering, can be evaluated using criteria based on the Rayleigh number and the Froude number.

When $St = fD/V$ is the Strouhal number and $Fr = U^2/gD$ is the Froude number are defined by the fuel flow velocity at the exit of the burner U, there is a correlation of $f \sim (g/D)^{1/2}$ for the scaling law of $St \sim Fr^{-1/2}$. Cetegen and Ahmed [16] extended the scaling law to account for the buoyancy-induced flow velocity by introducing a Richardson number correction factor, $(1 + Ri^{-1})^{1/2} + Ri^{-1/2}$, where $Ri = (\rho_\infty/\rho - 1)gD/V^2$, ρ is the flame density, and ρ_∞ is the ambient density. In single diffusion flames with little to no initial velocity, buoyancy is the primary factor driving the flame's transition to a self-sustained oscillation mode [45-48]. Recently, Xia and Zhang [24] have derived an analytical scaling law of the flickering frequency, grounded in vortex-dynamic analysis, as illustrated in Fig. 1.4(b).

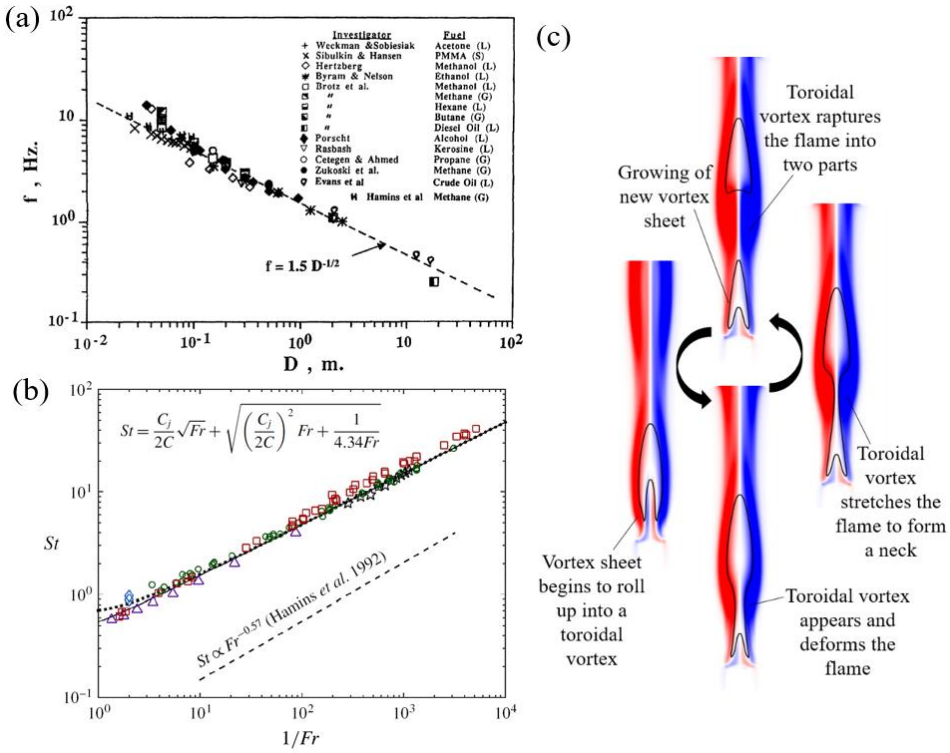

Figure 1- 4 (a) Correlation of flickering frequency f and flame size D of diffusion flames fueled by gas, liquid, and solid [16]; (b) Scaling law of Fr and St for flickering flames [24]; (c) The interactions between vortex and flame within a periodic process.

Xia and Zhang [24] calculated the circulation of a toroidal vortex within a flickering time and obtained a dimensionless relation:

$$\Gamma(\tau) = C_h Ri\, St^{-2} + C_j Fr^{-1/2} St^{-1} \tag{1.1}$$

where C_h is a prefactor due to the advective velocity and C_j is a prefactor due to the inlet flow circulation. Using the vortex shedding criterion of $\Gamma(\tau) = Constant$ [49-53], they got a generalized scaling law ($Fr \ll 1$ and $Ri \gg 1$) that collapsed the previous ones and concurs with experimental results.

From a physical perspective, flame flickering is linked to the dynamics of toroidal vortices [45], as shown in Fig. 1.4(c). In the early stages, the lower-density hot gas surrounding the non-premixed flame sheet rises due to buoyancy, resulting in the formation of a thin shear layer (or vortex sheet) just outside the flame sheet. This shear

layer then transitions into a toroidal vortex in the next stage, originating from the base where the flame is anchored. As Stage 3 progresses, the toroidal vortex expands and moves upward, altering the flame's shape to create a slender neck, leading up to Stage 4 where the neck breaks, resulting in the flame being pinched off. The detached flame pocket is subsequently elevated by the flow generated by the detached toroidal vortex [23, 45], while a new vortex sheet begins to develop outside the attached flame sheet, leading to the formation of the toroidal vortex in the next cycle. Following this, numerous studies have sought to unravel the physics behind flickering diffusion flames, particularly our recent investigations into coupled flames.

1.3 Buoyant Diffusion Flames in Swirling Flows

Swirling flows and flames frequently coexist in both natural phenomena and engineered systems. For instance, naturally occurring fire whirls [54-60] often driven by ambient swirling winds, demonstrate potent but destructive combustion. Figures 1.5(a) and 1.5(b) are the laboratory flame without and with spin, respectively. Many combustion engines utilize actively induced swirling flows to stabilize their diffusion flames [61] and the flame-vortex interaction mechanism is significant [62].

For the swirling combustion with the air injected tangentially into the central region, spinning flames [63-68] usually emerge, where whirling eddies of air, like a tornado-like vortex, suck fuel from the ground and form a slender fire downstream, for example, Fig. 1.5 (c) and Fig. 1.5(d). Recently, the blue whirl flame [68] was discovered in Fig. 1.5(e), as it has the potential to be used in combustion with higher efficiency and lower emission rate.

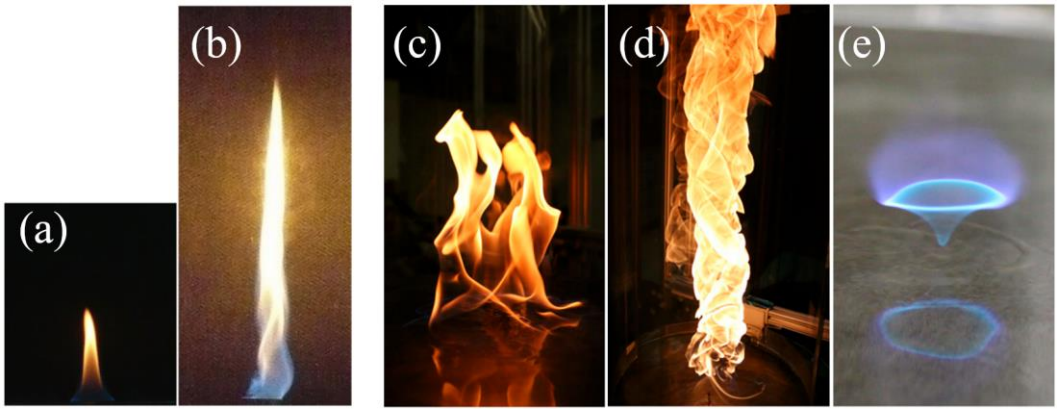

Figure 1- 5 Laboratory flame without (a) and with (b) spin [67]; (c) A pool fire becomes a (d) fire whirl or (e) blue whirl [68].

In particular, grasping the impact of swirling flows on flame flickering is essential, leading to a variety of important studies employing both experimental approaches and numerical analyses. Chuah and Kushida [69] demonstrated that external vortex flows contributed to the stabilization of the flickering flame while increasing its height. Over the past few decades, numerous experiments have examined the influence of burner rotation on flame stabilization, with an emphasis on the dynamic characteristics of buoyancy-induced flame oscillations. Gotoda together with coworkers [70-75] reported that the flame axisymmetric flicker could be self-sustained when the rotational speed is small while transitioning into low-dimensional deterministic chaos when the rotational speed is sufficiently large. As shown in Fig. 1-6(a), the flame becomes non-axisymmetric and exhibits spiral oscillation.

Another experimental approach is to tangentially import airflow from the ambient into the central flame region. This approach was usually used for producing a fire whirl, where whirling eddies of air, like a tornado flow, suck the ground fuel and form a slender fire downstream. By creating a rotational flow via spiral air entrainment in Fig. 1.6(b), Coenen et al. [58] reported that sufficiently strong swirling flows could curb the puffing instability and pool fires might transition into other states such as vortex bubble.

These flames exhibit complex geometric fashions. In Fig. 1.6(c), Lei et al. [76] used a rotating mesh screen to generate a vortical flow around a buoyant diffusion flame, discovering different flame patterns such as pulsating, inclined, steady, transitional, and cylindrical flames. It was especially noted that azimuthal pressure variations created asymmetry in the flow field and influenced the flame's tilt.

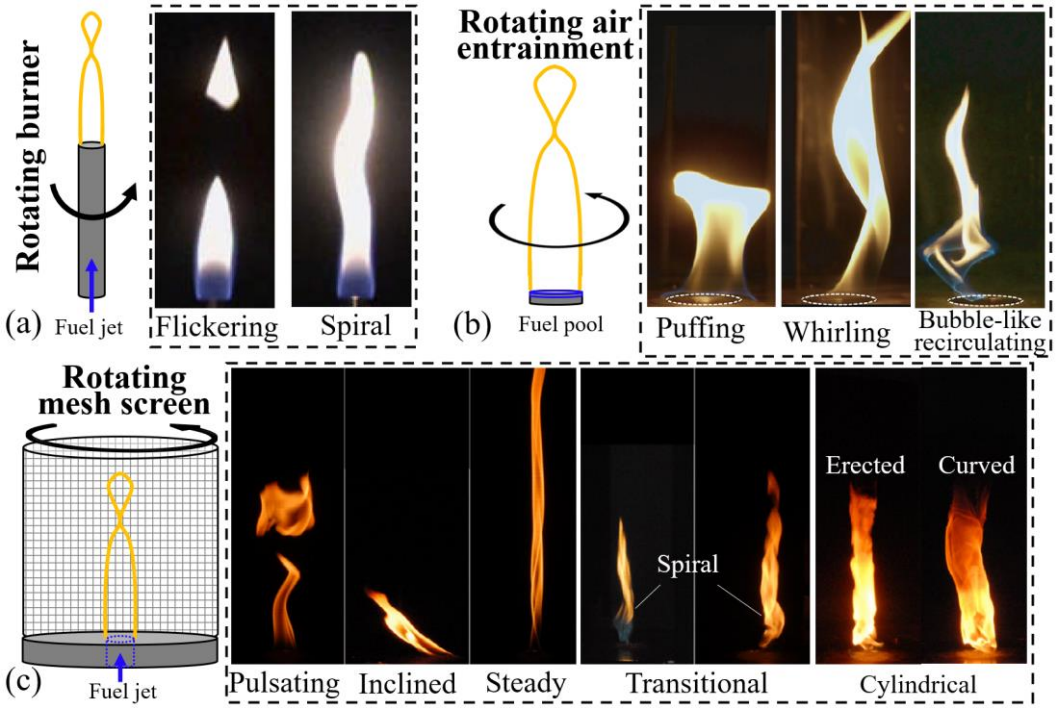

Figure 1- 6 Various modes of flickering flames or puffing fires with swirl: (a) a burner with rotating [73], (b) air entrainment caused by externally positioned vanes [58], and (c) a screen with rotating mesh [76].

Particularly, Lei et al. [56] observed the buoyancy-driven oscillation of small-scale flame still present in the fire with whirls, with flickering frequencies exceeding that. without any swirl (i.e, the quiescent environment) in Fig. 1.7(a). Recently, Ju et al.'s experiments [60] reported a higher pulsating frequency of a fire whirl under increased circulation conditions. Coenen et al. [58] reported that the puffing instability of pool fires is diminished under sufficiently strong rotating flows, leading to the emergence of a helical instability, which can also cause the flame to lift off., as shown in Fig. 1.7(b).

Although considerable progress has been achieved in understanding buoyant diffusion flames affected by externally swirling flow conditions, the dynamic behaviours of small-scale buoyant diffusion flames over a broad spectrum of swirling flow intensities are still not well understood, and the applications of vortex dynamics in this context have been inadequately examined. Consequently, this study aims to provide a more comprehensive analysis of the dynamic behaviours of flickering buoyant diffusion flames exposed to different external swirling flow conditions, accompanied by a vortex-dynamical analysis of the various dynamic responses.

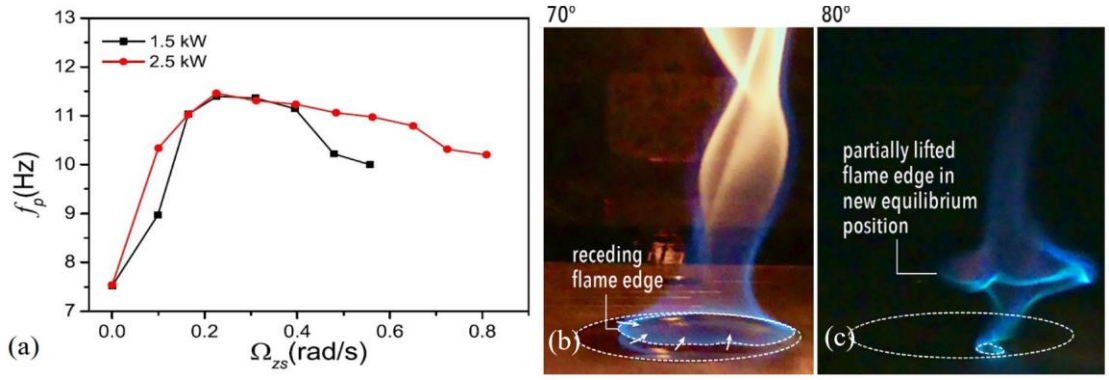

Figure 1- 7 (a) Flame pulsation frequency versus the screen angular speed [56]; (b) Lift-off of flame with a strong swirl [58].

The stabilization of flames under rotatory flows is a long-lasting and practically relevant problem. In this thesis, an interesting work is to exploit the problems of flickering buoyant diffusion flame in rotating environments. All the flickering flames mentioned above were produced in a quiescent environment, and their interaction with externally forced flows is apparently of interest but insufficiently investigated.

1.4 Dynamical Modes of Coupled Flickering Diffusion Flames

Couple flames [77-82] are ubiquitous in nature, domestic applications, and industrial applications (such as urban fires, gas stoves, and rocket engines). In fact, their

interaction is a key issue affecting the ability of a flame to maintain a consistent and controlled form while minimizing the risk of uncontrolled combustion in numerous practical applications. Flickering also exists in multiple coupled flames. Simply, researchers [80, 83] found that a few flickering candle flames put together can behave in a variety of synchronization modes, which largely depend on the gap distance and arrangement of flames. Kitahata et al. [83] observed that two flickering candle flames exhibit a transition from in-phase synchronization to anti-phase synchronization when the candle distance becomes bigger, as shown in Fig. 1.8.

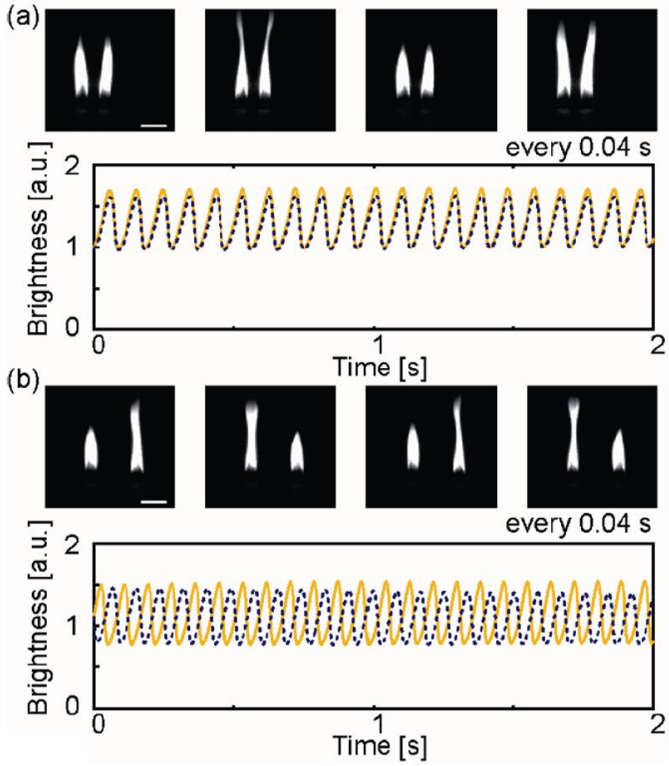

Figure 1- 8 Snapshots every 0.04 s of two sets of candles in-phase (a) and anti-phase (b) synchronization [83].

Similar behaviours were also found by Forrester [84] and Manoj et al. [78] by using candles. Dange et al.'s [85] high-speed shadowgraph and CH* indicated that the interaction among buoyancy-induced vortices may have a crucial impact on generating varying dynamic modes. This vortex-dynamical understanding was also supported by

PIV velocity field measurement of diffusion flames [86] and by experiments of jet diffusion flames [87, 88].

Coupled flickering diffusion flames appear as richer dynamical phenomena. For triple or more flames, previous experiments [77, 78, 80, 83, 89-91] reported that non-linear coupled oscillation is more diverse and complexed, as the synchronizing patterns are time varying. Three coupled flickering candle flames in an equilateral triangle arrangement were studied [80], each of which is made of bundling three identical candles of 9 mm in diameter. As shown in Fig. 1.9, four unique dynamic modes were observed from in-phase mode, partial in-phase, rotational, to flickering death modes. The interaction of toroidal vortices around the flames was interpreted to the generation of those modes.

An initial-arch-bow-initial "worship" oscillation mode was found in Forrester's experiment [84], as shown in Fig. 1.10(a). Interestingly, a chimaera state [77, 92], defined by the combinations of synchronized and desynchronized flames, is conjectured in the experiment. the coupled four flickering candle flames in a rectangle arrangement were studied [91], in which each of which was made of bundling four identical candles 10 mm in diameter. They are clustering mode, where the flames divide into two groups of synchronized flames, the chimera mode, in which the flames are split into synchronized and desynchronized flame groups, and the weak chimera mode, where three frequency-synchronized flames coexist alongside one desynchronized flame.

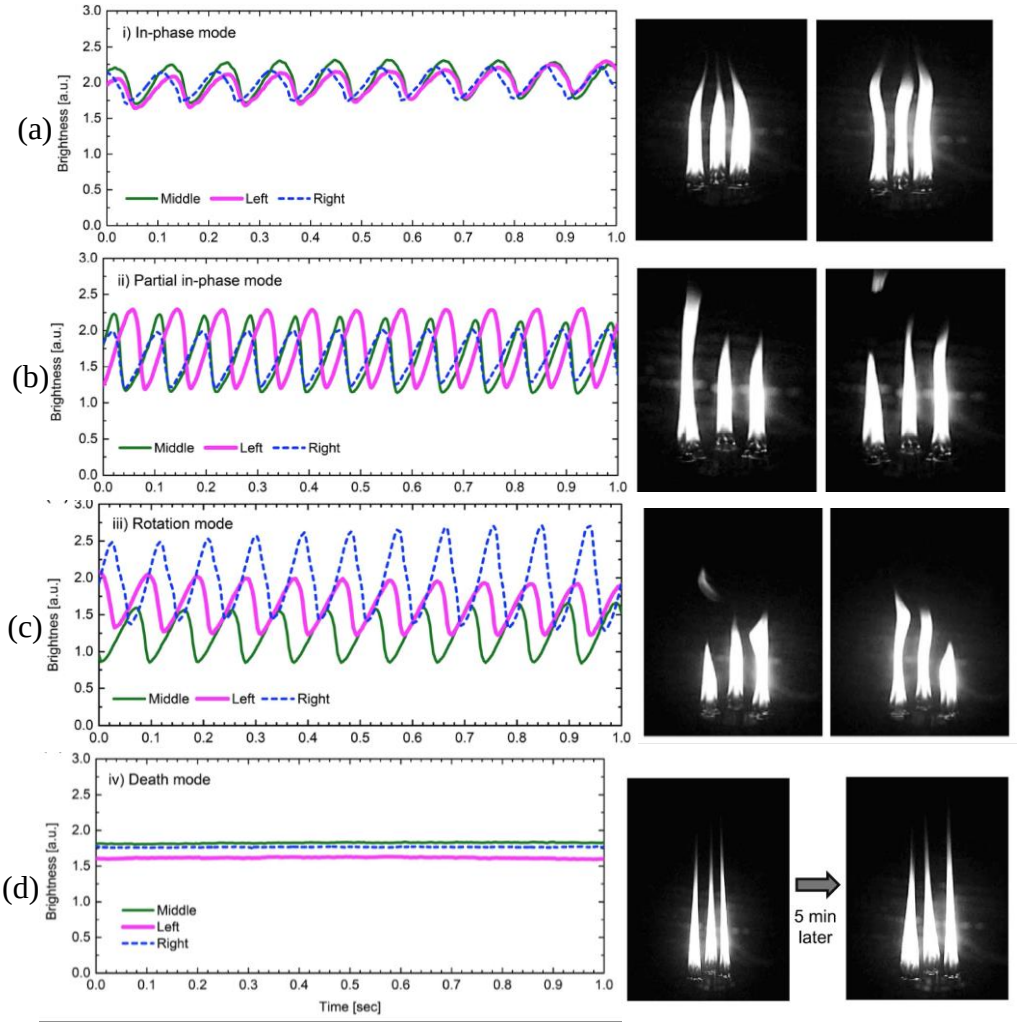

Figure 1- 9 Four synchronization modes of the three-coupled candle flames [80]: (a) in-phase, (b) Partial in-phase, (c) Rotation, and (d) Death modes. Time series of flame brightness (left) and snapshots of the oscillating flames (right).

Dynamical behaviours of coupled multiple flickering diffusion flames in various geometrical arrangements have been experimentally investigated. Forrester [84] found that flames in a ring array can increases or decreases the height of another flame at the centre. As shown in Fig. 1.10(b), Manoj et al. [90] identified highly diverse dynamic states in a network of flames with different configurations. The symmetric arrangements of flames have been investigated widely. Interestingly, Chen et al. [79] reported that the phase difference of the non-identical flames in a dynamical mode is not very distinct and has a continuous change with time, resulting in a periodically

changing frequency. The flame asymmetry can cause different dynamical behaviours, comparing with the identical flames.

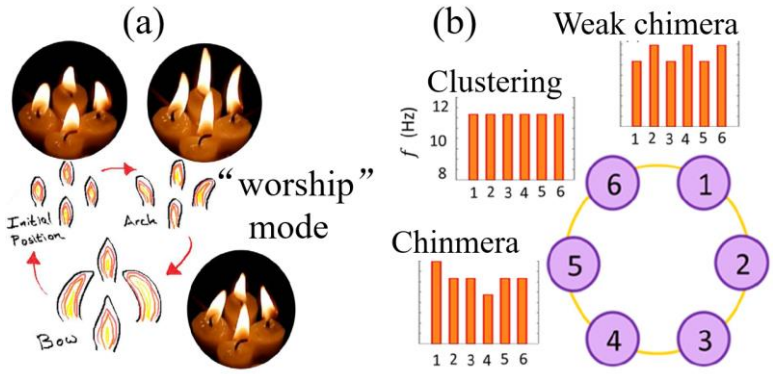

Figure 1- 10 (a) Collective oscillation mode of four candle flames [84]. (b) Three dynamical states, namely clustering, weak chimera, and chimera, of an annular flame oscillator [90].

However, very few studies attempted to establish dynamical models to reproduce the experimental findings. Kitahata et al.[83] believed that a lack of oxygen is a key factor in producing the flickering flame and that the thermal radiation coupling causes the synchronization of two flames. Therefore, they established an ordinary differential equation dynamical model to qualitatively reproduce their results of coupled dual candle flame after adopting many specified parameters. Subsequently, Gergely et al. [89] found that Kitahata et al.'s dynamical model [83] is not good for their experimental results and that the model is very sensitive to the fitting parameters. Besides, their radiation measurement does not support the previous radiation coupling hypothesis.

Consequently, Gergely et al. [89] proposed a modified model based on the responsible role of the oxygen flow induced by the thermal expansion. Recently, Manoj et al. [78] used time-delay coupled identical Stuart-Landau oscillators to represent candle-flame oscillators and generally reproduced the collective behaviour of coupled flames, including the in-phase, amplitude death, anti-phase and desynchronized modes.

Particularly, the amplitude death only occurs for small size candles and There exists a bifurcation between two flickering synchronizations for larger candles.

1.5 Circular Array of Flickering Flames: A Laboratory Annular Systems for Combustion Dynamics

Many important industrial devices involve circular or annular fluid systems, [5, 93-96], consisting of many identical units symmetrically arranged in a circle or ring shape, such as, turbomachinery rotors [97], annular combustors [98, 99], and aircraft engines [100]. The circular layout of multiple combustion chambers is commonly employed to achieve increased energy density and combustion efficiency.

A prominent scientific problem emerging in utilizing these systems is that their safe and efficient operation relies on controlling some collective behaviours of all units, which cannot be fully understood by studying the dynamical behaviours of a single unit through imposing appropriate periodic boundary conditions to substitute/replace the influence of its neighbour units. Recently, azimuthal instability mode has received increasing attention in Fig. 1.11(a).

The instability originates from the combined behavior of several flames and is not conducive to simplified studies, as the integrated system is partitioned by one or a few flame modules with appropriate periodic boundary conditions. While turbulent flames are the most common combustion phenomena observed in both natural and industrial settings, they display intricate flow patterns and robust turbulent-chemical interactions. Analyzing multiscale spatiotemporal effects requires considerable computational resources. Vignat et al. [5] found that laminar flames produced by the matrix injectors depicted in Fig. 1(b) are crucial for studying annular systems linked by azimuthal

modes in the absence of swirl and turbulent fluctuations. In an annular combustor, emergent behaviors arise from the interactions between individual entities. Much like flocks of birds, schools of fish, or crowds of people, the collective dynamics of multiple interacting units cannot be directly inferred from the characteristics of each individual entity [101].

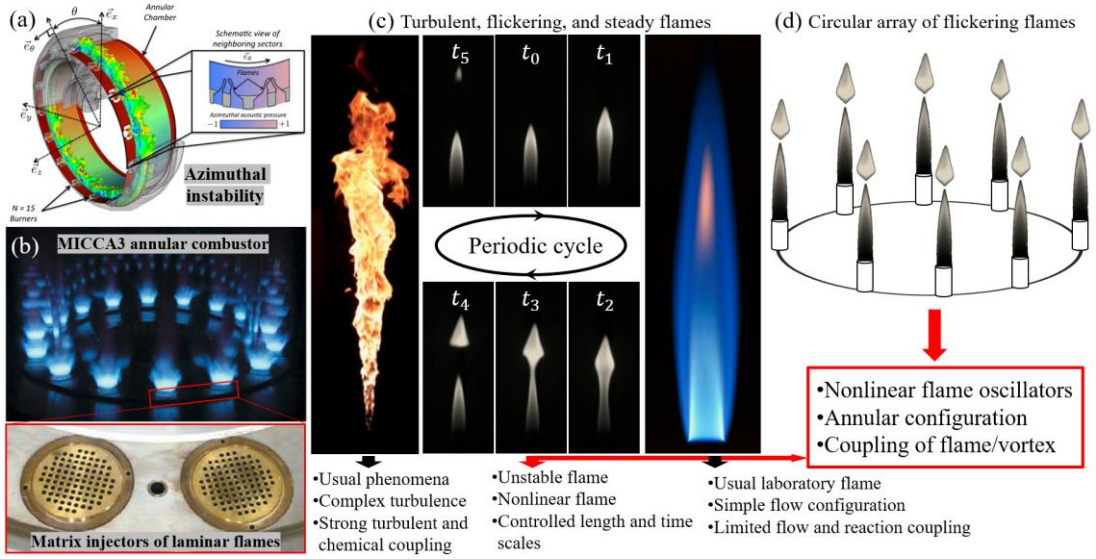

Figure 1- 11 (a) Azimuthal combustion instability (pressure fluctuations along the azimuthal direction) in an annular engine and zoom on two neighbouring burners [94], (b) MICCA3 combustor [5], single flames in (c) turbulent [58], flickering [102], and steady [22] states, and (d) circular flickering flames.

1.6 Dynamics of Droplet Impacting on Surface

Droplet collision with a solid surface is frequently observed in numerous natural and industrial processes [103, 104], such as inkjet printing and spray cooling. Since the investigation of drops impacting the solid was pioneered by Worthington in 1876 [105], the deceptively simple problem still attracts much interest from physicists, engineers, and mathematicians. The drop impact dynamics were systematically reviewed in [106-108]. Drop impacts on dry surfaces exhibit various flow patterns. For the morphology

of drop impact on a dry surface, Rioboo et al. [109] systematically reported six possible outcomes in experiments, as shown in Fig. 1.12. On a cold wall, the droplet-wall interaction generally results in various outcomes including deposition, rebound, thin-sheet splash (many tiny droplets ejected from the thin liquid film), and prompt splash, which are dependent on impacting parameters, liquid properties, surface wettability, roughness, etc.

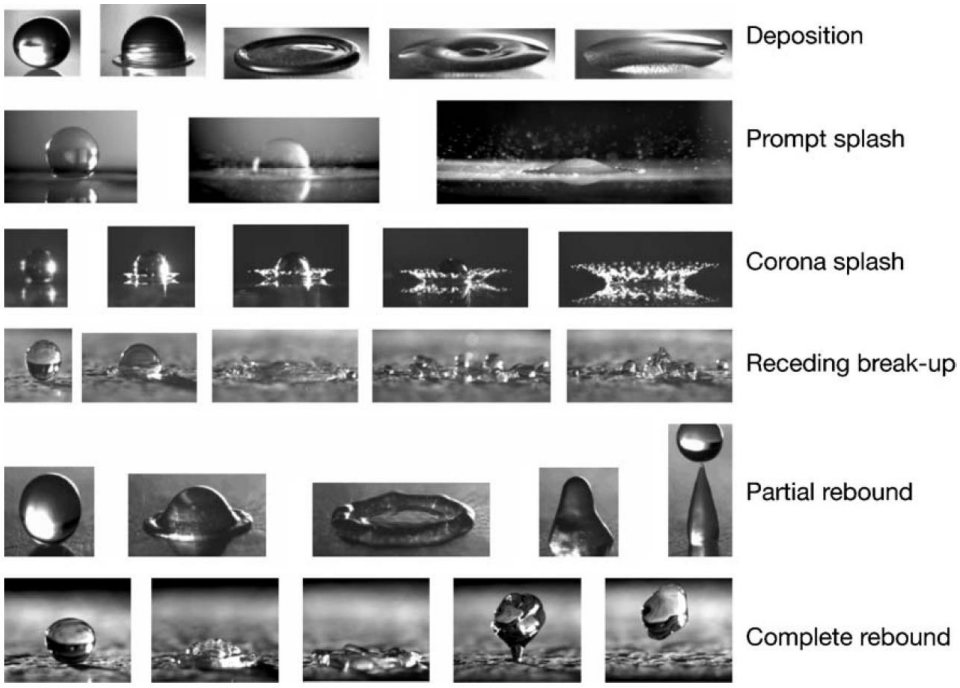

Figure 1- 12 Various outcomes of drop impact on a dry surface [109].

Droplet impact on a wall is a multifaceted phenomenon that encompasses various physical processes and is of significant interest in fields ranging from fluid dynamics to material science. Advances in droplet-wall interactions continue to deepen our understanding of the complexities involved in simulation and application. To establish quantitatively predictive spray-wall models, further understanding of droplet/surface interaction is of the essence[110], as it may cause fuel deposition, evaporation, and secondary droplet generation [9]. Splashing plays a significant role in the droplet size and distribution in fuel spray-wall impingement prior to combustion, and then affects

the thermal efficiency and emissions (such as soot and CO) of spray combustion in engines [111-113].

1.7 Droplet Splash on Unheated and Heated Surfaces

The drop impact on a solid surface is a ubiquitous phenomenon. During the droplet/wall impact, the disintegration of a droplet is defined as the droplet splashing [103, 114], in which at least one secondary droplet is formed. A great variety of studies on the liquid drop, solid surface, and ambient gas have been carried out to understand the splashing behaviour [115-122]. Multiple associated phenomena and physical features of droplet splashing have been comprehensively compiled in several excellent review articles [103, 106, 123].

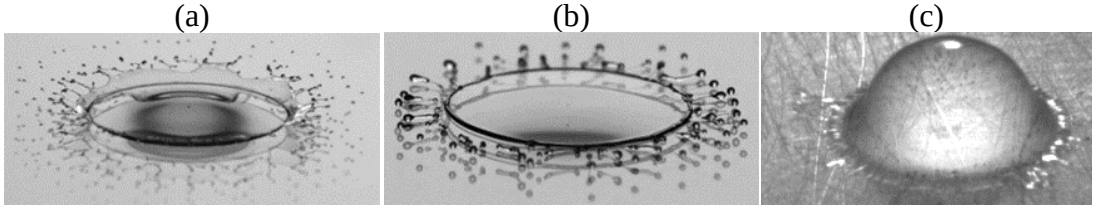

Figure 1- 13 (a) Corona splashing and (b) receding breakup of droplets on a smooth sold surface [124]. (c) Prompt splashing of a droplet on a rough sold surface [125].

As a special one of miscellaneous outcomes, a straightforward and essential calling is to find a criterion that clearly delimits the deposition and splash. On a smooth dry surface, the two splashing patterns are the corona splash and the receding break-up [124], as shown in Fig. 1.13(a) and 1.13(b). Specifically, the corona splash displays that the rim of lamella rolls up and then shatters into thousands of tiny pieces, while the humped fingers break up from the receding lamella in the receding break-up. In addition, when the surface is rough, the prompt splash (small shatters jet directly along the contact line) usually occurs [125, 126], as shown in Fig. 1.13(c).

When the impacting velocity is sufficiently high, a thin-sheet splash typically occurs on a smooth surface. Recently, Qin et al. [121] identified the thin-sheet splash as three sub-patterns in terms of different disintegration locations (levitated film, ligaments, or rim), and also obtained the phase diagram of outcomes of the droplet impact by varying Webber number ($We = \rho D U^2/\sigma$) and Ohnesorge number ($Oh = \mu/\sqrt{\rho\sigma D}$), as shown in Fig. 1.14. When the surface is heated, thermos hydraulic behaviours of the impacting droplet arise such as film evaporation, nucleate boiling, transition boiling and film boiling[127]. Therefore, the regime map of the droplet impact on a heated surface involves both kinetic and thermodynamic aspects and would be more complicated than the isothermal condition.

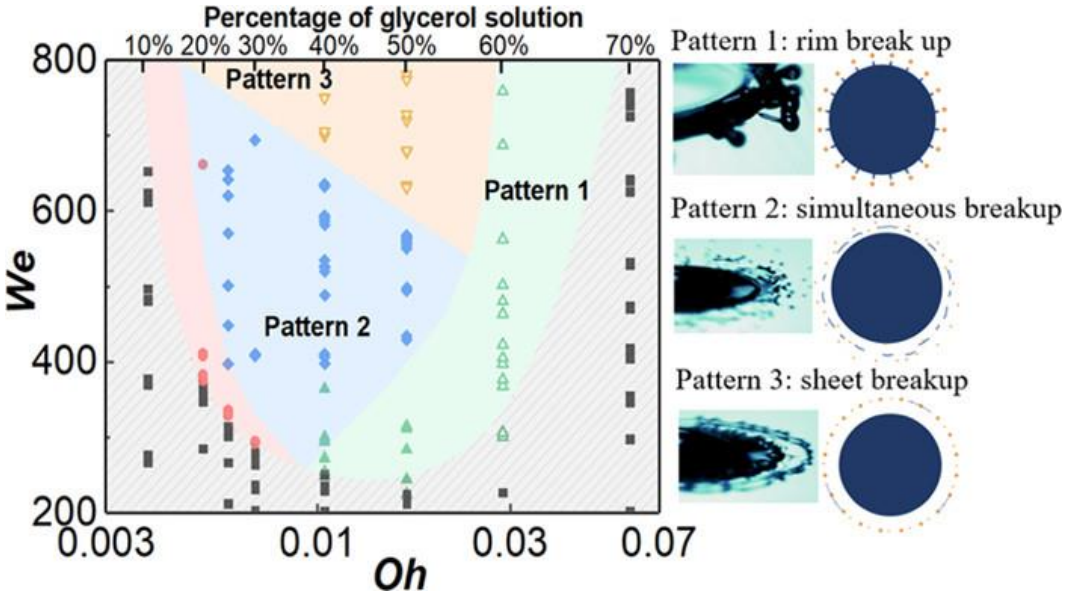

Figure 1- 14 Four impact outcomes of deposition, prompt splash, rim break up, simultaneous breakup, and sheet breakup in the space of We and Oh [121].

Many previous studies have focused on effects of the wall temperature (T_{W}) on outcomes of the droplet impact. Bertola [128] experimentally studied the impact morphology of a water droplet on a heated surface and defined five impact regimes as secondary atomization, rebound, splash, rebound with secondary atomization, and

splash with secondary atomization. Liang et al. [129] identified three outcomes (reflection rebound, explosive rebound, and explosive detachment) and found that T_{W} can affect the maximum spreading diameter and the rebound time in the rebound regime. On superheated surfaces, three regimes (contact boiling, gentle film boiling, and spraying film boiling) of water droplet impact were identified by Tran et al. [130]. With Weber number increasing, the transition temperature (the so-called dynamic Leidenfrost temperature, T_{L}) of the former two regimes increases monotonically, while one of the latter two regimes decreases gradually due to the bursting of vapour bubbles inside the liquid film. Staat et al. [131] investigated the phase diagram of ethanol droplets impacting on a temperature-controlled sapphire plate and reported four outcomes of deposition, contact-splash, bounce, and film-splash in Fig. 1.15. While they found T_{L} is weakly dependent on We, the splash threshold (critical We) shows a monotonic dependence on temperature up to T_{L}.

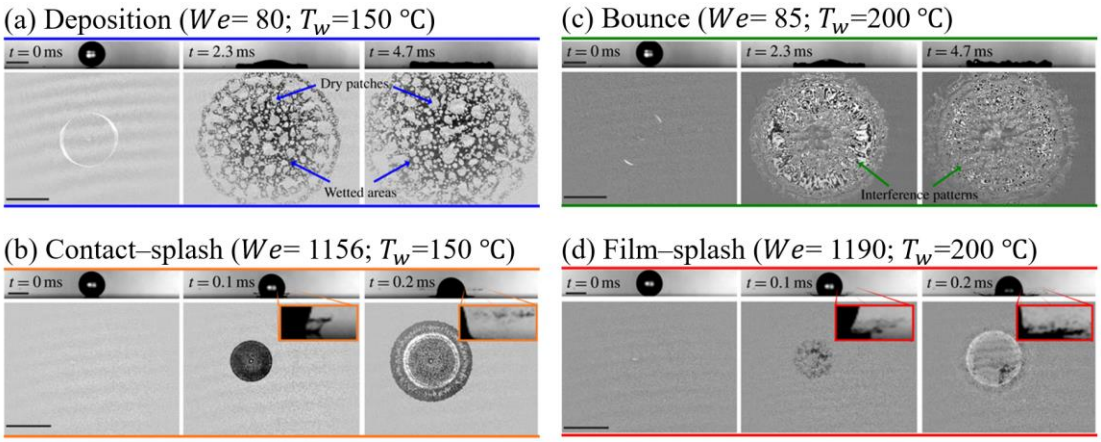

Figure 1- 15 Four impact outcomes of ethanol droplets on a sapphire plate [132].

In addition, the droplet/heated-wall impact can be dramatically altered by the surrounding gas, liquids, and surface properties [133, 134]. Tran et al. [135] reported that the T_{L} of water droplets can be varied by controlling the surface roughness (i.e., micro-structures fabricated on silicon surfaces). On a textured and chemically treated

surface, Zhang et al. [136] mapped six distinct impact modes (wetting, contact boiling, transition, breaking, rebounding, rebounding with satellite) of de-ionized water droplets in the parameter space of We (up to 85) and T_{W} (up to 320℃). Jadidbonab et al. [137] investigated the influence of ambient pressure on diesel droplets impacting on a heated aluminum substrate and identified six regimes in the parametric space of We and T_{W}.

1.8 Droplet Complete Rebound on Surface

The complete rebound refers to the phenomenon that the entire drop rebounds on the surface after impact, while the partial rebound refers to that a part of the drop remains attached to the surface even though the droplet mass centre has rebounded. Chen et al. [138] showed that completely rebounding droplets have a lower and an upper threshold of the impact velocity U_0, which are much smaller than the velocity to make the partial rebound occur. Previous works have studied the influences of various factors on the complete rebound of a droplet impacting a solid surface [106], such as contact angle [139] and roughness [140]. Yang et al. [124] systematically showed the critical We numbers of the complete droplet rebound from different liquids and soft surfaces. The physical mechanisms of the lower and upper critical Weber number cases are also analyzed and explained, as shown in Fig. 1.16.

In addition, Antonini et al. [139] reported that the complete rebound can be observed only when the receding contact angle is greater than $100°$. Bartolo et al. [140] observed that the drop bounced off a hydrophobic rough surface at certain velocities. Okumura et al. [141] neglected the effect of liquid viscosity and established a model for bouncing drops on a super-hydrophobic substrate. Sanjay et al. [142] elucidated the mechanism of bouncing inhibition in the limiting regimes of heavy and viscous droplets.

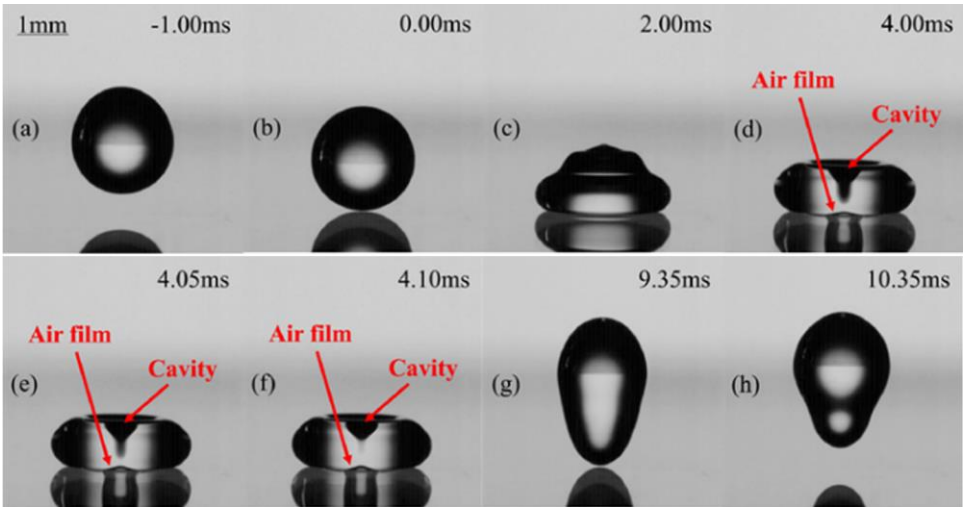

Figure 1- 16 The droplet rebounds completely on a soft surface [124].

Recent studies have found that droplets under suitable conditions can also achieve a full rebound when surfaces are flexible hydrophobic. Chen et al. [138, 143, 144] systematically studied the physical mechanism of the complete rebound of water droplets impinging the viscoelastic surface at the low Weber number ($We < 3.4$) and gave the critical impact velocities of the complete rebound. To quantify the energy loss of a bouncing droplet, a recovery coefficient, e (also called the restitution coefficient [145-149]) is defined as the ratio of the rebound and impact velocities, U_1/U_0. Biance et al. [146] found e abruptly increases from 0 to a maximum value of about 0.85 with increasing U_0 from 10 cm/s to 25 cm/s and then decreases gradually with further increasing U_0. Recently, Thenarianto et al. [149] proposed simple scaling relations $e = (1 - 12C/We)^{1/2}$ and $e \sim (2/We)^{1/4}$ at relatively small and large We respectively, where C is a small parameter relating to the material property of surfaces.

1.9 Research Overview and Objectives

In summary, the aforementioned literature covers two physical problems: the first focuses on flickering flames, vortex dynamics, flame behaviour in swirling flows, and various dynamical modes of coupled flickering flames; the second problem examines

droplet splash and rebound on smooth surfaces. These issues are fundamental for understanding the physical processes of flame and droplet involved in complex flame dynamics and spray impingement within combustors. Therefore, this thesis is motivated to investigate flame-vortex dynamics and droplet-surface interactions through both theoretical and computational approaches. The combination of flame and droplet dynamics is beneficial to modelling spray flames, but it is absent in this thesis.

The present thesis focuses on two parts: 1) the dynamics of flame and vortex in multiple coupled flickering flames, with emphasis on the identification and physical interpretation of distinct dynamical modes, and 2) the dynamics of droplet and surface in droplet impact, with emphasis on the determinations of splash threshold on the unheated or heated surface as well as the theoretical modelling of complete rebound of oscillating droplet.

Part I mainly includes two issues: the synchronization modes of multiple coupled flickering flames and the dynamical behaviours of single flickering flames in rotatory flows. In nature, both problems are involved with the flame-vortex and vortex-vortex interactions, but the different emphasises on the surrounding flows with a swirl or not. According to the comprehensive literature review in chapters 1.1-1.5, in-depth investigations are potential, while abundant phenomena are experimentally observed and model analyses are given. Hereto, a few research gaps can be identified, particularly the underlying mechanisms of various dynamical modes observed in experiments as well as the analysis approaches of the physical problems. In this part, there are some key problems to be addressed:

1. What are the synchronization patterns for coupled multiple flames? Building on the understanding of dual-flame synchronizations, it is crucial to extend the investigation of flickering flames to include group flickering modes of multiple

coupled flames, which exhibit vibrant dynamics and have greater relevance to real-world fires and industrial applications.

2. What is a general dynamics model for representing coupled multiple flames in circular arrays? This model should also probe the nonlinear effects of vortex-vortex interactions on collective flame behaviours
3. What is the scaling law for flickering flames under complex flow conditions? For instance, it should be applicable to rotating environments when calculating frequency. The applicable ranges should be clarified further.
4. When the rotational strength reaches a sufficient level, do buoyant diffusion flames flicker and possibly lift off? Numerous previous experiments have shown that flames become more pronounced, such as the occurrence of fire whirls and blue whirls, when the surrounding swirl is altered across a wide range. The mechanisms behind these stabilizations deserve more in-depth study.

Part II mainly includes two issues: the splash threshold of a droplet impacting on dry smooth unheated and heated surfaces and the complete rebound of oscillating droplets impacting on dry smooth surfaces. In nature, both problems are involved with the droplet-air and droplet-surface interactions but emphasize different droplet outcomes. According to the comprehensive literature review in chapters 1.6-1.8, in-depth investigations are potential, while abundant phenomena are experimentally observed and model analyses are given. Hereto, a few research gaps can be identified, particularly the underlying mechanisms of splashing and rebounding behaviours observed in experiments as well as the unified splash criterion of the droplet splashing. In this part, there are some key problems to be addressed:

1) What roles does liquid viscosity play in affecting the transition between deposition and splash? The experimental finding shows that the critical Weber number We of

droplet disintegration decreases and then increases with increasing viscosity of droplets. The non-monotonic effect of viscosity manifests in different splash regimes and is of vital importance in quantitatively predicting the droplet distribution in a spray combustion system.

2) How does thin-sheet splash on a heated surface exhibit different regimes in the three-dimensional phase diagram of $Oh - We - T_{\mathrm{W}}$? The wall temperature (T_{W}) is essential in determining the outcomes of the droplet impact, as T_{W} can cause the phase change and the corresponding regimes are totally distinct. Understanding splash on heated surfaces is beneficial to industrial applications, for example, internal-engine combustion and spray cooling.
3) What is a unified splash criterion that can perform well in a wide range of controlling parameters? Many previous criteria are limited to the valid scopes, or expressed in piecewise approximations, due to the nonmonotonic effects of liquid viscosity and ambient gas. A unified scaling law of droplet splash is conducive to establishing simple and efficient models in simulations of spray and spray combustion.
4) Why does the recovery coefficient of droplet complete rebound exhibit a fluctuating trend with increasing We? Experimental results show that the droplet can rebound on the non-superhydrophobic surface, and the recovery coefficient has fluctuation variations with increasing We. The shape deformation of the droplet before impacting the surface is concerned and theoretically interpreted.

1.10 Thesis Structure and Related Publications

The thesis remaining is organized as Chapters 2-7 for dynamical behaviours and modes of flickering buoyant diffusion flames, Chapters 8-10 for splashing threshold

and rebounding modelling of droplet impacting on surfaces, and Chapter 11 for concluding remarks and future work. Chapter 2 gives a detailed introduction to the computational methodology of simulating flickering flames with various assumptions and models, as well as the computation validation of single flickering flames. The chapter is the base of simulation results in Chapters 3-7.

In the thesis, most studies on the problems presented in Parts I and II have already been published as journal articles.

Chapter 3: Flickering flames in weakly rotating flows are explored through computational and theoretical approaches. Related work is published in Theoretical and Computational Fluid Dynamics, 37 (6), 781-798 (2023).

Chapter 4: Flickering buoyant diffusion flames are examined computationally under the swirling flows. Various distinct dynamical behaviours of the flames are identified and characterized. Related work is published in Symmetry, 16(3), 2920 (2024).

Chapter 5: Flickering modes of dual flames are studied through numerical simulations and theoretical analysis. from the perspective of vortex dynamics. Related works are published in Physical Review Fluids, 4(5), 053202 (2019) and arXiv preprint arXiv:2312.02018 (2023).

Chapter 6: Triple flickering buoyant diffusion flames with symmetric and asymmetric arrangements were computationally investigated and physically interpreted. Related work is published in Proceedings of the Combustion Institute, 39 (2), 1893-1903 (2022).

Chapter 7: Collective behaviours of octuple flickering flames in circular arrays are investigated in computational and modeling manners. Related work is published in arXiv preprint arXiv:2312.02018 (2023).

Chapter 8: Droplet impact on a smooth solid surface without and with heating is physically interpreted and modeled. Related works are published in Langmuir, 37(36), 10838-10848 (2021) and Langmuir, 38(2), 810-817 (2021).

Chapter 9: Two combinations, Π_L and Π_G, in four dimensionless numbers regime (Re, Oh, Kn and μ_G/μ_L) are utilized to characterize the threshold between deposition and splash of droplets impacting on a smooth solid surface.

Chapter 10: A theoretical model of oscillating droplet rebound is established for the fluctuating recovery coefficient over a wide impacting range. Related work is published International Journal of Multiphase Flow, 178, 104901 (2024).

Part 1

Vortex-dynamics and Synchronization of Multiple Flickering Diffusion Flames

Chapter 2. Computational Methodology

In combustion science, fire or flame is arguably considered a complex phenomenon, in which fluid dynamics, combustion, kinetics of chemical reaction, radiation, and phase transition from liquid to gas are closely linked together. In many cases, fluid dynamics and combustion are predominant and can be investigated numerically by using computational fluid dynamics (CFD), which has been a cost-effective and time-efficient manner to aid experimental investigations and design development. By using computers to perform the calculations required to simulate the interaction of liquids and gases with surfaces defined by boundary conditions, CFD, often predicting real-world behaviour with considerable accuracy, allows engineers and scientists to model and predict how fluids will behave in a variety of scenarios. For example, designing aircraft, missiles, and spacecraft in aerospace, analyzing wind effects on buildings, bridges, and other structures in civil engineering, optimizing wind turbines, hydroelectric dams, and combustion processes in energy, and modelling pollutant dispersion and water treatment processes in environmental engineering.

For fire and flame dynamics, CFD has been widely utilized to understand, predict, and control behaviours of various reacting flows. Actually, mathematical modelling of the fire has been developed widely to solve and analyze problems that involve fluid flows [150]. In this chapter, we mainly introduce the basic frames of the numerical methodology used in simulating flickering flames.

2.1 Fire Dynamics Simulator

Computational fluid dynamics method of the present problem is used as Fire Dynamics Simulator (FDS) [151], first released to the public in 2000 and developed by the National Institute of Standards and Technology (NIST). FDS is an open-source

program coded in FORTRAN language for solving practical fire problems and provides a tool to study fundamental fire dynamics and combustion. Here are some key features and capabilities of FDS:

Hydrodynamic Model The Navier-Stokes equations are simplified for low-Mach and thermally-driven flow conditions and solved numerically. The central algorithm employs an explicit predictor-corrector scheme, which achieves second-order accuracy in both space and time. By using a sufficiently fine numerical mesh, Direct Numerical Simulation (DNS) can be conducted, whereas a turbulence model is utilized for Large Eddy Simulation (LES).

Combustion Model A single-step, mixing-controlled chemical reaction is adopted mostly, in which three lumped species (air, fuel, and products) are used. Multiple and complex reactions that are not necessarily mixing-controlled are available.

Radiation Transport Radiative heat transfer is included by solving the radiation transport equation for a grey gas, which is similar to finite volume methods for convective transport.

Geometry The governing equations on a rectilinear mesh system are computed so that rectangular configurations are well captured. Multiple meshes are available to refine the local region of the computational domain.

Parallel Processing Message Passing Interface (MPI) is employed to use multiple processing units on computer clusters for large-scale computations.

Boundary Conditions It is flexible to assign a variety of boundary conditions for gas, liquid, and solid surfaces. Obstruction is treated by the immersed boundary method.

Output and Post-Processing Comprehensive data of computations are saved and exported for analysis. A companion program for visualizing FDS simulation results, including temperature, velocity fields, concentrations of gases, and other variables.

User Interface and Scripting A straightforward text-based input file format is adopted for specifying simulation parameters. Scripting is supported to automate simulation setups and batch processing.

Over the past ten years, FDS has been extensively demonstrated to be effective in capturing unsteady and dynamic phenomena in fire-induced flow problems, including the soot model of laminar flames [152], small-scale fire whirls [66, 153, 154], large eddy simulation of turbulent buoyant flames [155-157], and nonlinear dynamics of turbulent flames [158-160]. Specifically, a 1 m diameter methane pool fire was simulated qualitatively and quantitatively by FDS [156]. Burning rates of liquid heptane were simulated [161] for a very well results with the experiments. The radiation solver of FDS was evaluated for modeling small pool fires [21]. In particular, our works presented in this thesis on the single flame in rotating flow [162], dual interacting flames [163], and triple interacting flames [164] have shown the reliability of this computational platform in accurately replicating flame and vortex interactions flickering flames, corresponding to various dynamic behaviors observed in experiments.

2.2 Mathematical Model

The equations governing the evolution of a low-Mach, variable-density fluid are continuity, momentum, energy (sensible enthalpy), and the ideal gas equation of state:

$$\frac{\partial \rho}{\partial t} + \nabla \cdot (\rho \boldsymbol{u}) = 0 \tag{2.1}$$

$$\frac{\partial}{\partial t}(\rho \boldsymbol{u}) + \nabla \cdot (\rho \boldsymbol{u}\boldsymbol{u}) = -\nabla p' - \nabla \cdot \boldsymbol{\tau} + (\rho - \rho_\infty)\boldsymbol{g} \tag{2.2}$$

$$\frac{\partial}{\partial t}(\rho h_s) + \nabla \cdot (\rho h_s \boldsymbol{u}) = \frac{DP}{Dt} + \dot{q}''' - \nabla \cdot \dot{\boldsymbol{q}}'' \tag{2.3}$$

where ρ is the mass density and $\boldsymbol{u} = (u, v, w)$ the velocity vector; the spatially and temporally resolved pressure consists of the pressure perturbation p' and the

backpressure P, $\boldsymbol{\tau}$ the viscous stress tensor, ρ_∞ the background air density, and $\boldsymbol{g} = (0,0,-g)$ the gravitational acceleration vector; h_s is the sensible enthalpy (a mass-weighted average of the enthalpies of the individual gas species), $\dot{q}'''$ the heat release rate per unit volume, and $\dot{\boldsymbol{q}}''$ the conductive and diffusive heat fluxes.

Due to the occurrence of the flame flicker in liquid-pool and gas-jet flames, the present simulations also consider the diffusion flames of liquid pools. Specifically, the continuity equation should contain an extra term of $\dot{m}_F$ for the mass production rate per unit volume of liquid or solid fuel by evaporation. In this way, Eq. (2.1) is rewritten as

$$\frac{\partial}{\partial t}(\rho) + \nabla \cdot (\rho \boldsymbol{u}) = \dot{m}_F \tag{2.4}$$

where $\dot{m}_F$ is moulded as a boundary condition according to the Clausius-Clapeyron relation [151], as the volume fraction of the fuel vapour above the surface is a function of the liquid boiling temperature. In the present simulations, the mass production of liquid fuel is implemented at the surface of the liquid pool (a boundary condition with evaporation of the fuel), as there is no consideration of the internal mass and heat transfer in the pool. It is worth noting that pool flames and jet flames can generate similar flickering behaviours when the flame size and gravity are appropriate [24]. In other words, the flickering frequency is insignificantly affected by the evaporation of liquid fuels.

In addition, Eq. (2.3) is not solved explicitly but satisfied through guaranteeing the velocity divergence, which is factored out as follows:

$$\nabla \cdot \boldsymbol{u} = \frac{1}{\rho h_s}\left[\frac{D}{Dt}(P - \rho h_s) + \dot{q}''' - \nabla \cdot \dot{\boldsymbol{q}}''\right] \tag{2.5}$$

where h_s is calculated by summing $h_{s,i} = TY_i c_{p,i}$ of all gas species, where T is the temperature, Y_i the mass fraction of specie i, and $c_{p,i}$ the specific heat of specie i at constant pressure; $\dot{q}'''$ is calculated by summing $\dot{m}_i''' \Delta h_{f,i}$, where $\dot{m}_i'''$ is the mass

production rates of specie i and $\Delta h_{f,i}$ is the respective heats of formation; $\dot{\boldsymbol{q}}''$ contains $-k\nabla T$ and $-\sum_i \rho h_{s,i} D_i \nabla Y_i$, where k the thermal conductivity and D_i is the diffusivity of species i. The background pressure is retained in the equation of state (ideal gas law)

$$P = \frac{\rho \mathcal{R} T}{\overline{W}} \tag{2.6}$$

where $\overline{W}$ is the molecular weight of the gas mixture, $\mathcal{R}$ the universal gas constant, and T the temperature. Finally, the transport equations of Y_i need to be solved for closure of the governing equations.

In the context of the thermally induced motion of a flickering flame, buoyancy forces play a dominant role. The dynamic patterns and structures observed in flames remain largely uninfluenced by assumptions related to rapid chemical reactions. The primary driver of the flame's behavior is the thermal buoyancy effect rather than the speed of the chemical processes involved [165]. Our recent works [162, 166] compared infinitely fast chemistry and one-step finite rate chemistry for reproducing flickering flames and confirmed that the reaction has slight influences on the flickering frequency. Thus, to avoid the complexity and high computation cost of a detailed reaction mechanism, the mixing-limited, infinitely fast reaction was used to calculate species mass fractions and the heat release rate. Specifically, the single-step reaction of methane and air is adopted to simplify the combustion in buoyancy-dominated flames. The transport equations of five gas species (CH_4, O_2, CO_2, H_2O, and N_2) are solved explicitly by

$$\frac{\partial}{\partial t}(\rho Y_i) + \nabla \cdot (\rho Y_i \boldsymbol{u}) = \nabla \cdot (\rho \mathcal{D}_i \nabla Y_i) + \dot{m}_i''' \tag{2.7}$$

where Y_i is the mass fraction of specie i, $\mathcal{D}_i$ the diffusion coefficient, and $\dot{m}_i'''$ the mass production rate per unit volume by chemical reactions. For the evaporation mass from the liquid or solid surfaces, Eq. (2.7) should be

$$\frac{\partial}{\partial t}(\rho Y_i) + \nabla \cdot (\rho Y_i \boldsymbol{u}) = \nabla \cdot (\rho \mathcal{D}_i \nabla Y_i) + \dot{m}_i''' + \dot{m}_F \tag{2.8}$$

To ensure the realizability of species mass fractions (i.e., $Y_i \geq 0$ and $\sum Y_i = 1$), FDS's strategy is to solve all species equations for $\rho = \sum(\rho Y)_i$ and then to obtain mass fraction by $Y_i = (\rho Y)_i / \rho$. Specifically, the primitive species are lumped into reacting groups, such as $Fuel + Air \rightarrow Products$ and the lumped species approach (a simplified reaction progress variable approach [167]) is used to avoid any complications related to boundedness and ill-defined initial and boundary conditions. More details on the simplified approach will be expounded in the next section.

The basic solution procedure of the governing equations is a predictor-corrector explicit-time integration scheme for capturing unsteady and dynamic processes in thermally driven buoyant flows. All the spatial derivatives of the governing equations are discretized by the finite difference method on structured, uniform, staggered grids in parallel using MPI libraries. A staggered grid is used to assign scalar quantities to the centre of each cell and vector components at the cell faces. The time step is adjusted to ensure numerical stability by checking the Courant–Friedrichs–Lewy (CFL) condition at the end of the prediction step. The solver algorithm has evolved over roughly three decades. Further details of the solver and a wide array of validation/verification applications can be found in [151].

2.3 Sub-models of Combustion

In the species transport equation of Eq. (2.7), the mean chemical mass production rate of species i per unit volume $\dot{m}_i'''$ need to be determined via modelling the chemical reactions in combustion. To ensure accurate modelling in cases where the grid spacing is generally tens of centimetres, a closure model becomes necessary due to the flame thickness being around one millimetre. For most large-scale fire scenarios, in which

non-premixed combustion and fast chemistry conditions prevail, the combustion model simplifies to the Eddy Dissipation Concept (EDC) [168], a straightforward "mixed is burnt" approximation. In addition, the heat release rate for per unit volume $\dot{q}'''$ is a critical parameter in fire physics, often the primary contributor to the velocity divergence as indicated in Eq. (2.5). By establishing $\dot{m}_i'''$, the combustion model allows for the calculation of the heat release rate through the summation of mass production rates for each species multiplied by their individual heats of formation.

In reactive flow, the number of transport equations we need to solve plays a vital role in speeding up simulations. To reduce the computational burden of the full chemical system and save time by tracking fewer species, FDS is able to combine species into groups that transport and react together. The mixing-controlled, fast chemistry combustion model is common, while kinetic mechanisms from infinitely fast chemistry to Arrhenius rate laws and reversible reactions are available. The focus of the thesis is the buoyance-driven thermal flow problems so that the mixing-mixed model is sufficient.

2.3.1 Lumped Species Approach

In FDS, the lumped species approach is a simplified reaction progress variable approach, in which all the progress variables are mass fractions. As long as the assumption that all primitive species in a lumped species are transported together is appropriate, the primitive species are lumped into reacting groups of $Fuel$, Air, and $Products$ and the simple reaction is considered by

$$Fuel + Air \Rightarrow Products \tag{2.9}$$

It is beneficial to steer clear of complexities associated with boundedness issues and ambiguities in defining initial and boundary conditions [151]. Assuming is appropriate,

as transport is driven by the diffusivity values and not the molecular values for most fire applications of FDS where grid cell sizes are centimetres or multiple centimetres.

Taking an example of methane and air reaction, we have the reactants of fuel Y_{CH_4} and air (oxygen Y_{O_2} and nitrogen Y_{N_2}) and the products of carbon dioxide Y_{CO_2}, water vapor Y_{H_2O}, and nitrogen Y_{N_2}. Consequently, we obtain a composition vector Y consisting of mass fractions of the primitive species:

$$Y = [Y_{O_2} Y_{N_2} Y_{CH_4} Y_{CO_2} Y_{H_2O}]^T \tag{2.10}$$

Air is regarded as a lumped species including O_2:N_2 = 21:79 by volume. Based on the key assumption of the primitive species transporting with equal diffusivities and reacting together, a one-step reaction of methane-air combustion can be expressed by

$$\underbrace{x(0.21O_2 + 0.79N_2)}_{Z_0,\ Air} + \underbrace{yCH_4}_{Z_1,\ Fuel} \Rightarrow \underbrace{y(CO_2 + 2H_2O + 0.79\,x/y\,N_2)}_{Z_2,\ Products} \tag{2.11}$$

where $0.21x = 2y$, Z_i denoted the mass fraction of lumped specie $i = 0,1,\dots,N$, where N is the specie number to track. $Z_0 = 1 - \sum_{i=1}^{N} Z_i$ corresponds to the background species.

In this way, only $Fuel$ and $Products$ transport equations need to be solved. Given the mass fraction of lumped species, we can employ the linear transformation for ones of primitive species by

$$\boldsymbol{Y} = A\boldsymbol{Z} \tag{2.12}$$

where the transformation matrix A consists of N_y species as rows and $N_z + 1$ lumped species as columns. For example, $\boldsymbol{Z} = [0.3\ 0.3\ 0.4]^T$, we can have lumped species as

$$Y = \begin{bmatrix} Y_{O_2} \\ Y_{N_2} \\ Y_{CH_4} \\ Y_{CO_2} \\ Y_{H_2O} \end{bmatrix} = \begin{bmatrix} 0.23 & 0 & 0 \\ 0.77 & 0 & 0.73 \\ 0 & 1 & 0 \\ 0 & 0 & 0.15 \\ 0 & 0 & 0.12 \end{bmatrix} \begin{bmatrix} 0.3 \\ 0.3 \\ 0.4 \end{bmatrix} = \begin{bmatrix} 0.069 \\ 0.523 \\ 0.300 \\ 0.060 \\ 0.480 \end{bmatrix} \tag{2.13}$$

Vice versa, we can transform back to lumped species from primitive species via

$$\boldsymbol{Z} = B\boldsymbol{Y} \tag{2.14}$$

where $B = (A^T A)^{-1} A^T$ is obtained according to the transformation matrix A.

2.3.2 Mixing-Controlled Fast Chemistry

In the majority of fire scenarios, employing the "mixed is burnt" assumption proves sufficient in simulating the reaction system, with the mean chemical source term for Fuel being represented through the EDC model [168]:

$$\dot{m}_F''' = -\rho \frac{\min(Z_0, Z_1/s)}{\tau_{mix}} \tag{2.15}$$

Where Z is the lumped mass fractions of $Fuel$ or Air, s represents the mass stoichiometric coefficient for Air, τ_{mix} is a time-scale quantity for mixing determined by the immediate condition of the flow field. Subsequently, the fuel consumption rate in the EDC model is directly related to both the prevalent concentration of the limiting reactant and the local mixing rate. The heat release per unit volume $\dot{q}'''$ is calculated by summing the species mass production rates times the respective heats of formation as

$$\dot{q}''' = -\sum_{\alpha} \dot{m}_{\alpha}''' \Delta h_{f,\alpha}^0 \tag{2.16}$$

where $\dot{m}_i'''$ is the mass production rates of specie i and $\Delta h_{f,i}$ is the respective heats of formation.

2.3.3 Fuel Vapor of Liquid Pool

In Eq. (2.4) and Eq. (2.8), the fuel mass rate of $\dot{m}_F'''$ caused by liquid evaporation is obtained by Stefan diffusion.

$$\dot{m}_F''' \sim \ln\left(\frac{X_{F,g} - 1}{X_{F,l} - 1}\right) \tag{2.17}$$

where $X_{F,g}$ and $X_{F,l}$ are the volume fraction of fuel vapor adjacent to and above the pool surface, respectively. According to the Clausius-Clapeyron relation [169], the fuel vapor is a function of the liquid boiling temperature:

$$X_{F,l} = exp\left[\frac{h_V}{R^o}\left(\frac{1}{T_b} - \frac{1}{T_s}\right)\right] \tag{2.18}$$

where h_V is the evaporation heat, T_b is the boiling point temperature, and T_s is the surface temperature. In addition, the pool surface in FDS has heat conduction, like a thermally thick solid, but no convection within the liquid pool.

2.3.4 The Radiant Heat Flux Vector

In large-scale fire simulation, the grey gas assumption is utilized to calculate the radiant heat flux vector in the energy equation

$$\dot{q}'' = \int_{4\pi} \boldsymbol{s} I(\boldsymbol{x}, \boldsymbol{s}) d\boldsymbol{s} \tag{2.19}$$

where $I(\boldsymbol{x}, \boldsymbol{s})$ is the total radiation intensity, $\boldsymbol{x}$ is the position vector, $\boldsymbol{s}$ the direction vector of the intensity. The equation is solved using a technique similar to finite volume methods for convective transport, thus the name given to it is the Finite Volume Method (FVM) [170]. However, the net contribution from thermal radiation in the energy equation is not considered in the present problems of small-scale diffusion flames.

2.4 Validation of Computational Methodology for Pool Flames

It is well-studied that the self-sustained flickering behaviour is contributed to the vortex dynamic [15, 23, 36]. Chen et al. [15] reported that vorticity was induced by the buoyancy gradient, resulting from ununiformed density distribution caused by the rapid and huge heat release near the flame sheet. From the view of dynamics, a single

flickering flame could be regarded as an oscillating system, here called the flame oscillator. In this section, we have set up simulations of single pool and jet flames and finished the validation with experiments and theoretical relations.

2.4.1 Numerical Configurations

In the present work, the computational analysis is conducted within a cubic domain measuring $16\times16\times24$ cm^3 with $160 \times 160 \times 240$ mesh. This domain utilizes a structured, uniform, and staggered grid system. In Figure 2.1(a), the outer boundaries of the domain, depicted in grey, are treated as non-solid exterior boundaries. These boundaries allow gases to flow in and out freely. The blue surface in the figure represents the liquid heptane fuel pool. At the bottom of each fuel pool, solid-wall boundary conditions are implemented. The buoyancy-induced velocity, U, is estimated by $\sqrt{gd}$ with $g = 9.8\ \mathrm{m/s^2}$ and ν_A is air viscosity of 1.6×10^{-5} $\mathrm{m^2/s}$ so that the Reynold number, $Re = Ud/\nu_A$ of pool flames is about 550.

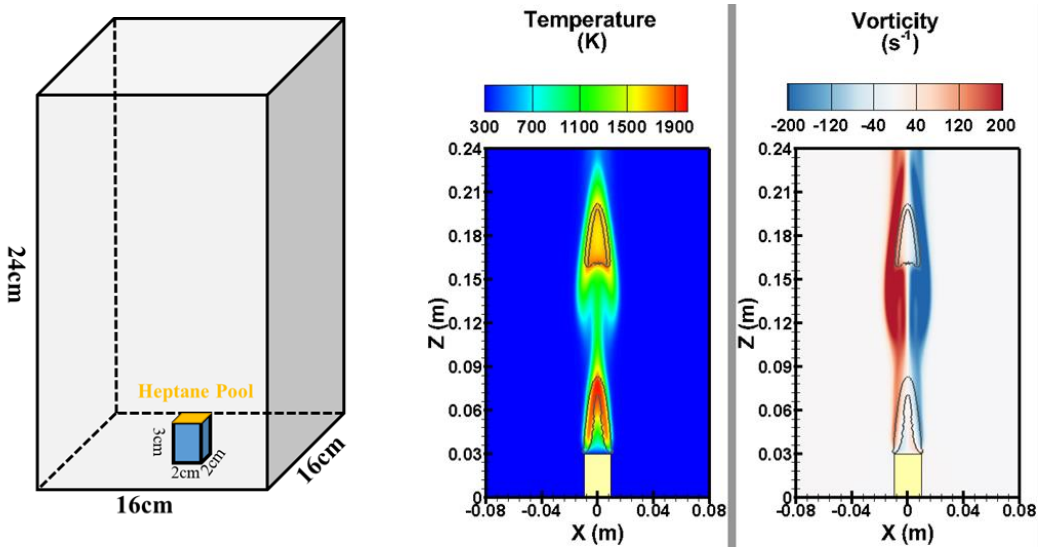

(a) (b)

Figure 2- 1 (a) Schematic of the computational domain for a square heptane pool flame. (b) Temperature and vorticity contours corresponding to the flame pinch-off.

This setup allows for an accurate simulation of the fuel pool's behavior and its interaction with the surrounding environment. Figure 2.1(b) shows the flame pinch-off depicted by the temperature and vorticity contours, in which the line denotes the flame sheet. Basically, the present simulations can capture the important flame flicker, which is key and base for the following works.

2.4.2 Grid- and Domain-independence Analysis

In a laminar flickering flame, the basic frequency is prominent, but the sub-harmonic frequencies always emerge and are difficult to capture, because they are below the basic frequency in a ratio of 2^n, with n being a positive integer number. For example, the basic frequency, f_0, and three sub-harmonic frequencies, f_1, f_2, f_3 for case 3 are 9.9, 19.8, 29.6, and 39.7, respectively in Fig. 2.2(a).

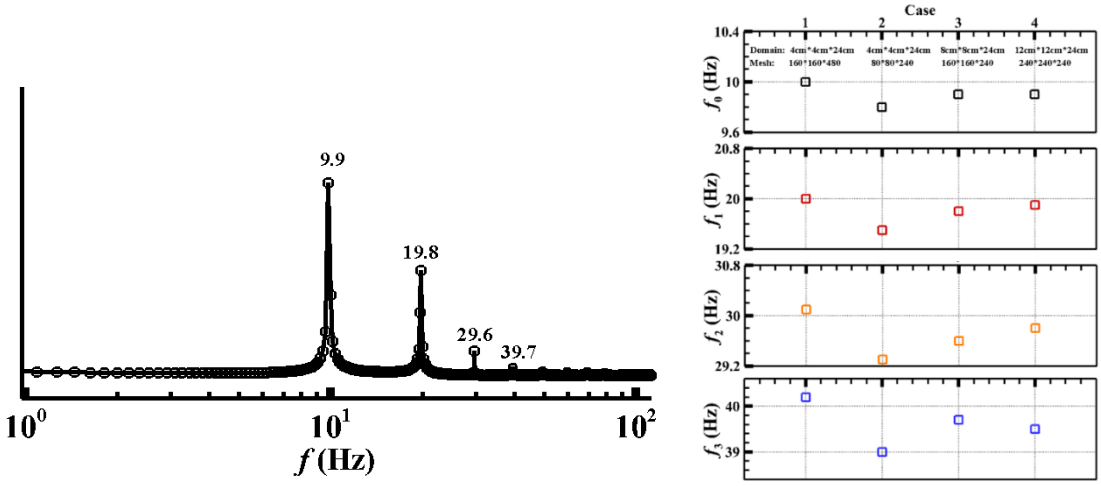

(a) (b)

Figure 2- 2 The frequencies of Case 3; The comparison of flame basic and sub-harmonic frequencies from Case 1-4.

The simulations were done by comparing the frequencies of four cases in Fig. 2.2(b). For a balance between computational cost and accuracy, we chose the grid and domain setting of Case 3, sufficiently satisfying the accuracy of capturing the

characteristic frequency of flickering flames. While the sub-harmonic frequencies, f_1, f_2, f_3 are not converged yet, the dominant frequency, f_0 is considered for the validations with experimental results (most experiments just reported f_0 information). Using a more refined mesh resolution can cause a higher computation cost but does not give a better understanding of flame flicker in the present problem.

Table 2- 1 Domain, mesh, and flickering frequencies of simulation cases.

Cases	Domain	Mesh	f_0	f_1	f_2	f_3
Case 1	4cm × 4cm × 24cm	160 × 160 × 480	10.0	20.0	30.1	40.2
Case 2	4cm × 4cm × 24cm	80 × 80 × 240	9.8	19.5	29.3	39.0
Case 3	8cm × 8cm × 24cm	160 × 160 × 240	9.9	19.8	29.6	39.7
Case 4	12cm × 12cm × 24cm	240 × 240 × 240	9.9	19.9	29.8	39.5

The grid- and domain-independence studies for the simulation of single heptane flames (20mm square pool) under normal gravity. The parameters of four cases are listed in Table 2-1. The frequencies were obtained by using Fast Fourier Transform (FFT) to analyze the burning mass of fuel for 10s at a 1000 Hz sampling rate. All data were sampled until the maximum and minimum burning rates converged.

2.4.3 Validation of Flickering Frequency

To verify the accuracy and reliability of the numerical method used in this study, simulations of flickering flames from various single pools were conducted. The flickering frequencies obtained from these simulations were then compared against both existing theoretical models and experimental data. This comparison serves as a validation process, assessing how well the adopted numerical approach aligns with established findings and real-world observations in flame behavior.

This validation step is crucial as it demonstrates the capability of the numerical method to accurately predict the dynamic behavior of flames, particularly their flickering frequencies, across different single-pool configurations. By benchmarking the results against both theoretical predictions and empirical measurements, the study establishes confidence in the numerical approach for further applications and analyses.

Previous studies have concluded a prominent scaling relation, $f = 0.48\sqrt{g/d}$, where f is the flickering frequency, g is the gravitational acceleration, and d is the characteristic length of the pool base. Figure 2.3 presents a comparison between the simulation results and previously established data. The simulations were conducted with varying gravitational acceleration (g) and pool diameter (d). The outcomes of these simulations show strong correlation with experimental data from previous studies [171-174] and the established scaling law [24, 172]. This alignment between the current simulation results and existing scientific knowledge serves as validation for the numerical methods employed in this study. It demonstrates that the computational approach used here is indeed appropriate and reliable for investigating the flickering behavior of pool flames.

The good agreement across different gravitational conditions and pool sizes further reinforces the robustness of the numerical methods. It suggests that the simulation can accurately capture the physics of flame flickering under various conditions, making it a valuable tool for studying this phenomenon in detail. The detailed simulation data of single pool flames with varying gravity, g, and pool size, d, as shown in Table 2-2. The pool sizes were chosen according to Drysdale's summary that the flames are laminar if the diameter of the liquid pool fire is less than 0.03m [175].

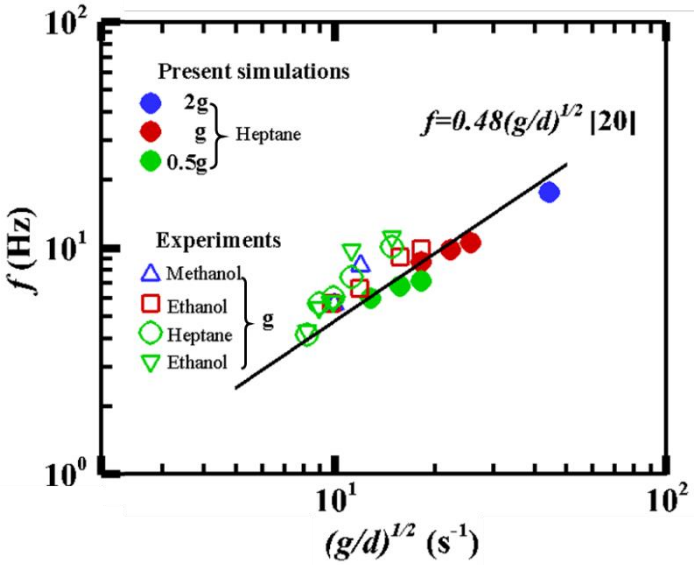

Figure 2- 3 Validation of single pool flames with the scaling law [16] and experiments obtained by Schönbucher et al. (Δ) [171], Maynard (□) [172], and Fang et al. (○,∇) [173].

Table 2- 2 Validation cases

Frequency, f (Hz)		Pool size, d (mm)			
(Error: 0.1)		10	15	20	30
Gravity, g (m/s^2)	4.9	-	7.2	6.8	6.0
	9.8	-	10.6	9.9	8.7
	19.6	17.7	-	-	-

2.5 Validation of Computational Methodology for Jet Flames

To further substantiate the reliability of the computational methodology and models used in this study for accurately representing the flickering behavior of buoyant diffusion jet flames, a series of additional simulations were performed. These simulations explored various combinations of jet diameter (d) and gravitational acceleration (g) in a quiescent environment. The validation process involves a qualitative comparison between flame morphologies observed during a complete

flickering cycle in the current simulations and experimental snapshots captured under nearly identical conditions

This comparison serves as an additional validation step, focusing on the visual aspects of flame behavior. By examining how well the simulated flame shapes and dynamics match those observed in real experiments, we can assess the capability of the computational approach to capture the complex, time-dependent characteristics of flickering flames. The qualitative validation described below aims to demonstrate that the present computational methodology not only produces numerically accurate results (as shown in the previous quantitative validation) but also realistically represents the visual phenomena associated with flame flickering.

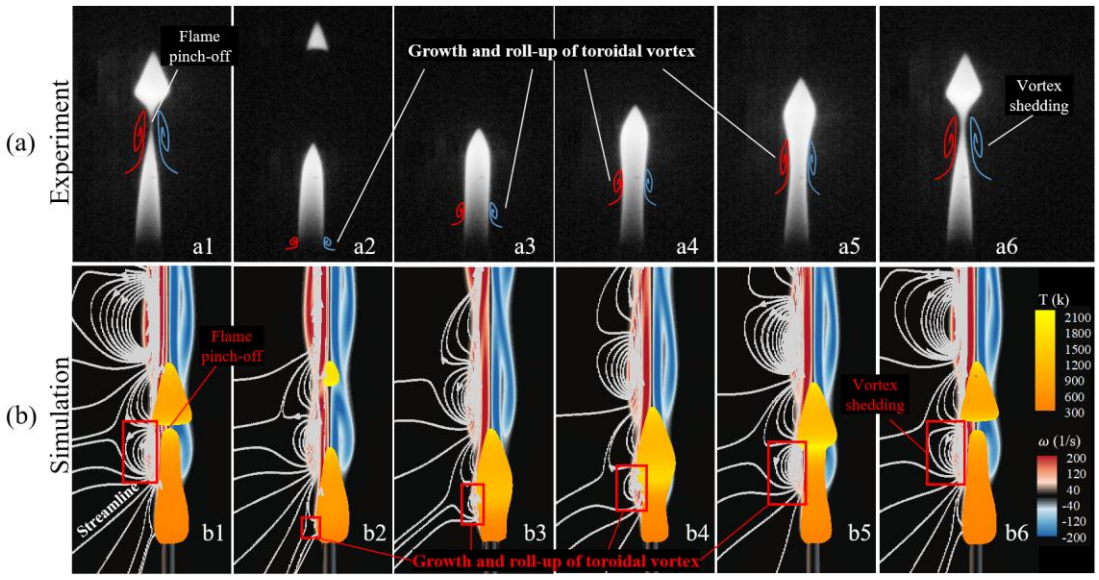

Figure 2- 4 Comparison of the flame flicker in (a) experimental and (b) numerical results of buoyant diffusion flame. The experimental snapshots are available in [102]. The present experiment and simulation have almost the same nozzle size of D=10 mm and nearly initial velocity of U=0.12 m/s.

Figure 2.4 shows the flame evolution of the experiment and simulation during a period. The flame pinch-off phenomenon results from vorticity accumulation in a

toroidal vortex, visualized by spiral streamlines. This vortex induces high velocities near the flame's center, causing the flame neck to deform and ultimately rupture. Post-rupture, the upper portion of the flame is carried downstream with the toroidal vortex. Overall, the computational results have similar flame shapes in the flickering dynamics, while further quantitative validations of flame morphologies, such as flame height, flame width, and pinch-off height, need to be implemented.

Before making a quantitative validation, it is necessary to draw out the physical picture of flickering dynamics. Specifically, a snapshot of the flickering buoyant diffusion flame at $D = 10$ mm and $g = 9.8$ m/s^2 is illustrated in Fig. 2.5(a) and 2.5(b). Around the flame, the outside shear layer (denoted by the vorticity contour) rolls up to form the toroidal vortex (denoted by the curly streamlines). The flame (denoted by the isoline of heat release) is pinched off into two parts (the main flame anchored to the ground and the separated flame bubble) by the vortex at $\hat{z} = 6$.

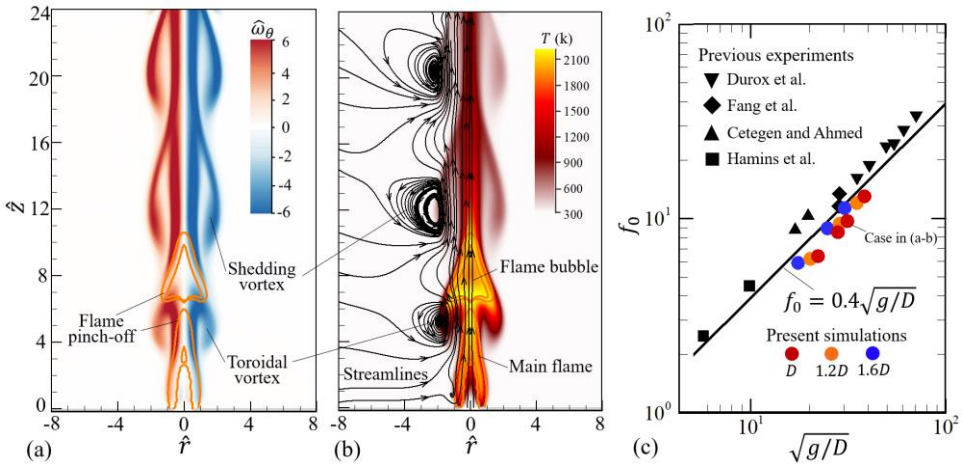

Figure 2- 5 The contours of (a) vorticity $\widehat{\omega}_\theta$ and (b) temperature T of a flickering buoyant diffusion flame. The black curly lines are the streamlines. The flame is denoted by the orange isoline of heat release at 5 MK/m^3. (c) The validation of single flickering jet flames (●●●) with the scaling law of $f_0 = 0.4\sqrt{g/D}$ and experiments obtained by Durox et al. (▼), Fang et al. (♦), Cetegen and Ahmed (▲), and Hamins et al. (■).

Figure 2.5(c) demonstrates that the flickering frequencies obtained from our current simulations show good agreement with experimental data from previous studies. This correlation is clearly evident in the graphical representation, indicating that the computational model accurately captures the oscillatory behavior of flickering flames as observed in experiments. [16, 174, 176, 177] at a small error range (<10%) and particularly predict the famous scaling relation of $f_0 \sim \sqrt{g/D}$ [14, 24], where the proportionality factor of 0.4 is close to 0.48 obtained from plenty of experimental data reported in the literature [24]. The specific parameters of validation cases are listed in Table 2-3.

Table 2- 3 The flames parameters in ten cases with different D, U_0 and g.

D (mm)	U_0 (m/s)	g(m/s^2)	f (Hz)	fD/U_0	Fr	Re
10	0.165	9.8	9.7	0.59	0.28	100
10	0.165	4.9	6.4	0.39	0.56	100
10	0.165	7.8	8.5	0.52	0.35	100
10	0.165	14.7	13.	0.79	0.19	100
12	0.165	9.8	9.4	0.68	0.23	120
12	0.165	4.9	6.2	0.45	0.46	120
12	0.165	14.7	11.9	0.87	0.15	120
16	0.103	9.8	8.9	1.38	0.07	100
16	0.103	4.9	5.9	0.92	0.14	100
16	0.103	14.7	11.3	1.76	0.05	100

In addition, we found that the gravity changes of $(0.5g - 1.5g)$ can significantly affect the flickering frequency, confirming that the buoyancy is predominant in the present diffusion flames. The boundary flow near the bottom wall has negligible

influence on the flickering of laminar diffusion flames, as the growth and shedding of the toroidal vortex occur downstream far from the bottom. Carpio et al. [178] reported that, in a strongly rotatory flow, the bottom corner flow might result in the lift-off of the flame base, which is absent in the problem focusing on weakly rotatory flows. Overall, present results show that computations can sufficiently reproduce flame flicker.

2.6 Dynamical Oscillator Model for Flame Flicker

Nonlinear dynamics of coupled oscillators is a long-lasting problem in the science of complex systems [179, 180]. The collective behaviours of coupled flickering flames are complex synchronization phenomena that widely occur across different fields such as physics, chemistry, biology, etc. The first human observation of synchronization was the coupled pendulum experiment by C. Huygens, in which several coupled pendulums, starting at random, achieve synchrony through mutual interaction [101]. To explore such phenomena, Kuramoto [181] proposed a simple yet insightful nonlinear model to describe the collective behaviour of N identical oscillators by

$$\frac{d\theta_m(t)}{dt} = \omega_m + \frac{K}{N}\sum_{n=1}^{N} \sin[\theta_n(t) - \theta_m(t)]\,, n = 1 \dots N \tag{2.20}$$

where $\theta_m(t)$ is the instantaneous phase of the mth oscillator at time t, $d\theta_m/dt$ its time derivative, ω_m the natural frequency, N the number of oscillators, and K represents the coupling strength between mth and nth oscillators. The model system requires only two types of parameters, including the coupling constant K and the intrinsic frequency ω_m, to display the rich dynamic behaviours of phase oscillators, which have been usually used to understand and predict synchronization in various real-world systems, including neuroscience, ecology, engineering, and social sciences [182].

Recently, Chi et al. [183] reported that the Kuramoto model failed to model the flickering death and partially flickering death modes experimentally observed as the

amplitude suppression of the flame flicker because the model only characterizes the information of phase but does not contain any information about the amplitude. Considering the evolution of the flame magnitude, they attempted the Stuart-Landau model [184] to investigate the coupled nonlinear dynamical systems with identical flame oscillators, especially for the study of amplitude death mode. Noteworthy, amplitude death is undesired in many systems, where oscillation is normal functioning, but oscillation disappearance is desired in combustion applications.

In the nonlinear dynamics field, the Stuart-Landau (S-L) model [184] has been universally accepted in helpfully explaining the behaviours of chemical, biological, and quantum oscillator systems, particularly the emergence of amplitude death. The well-known Stuart-Landau oscillator is expressed as:

$$\frac{dZ(t)}{dt} = (a + i\omega - |Z(t)|^2)Z(t) \tag{2.21}$$

where $Z(t) = \sqrt{a}e^{i\omega t}$ can be rewritten as a complex variable of $\sqrt{a}[\sin(\omega t) + icos(\omega t)]$ to represent the oscillation state, $dZ(t)/dt$ the time derivative of Z, $\sqrt{a}$ the oscillation amplitude ($a > 0$), and ω the intrinsic frequency of the oscillator. The term of $|Z|^2Z$ represents the nonlinear saturation that stabilizes the amplitude of the oscillations. More details on the S-L model can be referred to [184].

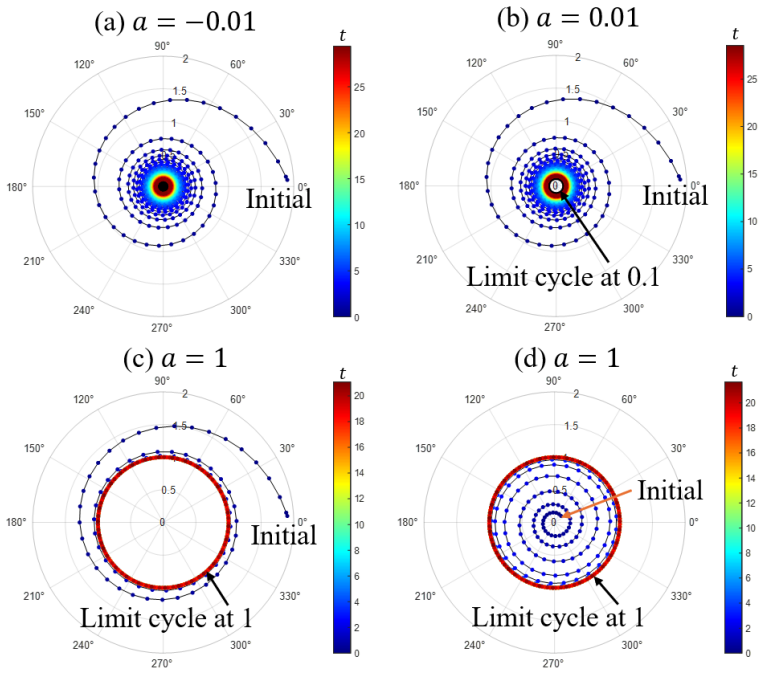

Figure 2- 6 Polar coordinate of Stuart-Landau oscillator with $a =$ (a) -0.01, (b) 0.01, (c) 1, and (d) 1. The initial point is (a-c) (1.9, 3°), and (d) (0.1, 30°), while the natural frequency ω is fixed 10.

The Stuart-Landau oscillator of Eq. (2.21) can be separated into real and imaginary parts and solved by using ode45 in MATLAB with setting the relative error smaller than 10^{-6}. It should be noted that as $a < 0$, the S-L oscillator is a stable rest state ($Z = 0$), as shown in Fig. 2.6(a). When a passes through zero (the supercritical Hopf bifurcation point), the stable point loses stability. The oscillation began to appear as a limit cycle for a positive a. Particularly, a determines the radius of the limit cycle, while the final state of the S-L oscillator is independent of its initialization (see three cases with different a and initial values in Fig. 2.6 (b-d)). The S-L mode is appreciated for its simplicity and generality in capturing the essence of oscillatory behavior emerging in complex systems.

Chapter 3. Faster Flicker of Buoyant Diffusion Flames by Weakly Rotatory Flows

This chapter presents a computational and theoretical examination of flickering buoyant diffusion methane flames within weakly rotatory flow conditions. The most significant result from the computational analysis reveals a nonlinear relationship between the flame's flickering frequency and the rotational intensity number, denoted as R, which quantifies the ratio of the rotational velocity and the fuel jet velocity. This finding is particularly noteworthy as it demonstrates how the introduction of a weak rotatory flow can significantly alter the dynamic behavior of buoyant diffusion flames. Particularly, the weaky rotatory condition satisfies that R is up to 0.24, because the present simulations present that the axisymmetry of flames could be broken when R is very high. For the strong rotatory flows, the flame dynamical behaviours are investigated in the next chapter.

We developed a scaling theory for the flicker frequency of buoyant diffusion flames in weakly rotating flows, based on the understanding that flicker is caused by periodic shedding of buoyancy-induced toroidal vortices. The theory shows that the flicker frequency f increase relative to the baseline at zero rotation follows the relation $f - f_0 \sim R^2$, aligning well with computational results. In physics terms, the external rotatory flow intensifies the radial pressure gradient around the flame, enhancing the baroclinic effect $\nabla p \times \nabla \rho$ and accelerating the shedding of toroidal vortices.

3.1 Computational Setups for Flickering Flames and Weakly Rotatory Flows

As shown in Fig. 3.1(a), the computational domain is a square column with $16D$ side and $24D$ height, where $D = 10$ mm is the fixed diameter of the fuel inlet. While the flickering flames in swirling flows, the weakly swirl is considered here and its orders of magnitude are smaller than or close to the strength of buoyance. In this way, a uniform structured mesh of $160 \times 160 \times 240$ is utilized as a balance of the computational cost and the grid independence, which was discussed in detail in the previous paper [163].

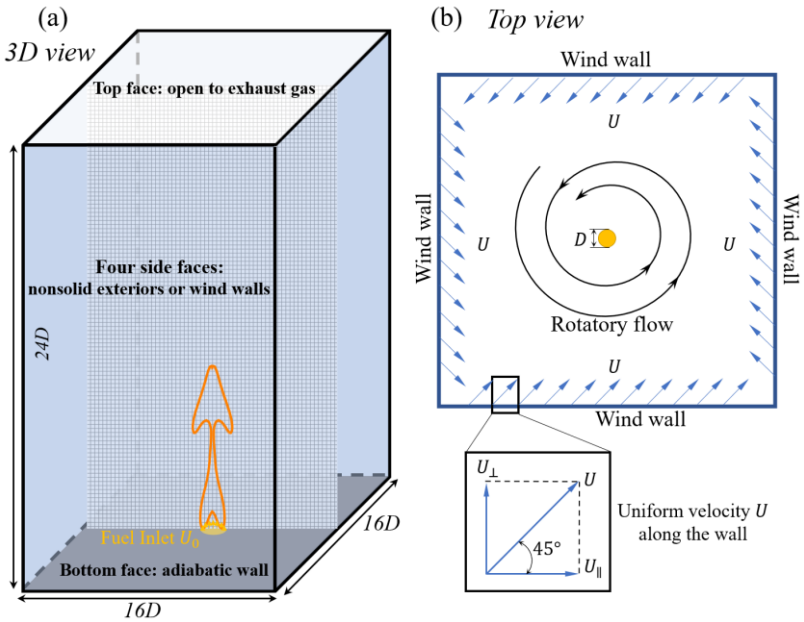

Figure 3- 1 (a) Schematic of the computational domain, mesh, and boundary conditions; (b) The rotatory flow is imposed by ejecting airflows from the four lateral wind walls.

An impermeable, non-slip, and adiabatic solid-wall boundary is used at the bottom ground (grey area), while a central circle (yellow area) is open for the fuel inlet. The ambient air is the density of $\rho_\infty = 1.20$ kg/m^3 at the room temperature. The methane gas jet of the density of $\rho_F = 0.66$ kg/m^3 is ejected out at the uniform velocity of $U_0 = 0.165$ m/s to sustain a laminar diffusion flame with $Re = 100$ and $Fr = 0.28$, where $Re = U_0 D/\nu_F$ is the fuel-jet Reynold number ($\nu_F = 1.65 \times 10^{-5}$ m^2/s is the viscosity of methane gas) and $Fr = U_0^2/gD$ is the Froude number ($g = 9.8$ m/s^2 is the

gravitational constant). The other sides of the computational domain are set as the non-solid exterior, through which gaseous products are allowed to flow in or out freely.

To generate a rotatory flow environment for the flickering flame, forced-ventilation walls can be specified at four lateral sides of the computational domain for tangentially ejecting airflows into the central region. The generated rotatory flows will be illustrated and analyzed shortly. In the present study, the fundamental conservation equations governing fluid dynamics are solved based on explicit, second-order, kinetic-energy-conserving numerics and shown in detail in the previous paper [163]. Turbulence modelling is not needed in the present laminar flows. The mixing-limited, infinitely fast reaction is used for modelling the present diffusion flames being far from extinction. The soot and radiation formation are not modelled in the present small-scale flames. The present computational validation of flickering buoyant diffusion flames will be expounded shortly.

It should be noted that the applicability of the computational approaches to the present problem relies on the two essential features of the small-scale flickering buoyant diffusion flames concerned. First, the flicker of the flames is due to the evolution of toroidal vortices, and the flames are away from the state of extinction followed by re-ignition. In the scenario, the characteristic time scales of chemical reactions are significantly smaller than those of the flow. Consequently, a complex reaction mechanism is not indispensable for computationally reproducing the flame flicker, and a simplified mixing-limited chemical reaction mechanism is adequate instead. Second, the flames concerned are of relatively small sizes, and the flow remains laminar almost everywhere except the far downstream of the flame, where the transitional or turbulent flow characteristics have however little influence on the vortices and the flame in the upstream.

3.2 Nonreacting Fuels Jets in Externally Rotatory Flows

In order to computationally setup the external rotatory flow, four lateral wind walls are loaded to eject horizontal airflows, as shown in Fig. 3.1(b). The inlet velocity on the wind wall is $\boldsymbol{U} = \boldsymbol{U}_{\perp} + \boldsymbol{U}_{\parallel}$, where $\boldsymbol{U}_{\perp}$ and $\boldsymbol{U}_{\parallel}$ are the normal and azimuthal velocity components respectively and the angle between them is fixed at $\alpha = 45°$. Consequently, the inlet airflows form a rotatory flow in the central region, and the rotation intensity can be controlled by adjusting the magnitude of inlet airflow $U = |\boldsymbol{U}|$. To facilitate the following presentation and discussion of results, D, $\sqrt{gD}$, and ρ_{∞} are used to nondimensionalize all kinematic and dynamic flow quantities.

To examine the generated rotatory flows, we simulated a few testing cases of non-reacting flows with different R, as shown in Fig. 3.2. The defined rotational intensity number R varying from 0.09 to 0.26 is significantly smaller than unity, which justifies the "weakness" of the rotatory flows concerned. In Fig. 3.2(a), the rotatory flow resembles a quasi-cylinder vortex, where the range and intensity of the vertical component $\hat{\omega}_z$ of vorticity vector remains approximately unchanged above $\hat{z} = 3$. Fig. 3.2(b) shows that the magnitude of $\hat{\omega}_z$ of the generated vortical flows increases with R, but the size of the vortex core (illustrated by the streamline-encompassed area) remains nearly the same. It should be noted that there are no vortical structures at the four corners in the present study. The flow converges gradually from the lateral sides of the square to the central region, as shown in Fig. 3.3.

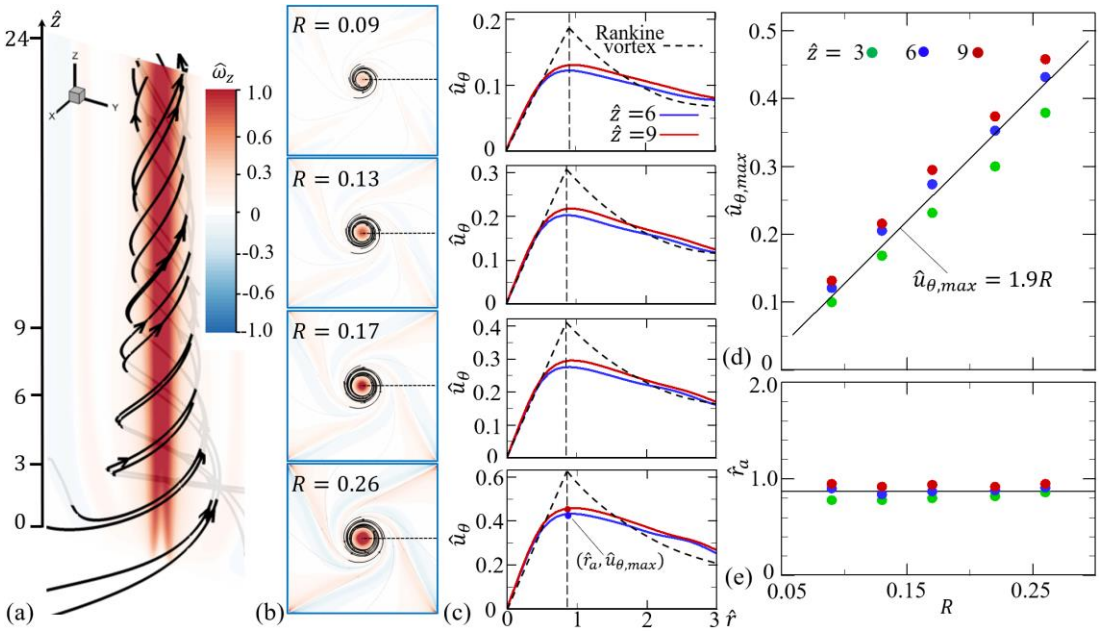

Figure 3- 2 The vertical component $\hat{\omega}_z$ of vorticity of a non-reactive methane jet in rotatory flows: (a) longitudinal section of $R = 0.17$ and (b) horizontal section at $\hat{z} = 9$. (c) The radial profiles of azimuthal velocity u_θ in the four cases. (d) The maximum azimuthal velocity $\hat{u}_{\theta,max}$ and (e) the radial location $\hat{r}_a$ of vortex cores generated at different R. The blue and red solid lines denote the vertical positions of $\hat{z} = 6$ and 9, respectively. The corresponding Rankine vortex approximation is plotted in the dashed line. The four cases correspond to $R = 0.09$, 0.13, 0.17, and 0.26 respectively.

To quantify the vortical flow fields, we plotted the radial profiles of azimuthal velocity $\hat{u}_\theta$ for four cases in Fig. 3.2(c). $\hat{u}_\theta$ linearly increases up to a maximum value (e.g., $\hat{u}_{\theta,max}$) at $\hat{r}_a$ and then gradually decays along the radial direction, which is similar to the experimentally measured transverse flow before the vortex breakdown occurs [185]. To facilitate the following comparison of computational and theoretical results, we approximated the calculated vortical flow as the Rankine vortex [186], which has an azimuthal velocity profile as $\hat{u}_\theta(\hat{r}) \sim \hat{r}$ within a vortex core of radius $\hat{r}_a$ and $\hat{u}_\theta(\hat{r}) \sim 1/\hat{r}$ outside the vortex core. As shown in Fig. 3.2(d), the present results show that $\hat{u}_\theta(\hat{r}_a) = \hat{u}_{\theta,max}$ is linearly proportional to R with the proportionality being about

1.9. In addition, Fig. 3.2(e) shows that $\hat{r}_a$ is nearly a constant of about 0.9, which indicates that the flickering flame has almost completely resided inside the vortex core.

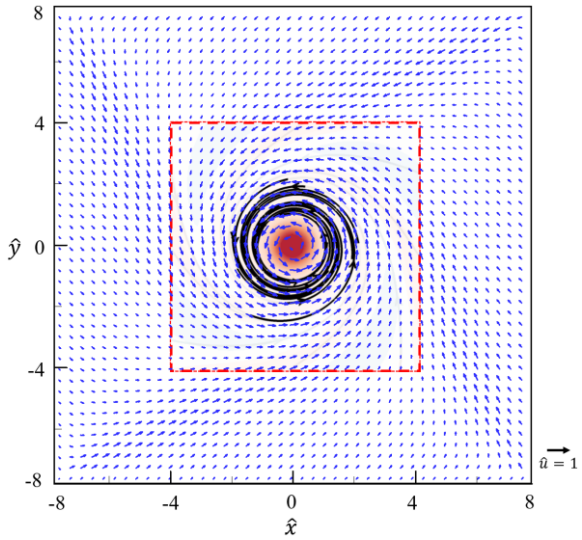

Figure 3- 3 The vortical flow in the horizontal section at $\hat{z}$ = 9. The blue arrows are the velocity vector. The red dotted box corresponds to the case of R= 0.17 in 3.2(b).

3.3 Phenomenological Description

In flickering buoyant diffusion flames, the buoyancy-induced shearing between the flame and the surrounding air is the precursor of the toroidal vortex [24, 163, 187]. During the lifecycle of the vortex, its formation, growth, and shedding correspond to the stretching, necking, and pinch-off of the flame, respectively. It can be seen in Fig. 3.4(a) for the case of $R = 0$ (without externally rotatory flow) that the vorticity layer forms at the flame base to stretch the flame (the normalized time $t^* = \hat{t}\hat{f}_0 = 0{\sim}0.3$), curlily grows along and necks the flame ($t^* = 0.3{\sim}0.8$), and sheds off ($t^* = 0.8{\sim}1.0$) to pinch off the flame. In this way, the flame performs a periodic flickering process. During $t^* = 1.0{\sim}1.1$, the shedding vortex moves downstream and the carried flame

bubble burns out soon, while a new vortex generates at the flame base and a new cycle starts.

A similar evolution of the toroidal vortex can also be observed in Fig. 3.4(b) for the typical case of $R = 0.17$, where the stretching, necking, and pinch-off of the flame remain in close associations with the formation, growth, and shedding of the vortex. An interesting observation is that the flame tends to be pinched off at a further downstream location with increasing R. Specifically, the flame pinch-off occurs at $\hat{z} = 6.0$ for the case of $R = 0$ but at $\hat{z} = 7.2$ for the case of $R = 0.17$. This observation can be understood by that the external rotatory flow induces an additional vertical flow, which convects the vortex to the downstream. It can be explained that the external air flows around the flame and finally outflows in the vertical direction, as the bottom boundary is a solid wall and the four sidewall surfaces are inlet wind in the present domain. In addition, the swirling flow causes a shear layer enclosing the flame, thereby changing the overall flow structure significantly.

To substantiate the understanding, the central axial profiles of the vertical velocity $\hat{u}_z$ in the two cases are plotted in Fig. 3.4(c) and 3.4(d), respectively. It is seen that $\hat{u}_z$ rapidly increases from the fuel inlet and reaches the first peak at the position of the toroidal vortex. The comparison of $\hat{u}_z$ clearly indicates that the external rotation enhances the vertical flow (with higher peak values) and thus contributes to the additional motion of the vortex (more downstream position of the first peak). The most interesting observation is that the flame pinch-off tends to occur earlier with increasing R. Specifically, the flame is pinched off at $t^* = 0.75$ for the case $R = 0.17$ compared with that at $t^* = 0.85$ for the case of $R = 0$. To further quantify and interpret this observation will be the focus of the following subsections.

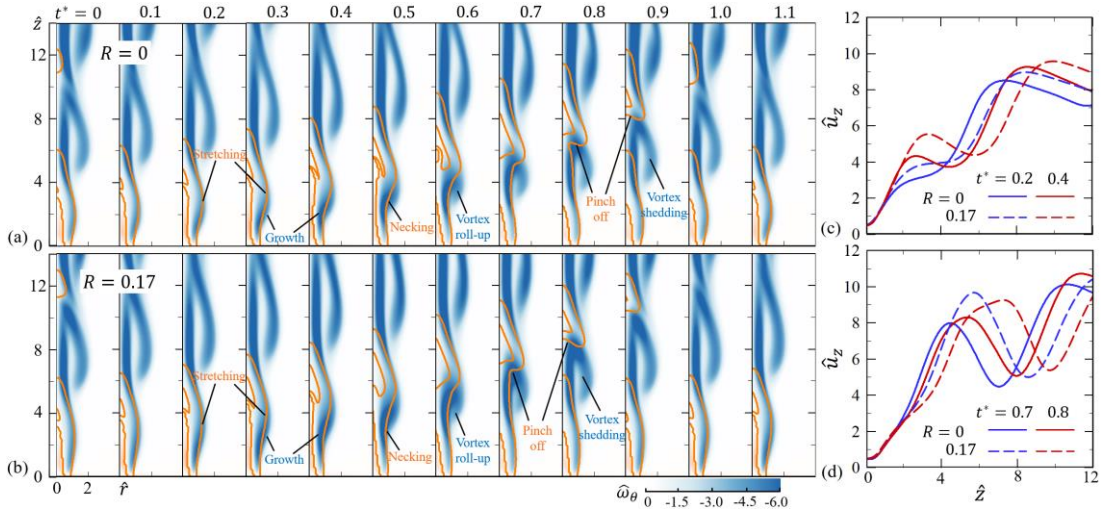

Figure 3- 4 The time-varying evolution of a flickering buoyant diffusion flame in (a) quiescent environment ($R = 0$) and (b) rotatory flow ($R = 0.17$). The comparison of their vertical velocity $\hat{u}_z$ along the central axis at (c) the instants $t^* = 0.2$ and 0.4 and (d) the instants $t^* = 0.7$ and 0.8.

The present results indicate that the dynamics of the toroidal vortex are affected due to the rotation of ambient flow. To clearly show the effects of rotatory flow, we plotted streamlines around the flames and coloured the local helicity density $\hat{h} = \hat{\boldsymbol{u}} \cdot \hat{\boldsymbol{\omega}}$ along the streamlines in Fig. 3.5(a) and 3.5(b) for the cases of $R = 0$ and $R = 0.17$ respectively. The zero value of $\hat{h}$ indicates that the streamline is orthogonal to the vorticity line. In contrast, a nonzero $\hat{h}$ measures the local geometric helix. In Fig. 3.5(a), the flow around the flickering flame in a still environment is lamellar, with $\hat{h}$ being zero everywhere and streamlines confined to the Y-Z plane due to axis symmetry. When the surrounding flow rotates, this laminar flow twists circumferentially, causing the streamlines to tilt out of the Y-Z plane and form a spiral ring, as shown in Fig. 3.5(b).

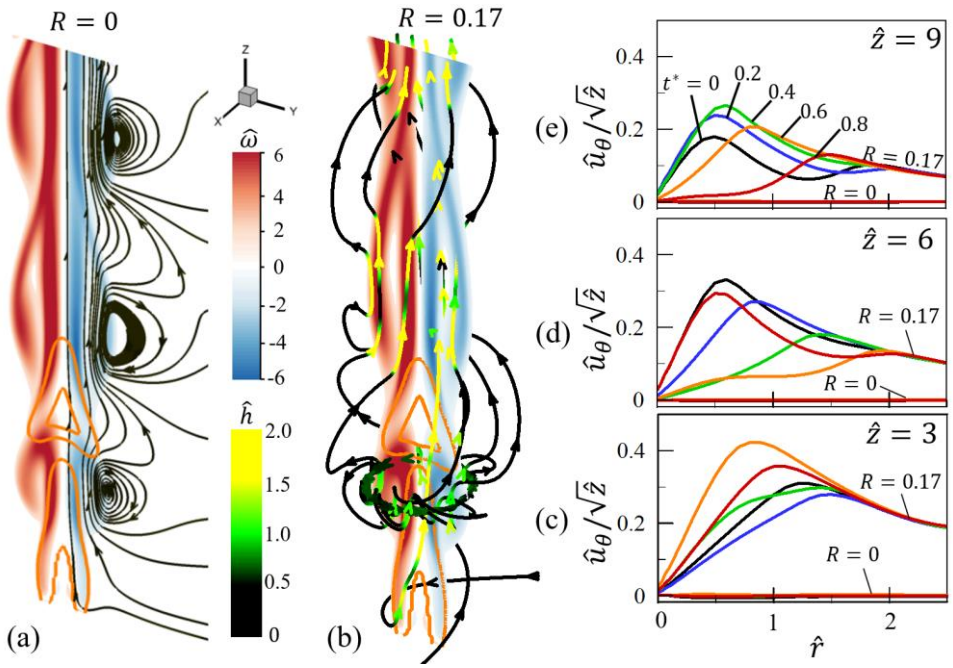

Figure 3- 5 Flickering buoyant diffusion flames in (a) quiescent environment and (b) rotatory flow, corresponding to the $R = 0$ and $R = 0.17$ cases respectively. The arrow on the streamlines denotes the flow direction. Their time-varying radial profiles of azimuthal velocity $\hat{u}_\theta$ at (c) $\hat{z} = 3$, (d) $\hat{z}$ =6, and (e) $\hat{z} = 9$. The flame and vorticity $\hat{\omega}$ in the Y-Z plane are plotted. The helicity density $\hat{h}$ is dyed along the streamlines.

Nonzero $\hat{h}$ appears in the vorticity layer around the flame and increases with the rotational intensity number R. Regardless of the local helix of the flow field, the flame morphology retains the approximate axis symmetry to a certain extent. Therefore, in the present problem concerning weakly rotatory flows, there is only moderate symmetry breaking to the flame shape and surrounding shear layer, which will be used as a useful approximation to simplify our theoretical modelling to be expounded in the next section.

To estimate the extent to which the presence of flame affects the rotatory ambient flow, we replotted the radial profiles of azimuthal velocity $\hat{u}_\theta$ at different streamwise locations of $\hat{z} = 3$, 6, and 9. It is clearly seen that, although the profile of $\hat{u}_\theta$ changes with time due to the flame flicker, it retains the similarity to the Rankine vortex flow as

$\hat{u}_\theta$ increases linearly with $\hat{r}$ within a certain range (i.e., the vortex core) that is sufficiently large to include the flame and its surrounding shear layer. It is also found that the decrease of $\hat{u}_\theta$ with $\hat{r}$ outside the vortex core is slower than the trend of $1/\hat{r}$ due to the additional flow induced by the thermal expansion around the flame. This does not have significant effects on the evolution of toroidal vortices within the vortex core. In addition, the decrease of $\hat{u}_\theta/\sqrt{\hat{z}}$ along the axial direction indicates that the circumferential motion caused by the external rotatory flow becomes weaker downstream. Consequently, the buoyancy-induced vortex flow still plays the predominated role in the present flickering flames in weakly rotatory flows.

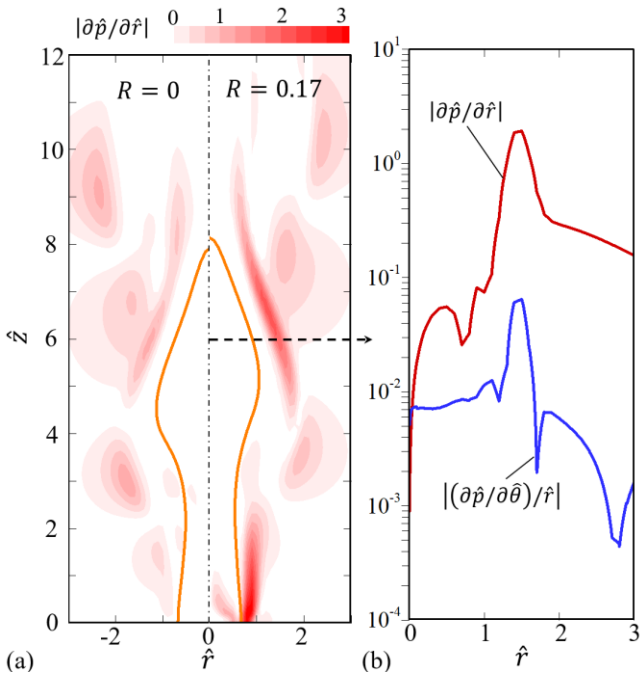

Figure 3- 6 (a) The radial component of the pressure gradient $|\partial\hat{p}/\partial\hat{r}|$ for the cases of $R = 0$ and $R = 0.17$, corresponding to the left and right subfigures respectively. (b) The radial component $|\partial\hat{p}/\partial\hat{r}|$ and azimuthal component $\left|\left(\partial\hat{p}/\partial\hat{\theta}\right)/\hat{r}\right|$ of pressure gradient at $\hat{z} = 6$ in the case of $R = 0.17$.

The previous study [24] has shown that the pressure gradient ∇p can be negligible for the vorticity generation in flickering flames if the ambient flow is quiescent and the

Froude number is small. In the present problem, we hypothesized that the formation and evolution of a toroidal vortex around the flame is affected by the baroclinity $\nabla\rho \times \nabla p$ due to the external rotatory flow. To verify this hypothesis, we plotted the radial pressure gradient $\partial\hat{p}/\partial\hat{r}$ around the flames in the cases of $R = 0$ and $R = 0.17$, as shown in Fig. 3.6(a). It is seen that the magnitude of $\partial\hat{p}/\partial\hat{r}$ is not negligible in almost entire flow domain and is significant in the domain close to the flame.

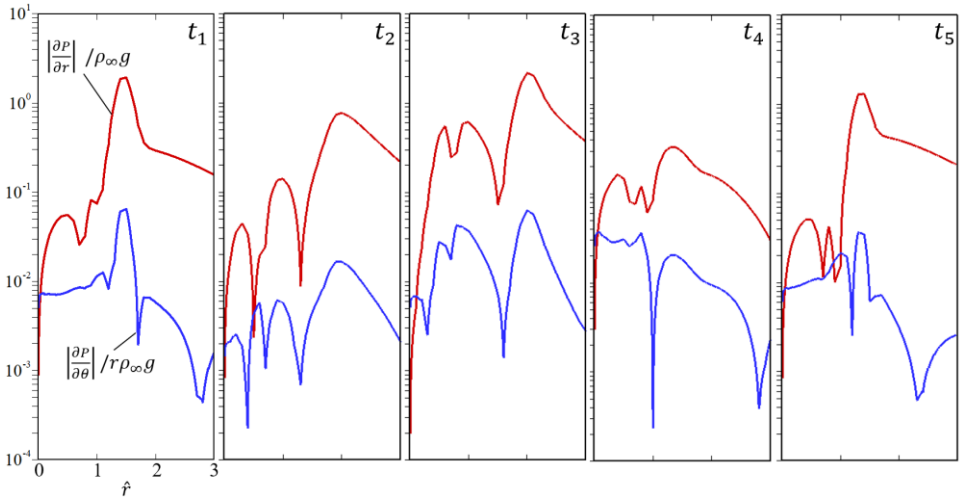

Figure 3- 7 Five instantaneous profiles of radial pressure gradient and azimuthal pressure gradient at $\hat{z} = 6$ in the case of $R = 0.17$.

Besides, Fig. 3.6(b) shows that the azimuthal pressure gradient $\left(\partial\hat{p}/\partial\hat{\theta}\right)/\hat{r}$ has a much smaller magnitude than $\partial\hat{p}/\partial\hat{r}$ so that we can neglect the azimuthal component in the following analysis. More details on their instantaneous comparisons during the periodic flickering process are provided in Fig. 3.7. Consequently, the pressure gradient along the radial direction should be considered in the present problem concerning the influence of the rotatory flows.

3.4 Influence of R on Flickering Frequency

To determine the frequency of flame flicker, it is required to choose an appropriate quantity that can characterize the dynamical behaviour of flickering flames. In the previous experiments, there is quite a freedom in selecting and acquiring characteristic (either local or global) flame quantities, for example, the pressure or temperature of flickering flame at a certain position [16, 188], the flame luminosity at a certain height [189, 190], and the flame morphology information (e.g., the flame height [12], width [74], size [191] and brightness [83, 192]) obtained from high-speed images. In the present computational work, we choose the total heat release rate Q and the vertical velocity u_z and temperature T at a fixed point to determine the frequency of flame flicker, as shown in Fig. 3.8(a), 3.8(b), and 3.8(c) respectively. The former one can be treated as a representative global quantity and the latter two are representative local quantities.

The present results show that all the quantities exhibit periodic behaviours with almost the same frequency for the ambient flow being rotatory or not, while there are slight phase differences among them. Interestingly, different quantities show the same frequency but different phases. The reason maybe induced by the differences between the global and local quantities, as well as the indirect mapping relationship of the local velocity and temperature. This observation and understanding deserve further study. This result is consistent with previous experimental observations [16, 192] that the dominant frequencies based on different quantities in the flickering flame have negligible differences. For simplicity and consistency, the global quantity Q will be adopted in the present study for analyzing the frequency variation in different cases.

It is seen in Fig. 3.8(a) that the periodic wave of Q for the case of $R = 0$ oscillates at the frequency of $f_0 = 9.6$ Hz, which is smaller than 10.6 Hz for the case of $R = 0.17$. The frequency comparison further confirms the observation that the external rotatory

flow causes the flame to pinch off at an early time. Fig. 3.8(d) shows a monotonically increasing trend of the frequency f with the rotational intensity number R, and the trend is noticeably nonlinear. It should be noted that the present study focuses on the weakly rotatory flows with $R < 0.24$, beyond which the stronger rotational flow may lead to the occurrence of vortex breakdown and local flame extinction [178, 185, 193]. More sophisticated computational approaches are needed to deal with these emerged phenomena in strongly rotatory flows and merit future work.

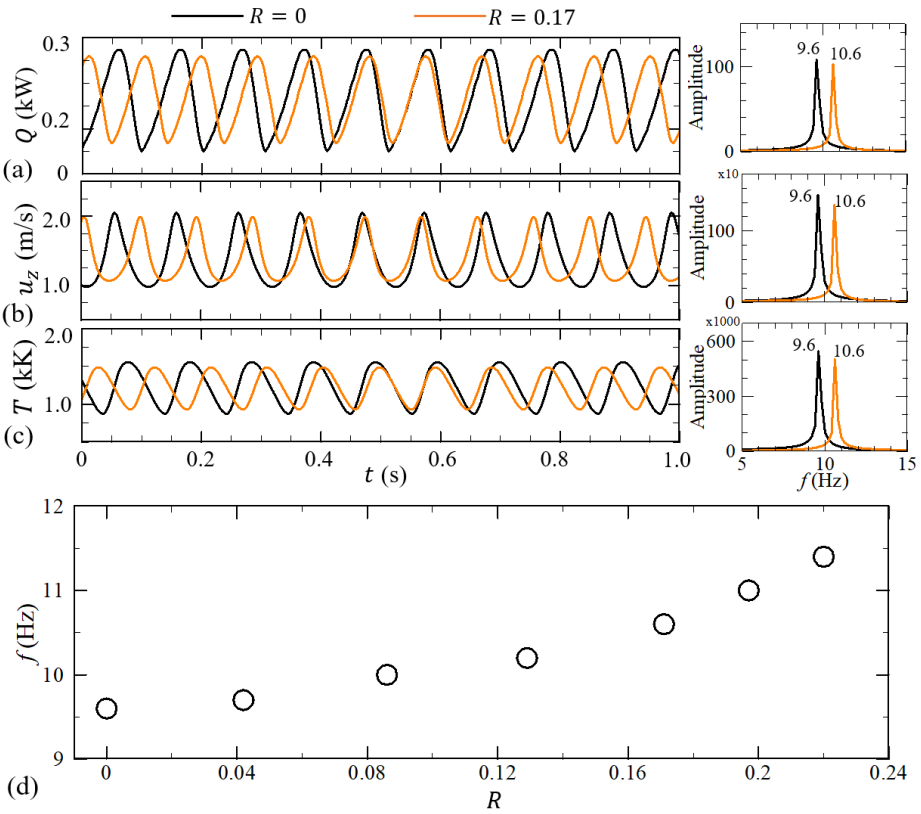

Figure 3- 8 Time and frequency domain graphs of (a) the total heat release rate Q, (b) the vertical velocity u_z and (c) the temperature T at $\hat{z} = 3$ of the central axis for flickering buoyant diffusion flames. The black and orange lines correspond to the $R = 0$ and $R = 0.17$ cases, respectively. (d) The correlation between the flickering frequency f and the rotational intensity number R.

3.5 Theoretically Modeling and Validation

The above computational results hitherto have demonstrated the influence of weakly rotatory flows on the formation of toroidal vortex and frequency augmentation. Next, we will reveal the underlying mechanism. Following the theory of Xia and Zhang [24], the present theoretical model for flame flicker is based on its connection with the shed-off of the toroidal vortex. To facilitate the comparison with the theory of Xia and Zhang [24], we adopted the same notation within this subsection. The central idea of the theory is that the flame flicker occurs when the circulation of the toroidal vortex reaches a threshold, which is an approximately universal constant [49, 51-53] and presumably does not have significant change in the present weakly rotatory environments. The frequency relation for buoyancy-driven diffusion flames in weakly rotatory flows will be theoretically derived through three steps as follows.

3.5.1 Theoretical Model of Flickering Flame in Weakly Rotatory Flows

Prior to introducing the theoretical model, the assumptions used below are given as follows: first, a quasi-steady assumption of vortex sheet growth is used, that is, the density and temperature across the vortex sheet are almost unchanged during a flickering period of diffusion flame; second, those diffusion flames are axisymmetric flow, while the surrounding flows are weakly swirling (in other words, the gravity is still dominated in the flame flicker); third, the flame pinch-off occurs within the flame height so that the vortex sheds off around the flame, not in the downstream region.

In the first step, the generation rate of total circulation Γ inside a control mass A is formulated based on the approximation of axis-symmetry. As illustrated in Fig. 3.9(a), a vortex layer segment around the flame is encircled by the red dashed box, which is the material contour ∂A of a control mass A. The zoomed subfigure clearly shows that

the domain of A is vertically between S_{v1} and S_{v2} and radially between S_{r1} and S_{r2}, where a material line element is represented as $\boldsymbol{s}ds$ and $\boldsymbol{s}$ is the unit tangential vector along the contour ∂A. According to the Kelvin's circulation formula [194], the rate of total circulation change is

$$\dot{\Gamma} = \oint_{\partial A} \boldsymbol{a} \cdot \boldsymbol{s} ds \tag{3.1}$$

where $\dot{\Gamma} = d\Gamma/dt$ is the change rate of circulation, $\boldsymbol{a} = D\boldsymbol{u}/Dt = -[\nabla p + (\rho_\infty - \rho)\boldsymbol{g}]/\rho + \upsilon\nabla^2\boldsymbol{u}$ is the acceleration of control mass [24]. As the diffusion term is not a source of vorticity production and vanishes on ∂A, the dimensionless $\hat{\boldsymbol{a}} = (D\boldsymbol{u}/Dt)/g$ can be expressed as

$$\hat{\boldsymbol{a}} = -\frac{\nabla\hat{p}}{\hat{\rho}} + \left(1 - \frac{1}{\hat{\rho}}\right)\hat{\boldsymbol{g}} \tag{3.2}$$

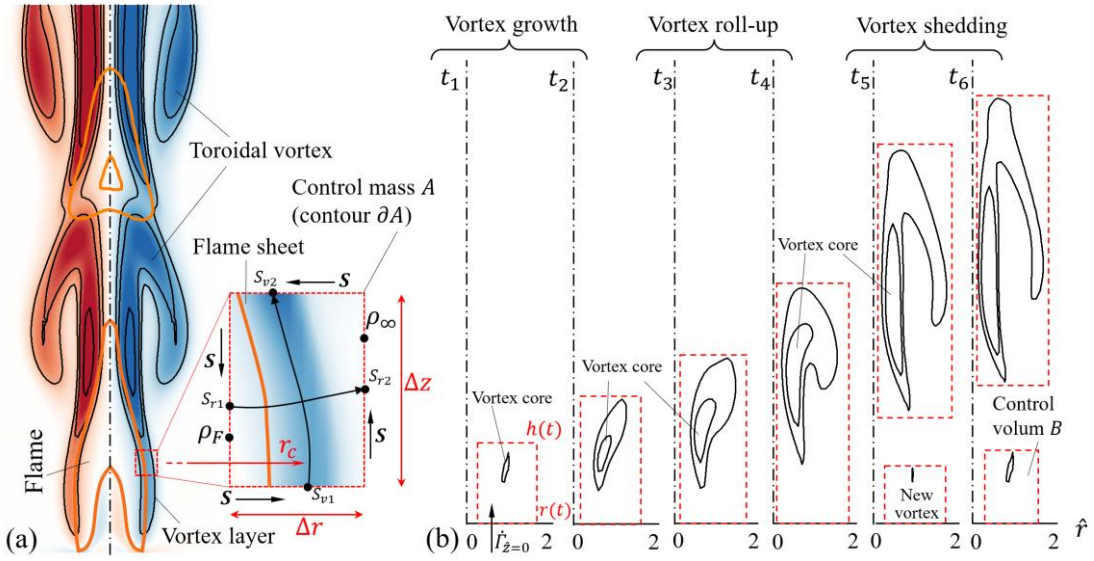

Figure 3- 9 (a) The vortex layer around the flame and the exaggerated segment illustrates the control mass A. (b) The periodic formation process of a toroidal vortex, which is represented by the vorticity contours and tracked by the red dashed box for the control volume B.

For the pressure gradient term $\nabla\hat{p}$, we only consider the radial component $\partial\hat{p}/\partial\hat{r}$. Considering that the present rotatory flows resemble the Rankine vortex, we use the relationship between the azimuthal velocity and the radial pressure gradient

$$\frac{\partial\hat{p}}{\partial\hat{r}} = \frac{\hat{\rho}\hat{u}_\theta^2}{\hat{r}} \tag{3.3}$$

where the azimuthal velocity $\hat{u}_\theta$ has a linear correlation with $\hat{r}$, namely $\hat{u}_\theta = C_\theta\hat{r}$ with a measurable quantity $C_\theta = \hat{u}_\theta(\hat{r}_a)/\hat{r}_a$ for a given rotatory flow. Applying Eq. (3.3) and Eq. (3.2) in Eq. (3.1), we have

$$\hat{\dot{\Gamma}} = \oint_{\partial A} -C_\theta^2\hat{r}\boldsymbol{r}\cdot\boldsymbol{s}d\hat{s} + \oint_{\partial A}(1-\frac{1}{\hat{\rho}})\hat{g}\boldsymbol{z}\cdot\boldsymbol{s}d\hat{s} \tag{3.4}$$

where $\boldsymbol{r}$ is the unit radial vector and $\boldsymbol{z}$ is the normal vector. The first term is the radial integration along ∂A due to the external rotatory flow, while the second term is the vertical integration along ∂A due to the buoyance-induced flow. Compared with the theory of Xia and Zhang [24] for flickering flame in a quiescent environment, the first term in Eq. (3.4) is due to the baroclinic effect caused by the rotatory flow. The two terms can be further simplified as

$$\oint_{\partial A} -C_\theta^2\hat{r}\boldsymbol{r}\cdot\boldsymbol{s}d\hat{s} = -C_\theta^2\int_{S_{r1}}^{S_{r2}} d\hat{r}^2 \tag{3.5a}$$

$$\oint_{\partial A}(1-\frac{1}{\hat{\rho}})\hat{g}\boldsymbol{z}\cdot\boldsymbol{s}d\hat{s} = \left(\frac{1}{\hat{\rho}_f}-\frac{1}{\hat{\rho}_\infty}\right)\int_{S_{v1}}^{S_{v2}}\hat{g}d\hat{z} \tag{3.5b}$$

where $\hat{\rho}_f = \rho_f/\rho_\infty$ and $\hat{\rho}_\infty = 1$ are the dimensionless density inside and outside the vortex layer respectively. Integrating along the paths of $S_{r1}-S_{r2}$ and $S_{v1}-S_{v2}$, as shown in Fig. 3.9(a), we can rewrite Eq. (5.4) as

$$\hat{\dot{\Gamma}} = -[2C_\theta^2\hat{r}_c\Delta\hat{r} + (C_\rho - 1)\hat{g}\Delta\hat{z}] \tag{3.6}$$

where $\hat{r}_c$ is the radial position of the vortex layer and close to the flame sheet; the density ratio $C_\rho = \rho_\infty/\rho_f$ is a measurable quantity for a given flame, for example C_ρ is

about 7.5 for the present computational methane/air flames, $\Delta\hat{r}$ and $\Delta\hat{z}$ are the radial and vertical unit lengths of the vortex layer associated with the control mass A. It should be noted that the first term of Eq. (3.6) is attributed to the external rotatory flow, which is absent in the theory of Xia and Zhang [24].

In the second step, the periodic formation process of a toroidal vortex associated with the flame flicker is established. Fig. 3.9(b) illustrates the evolution of a toroidal vortex in the moving control volume B. During $t_1 \sim t_2$, a new vortex core of the toroidal vortex generates near the base of the flame and then grows downstream under the buoyancy-induced convection. During $t_3 \sim t_4$, the vortex head region rolls up outward and the central vortex core moves downstream. During $t_5 \sim t_6$, the vortex fully develops and detaches. Meanwhile, a new vortex is formed at the flame base and a new cycle starts. It can be seen in Fig. 3.9(b) that the increment of $\Delta\hat{z}$ is much larger than that of $\Delta\hat{r}$ during a periodic motion and $\hat{r}_c$ of the vortex core is approximately constant. For the total circulation $\hat{\Gamma}_B$ of the moving vortex enclosed in B, its change rate should include an additional term $\hat{\dot{\Gamma}}_{\hat{z}=0} = -C_j\widehat{U}_0^2$ [24, 195], which is caused by the fuel inlet. According to Eq. (3.6), then we have

$$\hat{\dot{\Gamma}}_B(\hat{t}) = -2C_\theta^2\hat{r}_c\dot{\hat{r}}(\hat{t}) - (C_\rho - 1)\hat{g}\hat{h}(\hat{t}) - C_j\widehat{U}_0^2 \tag{3.7}$$

where $\hat{r}(\hat{t})$ is the width of the right boundary of B, $\hat{h}(\hat{t})$ is the height of the upper boundary of B, and $-C_j\widehat{U}_0^2$ enters the system through the lower boundary of B. The constant C_j relies on the configuration and the jet inlet condition.

Focusing on the formation of the toroidal vortex from the new to the fully developed, we integrate Eq. (3.7) in a period $\hat{\tau} = U_0\tau/D$ and have

$$\hat{\Gamma}_{TV} = \int_0^{\hat{\tau}} \hat{\dot{\Gamma}}_B d\hat{t} = -2C_\theta^2\hat{r}_c\overline{R}\hat{\tau} - (C_\rho - 1)\hat{g}\overline{H}\hat{\tau} - C_j\widehat{U}_0^2\hat{\tau} \tag{3.8}$$

where $\overline{R} = \hat{\tau}^{-1}\int_0^{\hat{\tau}} \hat{r}(t)dt$ and $\overline{H} = \hat{\tau}^{-1}\int_0^{\hat{\tau}} \hat{h}(t)dt$ represent the time-averaged width and height of the growing toroidal vortex, respectively. According to the present computational results, the width of the toroidal vortex is nearly unchanged and the vortex core moves close to the flame sheet, we have $\overline{R} \approx 1.9$ and $\overline{\hat{r}_c} \approx 0.6$. In addition, $h(t)$ can be roughly estimated as $\sqrt{gDt}$, as the toroidal vortex is driven downstream by buoyancy. Thus, we have $\overline{H} = C_h\hat{\tau}/\widehat{U}_0$, where C_h is a constant prefactor. With being scaled by $-\widehat{U}_0$, Eq. (3.8) can be rewritten as

$$\hat{\Gamma}_{TV}^{*} = C_h Ri\hat{\tau}^2 + \left(C_j + C_r\right)\sqrt{Fr}\hat{\tau} \tag{3.9}$$

where $Ri = \left(C_\rho - 1\right)\hat{g}/\widehat{U}_0^2 = \left(C_\rho - 1\right)gD/U_0^2$ is the Richardson number, $Fr = \widehat{U}_0^2 = U_0^2/gD$ is the Froude number, and $C_r = 2C_\theta^2\hat{r}_c\overline{R}/\widehat{U}_0^2$ is a prefactor for characterizing the external rotational flow.

In the third step, a threshold for the accumulation of the circulation inside the toroidal vortex [49, 53] is applied to obtain the frequency relation. Applying $\hat{\Gamma}_{TV}^{*} = C$ to Eq. (3.9), we have

$$\frac{f}{\sqrt{g/D}} = \frac{\widehat{U}_0}{\hat{\tau}} = \frac{1}{2C}\left(C_{jr}Fr + \sqrt{C_{jr}^2Fr^2 + CC_hC_\rho}\right) \tag{3.10}$$

where $C_{jr} = C_j + C_r$ is a prefactor for the combined contributions of the initial jet flow and the external rotatory flow. Hereto, we complete the derivation of the frequency relation for flickering buoyant diffusion flames in rotatory flows. For the case of $R = 0$, the prefactor C_{jr} degenerates to C_j, and the frequency of flickering flames in a quiescent environment is obtained as

$$\frac{f_0}{\sqrt{g/D}} = \frac{1}{2C}\left(C_jFr + \sqrt{C_j^2Fr^2 + CC_hC_\rho}\right) \tag{3.11}$$

which is exactly the same as the scaling formula obtained by Xia and Zhang [24]. It is interesting to see that Eq. (3.10) and Eq. (3.11) have the same functional form and differ

in only the prefactor of the Fr-term. The underlying physics is that the externally rotatory flow plays a similar role as that of the initial jet for enhancing the vortex growth.

3.5.2 Comparison between Computation and Theory

Next, we compare the above theoretical formula with the present computational results. Based on Eq. (3.10), we can have the frequency increase of flickering buoyant diffusion flames due to the additional rotation of the ambient flow

$$\Delta\hat{f} = \hat{f}(R) - \hat{f}(R=0) = \frac{f(R) - f(R=0)}{\sqrt{g/D}} = \frac{5\Phi}{C}R^2 \qquad (3.12)$$

where $\Phi = 1 + \left(C_j + C_{jr}\right)/\left(\sqrt{C_j^2 + CC_hC_\rho/Fr^2} + \sqrt{C_{jr}^2 + CC_hC_\rho/Fr^2}\right)$ is a constant factor about $1\sim2$, and the approximation of $C_r = 10R^2/\widehat{U}_0^2$ is used due to $C_\theta = 2.11R$ and $\hat{r}_c\overline{R} = 1.14$. Therefore, we obtain a scaling law of $\Delta\hat{f}\sim R^2$ from Eq. (3.12). As shown in Fig. 3.10, the scaling law agrees very well with the present computational results.

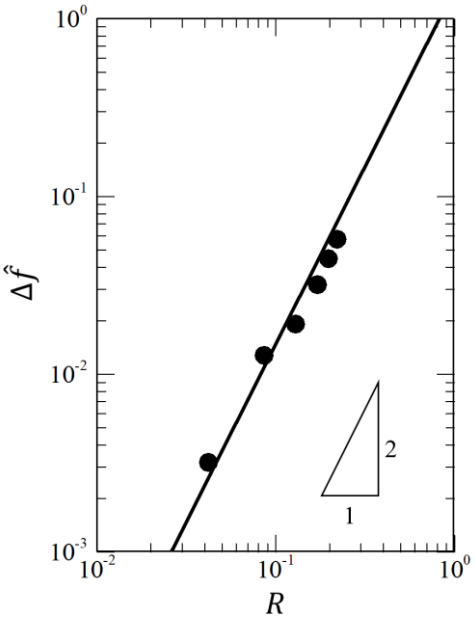

Figure 3- 10 Comparison between the correlation of $\Delta\hat{f}\sim R^2$ with the data in Fig. 3.8(d).

It should be emphasized that the present theoretical analysis is focused on the weakly rotatory flow. Consequently, the $\Delta\hat{f}\sim R^2$ scaling law is limited to sufficiently small R. When R is larger than 0.24 in the present study, the flame flicker may not be clearly observed, and the flame oscillates in its tip with a slight swing. This result implies that the circumferential motion of the toroidal vortex is not negligible and the axis-symmetry approximation becomes questionable. In addition, the sufficiently large R is likely to cause the occurrence of vortex breakdown and local flame extinction. This problem requires a completely differential computational and theoretical framework and merits further research.

3.6 Summary and Conclusions

Flickering diffusion flames in quiescent environments have been extensively studied in the literature, but their characteristics in complex external flows, particularly in externally rotatory flows, were investigated inadequately. The present study presents computational and theoretical investigations on the small-scale flickering buoyant diffusion flames in weakly rotatory flows and the conclusions are summarized as follows.

First, four lateral forced-ventilation walls were computationally imposed to generate a rotatory flow with variable rotational speed U around a methane jet diffusion flame with fixed jet velocity U_0 ($Re = 100$ and $Fr = 0.28$). The rotational intensity is controlled by the defined dimensionless number $R = U/U_0$. The generated rotatory flow was found to resemble the Rankine vortex as it has a linear velocity profile within a vortex core whose size slightly changes with R. As a validation, flickering buoyant diffusion flames of methane gas in a quiescent environment were computationally

reproduced, and the calculated flicker frequencies f_0 agree well with the famous scaling relation of $f_0 \sim \sqrt{g/D}$.

Second, the present computational results show that the external rotatory flow enhances the periodic flickering motion and accord with the experimental observations reported in the literature. Furthermore, the flicker frequency f is found to nonlinearly increase with R up to 0.24. It is worth noting that when R is higher, the flame asymmetry does not remain while the flow still is laminar. There is not doubt that a very high swirling flow tends to cause turbulent flow, but it is not considered in this thesis. By analyzing the flow and pressure fields around the flame, we found that there is only slight axis-symmetry breaking to the flame shape and surrounding shear layer in weakly rotatory flows and that the radial pressure gradient is significantly increased compared with that at $R = 0$. The approximate axis symmetry was subsequently used to simplify our theoretical investigation, and the significant radial pressure gradient implies that the baroclinic effect must be taken into account in our theory.

Third, we formulated the scaling theory for interpreting the frequency increase of flickering buoyant diffusion flames in weakly rotatory flows. This theory can be degenerated to that of Xia and Zhang [24] at $R = 0$. The predicted frequency correlation of $\Delta\hat{f} = \hat{f} - \hat{f}_0 \sim R^2$ agrees very well with the present computational results. The underlying physics can be understood as that the externally rotatory flow enhances the pressure gradient in the radial direction, and the significant baroclinic effect $\nabla p \times \nabla \rho$ contributes an additional source for the growth of toroidal vortices. Consequently, the toroidal vortices reach the threshold of circulation for shedding at an early time.

Chapter 4. Dynamical Behaviours of Buoyant Diffusion Flames in External Rotatory Flows

This chapter computationally examined small-scale flickering buoyant diffusion flames in swirling external flows, focusing on identifying and characterizing the flames' distinct dynamical behaviors. To explore the impact of finite rate chemistry on flame flicker, especially in sufficiently strong swirling flows, a one-step reaction mechanism is utilized for investigation. As the laminar diffusion flames are dominated by buoyance due to heat release, the one-step reaction is sufficient to present the reaction exotherm. In addition, this work is focused on the dynamical modes and not the exact reproduction of flame behaviour. By adjusting the external swirling flow conditions (the intensity R and the inlet angle α), six flame modes exhibiting distinct dynamical behaviors were computationally identified in both physical and phase spaces. These include the flickering flame, oscillating flame, steady flame, lifted flame, spiral flame, and flame with a vortex bubble. They were analyzed from the perspective of vortex dynamics. Particularly, the present numerical method can be validated qualitatively after comparing it with experimental observations. As mentioned in Section 1.3, those dynamical modes found in the present simulations are similar to various modes of flickering flames or puffing fires with the swirl.

The numerical investigation provides relatively comprehensive information on these flames. Under the weakly swirling condition, the flames retain flickering (the periodic pinch-off of the flame) and are axisymmetric, while the frequency nonlinearly increases with the swirling intensity. A relatively high swirling intensity can cause the disappearance of the flame pinch-off, as the toroidal vortex sheds around either the tip or the downstream of the flame. The flicker vanishes but the flame retains axisymmetric in a small amplitude oscillation or a steady stay. A sufficiently high swirling intensity

causes a small Damköhler number, leading to the lift-off of the flame (it may be caused by the local extinction occurring at the flame base). Under the same swirling intensity but large swirl angles, the asymmetric modes of the spiral and vortex-bubble flames were likely to happen. With R and α increasing, these flames exhibit axisymmetric and asymmetric patterns, and their dynamical behaviours become more complex.

To feature the vortical flows in flames, the phase portraits are established based on the velocity information of six positions along the axis of the flame, and the dynamical behaviours of various flames are presented and compared in the phase space. Observing the phase portraits and their differences in distinct modes could help identify the dynamical behaviours of flames and understand complex phenomena.

4.1 Computational Setups for Externally Rotatory Flows

In the chapter, a flickering buoyant diffusion flame is produced by jetting a methane flow in similary way in the last chapter. To impose swirling flows into the computational domain, the four lateral sides loading the inlet air, namely the "air wall" are set up, as shown in Fig. 4.2(b). $\boldsymbol{U_\alpha} = \boldsymbol{U_\perp} + \boldsymbol{U_\parallel}$ is the inlet velocity on the wind wall. $\boldsymbol{U_\perp}$ and $\boldsymbol{U_\parallel}$ are the normal velocity and azimuthal velocity with the angle α. Consequently, the air vorticity is generated around the center. The magnitude $U = |\boldsymbol{U_\alpha}|$ and the angle α of inlet airflow can be adjusted to control the central vortical flow. Similar approaches [196, 197] have been used by changing the incoming angle.

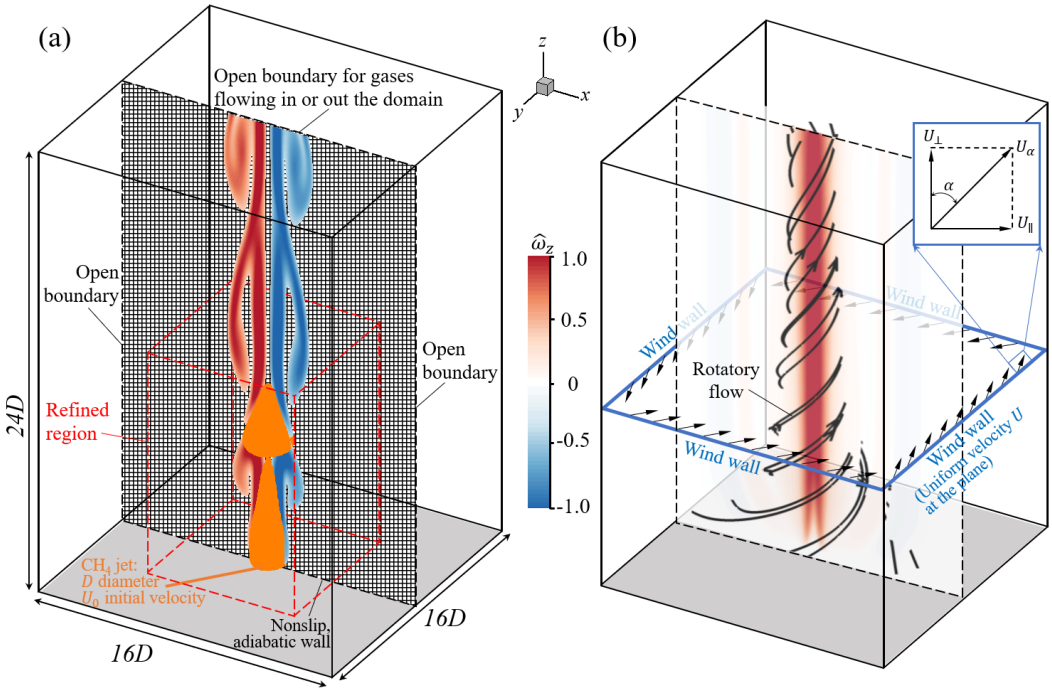

Figure 4- 1 (a) Schematic of the present simulations including the domain, mesh, and boundaries. (b) The swirling flow is adjusted by the four wind walls with inlet velocity $U = (U_{\perp}, U_{\parallel})$, where α is the included angle between velocity components and $R = U/U_0$. The contour of the Y-Z plane shows the vertical component $\widehat{\omega}_z$ of vorticity.

Besides, we carried out domain- and mesh-independence studies and adopted a uniform structure mesh of $160 \times 160 \times 240$ for the parametric studies to ensure high accuracy with reasonable computational cost. Our previous study [162, 163] can show that the mesh refinement (each grid has $\Delta\hat{x} = \Delta\hat{y} = \Delta\hat{z} = 10^{-2}$) is sufficient to capture the essential features of the buoyancy-induced flicker of a laminar diffusion flame. Due to the strong shear in the bottom region of the flames, the flow and flame structures can be significantly affected by the interactions of buoyancy-induced vortices and the shear layers neat the bottom wall. In Figure 4.2(a), the central region (8D × 8D × 12D with $\Delta\hat{x} = \Delta\hat{y} = \Delta\hat{z} = 5 \times 10^{-3}$) is further refined in the present cases to analyze closely the flame lift-off behavior. The previous study [11] reported that the emergence of local flame extinction could be related to the flame lift-off. Fig. 4.2(b) shows that the flame

frequency of the benchmark case (the flickering buoyant diffusion flame without the local flame extinction) in the $160 \times 160 \times 240$ mesh can be accurately calculated.

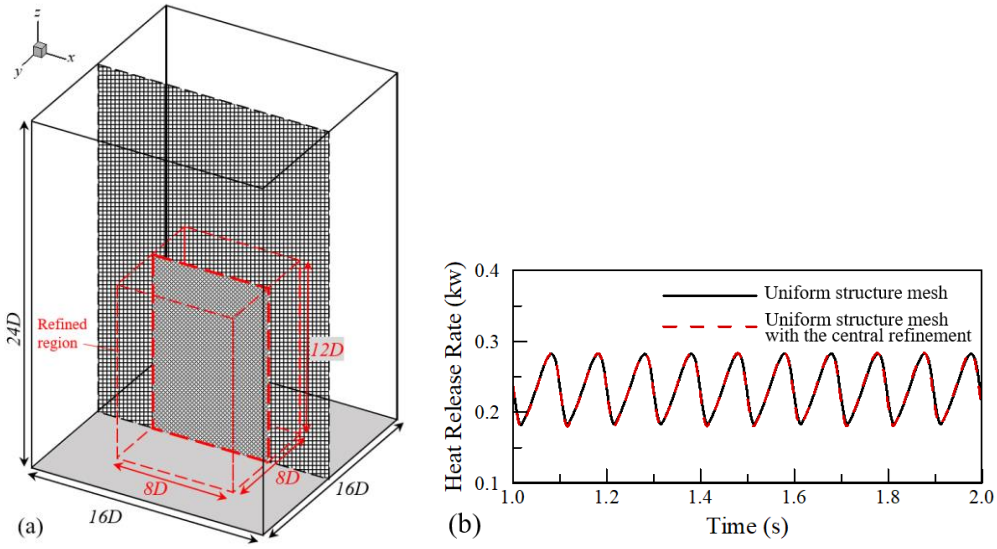

Figure 4- 2 (a) The local mesh refinement in the central region ($8D \times 8D \times 12D$) of the computational domain ($16D \times 16D \times 24D$). (b) The heat release rate of the flickering flame (benchmark case) varies with time. The black solid line indicates that the uniform structure mesh of $160 \times 160 \times 240$ is used, where each grid has the size of $\Delta\hat{x} = \Delta\hat{y} = \Delta\hat{z} = 10^{-2}$. The red dashed line corresponds to the mesh with the central refinement, where the grid size of $\Delta\hat{x} = \Delta\hat{y} = \Delta\hat{z} = 5 \times 10^{-3}$ is used.

To validate the swirling flow generated by the present approach, we conducted a series of simulations of non-reacting flows up to $R = 1.30$. For example, the flow fields are at $R = 0.17$ and $\alpha = 45°$ in Fig. 4.3(a). The vortical flow is characterized by a circular area of significantly concentrated vorticity, forming a vortex core, according to the velocity fields and streamlines in the Y-Z and X-Y planes at $\hat{z}$ =3, 6, and 9.

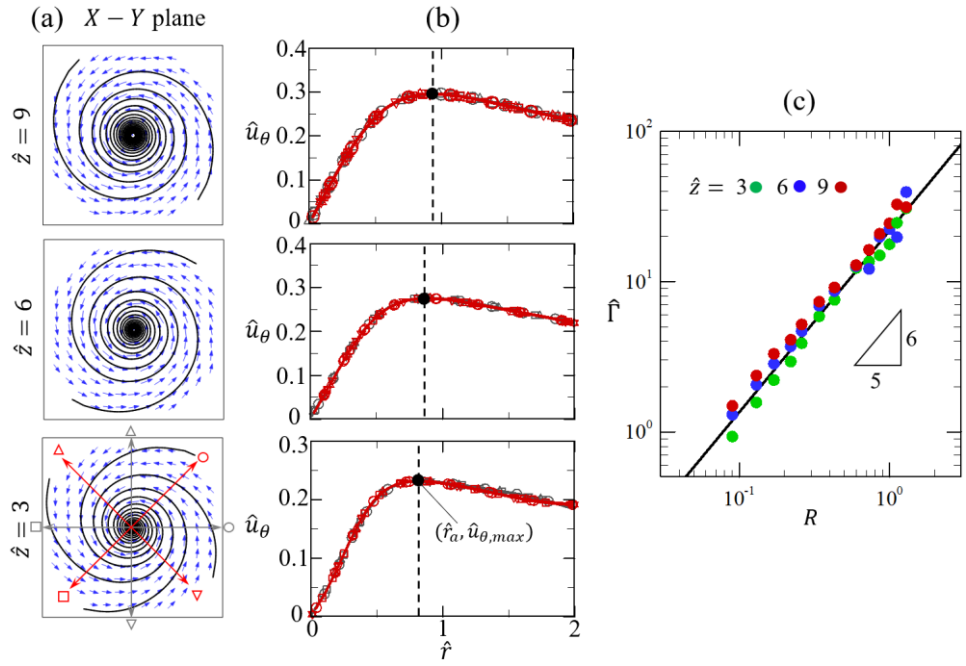

Figure 4- 3 (a) The flow field (velocity vector and streamline) of the X-Y planes at $\hat{z}$ =3, 6, and 9 for the case at $R = 0.17$ and $\alpha = 45°$. (b) The radial profiles of azimuthal velocity $\hat{u}_\theta$. (c) The correlation between the circulation $\hat{\Gamma}$ and the swirling intension R with the fixed $\alpha = 45°$. A vortex core is formed within the radial location $\hat{r}_a$, where increases monotonously up to the maximum $\hat{u}_{\theta,max}$. Eight azimuth angles that are distributed with 45° differences are denoted by different geometrical symbols. The circulation is defined as $\hat{\Gamma} = \int \boldsymbol{u}d\boldsymbol{l}/\sqrt{gD^3}$ along the closed circle $\boldsymbol{l}$ with the radius $\hat{r}_a$ at three cross-sections of $\hat{z} = 3$, 6, and 9.

As shown in Fig. 4.3(b), the radial profiles of azimuthal velocity $\hat{u}_\theta$ in several X-Y planes are plotted for quantifying the vortical flow fields. Importantly, along the radial direction $\hat{u}_\theta$ linearly increases up to $\hat{u}_{\theta,max}$ at $\hat{r}_a$ and then gradually decays. The trend of $\hat{u}_\theta$ is similar to the previous experimental measurement of transverse flow [59]. For the present vortical flows in a large range of R, $\hat{u}_\theta(\hat{r}_a)$ is proportional to R and $\hat{r}_a$ is around 0.8. In addition, the radial profiles of $\hat{u}_\theta$ from eight azimuth positions are almost the same within the range of $\hat{r} \leq 2$, indicating a good axis symmetry of the flow

in the region that is of interest. It is noted that a slight non-symmetry of the flow may occur around the fuel inlet, but this has negligible influence on the flame downstream.

Figure 4.3(c) shows that the vortical strengths, defined by the dimensionless circulation $\hat{\Gamma} = \int \boldsymbol{u}d\boldsymbol{l}/\sqrt{gD^3}$, are enhanced with increasing R when α is fixed at 45°. In addition, the scaling correlation of $\hat{\Gamma} \sim R^{6/5}$ is valid for a quite wide vertical range up to $\hat{z} = 9$.

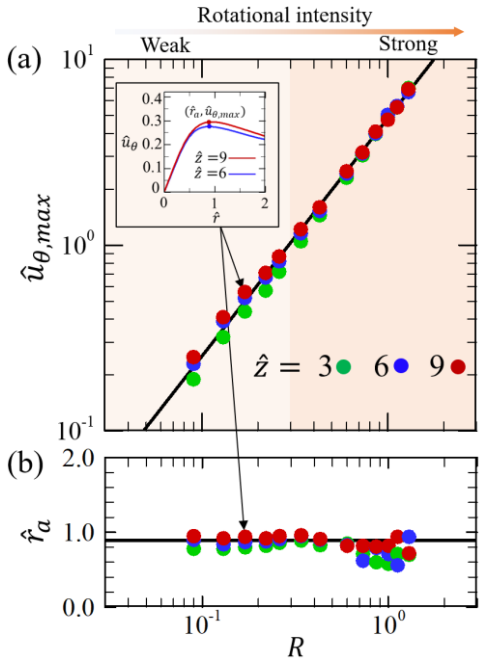

Figure 4- 4 (a) The maximum azimuthal velocity $\hat{u}_{\theta,max}$ and (b) the radial location $\hat{r}_a$ of vortex cores generated at different R. The inset figure shows the radial profiles of azimuthal velocity $\hat{u}_\theta$.

Figure 4.4 shows that the maximum azimuthal velocity $\hat{u}_{\theta,max}$ is proportional to U and the radial location $\hat{r}_a$ of vortex cores generated at different R is approximately a constant. Therefore, R is proportional to the nondimensional circulation imposed by the rotatory flow, which is evaluated as $2\pi\hat{r}_a\hat{u}_{\theta,max}$. It should be noted that the angular velocity of the swirling flow $\hat{\Omega}$ increases with R and is estimated to $\hat{u}_{\theta,max}/(2\pi\hat{r}_a)$.

4.2 Chemical Reactions for Simulating Flickering Flames

In the present problem of small-scale buoyant diffusion flames, the one-step overall reaction of the methane/air combustion is adopted to avoid the complexity and high computation cost of a detailed reaction mechanism. As a qualitative analysis, the one-step reaction model is accurate enough for the identification of the flame dynamical modes under the present scenarios of different external rotatory flows. For pool flames and jet flames with a low initial velocity, the flow motion is predominated by buoyance and the infinitely fast chemistry (i.e., the mixing-limited chemical reaction model) is sufficient for modelling the diffusion flames. The soot and radiation effects are not considered in the present small-scale flames. The finite rate chemistry (OFC) of the one-step methane/air reaction was used to capture the flame-off of diffusion flames. The Arrhenius equation (one-step finite rate reaction) of methane/air flame is used:

$$\frac{dC_{CH_4}}{dt} = -AT^{N_T} e^{\frac{-E_a}{RT}} C_{CH_4}^{N_{S,CH_4}} C_{O_2}^{N_{S,O_2}} \tag{4.1}$$

where the main parameters are listed in Table 4-1. The study investigates the flickering dynamics of flames under various swirling flows and ensures that the parametric studies are feasible from the aspect of reasonable computation cost. Here, the one-step reaction of Eq. (4.1) is utilized to qualitatively capture the flame-off process. Detailed reaction mechanisms should be used to investigate the flame-off mechanism in future work.

Table 4- 1 Parameters of 1-step reaction for methane/air flame.

A	N_T	$E_a\ (J/mol)$	$R\ (J/K \cdot mol)$	N_{S,CH_4}	N_{S,O_2}
1.3e9	0	202512.4	8.314	-0.3	1.3

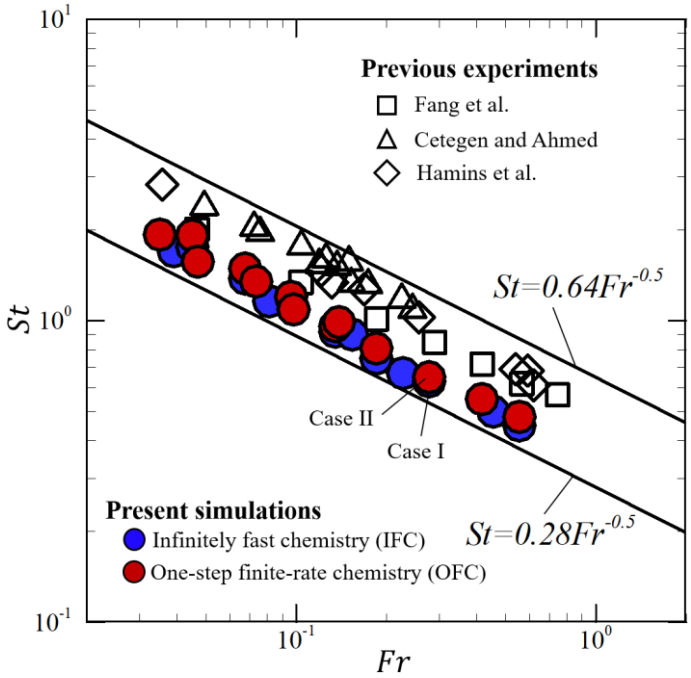

Figure 4- 5 Validation of single flickering flames with the scaling law of $St \sim \sqrt{Fr}$ and previous experiments.

To validate the present computational methodology and models for capturing the flickering phenomenon of buoyant diffusion flames, we conducted a number of simulation runs with different U_0, D, and g in the quiescent environment (i.e., $R = 0$). In Figure 4.5, the present results clearly show that the calculated frequencies of flickering flames agree fairly with previous experiments [16, 174, 176, 177], while the simulation results are lower a bit than that of experimental results. The frequency difference could be induced by the inaccurate reproduction of the flame sheet, due to a simple reaction mechanism (heat release, chemical components, density gradient etc. having a small deviation) in the present simulations. Particularly predict the famous scaling relation of $St \sim \sqrt{Fr}$ [14, 24], where $St = f_0 D/U_0$ is Strouhal number and $Fr = U_0^2/gD$ is the Froude number.

Two cases (Case I and Case II) of flickering buoyant diffusion flame at $D = 10$ mm and $g = 9.8$ m/s2 with infinitely fast and one-step finitely rate reactions are

illustrated in Fig. 4.6. Their dynamical behaviours are the same. Around the flame, the outside shear layer (denoted by the vorticity contour) rolls up to form the toroidal vortex. The flame is pinched into two parts by the vortex. In addition, we found that the gravity changes of $(0.5g - 1.5g)$ can significantly affect the flickering frequency, confirming that the buoyancy is predominant in the present diffusion flames.

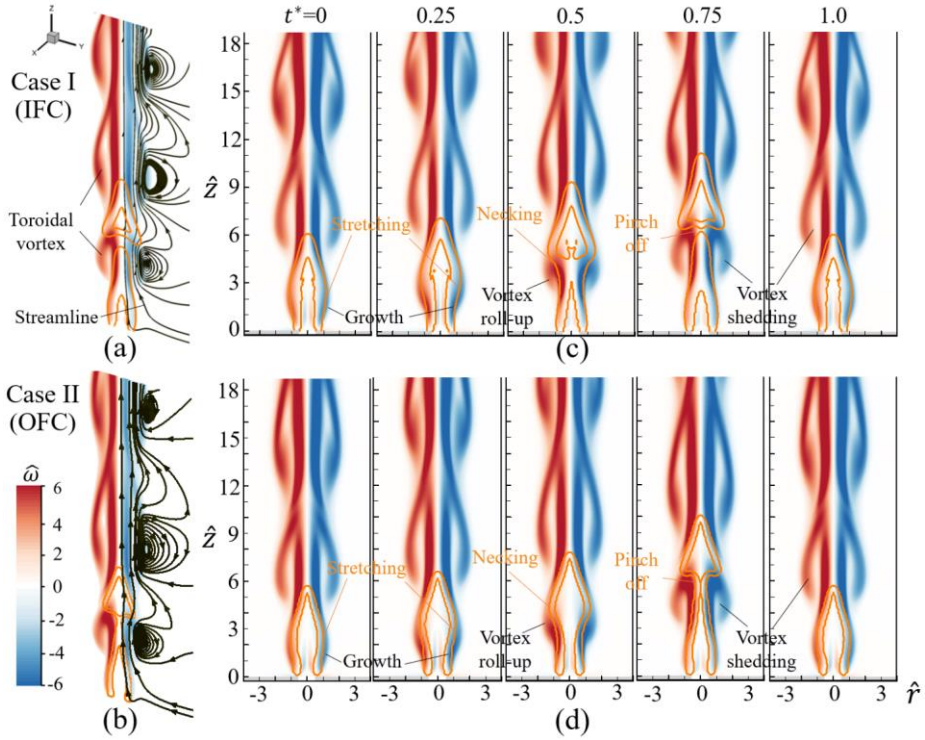

Figure 4- 6 The contour of vorticity $\hat{\omega}_\theta$ of flickering buoyant diffusion flames for the benchmark cases (U_0 =0.165 m/s, Re=100, Fr=0.28, and no swirling flow) in Fig. 4-5: (a) Case I (IFC) and (b) Case II (OFC). The flame is represented by the orange isoline of heat release. The streamlines are plotted around the flame. (c-d) The time-varying evolution of flames and vortices in the benchmark cases.

The flickering flame produced computationally here is ejected from a hole in the bottom wall, but slightly different from those flames ejected from a tube in previous studies. Consequently, the discrepancy results from the influence of the buoyance-induced flow at the flame base. In weakly rotatory flows, the boundary flow near the

bottom wall has negligible influence on the flickering of laminar diffusion flames, as the growth and shedding of the toroidal vortex occur downstream far from the bottom. However, the boundary effect becomes vital for flames in strong rotatory flows.

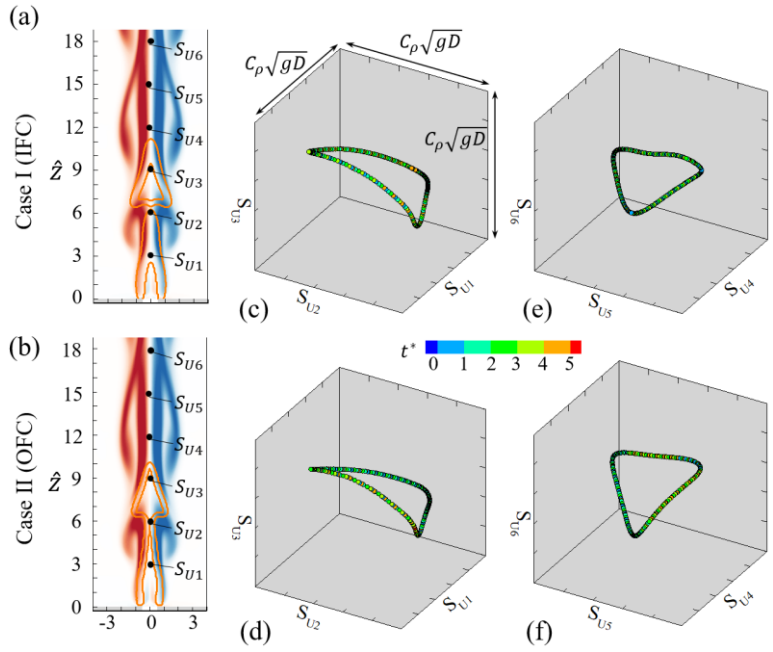

Figure 4- 7 (a-b) Six axial velocities S_{U_i}, i =1, 2, 3, 4, 5, and 6 at $\hat{z}$ =3, 6, 9, 12, 15, and 18 respectively along the central axis in the benchmark cases shown in Fig. 4-5. (c-f) Their phase portraits in the cubic space with the same range of $C_\rho\sqrt{gD}$, where $C_\rho = \rho_\infty/\rho_f = 7.5$ is the density ratio of ambient air and flame.

The phase portraits of flickering buoyant diffusion flames for Case I and Case II are depicted in Fig. 4.7. Each case exhibits two phase trajectories, plotted using the axial velocity components at three consecutive streamwise locations (three upstream and three downstream). During five periodic flickering processes, the upstream and downstream phase portraits for the flickering flames maintain the same closed ring shape, as illustrated in Fig. 4.7(c-f). Notably, the nearly identical phase space portraits for Case I and Case II suggest that the chemical reactions have minimal effects on flame flickering.

4.3 Faster Flickering Flames in Weakly Rotatory Flows

Compared with the above benchmark cases of $R = 0.0$, a similar evolution of the toroidal vortex for the case of R = 0.26 and $\alpha = 45°$ is shown in Fig. 4.8. The flame's stretching, necking, and pinch-off processes still correspond to the vortex formation, vortex growth, and vortex shedding, respectively. Besides, Figures 4.8(c) and 4.8(d) show that the phase portraits are still a closed ring shape, which means the external swirling flow does not break the topological structure of the dynamical system. Interesting observations can be made through a more detailed comparison.

First, the pinch-off of the flame tends to occur further downstream when R is increased and α is fixed at 45°. Specifically, the flame at R = 0 is pinched off at $\hat{z}$ = 6.0, while the pinch-off position is $\hat{z}$ = 6.6 in the case of R = 0.26.

Second, the R increase causes the flame pinch-off earlier. It can be seen that the flame in the case of R = 0 is just pinched off at t^* = 0.75, while it has already been pinched off for the case R = 0.26. Our previous study [162] addressed this phenomenon in detail and interpreted that the external swirling flow induces an additional vertical flow that expedites the shedding of the toroidal vortex.

Third, the streamlines around the flames at R=0 are plotted as the reference and 0.26 and colored by the local helicity density $\hat{h} = \hat{\boldsymbol{u}} \cdot \hat{\boldsymbol{\omega}}$. In fluid mechanics, $\hat{h} = 0$ represents the local orthogonality of the streamline and the vorticity line and $\hat{h} \neq 0$ is usually used to quantify the local geometrical helix.

Specifically, the reference case shows that the streamlines around the flame are in an axisymmetric plane as $\hat{h}$ of streamlines is zero everywhere. In the swirling flow of R = 0.26, streamlines are twisted along the circumferential direction to form a spiral ring in three-dimensional space, as shown in Fig. 4.8(a). $\hat{h} \neq 0$ appears in the region

with high vorticity, and also the value of $\hat{h}$ increases with R. The flame morphology retains the approximate axis symmetry to a certain extent in the local helix flow [162].

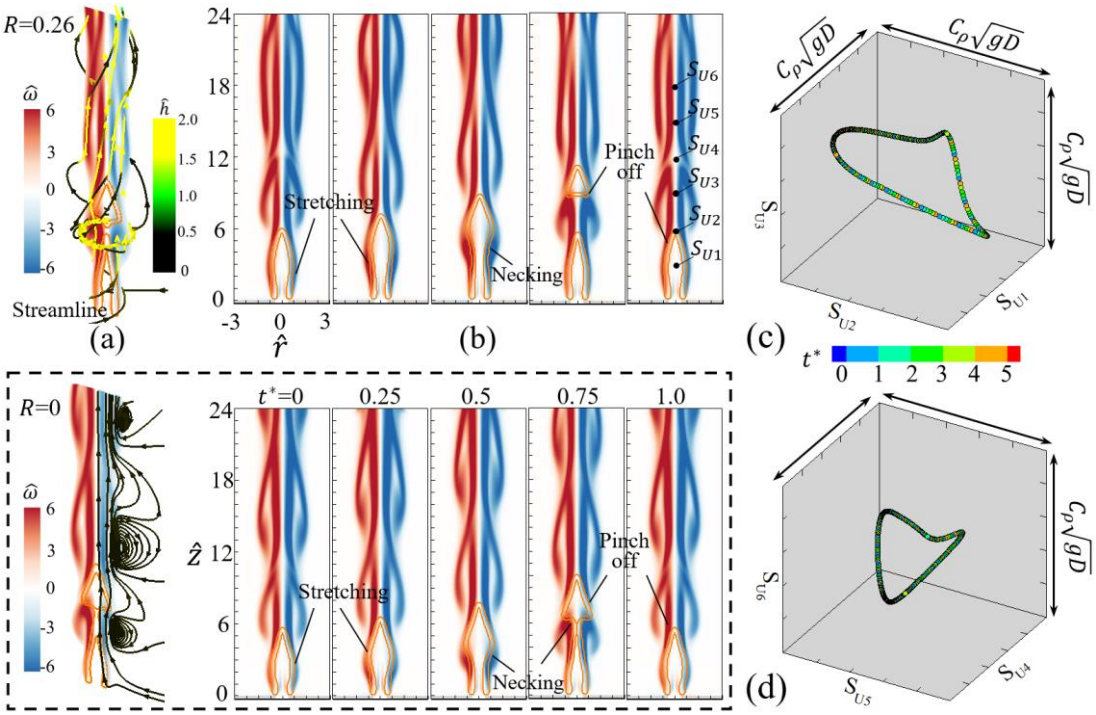

Figure 4-8 Faster flicker of the buoyant diffusion flame (Re=100, Fr=0.28) at $R = 0.26$ with the fixed $\alpha = 45°$: (a) the flow around the flame, (b) the time-varying evolution of the flame, (c-d) the phase portrait in the cubic space plotted by six velocity components S_{U_i}, i =1, 2, 3, 4, 5, and 6 at $\hat{z}$ =3, 6, 9, 12, 15, and 18 respectively along the central axis. All phase spaces have the same range of $C_\rho\sqrt{gD}$. The benchmark flame at $R = 0$ is shown in the dotted rectangle. The helicity density $\hat{h} = \hat{\boldsymbol{u}} \cdot \hat{\boldsymbol{\omega}}$ is dyed along the streamlines. The arrow on the streamlines denotes the flow direction.

Figure 4.9 shows that the frequency increase of flickering flames obeys the scaling relation of Eq. (3.12). This finding agrees very well with the scaling theory for flickering buoyant diffusion flames in weakly swirling flows [162]. In physics, the swirl of external airflow enhances the gradient of the radial pressure around the flame, which results in an additional source from the baroclinic contribution of $\nabla p \times \nabla \rho$ for the

growth of toroidal vortices [162]. Therefore, the toroidal vortices can satisfy the circulation threshold and shed off from the flames early. Noteworthily, the faster flickering mode is limited to the situation of weakly swirling flows, where the vortex breakdown is absent.

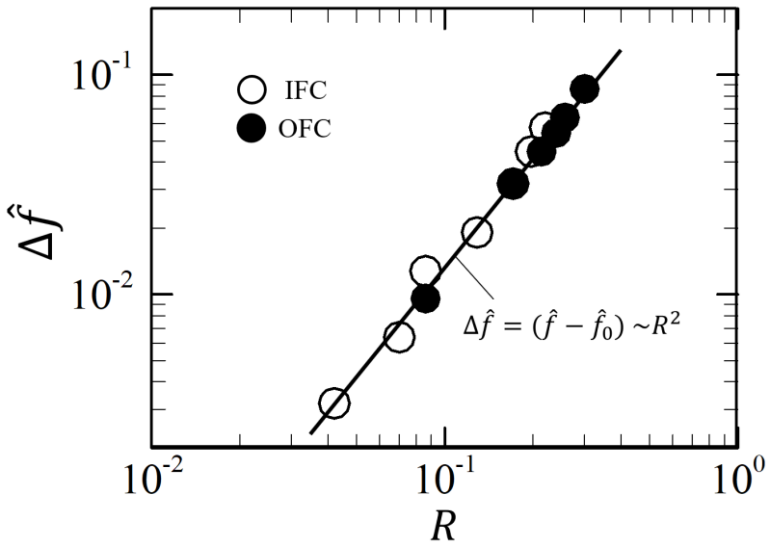

Figure 4-9 Comparison between the correlation of $\Delta\hat{f} = (\hat{f} - \hat{f}_0) \sim R^2$ with the numerical results of the infinitely fast chemistry (IFC) and the one-step finite rate chemistry (OFC) in the present study. The swirling flows are fixed at $\alpha = 45°$.

4.4 Dynamical Modes of Flickering Flames in Various Rotatory Flows

A sufficiently large R causes various flame modes, where the flame phenomena are governed by different physical mechanisms with rotatory flows becoming strong. As shown in Fig. 4.10, the flickering, oscillating, steady, and lifted flames form under different vortex interactions. When R exceeds 0.26, the vortex shedding occurs downstream so that the flame has no pinch-off and just oscillates. At bigger $R = 0.43$, there is no roll-up in the upstream shear layer and the flame turns into a steady state. A very strong rotatory flow ($R = 1.11$) causes local flame extinction and the flame detaches to the bottom.

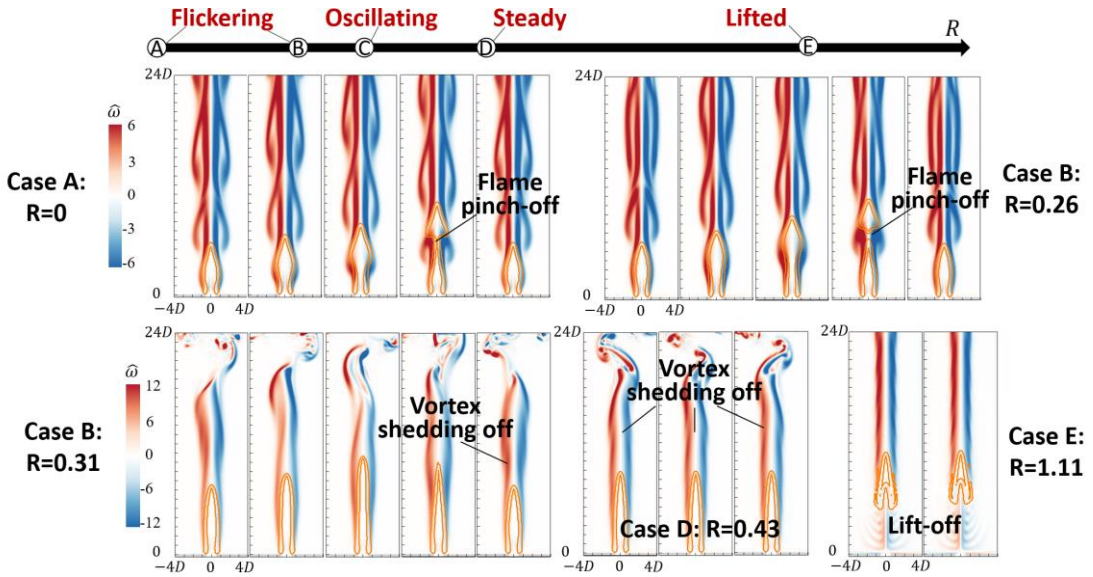

Figure 4-10 Snapshots of the flickering buoyant diffusion flame in different rotatory flows: five cases at $R = 0$, 0.26, 0.31, 0.43, and 1.11.

Figure 4.11(a) displays a buoyant diffusion flame at $Re = 100$ in a quiescent environment, with the toroidal vortex around the flame represented by the spiral of streamlines. From a vortex dynamics perspective, the buoyancy induced by the flame creates shear between the flame sheet and the surrounding air, ultimately leading to the formation of a symmetrical vortex [24, 198]. The symmetrical feature can be characterized by the zero helicity density [163]. It is important to note that the flickering flame consistently maintains axial symmetry throughout its oscillating behaviour.

Figures 4.11(b)-4.11(d) show the flickering buoyant diffusion flame in rotatory flows with different strengths. By comparing these results, several important observations for the swirling effect on a flickering buoyant diffusion flame.

First, the morphology of flickering flames has changed, specifically, the main flame becomes slimmer and taller with the swirling strength increasing, while their shapes remain axisymmetric.

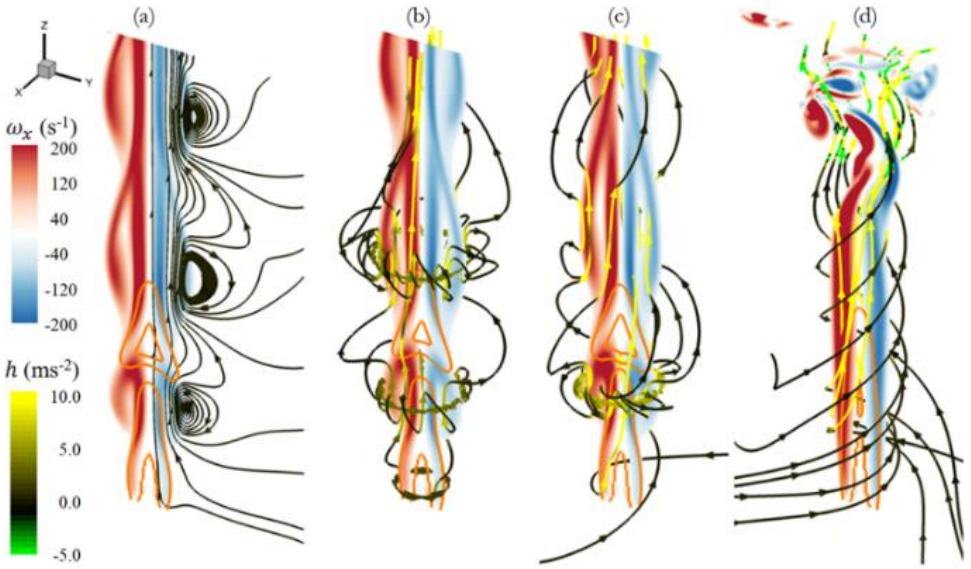

Figure 4- 11 Flickering buoyant diffusion flames in (a) a quiescent environment, and (b-d) a rotating flow of $R = 0.09$, 0.17, and 0.26, respectively. The flame is denoted by the contour line of the heat release rate. The vorticity ω_x is perpendicular to the $Y - Z$ plane.

Second, the shear layers around flames determine the flickering behavior. Their differences (the vorticity magnitude and the roll-up region) suggest that the rotatory flow can change the flame pinch-off up to a certain strength.

Third, the helicity density is colored on the streamlines to facilitate the quantitative comparison, which denotes the nonorthogonality of the vorticity and velocity vectors.

The results show that h in the shear layers increases from nearly 0 in Fig. 4.11(a), to about $0{\sim}5$ in Fig. 4.11(b), and to about $0{\sim}10$ in Figure 4.11(c). In Fig. 4.11(d), the value h almost remains high ($\gtrsim 10$) in the flame and jumps abruptly between the negative and the positive in downstream regions. The stronger the surrounding swirl is, the higher h in the flame becomes. Four, the twisting of streamlines demonstrates the swirling effect on the vortex. The roll-up and the twist occur concurrently to form the circumferentially spiral streamlines. When the external swirl is dominated, the vortex

ring is suppressed or postponed to downstream locations and the vortex helix grows and twines around the flame, as shown in Fig. 4.11(d).

4.5 Phase Space of Flickering Flames in Various Rotatory Flows

The phase portraits of those flame modes will be illustrated. Specifically, Various distinct dynamical modes of the flickering buoyant diffusion flame in externally swirling flows with a wide range of swirling intensity $R = 0{\sim}1.70$ and the airflow angle $\alpha = 27°{\sim}79°$ will be illustrated in detail. First, the angle α of inlet airflow is fixed at 45°, which sufficiently ensures that the generated region of swirling flow is much larger than flames. Then, α are adjusted to obtain asymmetrical flame modes including spiral and vortex-bubble flames. It should be noted that α is affected by the swirling intensity, the jet flow, and the computation geometry. A much smaller angle could cause no swirling flow, while a much larger angle would lead to constraints of the computational domain on swirling flow.

4.5.1 Oscillating Flames

As R increases up to 0.31 and α is fixed at 45°, the diffusion flame is not pinched off anymore and its top oscillates up and down at a frequency of 13.1 Hz, which is identical to the frequency of vortex shedding, as shown in Fig. 4.12. Compared with the benchmark case of R=0, the circumferential motion of the ambient air is significant as indicated by the very high helicity density in flame, and the shear layers are highly stretched so that the roll-up of the vortex vanishes. Remarkably, the vortex shedding occurs near the top of the flame. The flame oscillating mode is similar to the “tip flickering” phenomena without any swirl, in which no flame separation occurs and the top is merely oscillating or elongating periodically.

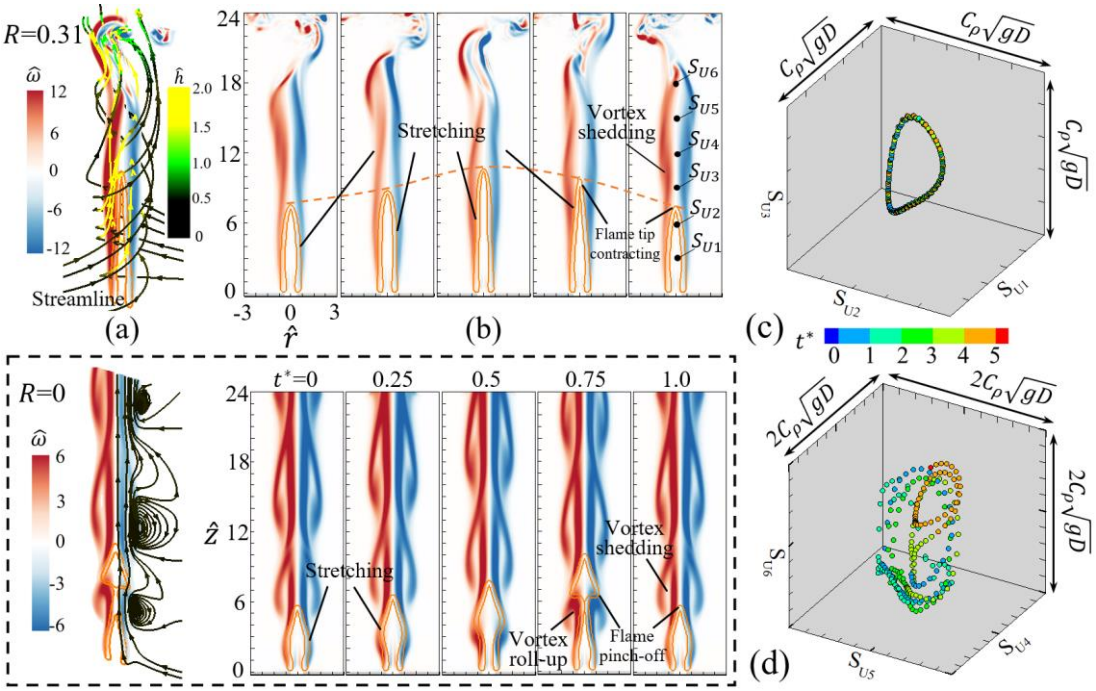

Figure 4- 12 Tip oscillation of the buoyant diffusion flame (Re=100, Fr=0.28) at $R = 0.31$ with the fixed $\alpha = 45°$: (a) the flow around the flame, (b) the time-varying evolution of the flame, (c-d) the phase portrait in the cubic space plotted by six velocity components S_{U_i}, i =1, 2, 3, 4, 5, and 6 at $\hat{z}$ =3, 6, 9, 12, 15, and 18 respectively along the central axis. The upstream phase space is twice as large as the downstream is. The benchmark flame at $R = 0$ is shown in the dotted rectangle.

Sato et al. [189, 199] reported that the tip flickering of flame appears under high fuel jet velocity conditions ($Fr \gg 1$), but the bulk flickering (called the flickering int the study) corresponds to the low fuel jet velocity ($Fr \ll 1$). This indicates that the external swirling flow has an equivalent influence with the increase of the inlet velocity and can restrain the flame from being separated, namely the occurrence of the (bulk) flickering. In addition, Fig. 4.12(c-d) shows that phase portraits of oscillating flame vary largely, as the downstream trajectory becomes a distinct disorder in a bigger range while the upstream is a smaller closed ring. The shear layer denoted by the vorticity

contour presents that the upstream is compact, but the downstream is unstable and the vortex develops into fragments.

4.5.2 Steady Flames

The steady flame at R = 0.43 and $\alpha = 45°$ is shown in Fig. 4.13. Similar to the oscillating flame in the case of R = 0.31, the buoyancy-driven flow around the flame is largely twisted compared with that in the benchmark case of R = 0. In the highly swirling flow, the flame has no periodic motion, and its shape maintains static all the time, as shown in Fig. 4.13(b).

This observation was also reported in previous studies [69, 76], where the flame flickering can be suppressed by a certain swirling flow. By adding vortical flows around Buk-Schumann diffusion flames, Chuah and Kushida [69] formulated an ideal fire whirl model in that the flame is more stretched and stabilized than the regular diffusion flame. Also, Lei et al. [76] experimentally reported that the weak fire whirl at a small heat release rate is steady with a smooth surface. Accordingly, the upstream phase portrait in Fig. 4.13(c) degenerates into a point, while the downstream portrait in Fig. 4.13 (d) shows an oscillation along the S_{U6} direction. It is seen in Fig. 4.13 (b) that the shear layers are stable for $\hat{z} < 12$ and the instability happens downstream of $\hat{z}$ = 15.

To facilitate the quantitative comparison between the vortex shedding and the change in flame height, we plot in Fig. 4.14 the vertical position H_v of the shedding vortex and the maximum flame height H_f at the fixed $\alpha = 45°$ but different R. The change of the vortex shedding-off has three regimes: within $R < 0.29$ (weak swirling flow regime), the buoyant diffusion flames retain the flicker (flickering mode) and H_v gradually increases with R; for $R = 0.29{\sim}0.35$, H_v increases rapidly and the pinch-off of flames is suppressed (oscillating mode); for $R > 0.35$, H_v remains almost constant

and the flames become steady (steady mode). Beyond the critical value of R about 0.31, the flame flicker is suppressed by the strong swirl. Meanwhile, H_f is nearly a constant between 9 and 10, with a slight decrease for $R = 0.29{\sim}0.35$. These three regions, corresponding to the small, intermediate, and large R, correlate with the three flame modes illustrated above: the flickering flame, the oscillating flame, and the steady flame.

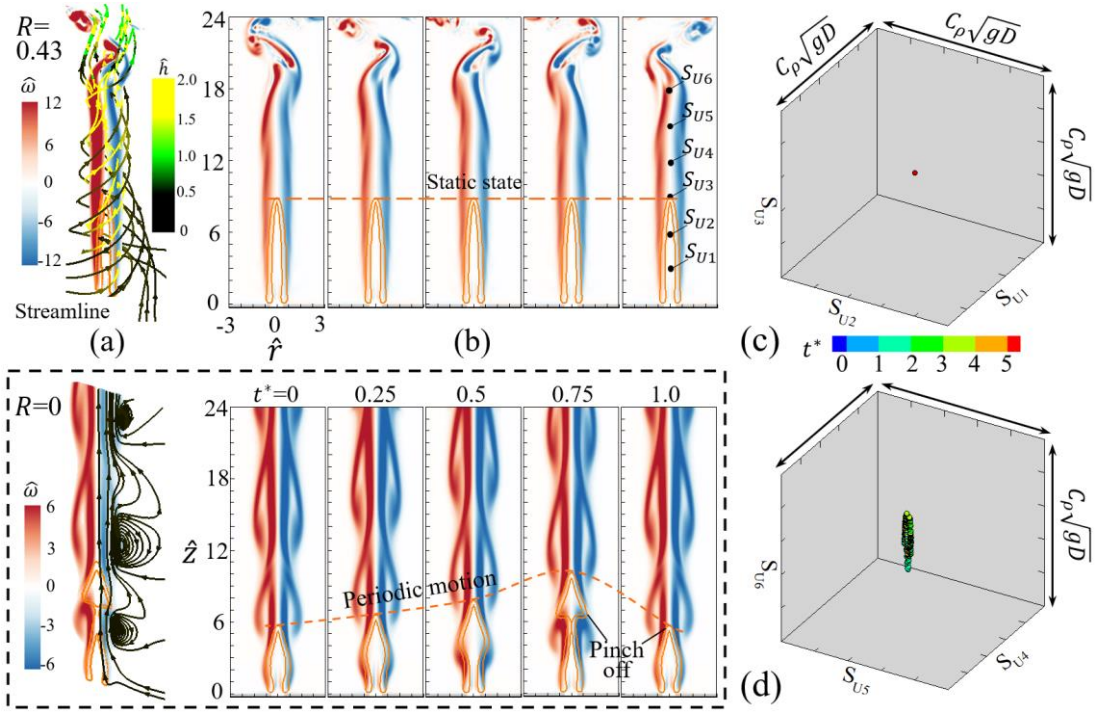

Figure 4-13 Steady-state of the buoyant diffusion flame (Re=100, Fr=0.28) at $R = 0.43$ with the fixed $\alpha = 45°$: (a) the flow around the flame, (b) the time-varying evolution of the flame, (c-d) the phase portrait in the cubic space plotted by six velocity components S_{U_i}, i =1, 2, 3, 4, 5, and 6 at $\hat{z}$ =3, 6, 9, 12, 15, and 18 respectively along the central axis. All phase spaces have the same range of $C_\rho\sqrt{gD}$. The benchmark flame at $R = 0$ is shown in the dotted rectangle.

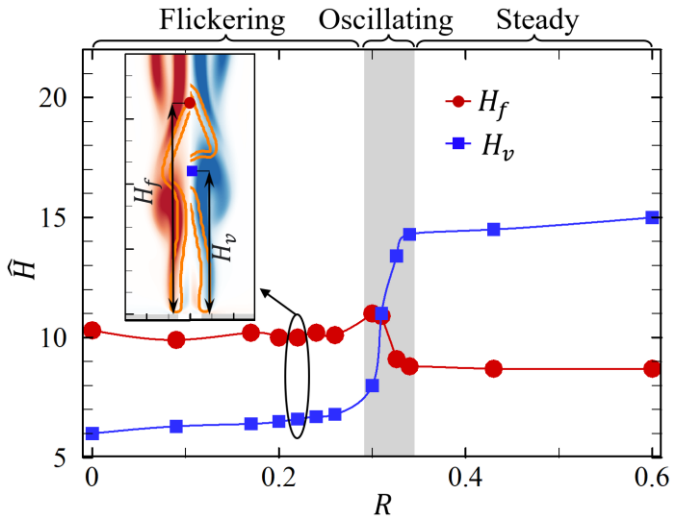

Figure 4-14 The vertical position of vortex shedding-off H_v vs. the maximum flame height H_f at the fixed $\alpha = 45°$ but different R.

4.5.3 Lifted Flame

As R increases up to 1.11, the diffusion flame does not attach to the bottom due to the local extinction, and the lifted flame is formed with the lifted height of about $4{\sim}6D$, as shown in Fig. 4.15. The streamlines twist and exhibit higher $\hat{h}$ at smaller $\hat{r}$. Additionally, a fishbone-like flow arises in the central region due to the new vorticity. Different with the nonswirling case, Fig. 12 (b) indicates that the flame is steady. he strongly swirling flow results in corner-like flow near the fuel inlet, rather than the vortex roll-up caused by buoyancy in the benchmark flickering flame. The inflow with radially outward streamlines is produced by the turning of the incoming flow within the bottom boundary layer. Fig. 12(c-d) illustrate the nearly motionless phase trajectories of the lifted flame, with only slight changes in the upstream portrait and minimal alteration in the downstream one.

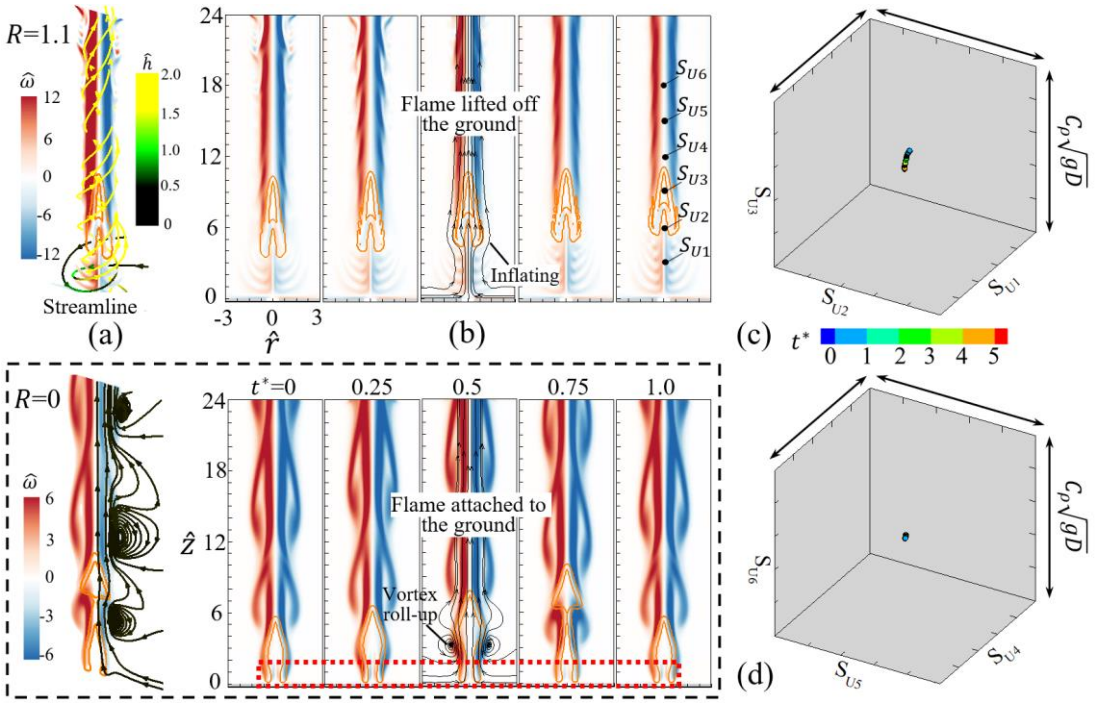

Figure 4-15 Lift-off of the buoyant diffusion flame (Re=100, Fr=0.28) at $R = 1.11$ with the fixed $\alpha = 45°$: (a) the flow around the flame, (b) the time-varying evolution of the flame, (c-d) the phase portrait in the cubic space plotted by six velocity components S_{U_i}, i =1, 2, 3, 4, 5, and 6 at $\hat{z}$ =3, 6, 9, 12, 15, and 18 respectively along the central axis. All phase spaces have the same range of $C_\rho\sqrt{gD}$. The benchmark flame at $R = 0$ is shown in the dotted rectangle.

In the present case, the swirl time scale $1/\Omega \sim 10^{-3}s$ is much smaller than the buoyancy time-scale $(D/g)^{1/2} \sim 10^{-2}s$ and the flow time-scale $D/U_0 \sim 10^{-2}s$. Therefore, Da can be caculated by $A\Omega^{-1}e^{-E_a/(RT_f)} \sim 1$ at $T_f = 1800\,K$. In the presence of strong swirling flow, the ratio of residence time to chemical time is very small. When flame lifts off and the circulation insreases a threshold, the reaction and transport effects both work. To determine the critical circulation for formation, further exploration of additional scenarios that take into account detailed reactions and complex flow dynamics is necessary.

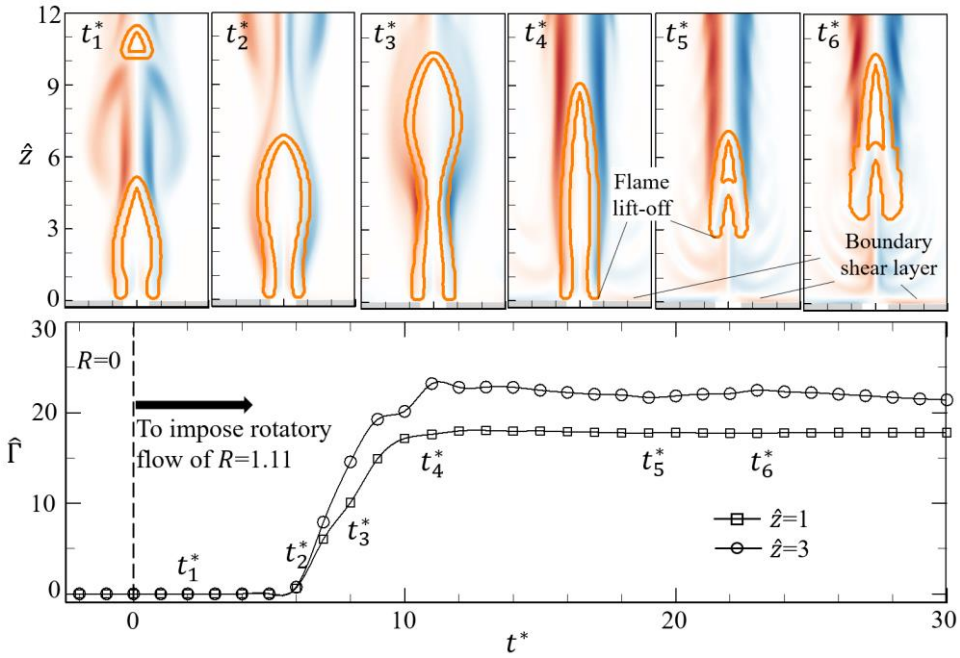

Figure 4-16 The variation of circulation with time during the lift-off formation from the attached flame. The circulation is defined as $\hat{\Gamma} = \int \boldsymbol{u}d\boldsymbol{l}/\sqrt{gD^3}$ along the closed circle $\boldsymbol{l}$ with the radius $\hat{r} = 3$. The two lines represent the cross-section at $\hat{z} = 1$ and 3, respectively. Six instantaneous snapshots of flame and vorticity are included.

To further understand the formation mechanism of lifted flame, the flame formation process at the onset of lifted flame was investigated. The circulation evolution and the representative flame snapshots during the lift-off formation from the attached flame are shown in Fig. 4.16, which shows that the circulation first grows and then plateaus around a constant value. From the beginning to t^*=6, no change of the circulation is observed, during which the swirling flow is still not imposed upon the central flame. The flame keeps flickering very well (t_1^* and t_2^*). From t^*=6 to t^*=11, the circulation continues to increase gradually, rendering a tall and slender flame (t_3^* and t_4^*). After t^*=11, the growth of circulation stops, which is accompanied by a steady flame mode (t_4^*). During t^*=11~19, the flame lifts off, the boundary shear layer (a corner flow) intrudes into the central region, and a fishbone-like vortical structure is

formed. In the initial stage of lift-off, the flame transitions into a small one (t_5^*). Subsequently, the flame stabilizes gradually, and its size becomes big (t_6^*).

4.5.4 Spiral Flame

An asymmetric flame was identified for the case of $R = 0.60$ and $\alpha = 79°$ in Fig. 4.17, where the flame presents a spiral motion, especially the irregular spin of the top of the flame. The spiral flame is similar to the sinuous mode of non-swirling jet flames at large Froude number [198, 200], in which the outer vortex helix grows and twines around the flame. In the downstream region, the flame tip inclines apparently, and the nearby streamlines are in the disturbance.

The present simulations captured the dynamical feature of spiral flame. The top of the flame behaves like a swing instead of symmetrically up-and-down for the case of $\alpha = 45°$ and the same R. To clearly show the asymmetric swing, the streamlines crossing the flame are plotted within the vorticity contour. In the downstream region of $\hat{z} > 9$, there is a symmetry break of shear layers around the flame, leading to the curved streamlines, while the symmetry of flame, vortical flow, and streamlines retain well for the case of $\alpha = 45°$.

These observations provide more information about similar phenomena and could be useful to make comparisons in future experiments. In Fig. 4.17(c), the upstream phase portrait is a slender ellipse, while the downstream portrait shows a quasi-cycle in the bigger range, particularly S_{U6} at $\hat{z} = 18$. Their two-dimensional projections are shown in Fig. 4.18. The features of phase portraits are consistent with the dynamic behaviours of the spiral flame.

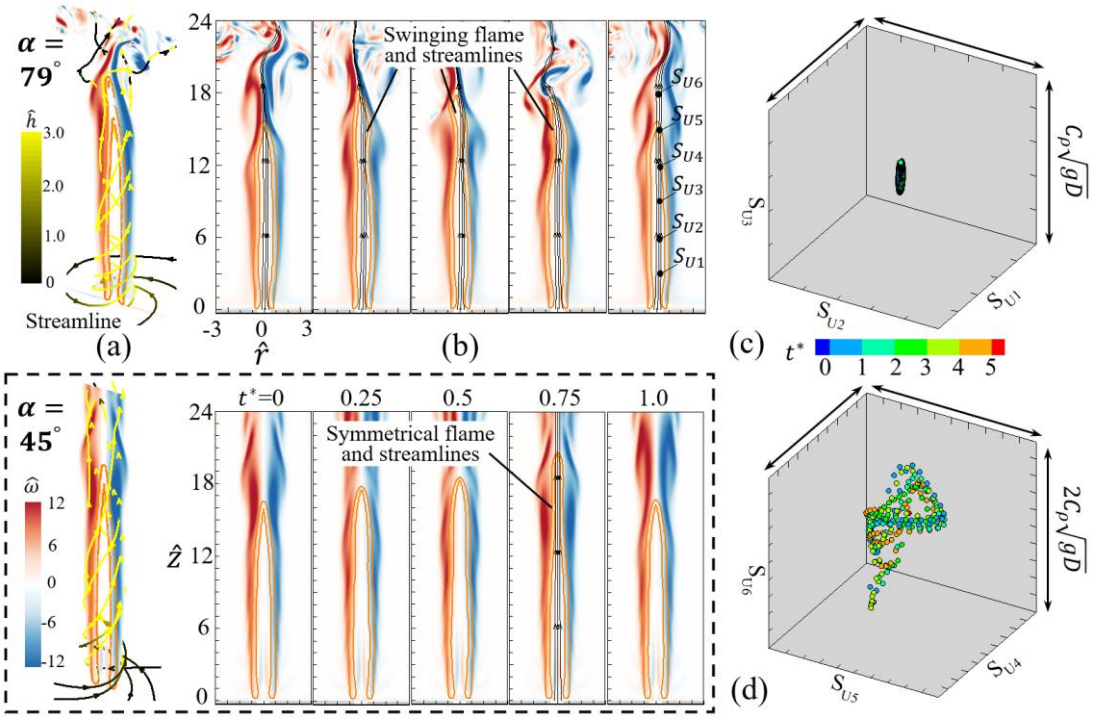

Figure 4-17 The spiral structure of the buoyant diffusion flame ($Re = 120$, Fr=0.40) in the swirling flow with $R = 0.60$ and $\alpha = 79°$. (a) the flow around the flame, (b) the time-varying evolution of the flame, (c-d) the phase portrait in the cubic space plotted by six velocity components S_{U_i}, i =1, 2, 3, 4, 5, and 6 at $\hat{z}$ =3, 6, 9, 12, 15, and 18 respectively along the central axis. All phase spaces have the same range of $C_\rho\sqrt{gD}$. In the dotted rectangle, the oscillating flame ($Re = 120$, Fr=0.40) at $R = 0.60$ and $\alpha = 45°$ is shown to facilitate comparison.

Detailed comparisons between the two flames in the three-dimensional view and their orthogonal projections are presented in Fig. 4.19. By comparing the patterns of flames (the orange iso-surface of heat release) and vorticial structures (the grey iso-surface of vorticity) in the two cases, it should be noted that the external swirling flows with different α have an impact on the vortical flow due to the formation of the twisted vortex around the flame surface.

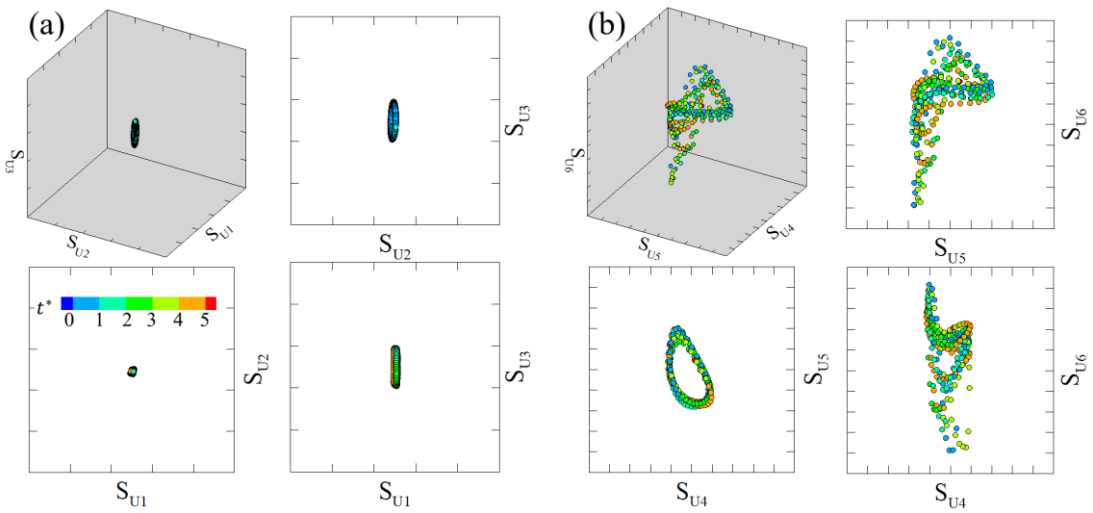

Figure 4- 18 Three-dimensional phase portraits and their two-dimensional projections in the (a) upstream and (b) downstream regions for the spiral flame in Fig. 4-17 (c-d).

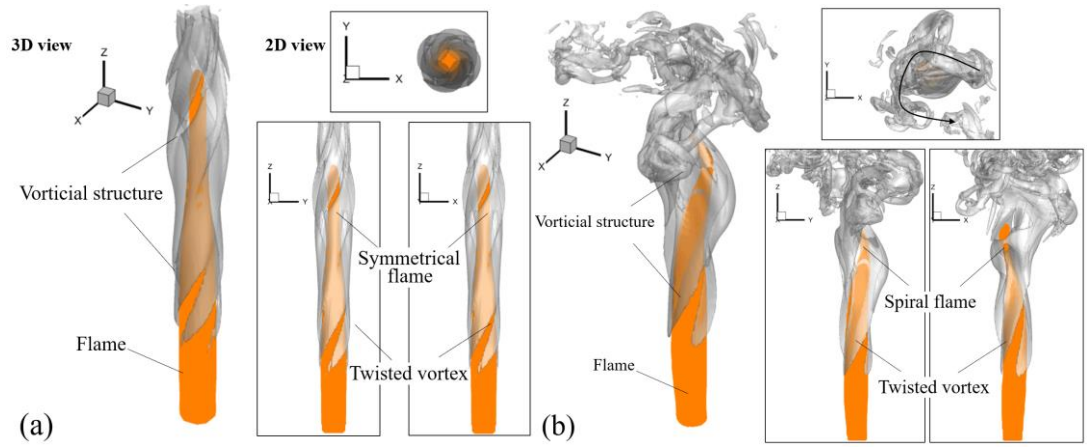

Figure 4-19 The three-dimensional view and their three-view drawings of (a) the oscillating flame ($\alpha = 45°$) and (b) the spiral flame ($\alpha = 79°$) corresponding to Fig. 4-17, respectively. The flame is represented by the orange iso-surface of heat release. The vorticial structure is denoted by the grey iso-surface of vorticity.

However, the vortical structure in the spiral flame presents a stronger spin than that in the case of $\alpha = 45°$. The outer vortex is dynamically coupled with the flame and shapes it into the sinuous. Particularly, the shedding vortex breaks into some small-scale structures (many small vortex tubes denoted by the iso-surface of vorticity in the downstream region) when the swirling flow has a big inlet angle. At the same $|\boldsymbol{U}|$, the

bigger α is, the smaller the radial component of the inlet velocity is. Therefore, the central flow in case $\alpha = 79°$ is more likely to spread out than that in case $\alpha = 45°$.

4.5.5 Vortex-bubble Flame

A hat-like flame is captured for the case of $R = 1.30$ and $\alpha = 64°$, in which the lifted flame has a vortex bubble at the flame base. Different from the lifted height $4{\sim}6D$ for the case of $R = 1.30$ and $\alpha = 45°$, the vortex bubble is closer to the fuel inlet and stays close around the vertical position of $2D$, as shown in Fig. 4.20(a).

Particularly, the higher helicity density in the vortex-bubble flame can be observed along the streamlines at the bottom region, compared with that in the case of $R = 1.30$ and $\alpha = 45°$. To clearly illustrate the dynamic features of the vortex bubble flame, the flame and vortex structures within the time interval of $\Delta t^* = 1$ are shown in Fig. 4.20(b). Different from the lifted flame shown in Fig. 4.15(b), in which the inflating streamlines go through the flame and no circulation exists, the base of the vortex bubble flame kicks outward to form an apparent vortex bubble.

To understand the mechanism underlying the formation of vortex-bubble flame, it should be noted that the basic definition of vortex breakdown is the abrupt change in vortex structure with retardation along the vortex core and the corresponding divergence of stream surfaces [201, 202]. It is seen from Fig. 4.20(b) that the streamlines contract in the central region, diverge outwardly, and finally form a convergence toward the downstream. The abrupt change causes a circulation zone where the flow velocities have relatively small magnitudes. In particular, the small vortex cores are generated within the range of $|\widehat{\boldsymbol{u}}| < 1$. The bubble region for the vortex breakdown is unstable, and its barycenter and shape vary with time. As shown in Fig.

4.20(c-d), the phase portraits are a warping string within a relatively small range, instead of a closed topological structure within a relatively big range.

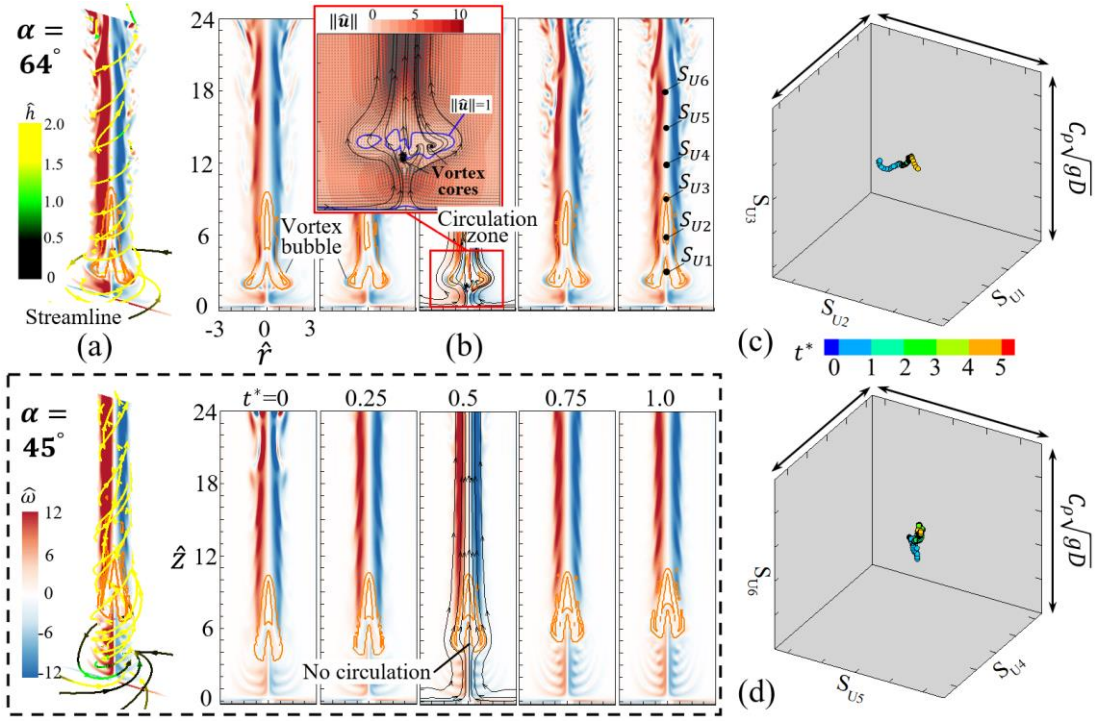

Figure 4-20 Vortex bubble of the buoyant diffusion flame (Re=100, Fr=0.28) in the swirling flow with $R = 1.30$ and $\alpha = 64°$: (a) the flow around the flame, (b) the time-varying evolution of the flame, (c-d) the phase portrait in the cubic space plotted by six velocity components S_{U_i}, i =1, 2, 3, 4, 5, and 6 at $\hat{z}$ =3, 6, 9, 12, 15, and 18 respectively along the central axis. All phase spaces have the same range of $C_\rho\sqrt{gD}$. In the dotted rectangle, the lifted flame at $R = 1.30$ and $\alpha = 45°$ is shown to facilitate comparison.

As an interesting extension of the present study, Fig. 4.21 shows a qualitative comparison of the vortex-bubble flame with Chung et al.'s simulation of the blue whirl [193]. Similar features of the flame and the flow are captured in the present simulations. Previous studies [59, 68, 178, 203] suggested that the formation of the blue whirl is accompanied by the occurrence of the vortex breakdown (the bubble, helical, or

whirling structures), which is consistent with the present finding (the flame structure is shaped by the vortex bubble).

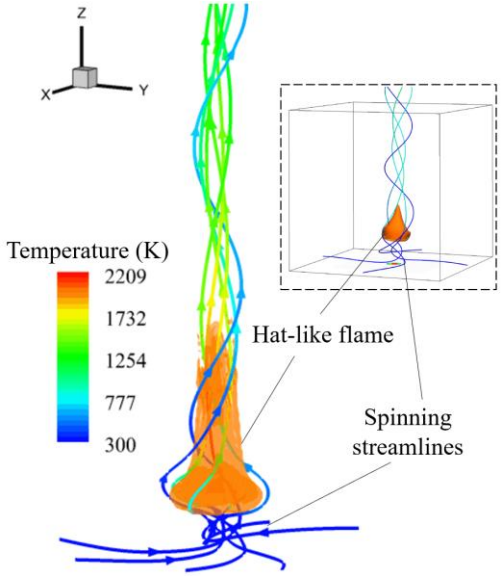

Figure 4- 21 Vortex-bubble flame mode and the blue whirl (dotted box) in [193].

Besides, the present numerical investigation that the vortex-bubble flame emerges at a relatively large R (it corresponds to the swirling condition of $\hat{\Gamma} > 1$) agrees with the previous experimental observation that the blue whirl falls in a circulation-dominated flow regime. The implications of the vortex-bubble flame for understanding blue whirl merits future studies.

4.6 Summary and Conclusions

Previous experimental works have made noticeable progress toward understanding buoyant diffusion flames in externally swirling flows. However, their dynamical behaviours in a large range of swirling flow intensity are still unclear, and the corresponding vortex interpretations were inadequately attempted due to the challenges of measuring the flow and temperature of flames. This study presents a comprehensive computational investigation of the small-scale flickering buoyant

diffusion flames in externally swirling flows with a wide range of swirling intensity $R = 0{\sim}1.70$ and the angle $\alpha = 27°{\sim}79°$of inlet airflow. Buoyant diffusion flames exhibit six distinct dynamical modes at different R and α, namely the flickering flame, the oscillating flame, the steady flame, the lifted flame, the spiral flame, and the flame with a vortex bubble, which were scattered and reported in a few previous experimental studies. These flames exhibit from axisymmetric to asymmetric patterns. The dynamical behaviours of these flame modes are illustrated in the phase space and analyzed from the perspective of vortex dynamics.

In the weak swirl regime (R< 0.31), the buoyancy-induced flame flicker becomes faster nonlinearly with increasing R, where the increase of f obeys the scaling relation of $(f - f_0) \propto R^2$. Since the vortex shedding occurs downstream of the flame, the flame flicker is suppressed, and instead, the flame has an oscillating tip or remains in a steady state. Higher R can induce higher circulation $\hat{\Gamma}$ at the flame base and a smaller Damköhler number to make the flame lift off the bottom. The flame lift-off phenomenon was qualitatively captured by using a one-step finite-rate chemistry model in the present simulation. In addition, the spiral flame mode and the vortex-bubble flame mode were computationally reproduced by using larger swirl angles α.

Based on the understanding that phase portraits are an invaluable tool in studying dynamical systems, different flame modes are illustrated and identified in the phase space. Specifically, the flame features and phase portraits for the six modes are summarized as follows:

1) The flickering flames have the distinct feature that the periodic shedding of the toroidal vortex around the flame. The portraits of these flames are the closed ring shape. Besides, the topological structure of the flames is broken when the externally swirling flow is weak, for instance, the weak swirling conditions of $R < 0.31$ and $\alpha = 45°$.

2) The oscillating mode exhibits that the toroidal vortex sheds off behind the flame and occurs at the intermediate R region (for instance, $R = 0.29{\sim}0.35$ and $\alpha = 45°$). The upstream portrait of these oscillating flames is the closed ring, while a big disturbance occurs in the downstream portrait.

3) The steady mode hardly has the formation of a toroidal vortex around the flame, as the vortex shedding occurs far behind the flame. In the steady flames, the upstream phase portrait degenerates into a point, while the downstream portrait exhibits small oscillation. The formation of steady flames corresponds to the relevantly large R region, for instance, $0.35 < R < 1.11$ and $\alpha = 45°$.

4) The lifted flames detach from the bottom wall due to the relatively small Da number. The phase portraits of the flames are nearly motionless. The present study shows that the large R (>1.10) with the fixed $\alpha = 45°$ causes a very small ratio of the residence time to the chemical time at the flame base, thereby leading to the lift-off of the flame.

5) The spiral flames have a distinct feature in that the symmetry of shear layers around the flame is broken, compared with the four modes of flickering, oscillating, steady, and lifted flames. In these flames, the upstream phase portrait is a small ellipse, while the downstream portrait shows a big quasi-cycle. The asymmetric flames occur at a large α, while R is the same. For instance, R=0.60 and α=79°.

6) The vortex-bubble flames show a different pattern in the occurrence of the vortex bubble for the vortex breakdown in the flame base, compared with the lifted flame. The phase portraits present a warping string within a relatively small range as the unstable bubble has time-varying barycenter and shape. These flames occur at the relatively large R and α, for instance, R=1.30 and α=64°.

Chapter 5. Vortex-dynamical Interpretation of Anti-phase and In-phase Flickering of Dual Buoyant Diffusion Flames

In this chapter, we conduct a numerical investigation and theoretical analysis of the anti-phase and in-phase flickering modes of dual buoyant diffusion flames. The coupled behaviors of two laminar flame oscillators present an intriguing area of study. Consistent with previous experimental findings [83], we identify two distinct flame modes in double flickering flames by varying the gap distance between them. The flickering synchronization of two adjacent flames occurs in two distinct modes, each maintaining self-sustained oscillation at a fixed gap distance. Drawing on the flickering mechanism of a single buoyant diffusion flame—where deformation, stretching, and pinch-off arise from the formation and evolution of toroidal vortices—we explore the anti-phase and in-phase flickering of dual flames through vortex dynamics. A key aspect of this is the interaction between the inner-side shear layers of the flames, which determines the different flickering modes.

We begin by examining the anti-phase mode with a large gap, illustrating its mechanisms through visualization of the heat and flow fields. Next, we investigate the in-phase mode. The transition between these anti-phase and in-phase flickering modes can be predicted using a unified regime nomogram, which plots normalized flickering frequency against a characteristic Reynolds number, considering the viscous effects on vorticity diffusion between the inner-side shear layers. This transition in vortical structures—from symmetric (in-phase) to staggered (anti-phase) in a dual-flame system—resembles the flow transition behind a bluff body that results in the formation of a Kármán vortex street.

5.1 Computational Setups and Preliminary Results

For double pool flames, the configuration was set up as shown in Fig. 5-1. For the simulation setup, the gray exterior surfaces are designated as open boundary conditions, permitting gases to flow in the inside and outside of the computational domain. Specifically, the Poisson solver requires a Dirichlet condition for the quantity, $\Omega = \tilde{p}/\rho + \boldsymbol{u}\cdot\boldsymbol{u}/2$, which means that Ω should remain constant along a streamline. Thus, for incoming flow Ω_{ext} at the boundary equals that at infinity of the ambient flow, whereas for outgoing flow Ω_{ext} is set to the value of its adjacent interior grid cell. The blue surface denotes the liquid fuel of heptane, whose vaporization rate is a function of the liquid temperature and the vapor concentration according to the Clausius-Clapeyron relation [169]. The base of each pool is enforced with the solid-wall boundary condition, which is impermeable, non-slip, and adiabatic. The typical computational domain measures 16 cm × 16 cm × 24 cm, with a grid resolution of $160 \times 160 \times 240$, established through domain and grid-independent studies in Chapter 2. Figure 5.2 systematically shows in-phase and anti-phase flickering flames.

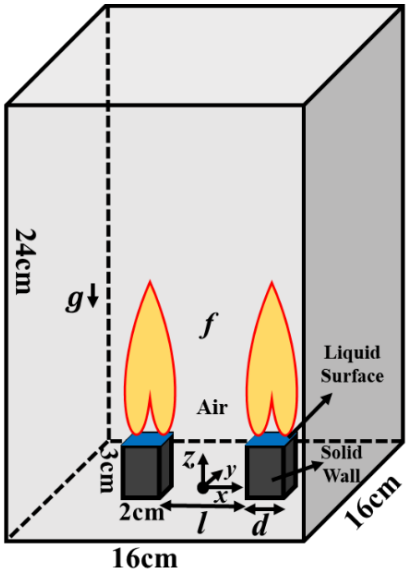

Figure 5-1 Computational domain and relevant parameters.

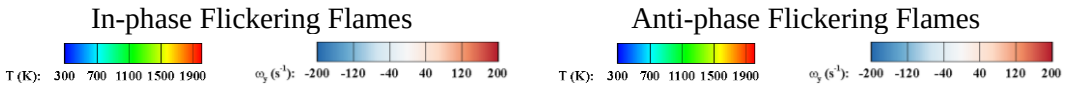

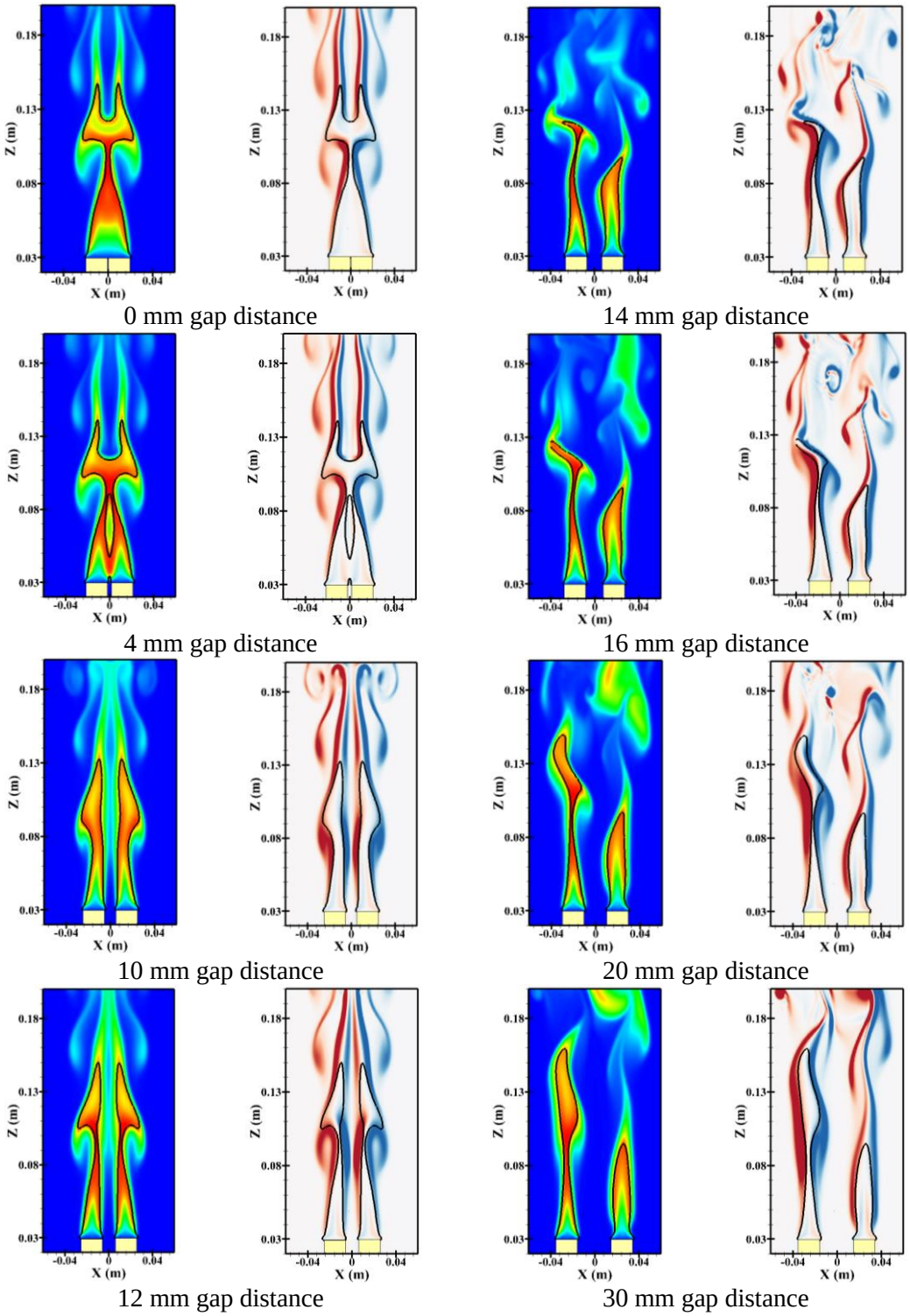

Figure 5-2 The temperature and vorticity contours of two flames with distinct flickering modes.

To reproduce the experimental results of ani-phase mode as well as possible, we consider the surrounding environment is at the standard atmospheric condition and the

air flow is quiescent without any disturbance. In addition, the initial condition of the present simulations is insignificant, as the fully developed state of flame dynamics is used to compare with experiments. The flame flicker is an unsteady state, and the coupling of flames is so strong that small external disturbances are not necessarily considered. Although investigating the flickering modes is the core task of the study, differences in the fuel inflow conditions and the geometric shape of the fire base may lead to variations between the simulated pool flames and the experimental candle flames, as shown below. Based on the present simulations with detailed flow and temperature fields, the underlying mechanism of flickering modes of flames can be illustrated, different from previous experiments with only focused on phenomenal reports and conjectures. Giving physical interpretations and verified conclusions is the most significant contribution of this study.

5.2 Anti-phase Flickering of Dual Pool Flames

For two identical pool flames with a considerable distance, Kitahata et al. [83] reported the existence of an out-phase synchronization of flickering, and their experimental images during one periodic time, T, are shown in Fig. 5.3(a). It is seen that each flame still stretches and shrinks in a periodic manner, while the flickering of the dual-flame system displays a “seesaw” pattern. It is evident that the flame pinch-off occurs at $0T\sim1/5T$ for the left flame and at $2/5T\sim3/5T$ for the right flame, and that the two flames are in opposite phases to each other. Thus, this oscillation mode is dubbed “anti-phase” synchronization in this thesis.

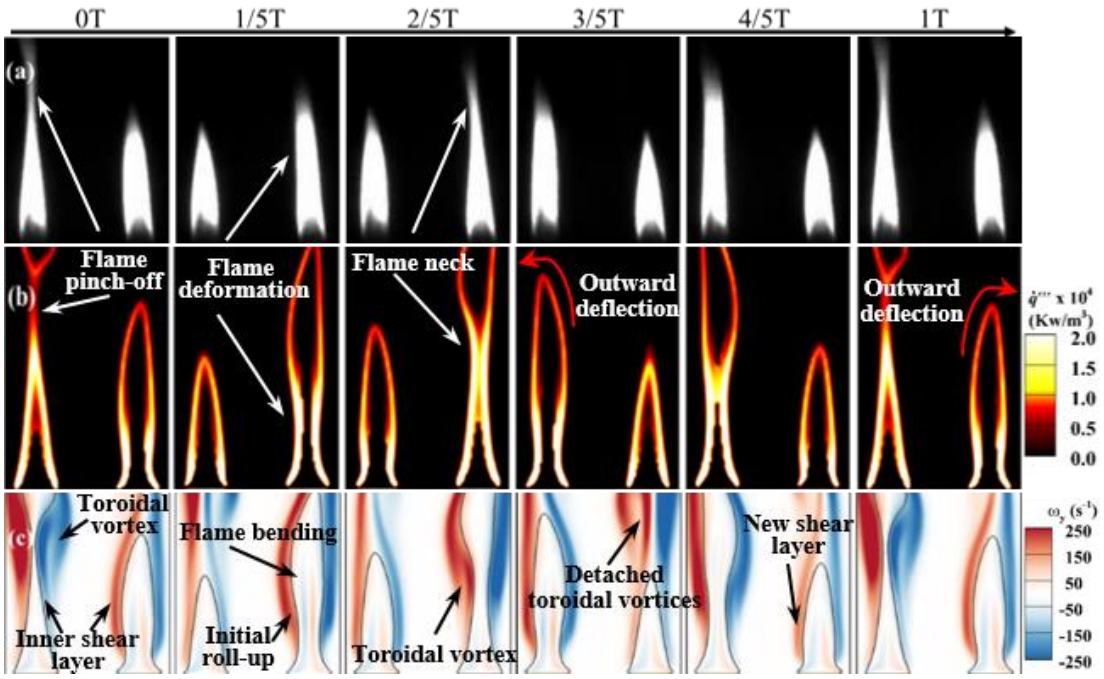

Figure 5- 3 Snapshots of flickering flames in the anti-phase synchronization from the experiment [8] based on brightness (a), and from the present simulation based on heat release (b) and vorticity (c).

The simulated heat release field is presented in Fig. 5.3(b) for comparison. It should be clarified that this simulation does not replicate the exact conditions of the original experiment [83] and, therefore, is not meant to be a rigorous numerical reproduction. This is because the experiment was conducted by using candle flames, with each “single” flame created by bundling three small candles together so that the large “single” flame could pinch off [83]. Nevertheless, the simulation still qualitatively captures the pinch-off of each individual flame as well as the “seesaw” oscillation pattern of the dual-flame system. Furthermore, it can be observed from the pinch-off behaviours of the simulation that the phase difference between the two flames is also around half a period, quantitatively verifying the establishment of the same anti-phase synchronization. The quantitative validation of the simulations is not necessary to give a big help in understanding the underlying mechanisms, as the dynamical modes are focused and slightly affected by some secondary influences.

Since the flickering of a single flame is caused by the vorticity generation and toroidal vortex formation induced by flow heating under gravity, we hypothesize that the synchronization in the flickering of two flames must be closely related to the vortex flows, especially the interactions between the shear layers or the rolled-up toroidal vortices of different flames. To this end, in Fig. 5.3(c) we plot the vorticity contours corresponding to the flame snapshots of Fig. 5.3(b). Here, the black contour is obtained based on the stoichiometric mixture fraction to represent the flame sheet, which agrees well with the flame sheet visualized by heat release in Fig. 5.3(b). It can be observed that the flame sheet is indeed accompanied by strong vortex flows, which is similar to the flame-vortex configuration of a single flame. Moreover, for each individual flame the connection between the roll-up of the toroidal vortex and the flame pinch-off process during $0T\sim1/5T$ and $2/5T\sim3/5T$, can still be identified. However, the difference is that the symmetry associated with each individual flame is disrupted as the flame and the shear layer seems to bend outwards, away from each other, as illustrated by the red arrows in Fig. 5.3(b). This can be understood that the closeness of another flame can be considered as an addition of another pair of shear layers, the net effect of which is to induce a rotary velocity field to deflect the current flame. This induced velocity field is in the direction opposite to the other flame because it is dominated by the vorticity in the inner-side shear layer of the approaching flame, which is closer to the current flame than the outer-side shear layer and thus exerts a stronger influence.

Based on the vorticity contour in Fig. 5.3(c), the mechanism responsible for the anti-phase synchronization is further interpreted below. We can verify the conjecture stated that in this mode the toroidal vortex is still the dominant factor for the behaviours of each flame. The effect of the other flame can be treated as a small perturbation which,

from a vortex dynamics perspective, causes an induced velocity field and slightly deforms the existing flame. One would expect this effect to be marginal; however, the interaction between these shear layers as well as the toroidal vortices of different flames clearly causes the staggered distribution of the toroidal vortices, which might be the fundamental reason for the half-period phase difference between the two flames.

5.3 In-phase Flickering of Dual Pool Flames

As the distance between the two flames is sufficiently small, their flickering mode changes dramatically so that the two flames exhibit an in-phase synchronized oscillation. Here, the experiment of Forrester [84] is adopted as the reference for our simulation because single candle instead of bundled candles were used in his experiment. Fig. 5.4(a) and 5.4(b) illustrate the experimental snapshots and the correlated simulation results, respectively. Both results show that the two flames flicker along with each other symmetrically as an integrated flame. The agreement between the experiment and the simulation is good, except for the shape of the flame pocket during pinch-off (from $2/5T$ to $1/2T$). The mismatch could be attributed to the differences in the fuel inflow condition and the fire base shape between the circular candle flame and the rectangular pool flame.

To understand the in-phase synchronization, we again refer to the vorticity evolution during one period of flame flickering, as shown in Fig. 5.4(c). It is interesting to note that the flames still pinch off under the deforming and stretching effect of the toroidal vortices, which is not fundamentally different from a single flame. However, the toroidal vortex for each individual flame displays a distinct asymmetric feature that the shear layer only rolls up into a vortex on the outer side with the inner side remaining a rather linear shear layer, as observed at $2/5T$ and $1/2T$ in Fig 5.4(c). Since the vortex roll-up is essentially an outcome of vorticity accumulation, the asymmetric roll-up of

the toroidal vortex can be translated into an imbalance of vortex strength between the outer and inner shear layers. This imbalance can be further justified by the contour of each flame which tends to lean inward towards each other, as indicated by the red arrows in Fig. 5.4(b), opposite to the outward flame deflection in the anti-phase synchronization.

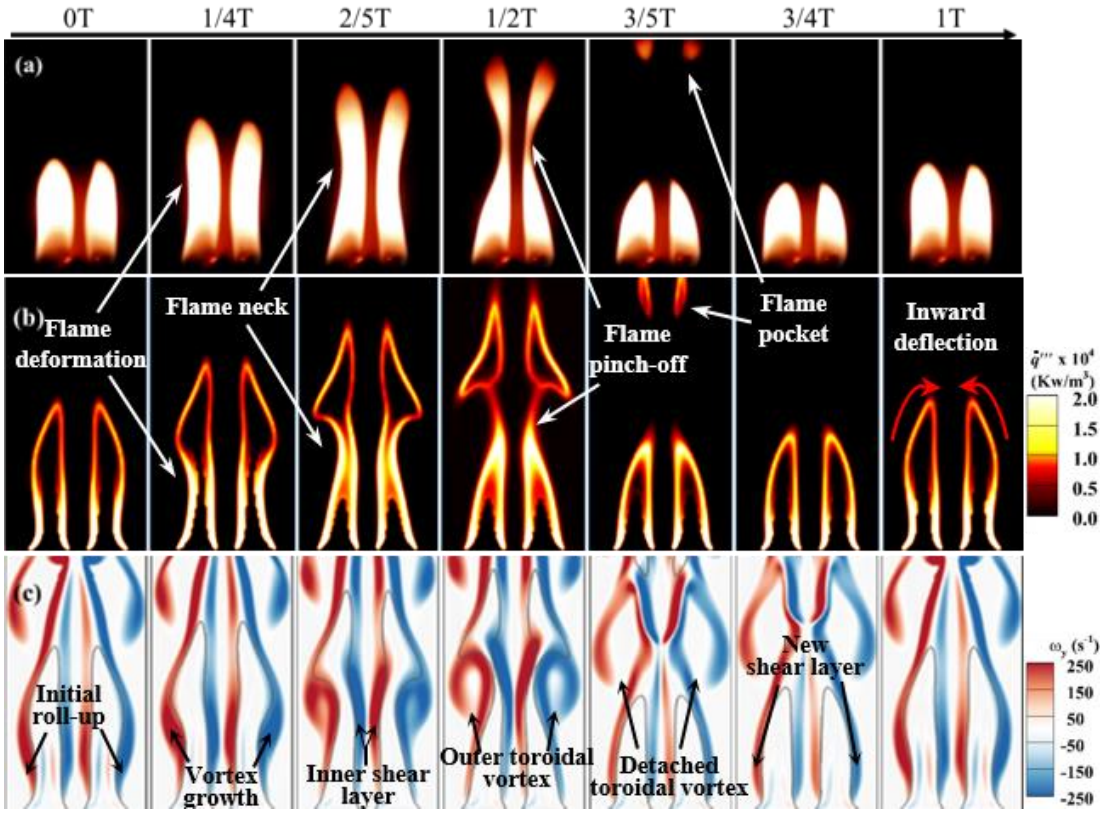

Figure 5-4 Snapshots of flickering flames in the in-phase synchronization from the experiment based on brightness (a), from the present simulation based on heat release (b) and vorticity (c).

To further illustrate the interactions of two jet flames, Fig. 5.5 shows that flickering flames symmetrically stretch and pinch off in a simultaneous manner as one flickering flame (no phase difference between their temperature signals), while the anti-phase flickering flames display a distinct asymmetric feature and each flame experiences pinch-off alternatively, like playing a “seesaw” game (a phase difference

of π between their temperature signals). The vortex-dynamical mechanism of coupled dual flames has been substantiated that the interaction between two vortex rings, generating around each flame respectively, is responsible for the different flickering modes [86, 88, 160, 163].

Similar to the dynamical behavior of a single flickering flame, the flame deformation, necking, and pinch-off are respectively coupled with the initial roll-up, growth, and detachment of the vortex ring. The interacting vortex mechanism has a decisive effect on the transition between the two different flickering modes. Figures 5.5(a) and 5.5(c) illustrate the vorticity diffusion and vortex-induced flow mechanisms of inner shear layers between the two flames respectively, determining the interaction of two vortex rings. Specifically, the vorticity diffusion (denoted by the color gradient area at t_1) between the shear layers causes the vorticity reconnection of the two vortex rings at t_2 and forms a big vortex ring at t_3, while the vortex-induced flow (denoted by the dotted lines at t_1) between the shear layers leads to the instability of the inner shear layers at t_2 and the vortex rings evolve in a staggered manner at t_3. Therefore, the vorticity diffusion notably weakens the inner-side shear layers of the two flames in the in-phase mode, as shown in Fig. 5.5(a), while the inner-side shear layers become staggered without being diminished in the anti-phase mode, as shown in Fig. 5.5(c).

As discussed in Chapter 3, the flame deflection is caused by the induced velocity of the shear layers of the other flame, the current inward deflection corresponds to a velocity direction same as that induced by the outer-side shear layer. As the outer-side shear layer is farther away, it turns out that the outer-side shear layer together with the rolled-up vortex must have a significantly larger strength in order to dominate over the inner-side shear layer. This suggests the existence of an additional mechanism that dissipates the vorticity of the inner-side shear layer, given that the vorticity growth

should not be much different between the inner and the outer sides. As will be further analyzed in the next section, this mechanism is exactly the viscous diffusion, which is essential to the synchronization of a dual-flame system.

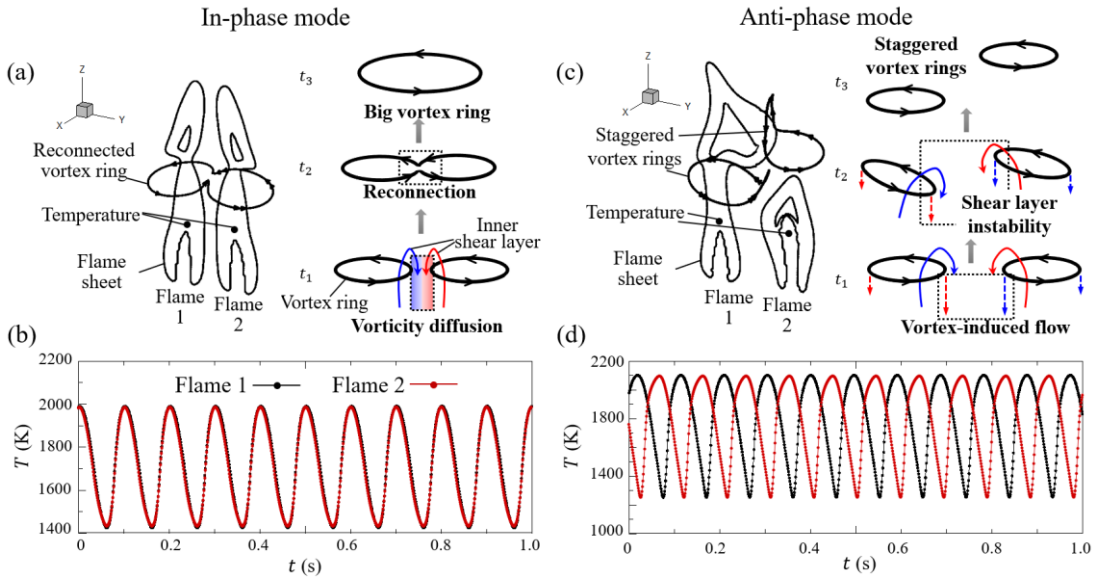

Figure 5-5 (a-b) In-phase mode and (c-d) anti-phase mode of dual flickering flames at small and big gaps respectively: the vortex interactions of (a) vorticity diffusion and (c) vortex-induced flow; the time-varying temperature in each flame with the phase difference of (b) 0 and (d) π. The inner shear layers between the two flames determine the interaction of two vortex rings. The vorticity diffusion (denoted by the colour gradient area at t_1) between the shear layers causes the vorticity reconnection of the two vortex rings at t_2 and forms a big vortex ring at t_3, while the vortex-induced flow (denoted by the dotted lines at t_1) between the shear layers leads to the instability of the inner shear layers at t_2 and the vortex rings evolve in a staggered manner at t_3.

It's noteworthy that flame flicker is dominated by buoyance, instead of chemical reactions so many previous studies [204, 205] reported that the gaseous fuels for jet flames and liquid fuels for pool flames both can generate the flickering phenomenon, when the gravity and flame size are appropriate. Particularly, the two primary kinds of

flames (liquid pool flames with the evaporation and jet flames with the injection of gaseous jets) follow the same flickering scaling of buoyant diffusion flames [24].

5.4 Unified Mechanism for Distinct Flickering Modes

So far, we have linked the anti-phase and in-phase synchronizations in the flickering of a dual flame system to the development of vortical structures within the flow field. This differs from the perspective [83] for attributing synchronization to radiation, integrating it with the symmetric Hopf bifurcation theory [80] to anticipate the synchronization modes. However, their model entirely overlooked the influence of fluid dynamics, a fact acknowledged by the authors in a more recent publication [206]. In this section, we will concentrate on clarifying the interaction between the inner-side shear layers of the two distinct flames in order to comprehend the fundamental mechanism underlying the emergence of various synchronization modes.

It appears that the inner-side shear layers merely become staggered rather than diminished in the anti-phase synchronization mode, while the vortex strengths of the inner-side shear layers are significantly reduced in comparison to the outer-side in the in-phase synchronization mode. This effect is quantitatively confirmed in Fig. 5.6, where substantial vorticity diffusion occurs between the two inner-side shear layers, leading to an unbalanced vorticity annihilation in the in-phase synchronization mode.

With the assumption of axisymmetric incompressible flow with non-swirling and neglecting tiny pressure gradient, the vorticity transport equation is simplified as

$$\frac{D\boldsymbol{\omega}}{Dt} = \frac{\rho_A}{\rho^2}(\nabla\rho \times \boldsymbol{g}) + \nu\nabla^2\boldsymbol{\omega} \tag{5.1}$$

where $\boldsymbol{u}$ and $\boldsymbol{\omega}$ represent the velocity and vorticity vectors, ρ is the local density, $\boldsymbol{g}$ denotes the gravitational acceleration vector, ν is the kinematic viscosity, and ρ_A is the gas density of the surrounding environment.

Here, the vorticity diffusion term is calculated from $\nabla^2\boldsymbol{\omega}$, which is the term associated with the kinematic viscosity, ν, in Eq. (5.1), mathematically showing that the vorticity variation by means of diffusion intensifies with increasing vorticity gradient, and thus decreasing distance between the vortices. This explains the strong vorticity annihilation observed in the in-phase synchronization mode when the two inner-side shear layers approach each other.

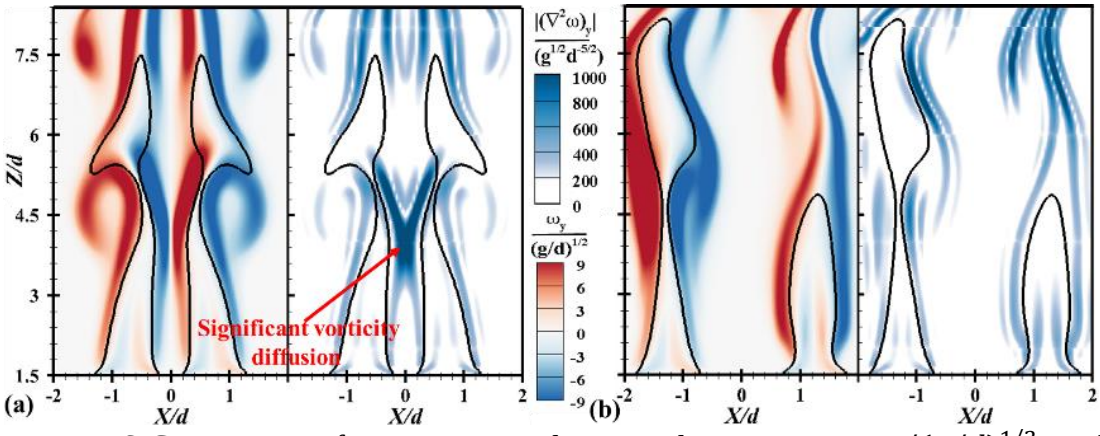

Figure 5-6 Comparison of instantaneous dimensionless vorticity, $\omega_y/(g/d)^{1/2}$, and dimensionless Laplacian of vorticity, $|\nabla^2\omega_y|/(g^{1/2}d^{-5/2})$, in (a) in-phase and (b) anti-phase synchronizations.

In addition, we will outline several reasons for utilizing two-dimensional (2D) flow analysis in addressing the current three-dimensional (3D) problem. First, the main interactions between the two flames occur in the plane connecting them, with interactions at greater distances resulting in secondary effects. Moreover, the instabilities and vortex interactions that might amplify 3D effects primarily happen in the far field and have little influence on the laminar flow in the near field. This is corroborated by the helicity plots. in Fig. 5.7. This definition means that helicity is generated by the "non-orthogonality" of the vorticity and velocity vectors. Physically, helicity in fluid dynamics is a measure of the knottedness and/or linkage of the vortex

lines, and its volumetric integral inside an ideal Euler flow is an invariant given no vorticity crossing at the boundary.

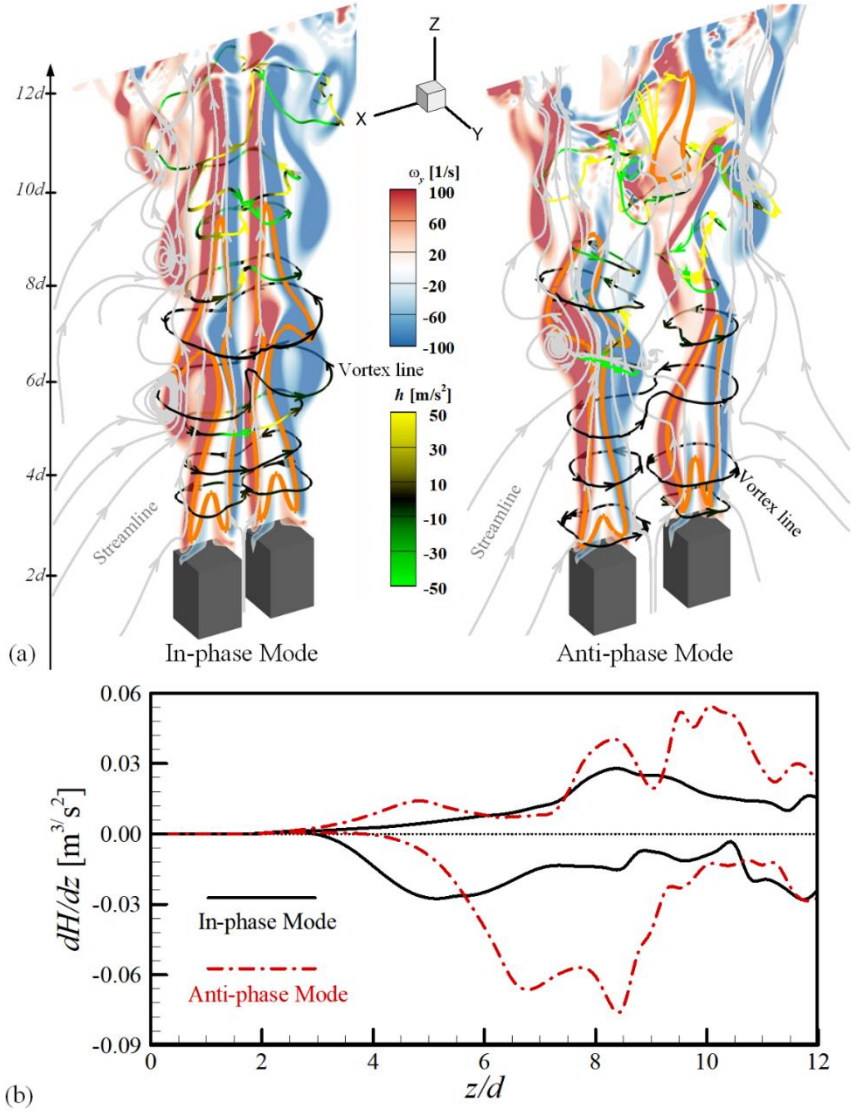

Figure 5-7 (a) The distribution of vorticity in the $X-Z$ plane for in-phase (left) and anti-phase (right) flickering modes. The flame sheets are represented by orange contours. The streamlines are denoted by the gray lines, and the vortex lines are colored by the helicity density, $h = \boldsymbol{u} \cdot \boldsymbol{\omega}$. (b) The area integral of helicity density, $dH/dz = \iint h\, dxdy$ $(x \geq 0, y \geq 0)$, along the z direction for in-phase (black solid lines) and anti-phase (red dash-dot lines) flickering modes. The two curves of each mode correspond to the upper and lower limits of dH/dz during an entire flickering period.

In the current context, helicity may serve as a reference for the intensity of 3D interactions between the vortical structures. It is evident from Fig. 5.7(a) that in both in-phase and anti-phase flickering modes vortex lines located approximately below $z/d = 5$, where the streamlines become spiral and flame pinch-off occurs, are in regular 2D shape and black colour (low h value), indicating relative weak knottedness or linkage of the laminar vortical structures in the near field. However, the vortex lines downstream become twisted and irregular, and dyed in high h-value colours, which implies strong 3D interactions between the vortices. This can be understood by that the flow is mainly dominated by 2D vortex interactions in the near field where the shear layers remain laminar so that the out-plane velocity component is insignificant; whereas the vortex interactions become 3D in the far field when the shear layers evolve into more complex vortical structures and are entangled with each other.

This understanding can be further demonstrated in Fig. 5.7(b), which shows the maximum and minimum of the areal integral of helicity density, $dH/dz = \iint h\, dxdy$ ($x \geqq 0, y \geqq 0$), within a flickering period at different z locations. It is seen that in both flickering modes, the helicity integral in the near field at $z < 5d$ is almost negligible while it increases notably in the downstream after the flame pinch-off location. Furthermore, the larger amplitude of helicity integral of the anti-phase mode compared with the in-phase mode clearly indicates a stronger 3D effect downstream of the anti-phase mode, reflecting a more unstable nature of flickering.

At this point, it is nature to compare the interaction between the inner-side shear layers of the two flames to that of the wake of a bluff body, e.g., the flow around a cylinder [207], based on the following considerations. One is the resemblance in the direction of the vorticities in the two counter-rotating shear layers. Furthermore, both flows involve a transition of the shear-layer configuration from symmetric to staggered,

which is also known as the von Karman vortex street [186]. From the above analysis, we are more convinced to make this analogy because the transition is closely related to viscosity in both cases. For the canonical flow around a cylinder, this flow transition can be dictated by a Reynolds number, Re, which quantifies the effect of inertia relative to viscosity. It was found that the transition from symmetric vortical structures to staggered vortex streets usually happens around a critical Reynolds number from several decades to a hundred. Therefore, we hypothesize that a similar mechanism is responsible for the transition between the two different synchronization modes of a dual-flame system. In analogy to the wake flow, a flame Reynolds number is defined here based on the two inner-side shear layers:

$$\alpha Gr^{1/2} = \frac{\sqrt{gdl}}{\nu_A} \sim \frac{Ul}{\nu_A} = Re_A \tag{5.2}$$

We shall demonstrate the relationship between Eq. (5.2) and the synchronization modes of two flickering flames. The new dimensionless number incorporates the viscous effects on vorticity diffusion between the two inner-side shear layers, enabling the prediction of transitions between anti-phase and in-phase flickering modes. It also facilitates the development of a unified regime nomogram for the normalized flickering frequency versus Re_A, as shown in Fig. 5.8. The interaction of vortexes around two flames can be regarded as two parallel "von Karman"–type of shear layers driven by the buoyance.

Next, the flame frequency is scaled by f_0 , the frequency of a single flicking flame, is plotted against Re_A in Fig. 5.8, based on Kitahata et al.'s experimental data [83] and the current simulation results. Note that the effective diameter of the bundled candles is estimated to be 13mm, based on the diameter of a virtual circle wrapping the candles. It is seen that the in-phase and anti-phase modes are distinguished by the different

trends of frequency variations. A noteworthy finding is the good agreement of the transitional region between the experiment of candle flame and the simulation of pool flame, indicating that Re_A is indeed the key mechanism governing the synchronized flickering mode between two flames.

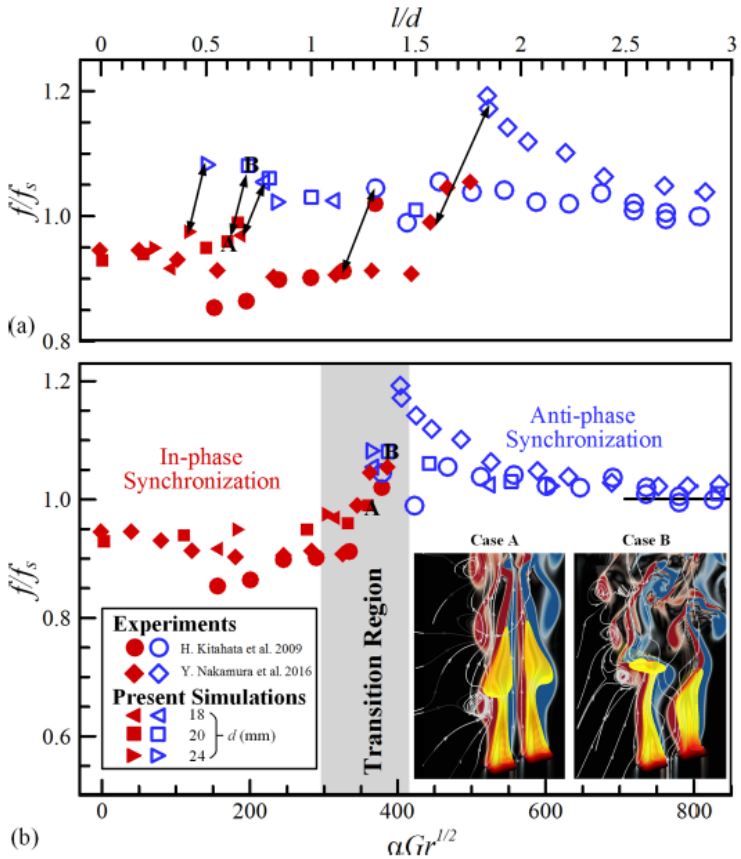

Figure 5-8 Comparison of (a) normalized f/f_s at different l/d and (b) normalized f/f_s at different $\alpha Gr^{1/2}$.

In addition, we generally defined the nondimensional number as

$$\alpha Gr^{1/2} = \frac{l-D}{D} \times \left[\frac{g(T_f - T_0)D^3}{\bar{T}\upsilon_A^2}\right]^{1/2} \simeq \gamma \frac{(gD)^{1/2}(l-D)}{\nu_A} \tag{5.3}$$

where Gr is the ratio of buoyant forces (induced by temperature change) to viscous forces and expressed as $g(T_f - T_0)D^3/\bar{T}\nu^2$. In the problem of flickering flames, Gr is proportional to gD^3/ν^2, as T_f is the flame temperature about 2100 K, T_0 is the ambient air temperature at 300 K, $\bar{T}$ is the average temperature of about 1200 K. Therefore, the

prefactor of $\gamma = \sqrt{(T_f - T_0)/\bar{T}}$ is constant about 1.22. It should be noted that $\alpha Gr^{1/2}$ is equivalent to a Reynolds number of $(gD)^{1/2}l/\nu$ that was proposed and verified in our previous work [163], where $(gD)^{1/2}$ is a characteristic velocity of the buoyancy-driven flow. Figure 5.9 shows that many experiment and simulation data of dual flickering jet flames are shrunk to a narrow band of a transition region of $400 < \alpha Gr^{1/2} < 500$. The frequency variation trend of the simulated dual flickering flames agrees well with existing literature [88, 208].

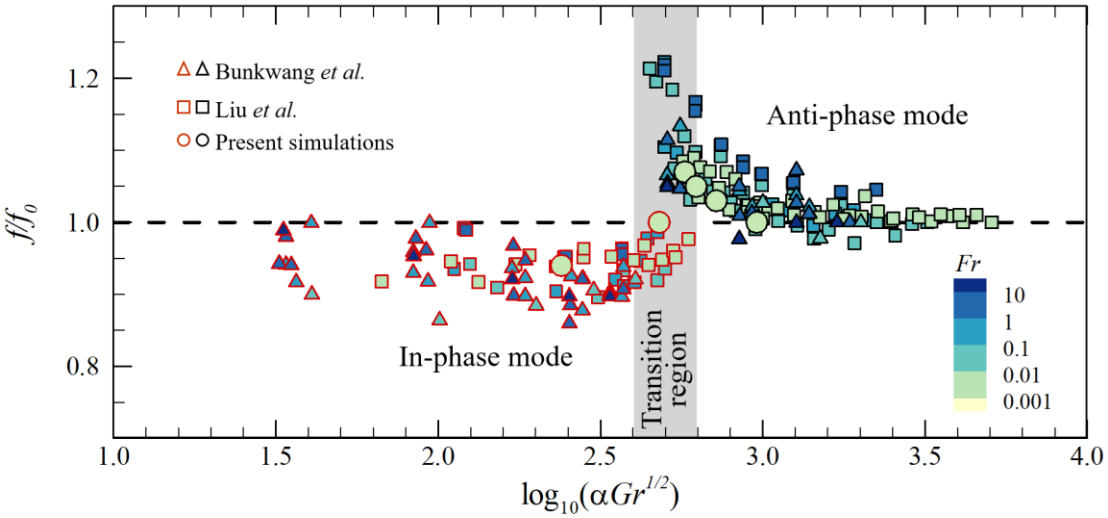

Figure 5-9 Regime diagram of the dual-flame system. Data are from previous experiments [88, 208] and present simulations of dual-flame systems. The systems consist of two identical flickering diffusion flames, of which each one is characterized by the Froude number Fr. The nondimensional number of $\alpha Gr^{1/2}$ is an equivalent Reynolds number [163], while the flickering frequency f of dual flames is normalized by the frequency f_0 of single flame. A transition region of $400 < \alpha Gr^{1/2} < 500$ distinctly separates the in- and anti-phase modes.

It should be noted that the vortex interactions of the dual-flame system have universality, as Fr has the change in $O(0.001)$~$O(10)$. It can be believed that the

present simulation methods are verified to predict the vortex interactions of flickering flames. Particularly, the flickering frequency f of dual flames varies with $\alpha Gr^{1/2}$ in a nonmonotonic manner and the in-phase and anti-phase modes are distinguished by a frequency "jump", where f/f_0 increases from below 1 to above 1 within the transition. The physical interpretation of the bifurcation parameter $\alpha Gr^{1/2}$ can be illustrated to make an analogy to the formation of a von Karman vortex street [163]. Equation (5.3) implies that the Reynolds-number-like quantity $(gD)^{1/2}l/\nu$, based on the flow properties of the inner-side shear layers, governs the transition the dual-flame system between in-phase and anti-phase modes.

It should be noted that the flickering death mode [78, 102] is located within the transition region, in which the two flames have not been pinched off anymore and only oscillate at a small amplitude or even cease to oscillate and become steady. Yang et al. [164] interpreted that the flickering death mode can be treated as a special case of in-phase mode due to the suppression of vortex shedding at small flames that vortex interactions mainly occur far behind the flames.

To further support the analogy between the gap flow of the two flames and the wake flow, we calculated the spacing ratio, l/h^+, for the staggered vortical structures in the simulated anti-phase flickering flames, where h^+ denotes the inter-core spacing of the main vortices in each inner-side shear layer. In practice, h^+ is the averaged vertical height between two vortex cores and obtained by averaging the instantaneous values over nine phases of a period as shown in Fig. 5.10. As a result, the phase-averaged spacing ratio l/h^+ for different anti-phase flickering flames is estimated to vary between 0.20 and 0.33. This is in reasonable agreement with the theoretical value of 0.28 suggested by von Karman [209] and the experimental values around 0.2 measured from different types of wakes [210], especially considering that the strength

of the buoyancy-induced shear layers are growing gradually along the flame and the vortex pattern in the near field is not yet fully developed.

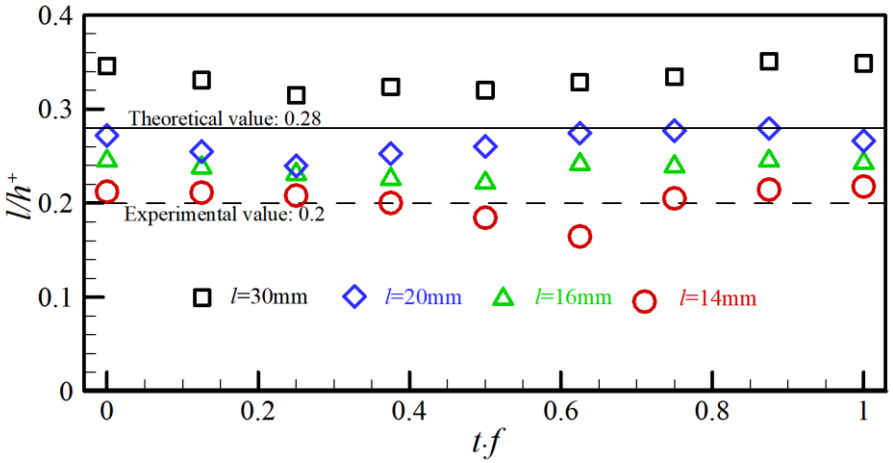

Figure 5-10 The spacing ratio l/h^+ during a period for four anti-phase flickering modes, which are marked by black □ ($l = 30$ mm), blue ◊ ($l = 20$ mm), green **Δ** ($l = 16$ mm), and red ○ ($l = 14$ mm), respectively. The solid line is the theoretical value of 0.28 given by Von Karman and the dashed line represents the experimental value around 0.2.

This definition is consistent with that for the classical Karman vortex street, and a sample calculation is shown in Fig. 5.11. Here, the vortex core, denoted by a black cross, is identified by calculating the second invariant Q [211] and then finding the local maximum along each branch of the shear layers as demonstrated in Fig. 5.11(b). It is noted that this calculation should be performed in the near field where the staggered vortical structures are prominent.

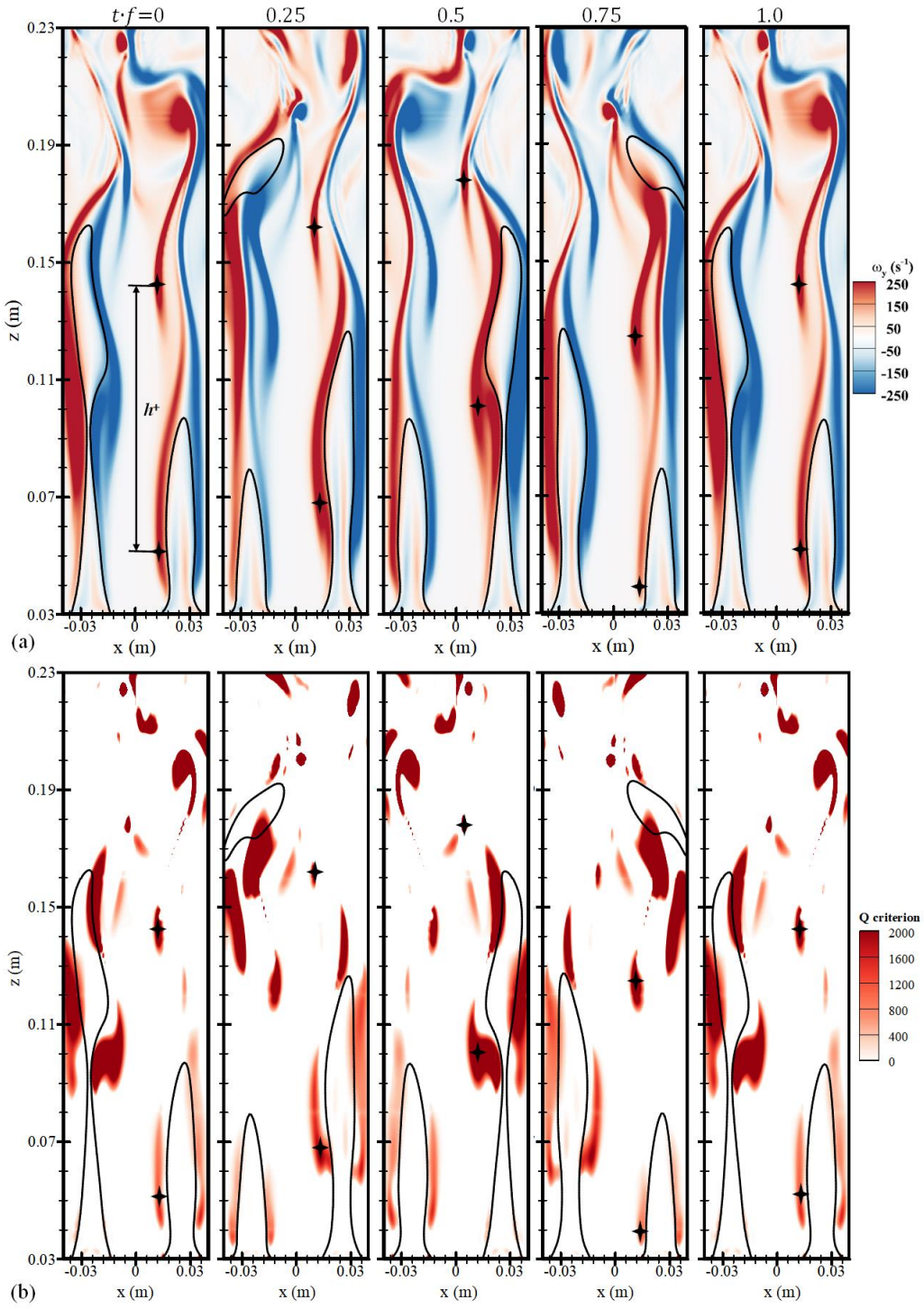

Figure 5-11 Five instantaneous (a) vorticity and (b) Q-criterion contours of anti-phase flickering flames ($d = 2$ cm) with a 30 mm gap.

5.5 Further Validation and Discussion

We further validated the mode transitions for the double pool flames of diameter $d = 20$ mm, at three different gap distances, 10 mm, 14 mm, and 20 mm, by numerically tuning the viscosity in Fig. 5.12 for ensuring that the mode transition is primarily influenced by the vorticity viscous diffusion mechanism. By changing the vorticity from $0.50\nu_A$, $1.10\nu_A$, and $1.35\nu_A$ to $0.45\nu_A$, $1.05\nu_A$, and $1.30\nu_A$, we found the mode transitions, which directly verifies our proposed mechanism that viscosity plays an essential role in the interaction between the inner shear layers of the flames. It is worth noting that the mode transition could occurs when the viscosity only is changed in the simulations, while previous studies just change the gap distance for mode transition.

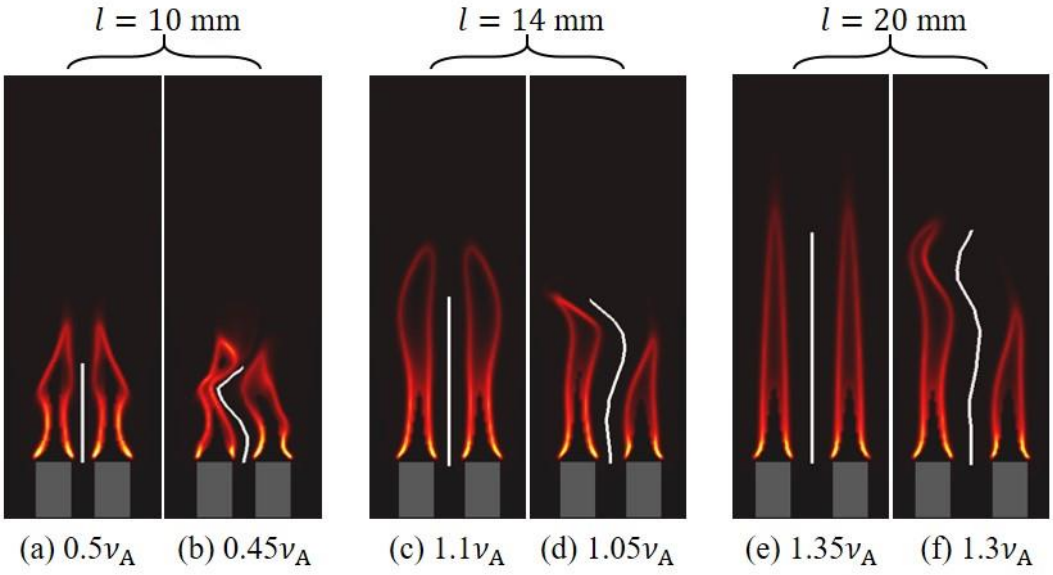

Figure 5-12 The contours of heat release for different simulation cases show the mode transition at different gap distances by changing the viscosity alone. The white lines are iso-contours of zero vorticity, along which the ambient flow temperature is estimated.

Another interesting observation is the flame interaction mode of Fig. 5.12(e), which is termed the "amplitude death" mode [212] meaning no flickering. While a future investigation is necessary, we believe this mode happens when the viscous

diffusion of every single flame is so strong that it prevents the shear layer from growing and rolling up into a toroidal vortex, meanwhile, the interaction between the inner shear layers is still in the small Re_A regime so that the flame system maintains a symmetric configuration. Therefore, this is considered as a special in-phase mode in the present study.

To further verify the mode transition criterion, we apply Eq. (5.3) to calculate the Re_A transition ranges for the three gap distances of Fig. 5.12 to be 554~616, 353~370, and 410~426, respectively. The Re_A ranges for the gap distances of 14 mm and 20 mm are in reasonable agreement with the predicted Re_A range of 300~420 from Fig. 5.8; however, the Re_A the range for $l = 10$ mm is notably above the prediction. We believe that this mismatch could be attributed to the increased viscosity associated with the increased temperature of the gap flow as the gap shrinks. It can be corrected by modifying Eq. (5.2) as

$$Re_E = \frac{\sqrt{gd}l}{\nu_E} \tag{5.3}$$

where ν_E is the effective kinematic viscosity estimated from Sutherland's law as

$$\frac{\nu_E}{\nu_{ref}} = \left(\frac{T_E}{T_{ref}}\right)^{5/2} \frac{T_{ref} + S}{T_E + S} \tag{5.4}$$

with $T_{ref} = 298$ K being the room temperature, ν_{ref} the reference viscosity at T_{ref}, T_E the effective temperature, and $S = 110.4$ K for air.

Note that the reduction of the density terms in Eq. (5.4) is based on the ideal gas law. Since the temperature of the gap flow is highly unsteady, T_E is only evaluated approximately based on spatial and temporal averaging. For each case in Fig. 5.12, we first identify the white line corresponding to the iso-contour of zero vorticity within the gap. Thus, the time-averaged temperature along the white line, which is plotted in Fig. 5.13, is that of the ambient flow outside the inner shear layers. Furthermore, we believe

that the flickering mode is decided by the vortex interaction upstream of the pinch-off location, z_{po}, which is marked by the dashed lines in Fig. 5.13.

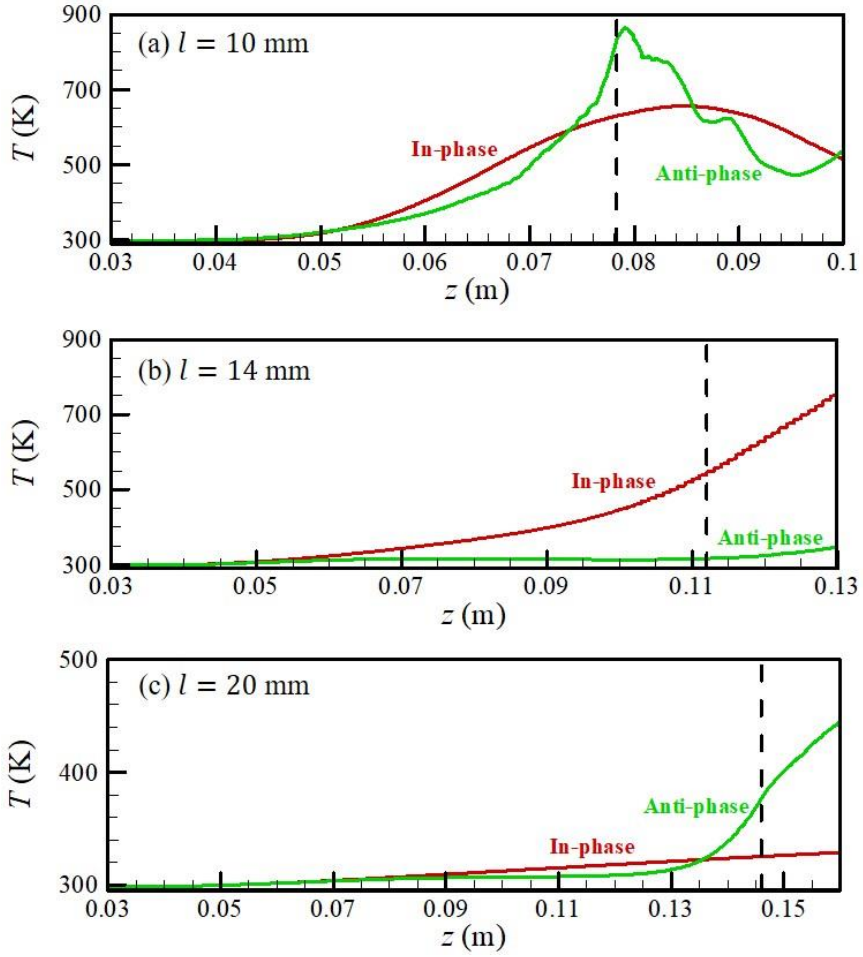

Figure 5-13 The temperature calculated within a period at the white lines in Fig. 5-12 varies with different flame flickering modes (red lines for the in-phase mode and green lines for the anti-phase mode). The flame pinch-off occurs at z_{po} (dashed line).

Consequently, T_E for each case can be calculated by averaging the corresponding temperature curve of Fig. 5.12 for z up to z_{po}. This allows the estimation of Re_E based on Eqs. (5.3) and (5.4), and the results are presented in Table 5-1. We can see that the agreement between the Re_E transition ranges and the range of 300~420 in Fig. 5.8 is significantly improved, especially for the $l = 10$ mm case.

Table 5-1 Reynolds number for mode transition by changing viscosity.

Gap distance	$l = 10$ mm		$l = 14$ mm		$l = 20$ mm	
Mode	In-phase	Anti-phase	In-phase	Anti-phase	In-phase	Anti-phase
ν_{ref}	$0.50\nu_A$	$0.45\nu_A$	$1.10\nu_A$	$1.05\nu_A$	$1.35\nu_A$	$1.30\nu_A$
Re_A	554	616	353	370	410	426
T_E	398.5	398.8	365.5	310.7	312.6	309.0
ν_E/ν_{ref}	1.660	1.662	1.430	1.076	1.088	1.066
Re_E	334	371	247	344	377	400

We have demonstrated that the increased flow temperature within the flame gap could cause reduced vorticity generation downstream, although this has limited impact on the upstream interaction between the two flames. In this part, we have shown that the heat effect could still affect the mode transition indirectly via temperature-dependent fluid properties, such as density and viscosity. Last, our model has certain limitations as it is based on each pool flame being flickering and laminar. This means that the pool diameter should vary in a range approximately between 10^{-2} and 10^{-1} m [44, 175], so that the dimension of the flame is large enough to flicker but small enough to not develop turbulence in the near field. The frequency prediction of the dual-flame system is also beyond the scope of this work.

5.6 Identical Stuart-Landau Oscillators with Time-delay Coupling

Time-delay coupling [184, 213] refers to a phenomenon where the dynamics of an individual oscillator are influenced by delayed feedback from other individuals, introducing a time delay in their interactions. Time-delay coupling is often studied in the context of coupled oscillators, and it can lead to rich and complex dynamical behaviours, such as synchronization, oscillation death, or pattern formation. Recently, Sujith and co-authors [78, 91] used time-delay coupled Stuart-Landau oscillators to model the dynamics of coupled candle-flame oscillators and numerically reproduced various flickering modes, such as the in-phase, amplitude death, clustering, and chimera modes. As a basic example, two Stuart-Landau oscillators denoted by 1 and 2 with time-delay coupling are modeled by:

$$\frac{dZ_1(t)}{dt} = (a_1 + i\omega_1 - |Z_1(t)|^2)Z_1(t) + K(Z_2(t-\tau_d) - Z_1(t)) \qquad (5.5a)$$

$$\frac{dZ_2(t)}{dt} = (a_2 + i\omega_2 - |Z_2(t)|^2)Z_2(t) + K(Z_1(t-\tau_d) - Z_2(t)) \qquad (5.5b)$$

where identical oscillators with $a_1 = a_2 = a$ and $\omega_1 = \omega_2 = \omega$ retain $a > 0$ for a limit cycle state, and their time-delay interaction is represented by an additional term, comprised of the coupling strength K and the time delay τ_d. Noteworthily, the trivial situation of $\tau_d = 0$ means that the interactions are instantaneous and independent of time history. For finite τ_d the interactions are non-instantaneous. Eq. (5.5) represents that Stuart-Landau oscillators are interconnected in such a way that their interactions are influenced not only by their own current states but also by the earlier states of the other ones. In the present study, $a = 1$ and $\omega = 10$ are used to keep the uncoupled state of each oscillator in the stable limit cycle state, as discussed in Chapter 2. Particularly, the Stuart-Landau equations with time-delay coupling are delay differential equations and solved by MATLAB dde23.

Through solving Eq. (5.5), the two identical time-delay Stuart-Landau oscillators exhibit three modes, including in-phase, death, and anti-phase oscillations. When τ_d is relatively small, corresponding to a weak interference on time history, the oscillators behave in an in-phase way (no phase difference), but their amplitude decreases a little, for example, in the case of K=25 and τ_d =0.05 in Fig. 5.14(a). As τ_d increases in a certain range, the oscillations are suppressed, and the amplitude becomes very small. The case of K=25 and τ_d =0.12 in Fig. 5.14(b) is the death state. For a big τ_d, the non-instantaneous interaction significantly affects the oscillations, and the phase difference between the two oscillators occurs. For instance, the oscillators with $k = 25$ and τ_d =0.25 are in an anti-phase mode (the phase difference of π), as shown in Fig. 5.14(c).

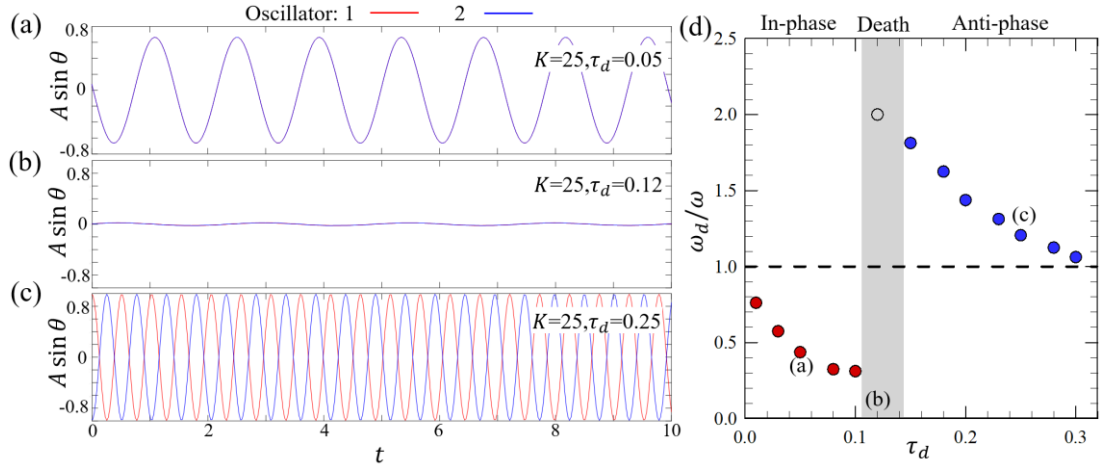

Figure 5-14 The stable states of S-L oscillators 1 and 2 in (a) in-phase mode, (b) death mode, (c) anti-phase mode as K=25, and τ_d =0.05, 0.12, and 0.25, respectively. (d) Three dynamical modes of two identical S-L oscillators with time-delay coupling in the parameter space of the normalized oscillation frequency ω_d/ω and time delay τ_d. The oscillator's real parts of $A_1(t)\sin\theta_1(t)$ and $A_2(t)\sin\theta_2(t)$ are plotted in red and blue lines respectively, where A is the amplitude and θ is the phase angle. a=1 and ω=10 are used to keep each uncoupled oscillator in the limit cycle.

Moreover, from an initial state to a stable state, the time-evolution of the amplitude A and phase angle θ of the oscillators at τ_d =0.05, 0.12, and 0.25 for these modes are plotted in Fig. 5.15. The phase trajectories consisted of $A_1 \sin\theta_1$ and $A_2 \sin\theta_2$, for the in-phase mode, death mode, and anti-phase mode qualitatively agree with previous experimental results [102].

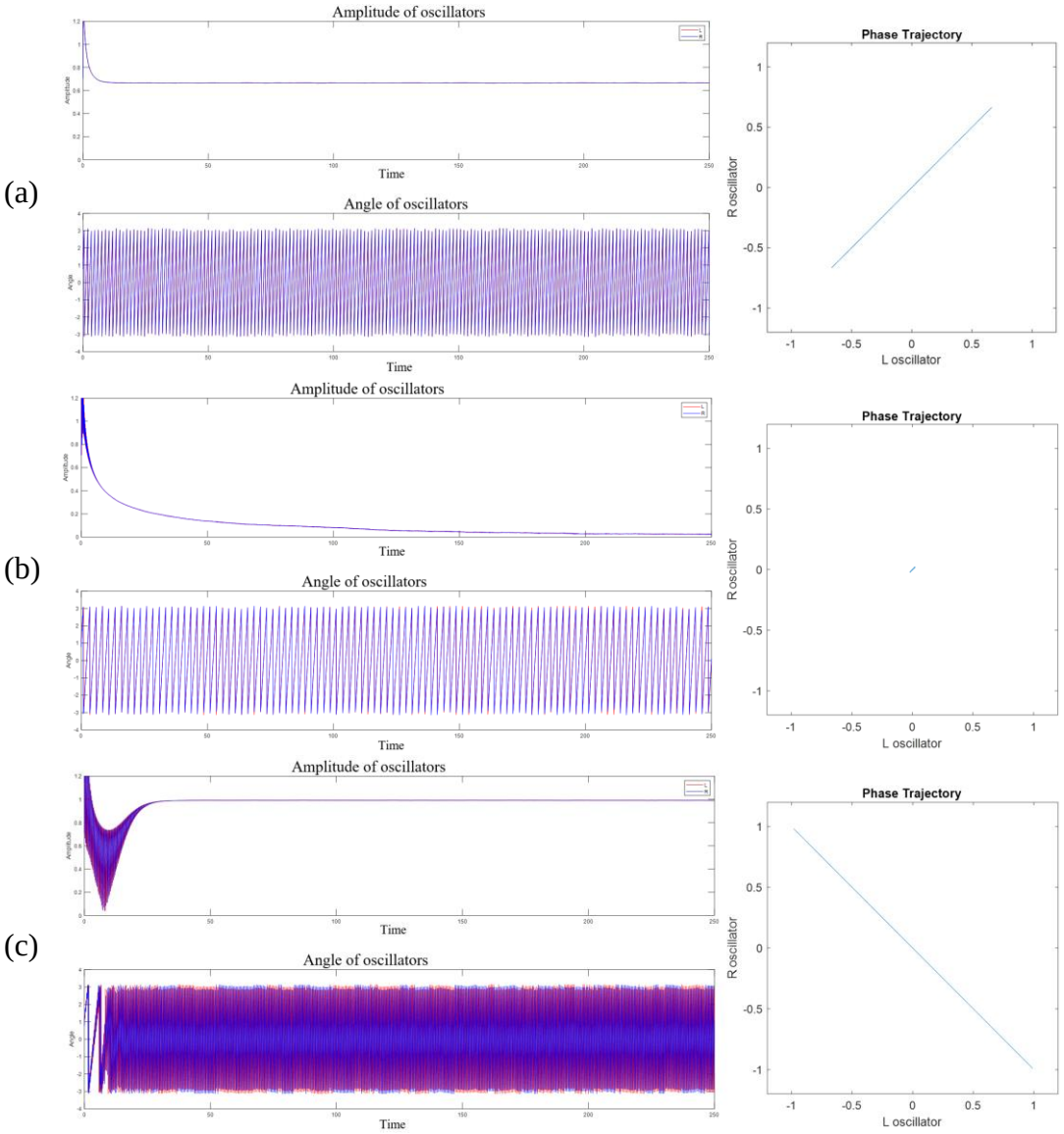

Figure 5-15 Time-varying amplitude A, angle θ, and phase trajectory of $A \sin\theta$ for two identical S-L oscillators in the (a) in-phase mode, (b) death mode, and (c) anti-phase mode.

To facilitate the investigation, we first fix the coupling strength at K=25 and gradually vary τ_d for the three types of interacting oscillators respectively, as shown in Fig. 5.14(d). With increasing τ_d, these Stuart-Landau oscillators exhibit in-phase, death, and anti-phase modes, where the transition occurs at $0.1 < \tau_d < 0.15$. It should be noted that the death mode is defined as the oscillation of $A < 0.1$ in the present study. In addition, the frequency trend of the Stuart-Landau oscillator model is aligned with that of the dual flame system in Fig. 5.8 and Fig. 5.9. Figures 5.14(a-c) plot the real parts of $Z_1(t)$ and $Z_2(t)$ in these modes, respectively. To further verify the universality of the time-delay coupled Stuart-Landau model in reproducing basic modes of dual flickering flames, we systematically investigate the Stuart-Landau oscillators at different coupling parameters of $15 \leq K \leq 35$ and $0.01 \leq \tau_d \leq 0.30$ and correspondingly plot the regime diagrams of amplitude and frequency.

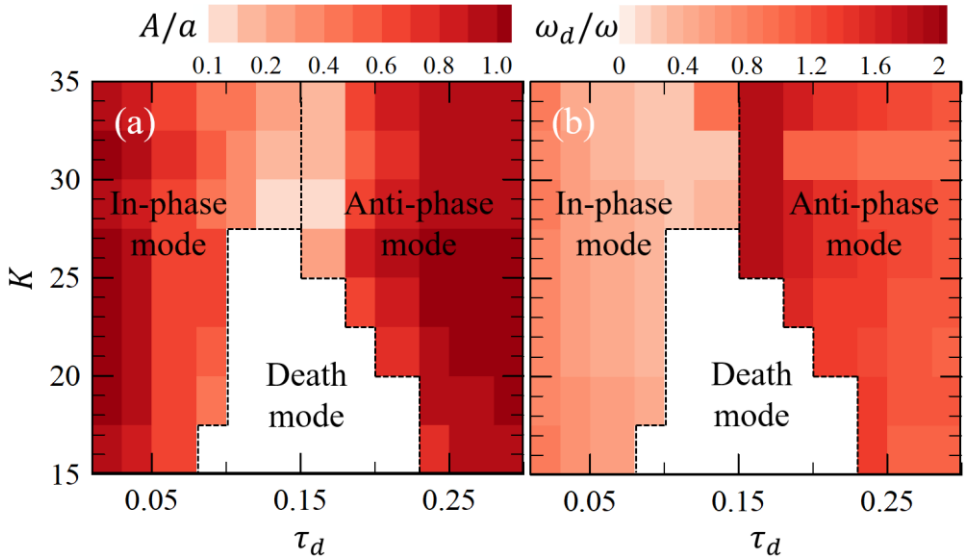

Figure 5-16 Regime diagrams of two identical S-L oscillators with time-delay coupling: (a) the normalized amplitude A/a and (b) the normalized frequency ω_d/ω. The modes are determined based on the phase difference and amplitude.

The space of $K - \tau_d$ is divided into three regions for in-phase, death, and anti-phase modes, as shown in Fig. 5.16. Specifically, in-phase mode occurs at relatively

small τ_d, while anti-phase mode does at relatively big τ_d. Between these two regions, the death mode exists when K is relatively small. The present results show a similar distribution of the modes with the two-parameter bifurcation plot [78], obtained from two flickering flames' experimental observations with varying single flame strength and gap distance. Interestingly, when K increases up to 27.5, there is disappearance of death mode, therefore, resulting in a border between the in-phase and anti-phase regions (i.e., the so-called phase-flip bifurcation [214]). In addition, the frequencies of coupled oscillators in in-phase mode are lower than their natural frequency, while those in anti-phase mode are higher than their natural frequency. When K is fixed and τ_d increases gradually, the frequency trend is consistent in keeping the decrease in in-phase region, the rapid rise to high value across death mode or phase-flip bifurcation, and finally advancing gradually to 1 in anti-phase region.

It's noteworthy that the Stuart-Landau model is a mathematical model used to describe the dynamics near a Hopf bifurcation. As the model is particularly useful in cases where the system's behaviour can be reduced to low dimensions, it's widely used in fields like physics, biology, and engineering to understand oscillatory phenomena. By capturing the essence of oscillatory phenomena and their stability, the Stuart-Landau model aids in understanding complex systems in a simplified yet powerful way. Understanding these parameters allows us to predict the behaviour of the system under varying conditions and to identify the transition points between different dynamical regimes. Although these parameters, such as K and τ_d, can relate to specific physical characteristics of the system being modelled in practical applications, to make a direct connection between model parameters and practical parameters is not something that is taken on lightly.

5.7 Summary and Conclusions

The flickering behavior of dual pool flames was examined through numerical and theoretical methods to gain insights into dynamic flame behaviors. The simulation successfully captured the anti-phase and in-phase synchronized flickering phenomena observed in experiments by Kitahata et al. [83] and Forrester [215]. Data from this study provide insights into the link between vortex dynamics and flame flickering. Specifically, the periodic pinch-off of each flame in the dual system is driven by the formation, evolution, and detachment of toroidal vortices, similar to the mechanism observed in single flickering flames. The distinct flickering modes arise from the coupling effects between the inner-side shear layers of the two flames. Additionally, the transition between anti-phase and in-phase flickering is influenced by a characteristic Reynolds number, Re_A, defined by the inner-side shear layer properties. This was validated by the correlation of the non-dimensional flickering frequency with Re_A, using data from the current simulation and the experiments conducted by Kitahata et al. and Nakamura et al. [83, 216]. The transition mechanism for different flickering modes resembles the transition of shear layers in wake flows, forming a von Karman vortex street.

The findings of this study extend beyond the buoyancy-induced dual-flame system. Since the analysis focuses on the interaction between two shear layers associated with the flame, it can be applied to multiple-flame systems. For instance, a planar tri-flame system could be viewed as the interaction of two parallel "von Karman" shear layers, potentially yielding additional synchronization modes, analogous to the behavior of parallel vortex streets behind double bluff bodies [207].

Moreover, although this research primarily addresses laminar flames, it has implications for studying turbulent flames. Natural fires are typically large-scale and turbulent, where interactions among multiple flames can be destructive and uncontrollable [217, 218]. In turbulent flames, flame height is significantly influenced by air entrainment, resulting from interactions between multiple flames and vortices, making it highly unsteady. Thus, this work serves as a foundational study that aids in understanding the more complex dynamics of turbulent flames.

Chapter 6. Vortex Interaction and Synchronization Modes of Triple Flickering Buoyant Diffusion Flames

In this chapter, we will first study the coupled oscillation of triple flames in a side-by-side way, as a simple extension of double flames. Although these flames are arrayed in a plane, it is valuable to investigate how two gap flows affect the flickering flames, particularly focusing on the behavior of central flames. Then, triple flickering flames arranged in an euqal-side triangle were studied in the simulations.

Symmetry breaking of the triple flame system, which is rarely studied in previous studies, is focused on investigating the symmetric and asymmetric arrangements. The four distinct dynamical modes—in-phase, death, rotation, and partially in-phase—originally observed in candle-flame experiments were computationally reproduced for the first time. This work effectively establishes a connection between vortex dynamics and the nonlinear dynamics of the triple-flame system, which is key to understanding larger dynamical systems involving multiple flickering flames. Multiple flames, analogous to flames found in wildfires, have an unknown mechanism to rule each flame how to oscillate in a certain way and frequency. Such flame patterns of multiple flames are of important value to reveal how to arrange a variety of flames to achieve fire control and the development of novel devices.

6.1 Triple Flickering Flames in Line Arrangements

6.1.1 Symmetric Arrangement

The last chapter illustrates that the gap flow between any two flames is the key factor in judging the flame modes. In this chapter, the triple flame system consists of identical flame individuals (the Reynold number of $Re_0 = U_0 D/\nu$ =100 and the

flickering frequency of f_0=10 Hz). Triple identical Bunsen burners (the gray square columns of $D \times D \times 3D$) are located with a gap distance of $l_1 = \alpha D$ and $l_2 = \beta D$ in a line. Their burner centers divide the circle into eight equal arc lengths, which is the characteristic gap distance between two adjacent flames. Overall, we have reproduced the synchronization modes of three side-by-side flames with the same gap distance. The three-coupled flames turned out to exhibit three classes of synchronized oscillation modes. If the central flame is thought of as the reference, triple flames in Case A are synchronized with the same phase, which is defined as in-phase flickering, while the ones in Case B would be called anti-phase mode as the central one has phase shift with the others.

The experimental results of the same dynamical modes are reported by Chi et. al. [102]. In the following parts, the experiments are utilized to compare with the present simulations. In particular, the dynamical modes of triple flickering flames with various arrangments are concerned only, as the collective behaviours are more interesting and the physical interpretations of these phenomena are focused in this study. As detailed information on flame scale and flickering time in experiments is absent, a detailed comparison between experiment and simulation is no available. It is fully identified that the exact reproduction of experimental results, such as the flame height and flickering frequency, merits further investigations.

Specifically, the essential features of the two modes are explained below:

In-phase mode This synchronization is identified that all three flames oscillate at an identical pace ($\alpha = \beta = 1.0$ in the present simulation). Figure 6.1 demonstrates the flame dynamics of the in-phase mode in a one-period duration. During the oscillation, the flames are elongated and contracted periodically in the vertical direction. In addition, it is easy to see the wave form of flames has a transverse oscillation that bowing to the

center and arching backward are repeated in the same frequency as that of the vertical oscillation. The three-flame form has central symmetry, but the two outer flames lose asymmetry. It should be noted that the in-phase mode observed in three-coupled side-by-side flames is stable.

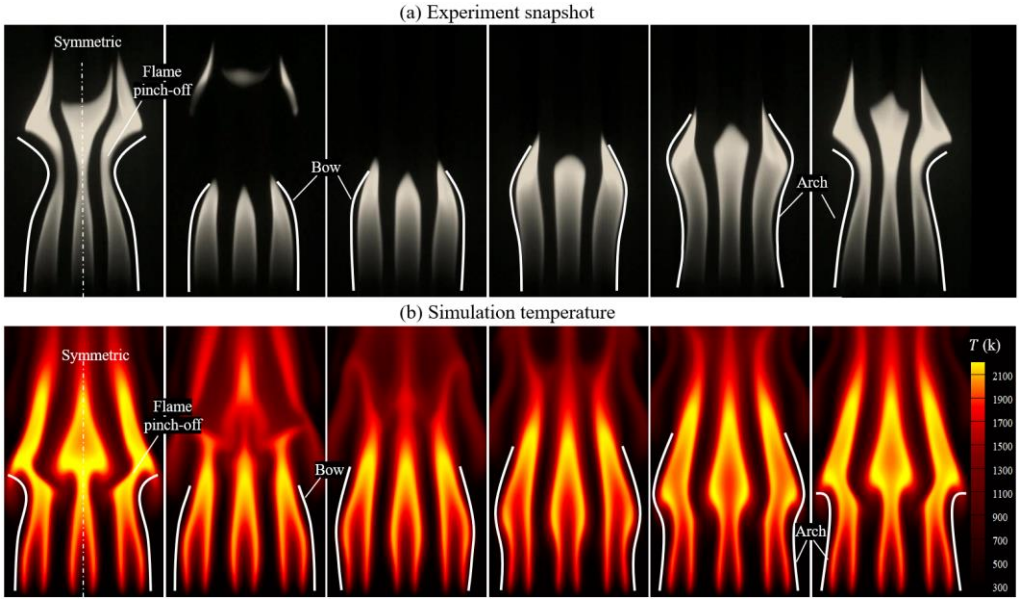

Figure 6-1 The in-phase flickering process for (a) experiment snapshot [102] and (b) simulation temperature of triple flames with the equal-gap arrangement in a line.

To further illustrate the vortex interactions between those flames, the heat release, and vorticity contours during a periodic process are shown in Fig. 6.2. First, the triple flames oscillate together, like a bigger one, although they are not merged according to the heat release. Second, the vorticity shows that there exist strong influences of vorticity diffusion between the adjacent flames. The same mechanism has been revealed in the last chapter on the vortex interaction in dual flickering flames.

0 T 1/3T

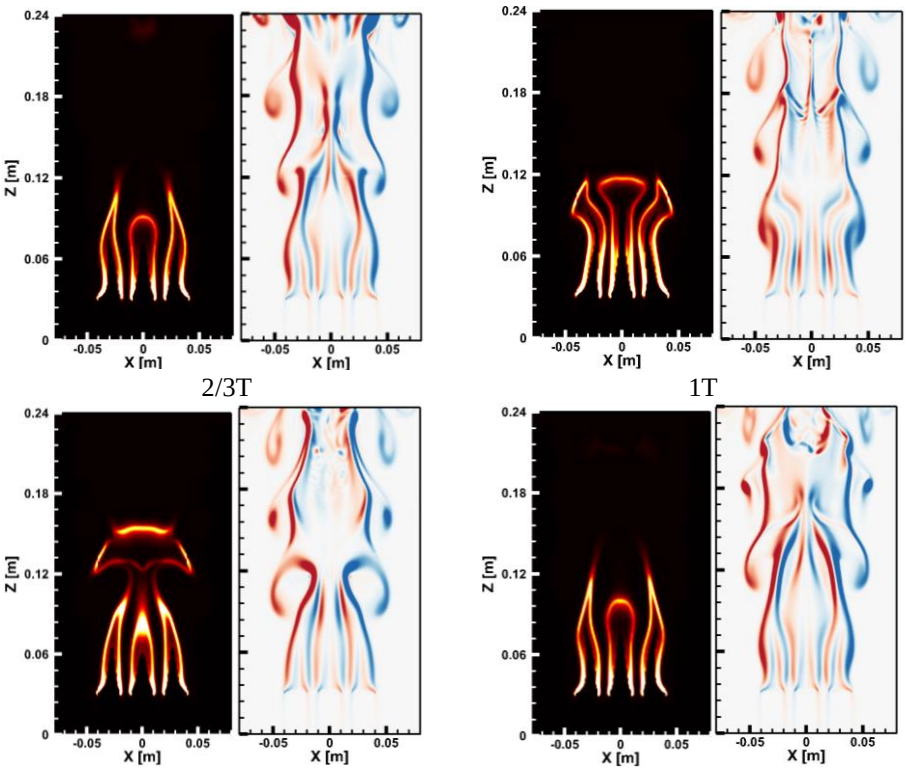

Figure 6-2 Snapshots of three flickering flames in the in-phase synchronization from the present simulation based on heat release (left) and vorticity (right). Three flames are arranged at $l_1 = l_2 =$10mm gap.

Partially in-phase mode This mode is a variation of anti-phase, in which two outer side flames have nearly the same pace ($\alpha = \beta = 2.0$ in the present simulation) and are in-phase, but the remaining one is phase-shifted by π. Figure 6.3 represents the flame variation in one-period duration when the inter-flame distance is bigger (). Once the partial in-phase mode occurs, there seems to be a preference for a pair of outer flames among the three oscillators to become in-phase coupled over the central one. Like the case of the in-phase mode, the partial in-phase mode is also stable and has central symmetry in the three-flame form.

Also, we compare the heat release and vorticity contours of the partially in-phase mode during a periodic process to understand the flame and vortex interactions in Fig. 6.4. Flame dynamics is induced by the shear layers around the flames, and the

synchronization mode results from the interactions of shear layers, namely the vortex dynamics. The present results of triple flickering flames in a line are very similar to the anti-phase mode of dual flickering flames. There is no obvious vorticity diffusion. The shear layer around the flame is affected by the vortex-induced flow of another flame.

Flickering death mode This interesting mode is presented as three flickering flames are pinched off and only have a slight oscillation at the tip of the flame, as shown in Figure 6.5. A similar mode was reported in the dual-flame system [102]. The suppression of the flame flicker should result in vortex interactions between flames. In the present simulations, the flickering death mode is developed from the flickering state of three flames, and then the flame oscillation gradually decays to a relatively steady state.

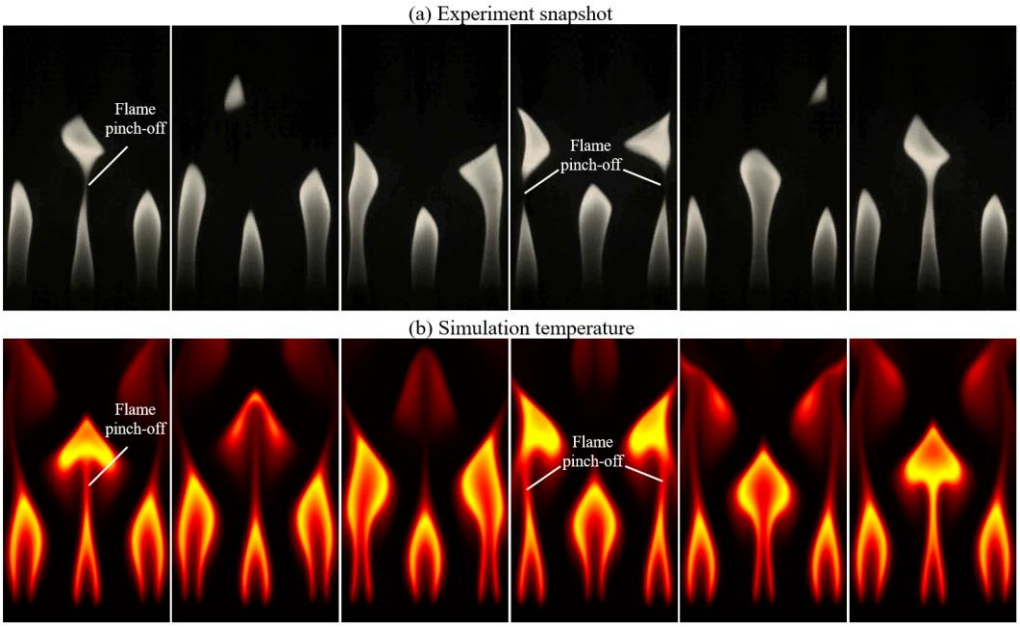

Figure 6-3 The partially in-phase mode for (a) experiment snapshot [102] and (b) simulation temperature of triple flames with the equal-gap arrangement in a line.

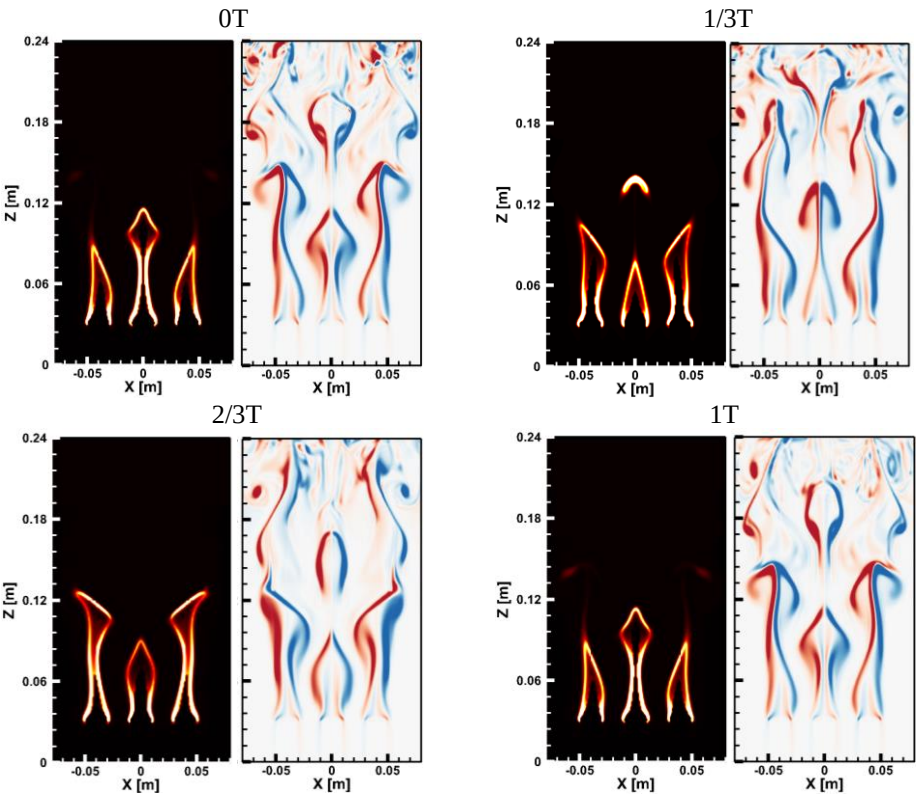

Figure 6-4 Snapshots of three flickering flames in the partially in-phase synchronization from the present simulation based on heat release (left) and vorticity (right). Three flames are arranged at the gap distance of $l_1 = l_2$ =20mm.

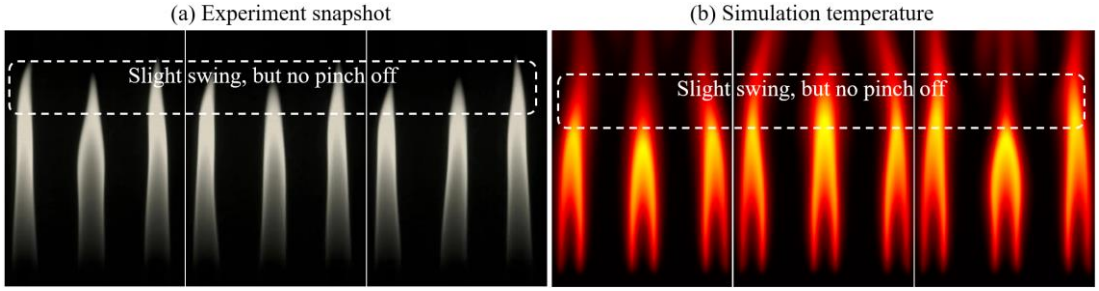

Figure 6-5 The flickering death process for (a) experiment snapshot [102] and (b) simulation temperature of triple flames with the equal-gap arrangement in a line.

6.1.2 Asymmetric Arrangement

As mentioned above, in-phase, partially in-phase, and flickering death mode in three-coupled side-by-side flames can be basically explained by the vortex dynamics, meaning that the unified mechanism for in-phase and anti-phase flickering modes of

the dual-flame system is valid in side-by-side flames system. In fact, the triple flames in a line are a system, in which the neighbour flames consists of dual flickering flames, that is, the left-middle flame system and the middle-right flame system. As an example of the asymmetric arrangement with identical gap distance, a case of $l_2 = 2l_1$ is simulated and compared with experiments.

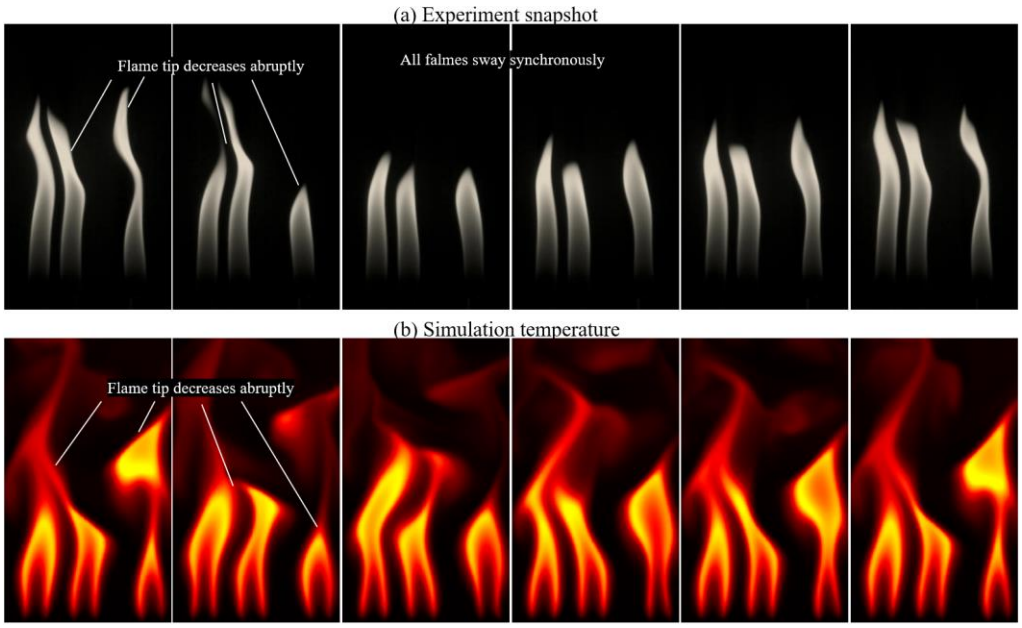

Figure 6-6 The in-phase swaying and anti-phase flickering process for (a) experiment snapshot [101] and (b) simulation temperature of triple flames with unequal-gap arrangement in a line.

In Fig. 6.6, the closer dual flames with a small l_1 grow up and down together, while another separated flame is phase-shifted by half period, called the in-phase swaying and anti-phase flickering mode. Due to the same behaviours of the left two flames, they can be regarded as a flame, seemingly being combined together, which becomes an anti-phase oscillation with the rightmost one, although the symmetry of three-coupled side-by-side flames completely vanishes in this flame pattern. Interestingly, when l_1 is fixed and only l_2 is increased, the dynamical mode turns into the situation that the left flames are in in-phase flickering, but anti-phase with the third

flame, as shown in Fig. 6.7. Those two dynamical modes of triple flickering flames can be understood from the perspective of vortex dynamics, as the dynamical mechanism of dual flickering flames is basic. A parametric study merits further work to explore the dynamical behaviours of flame systems with symmetry breaking.

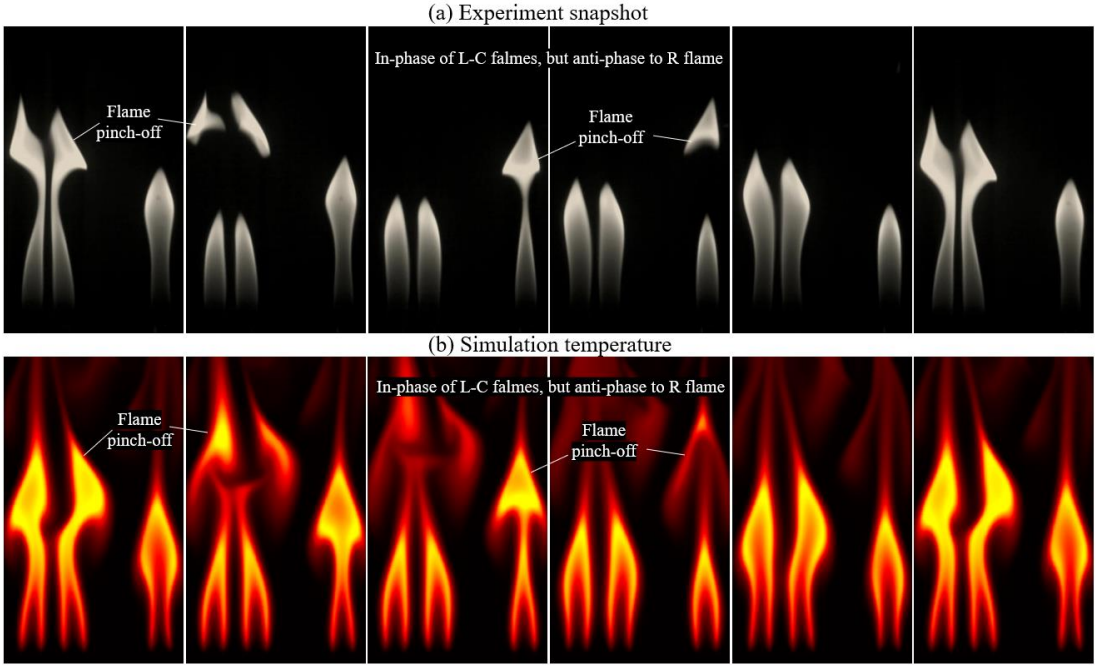

Figure 6- 7 The partially in-phase flickering for (a) experiment snapshot [101] and (b) simulation temperature of triple flames with unequal-gap arrangement in a line.

The present simulations successfully reproduced the dynamical modes induced symmetric and asymmetric arrangments. The breaking of symmetries can generate a wider range of possibilities and outcomes. Symmetry breaking generally refers to a situation where a balanced or symmetrical situation is disrupted and leads to a new and asymmetrically structured state. In essence, diversity can arise from the breaking of symmetries, leading to the emergence of varied patterns, behaviours, and characteristics within a system.

6.2 Triple Flickering Flames in an Equilateral Triangle arrangement

6.2.1 Vortex Ring and Computational Setups

To enhance the upcoming discussion on vortex dynamics within the triple-flame system, we present two illustrative examples of single flickering flames in Fig. 6.8. To visualize the toroidal vortex, we utilized the Q criterion, where $Q = (\|\Omega\|^2 - \|S\|^2)/2$, Ω, and S represent the anti-symmetric and symmetric components of the deformation quantity $\nabla\vec{u}$. The Q criterion identifies a vortex as a region where the vorticity magnitude exceeds that of the strain rate [219]. In this context, the toroidal vortex is depicted by the vorticity line that intersects at the maximum Q-value, while the flame shape is illustrated by the orange contour representing heat release. The periodic nature of a flickering flame and its corresponding toroidal vortices is distinctly observable in both cases. At the moment t_1, a toroidal vortex is in the process of growing and rolling up, while the previously shed toroidal vortex is seen moving downstream. In Fig. 2.5 of Chapter 2, the vorticity and the streamline around the flickering flame is plotted, the results show that the vortex generation is due to the inflected shear layer (the roll-up of streamlines) at the flame base. The vortex grows up with the accumulation of circulation at the flame sheet and moves downstream due to the buoyancy-induced vertical flow.

The Q-contours effectively illustrate the toroidal vortices. From t_2 to t_3, The toroidal vortex around the flame contracts inward, making the flame progressively narrow. At t_4, the toroidal vortex is shed, causing a flame pocket to be separated from the main flame. By t_5, a fresh toroidal vortex emerges at the base of the flame, initiating a new lifecycle. Although the shed toroidal vortices preserve their pattern, the vorticity fields surrounding them diminish in strength due to viscous dissipation.

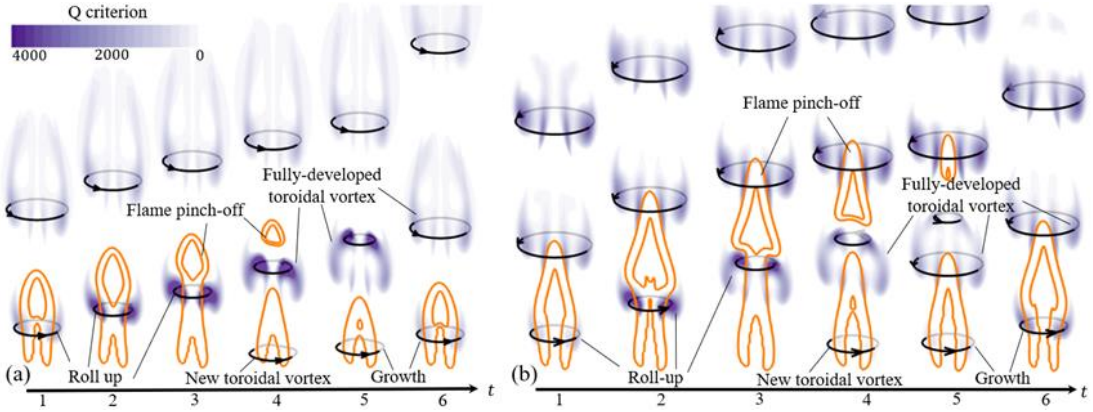

Figure 6-8 The lifecycle of a toroidal vortex generated by the flickering buoyant diffusion flame at (a) $Re = 50$, $Fr = 0.07$ and (b) $Re = 100$, $Fr = 0.28$.

Upon comparing the two scenarios, we observed that a reduction in the Froude number (Fr) markedly diminishes both the dimensions of the flame and the flame bubble. As a result, it can be concluded that a sufficiently low Fr can inhibit flame flickering [23, 220] or potentially stop flame oscillations altogether [43, 44]. significantly reduces the sizes of the flame and the flame bubble. From a physical standpoint, this means that a toroidal vortex necessitates a sufficiently large flame to reach the critical circulation needed for its shedding to occur. This is the rationale behind the use of a cluster of small candles in many earlier experiments to produce a more substantial candle flame capable of flickering.

To model three identical flickering flames arranged in an equilateral triangle configuration, as depicted in Fig. 6.9(a), we employed three square-shaped burners (represented by the grey square columns) that are uniform in size, each having a fixed edge length of 10mm. These burners are positioned at each vertex of the inscribed equilateral triangle within a circle of radius R. Methane gas is introduced from the base of each burner at a constant velocity, U_0, passing through an adiabatic solid-wall burner that has a height of $3D$. The gas then exits the burner to mix with the ambient air above the nozzle, as indicated by the blue arrows in the figure.

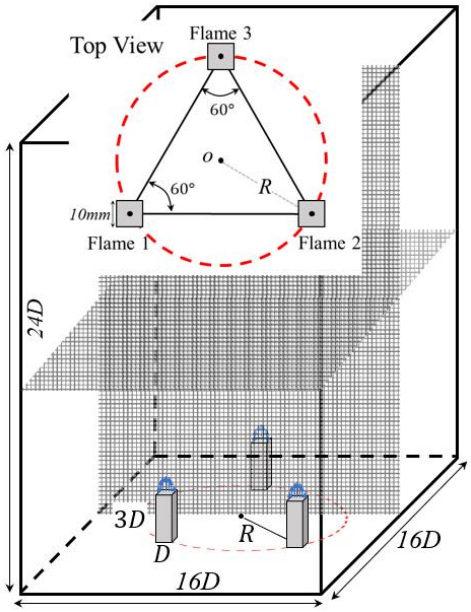

Figure 6- 9 Schematic of the computational setups for triple flickering flames.

The computational domain has been validated through prior studies on domain and grid independence [163]. We implemented a mixing-limited chemical reaction model capable of accurately capturing buoyancy-induced flame flickering. Although we acknowledged the quantitative effects of radiation and soot formation, these factors were neglected for simplicity. For all cases presented here, the flames reached a fully developed state, given that the simulation duration was at least 20 times greater than the characteristic time, $2R/U_0$. The experimental results in [80] are utilized to qualitatively validate the present simulations and the quantitative comparison is not carried out due to differences between candle flames in experiments and the methane jet flames in simulations, as well as the lack of quantity information in experiments.

6.2.2 In-phase and Flickering Death Modes

At $Re = 100$ and $R/D = 1.6$, the triple-flame system demonstrates in-phase synchronization, meaning that all three flames flicker simultaneously without any phase difference, as illustrated in Fig. 6.10. The pattern changes in each flame aligns

qualitatively with results from earlier experimental results [80]. Despite some discrepancies in comparison to experimental results, the current simulation effectively captures the in-phase dynamical mode, confirming its presence in the triple jet diffusion flames.

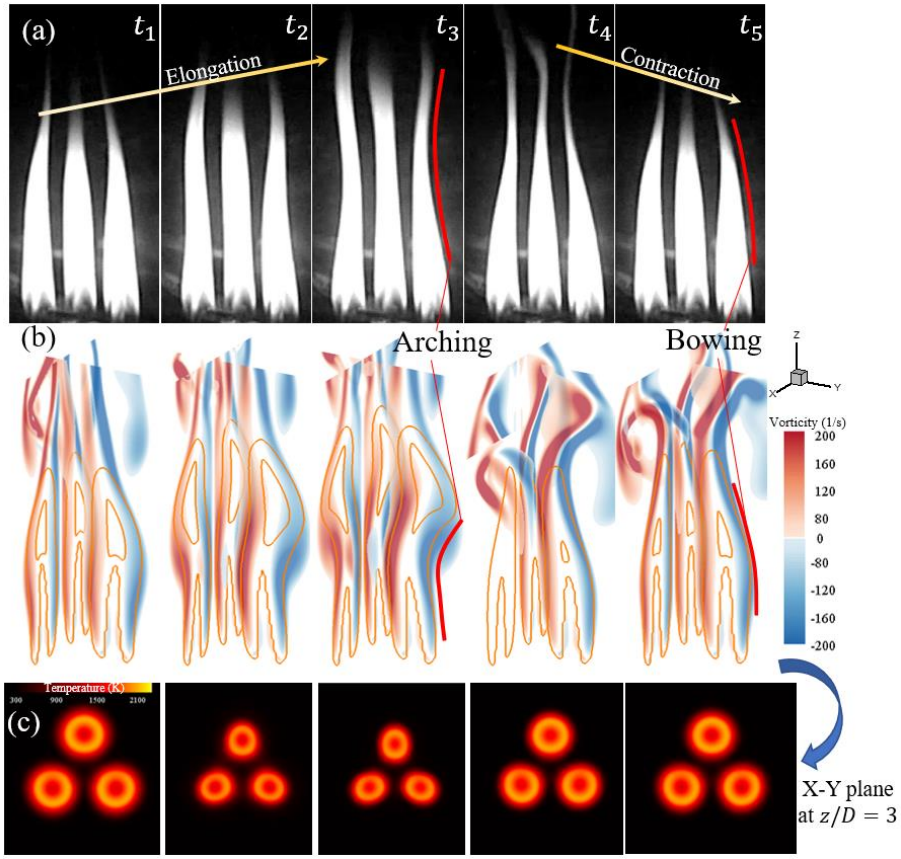

Figure 6-10 In-phase mode of triplet flames observed in (a) candle experiment [80] and in the present simulation for (b) the vorticity field and (c) the temperature profile at the horizontal plane z/D=3.

To elucidate this in-phase mode, we can once again examine the evolution and interaction of toroidal vortices that occur during a single flickering cycle, as illustrated in Fig. 6.11. In particular, the phenomena of flame stretching, necking, and pinch-off correspond to the growth, contraction, and shedding of a "trefoil" vortex during $t_3 \sim t_5$. Then, the “trefoil” vortex forming mechanism needs to be investigated. The

development of the three toroidal vortices from time t_1 to t_3 indicates that the vortices are simultaneously linked on the inner edges of the flames.

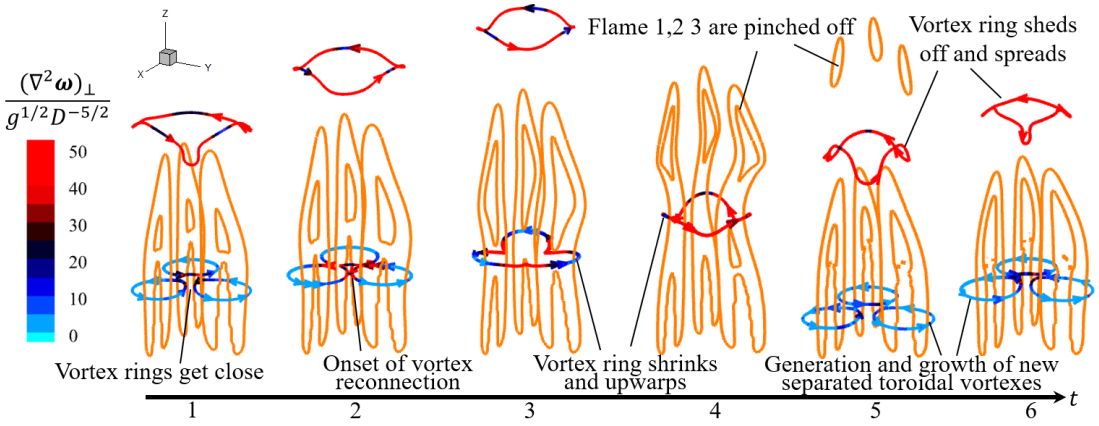

Figure 6-11 The triple flame system at $Re = 100$ and $R/D = 1.6$. The representative vorticity lines cross the highest Q-value and are colored by the normalized $(\Delta^2\omega)_\perp$. The flame is represented by the orange isoline of heat release.

Vortex interaction, especially the phenomenon of vortex reconnection, has been a persistent challenge in the field of topological fluid dynamics [221, 222]. This issue is crucial for comprehending the processes of energy cascade and the intricate mixing that occurs at fine scales in turbulent flows [223-225]. Vortex reconnection is a phenomenon in fluid dynamics, especially in the context of turbulence and superfluidity, where two vortex lines (or tubes in three dimensions) collide, touch, and then reconfigure by exchanging strands, effectively reconnecting in a different configuration. This process can redistribute energy and vorticity within the fluid, leading to complex and fascinating behaviours in the flow, as shown in Fig. 6.12. In the study [221], vortex reconnection encompasses three distinct concepts: scalar reconnection, vortex reconnection, and vorticity reconnection. These terms correspond to the alterations in the topology of iso-surfaces of a passive scalar, the magnitude of vorticity, and the lines of vorticity, respectively. In laboratory experiments, vortex reconnection is frequently

visualized through changes in the topology of a passive scalar, such as dye or smoke, which exhibit behavior that differs significantly from that of the vorticity field, whether referring to vorticity magnitude or the configurations of vorticity lines.

Vortex reconnection has been widely studied in both classical fluids and super-fluids. In superfluid helium, for example, the quantum nature of the vortices makes the study of reconnection highly insightful for understanding quantum turbulence. Additionally, numerical simulations and experiments with laser-induced vortices have provided deeper insights into the mechanisms of reconnection. In this study, we employed the concept of vorticity reconnection since it is applicable exclusively to viscous flows, whereas the other two concepts can occur in inviscid flows. Furthermore, we utilized the Q-criterion to identify vorticity lines within the current viscous flow, as elaborated in Chapter 6.2.1.

Kida and Takaoka [221] pointed out that helicity can be generated through vorticity reconnections; however, the reverse is not true, indicating that helicity is not a reliable indicator of vorticity reconnection. According to the Helmholtz vortex theorem, vorticity lines are "frozen" in inviscid flow, preventing their reconnection. Therefore, the breakdown of this frozen motion is attributed to the viscous diffusion of vorticity, $\nu\nabla^2\boldsymbol{\omega}$. When decomposing it in the direction of the vorticity vector, we obtain a parallel component $\nu(\nabla^2\boldsymbol{\omega})_{\parallel}$, which indicates the stretching rate of vorticity lines, and a normal component, $\nu(\nabla^2\boldsymbol{\omega})_{\perp}$, which reflects the deviation rate of vorticity lines. The latter serves as a more effective quantity for vorticity reconnection.

So, $(\nabla^2\boldsymbol{\omega})_{\perp} = (\Delta\boldsymbol{\omega} \times \boldsymbol{n}) \times \boldsymbol{n}$ is calculated, where the unit vector of vorticity $\boldsymbol{n} = \boldsymbol{\omega}/|\boldsymbol{\omega}|$ is normalized by $\sqrt{g/D^5}$, and subsequently plotted it along each vorticity line in Fig. 6.11. As the three toroidal vortices develop, they draw closer together, strengthening the likelihood of their reconnection, as evidenced by the red line

segments indicating large values of normalized$(\nabla^2\boldsymbol{\omega})_\perp$ at the time instant t_2. Following this, the three vorticity lines separate and reconnect, resulting in the formation of a "trefoil" vorticity line. This phenomenon signifies the beginning of vorticity reconnection at that particular time instant t_2. Additionally, it is noteworthy that the "trefoil" vorticity line bends upward along the direction of the three flames, creating a "saddle-trefoil" shape, a trend further emphasized by the high values of $(\nabla^2\boldsymbol{\omega})_\perp$.

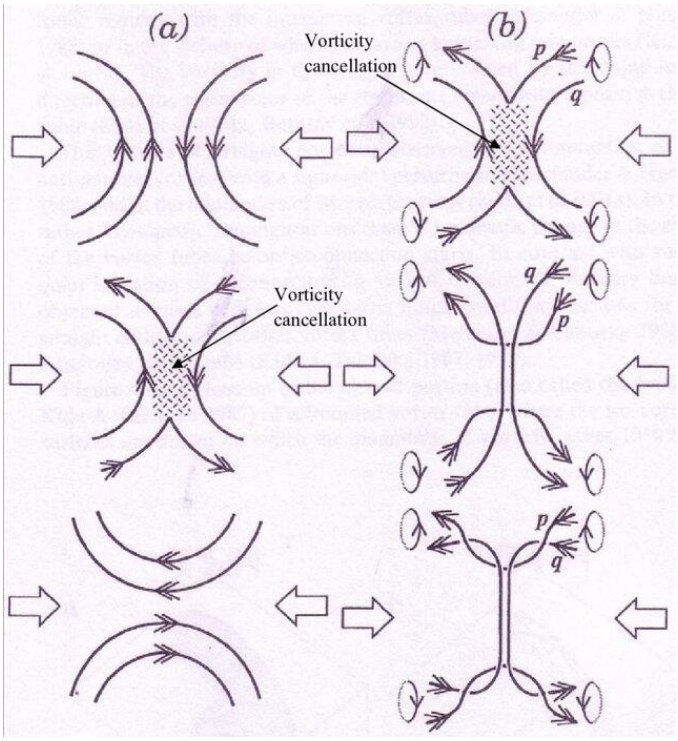

Figure 6-12 Mechanism of vortex reconnection [221]: (a) A basic scenario of vorticity cancellation caused by viscosity. (b) A detailed description of the reconnection process, showcasing the formation of vortex bridges.

A mode (the cessation of flickering in the three flames while they exhibit slight oscillations) was observed as the flickering death of flames at the same $R/D = 1.6$ but a smaller $Re = 50$. As shown in Fig. 6.13, the present simulation has qualitatively reproduced the experimental results of flickering death flames. In comparison to the in-phase mode illustrated in Fig. 6.11, a similar vorticity reconnection takes place among

the three toroidal vortices. However, in this case, the resulting "trefoil" vortex does not undergo substantial contraction or bending deformation prior to its shedding from the flames.

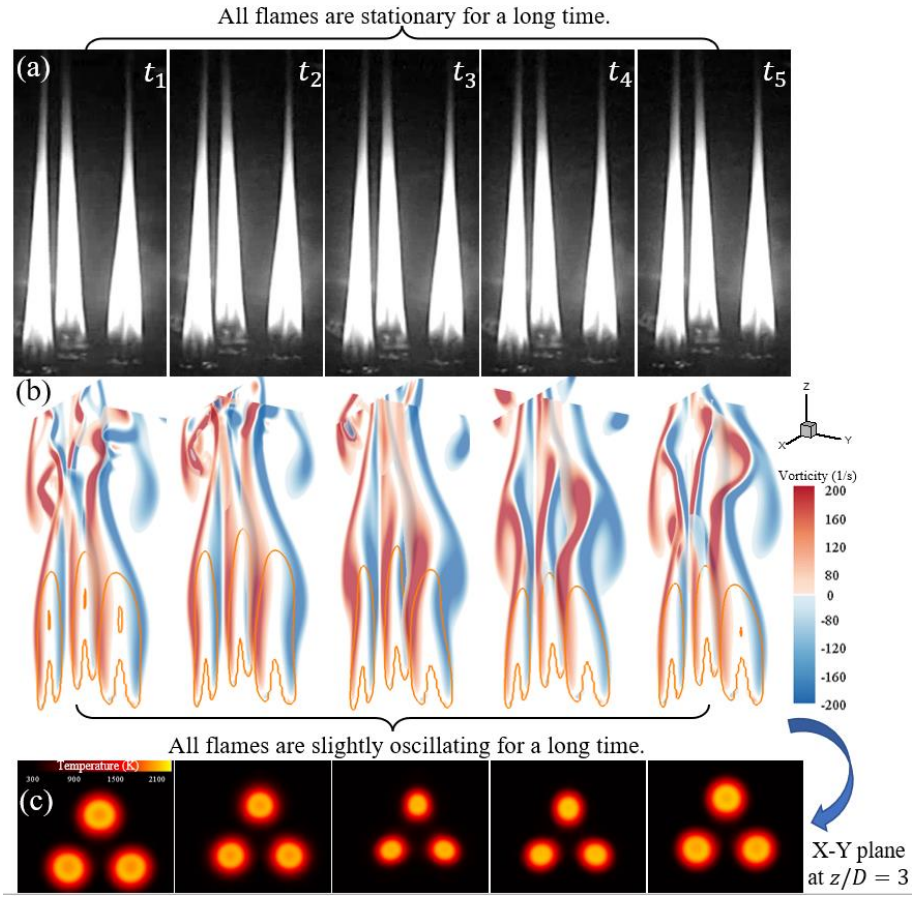

Figure 6-13 The flickering death mode of triplet flames was observed in (a) the candle experiment [80] and in the present simulation for (b) the vorticity field and (c) the temperature profile at the horizontal plane z/D=3.

As depicted in Fig. 6.14, there is an absence of significant flame necking and flame "bubble" pinch-off, which leads to the cessation of flame flickering. Given that the flames continue to exhibit a slight periodic oscillation without any phase difference, the flickering death mode can be regarded as a specific instance of the in-phase mode. It is important to highlight that a complete death mode, where all three flames stop oscillating and transition into steady combustion, could be achieved by significantly

suppressing vortex shedding through a further reduction in Re, thereby increasing viscous dissipation.

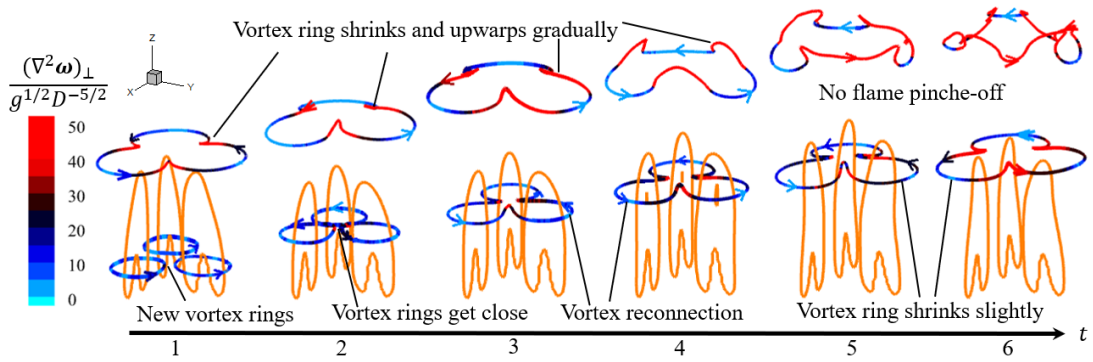

Figure 6-14 The triple flame system at $Re = 50$ and $R/D = 1.6$. The representative vorticity lines cross the highest Q-value and are colored by the normalized $(\Delta^2\omega)_\perp$. The flame is represented by the orange isoline of heat release.

6.2.3 Rotation and Partially In-phase Modes

In contrast to the modes described in Chapter 6.2.2, the rotation and partially in-phase modes fail to maintain the D3 symmetry characteristic of the equilateral triangle flame system, exhibiting traits of spontaneous symmetry breaking. At $Re = 100$ and $R/D = 2.0$, the triple jet diffusion flame system displays a rotation mode, in which the three flames flicker alternately, maintaining a consistent phase difference of $2\pi/3$ between them. Figure 6.15 shows that the pattern changes of each flame have a qualitative agreement with the experiments in [80]. The same phenomenon observed in the methane/air jet flame experiment demonstrates increased stability against external disturbances, attributed to the well-controlled nature of the flames [226].

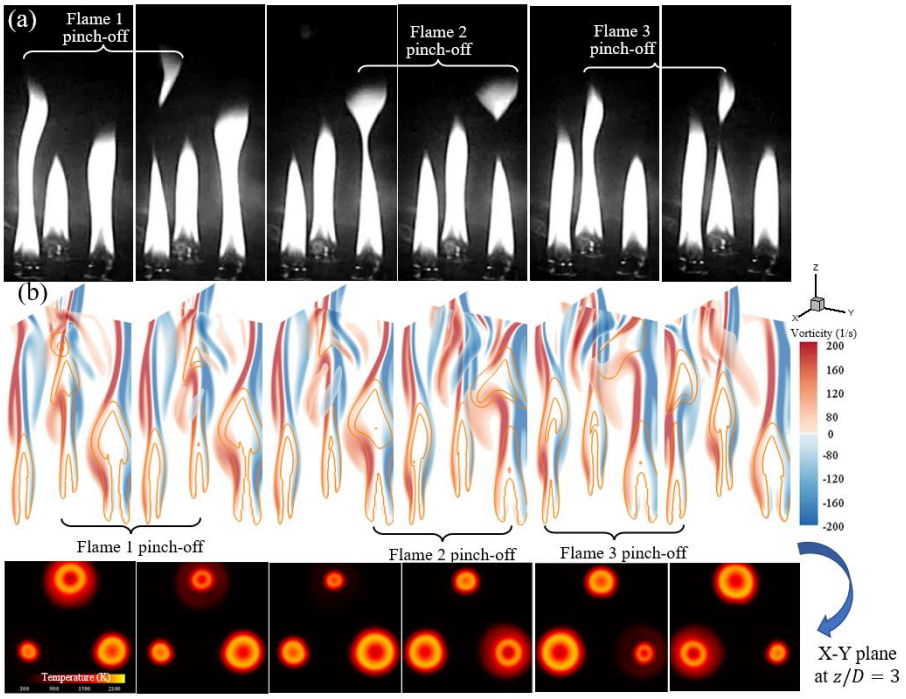

Figure 6-15 The rotational mode of triplet flames was observed in (a) the candle experiment [80] and in the present simulation for (b) the vorticity field and (c) the temperature profile at the horizontal plane z/D=3.

The evolution and interaction of the three toroidal vortices are depicted in Fig. 6.16. It is evident that there is no significant vorticity reconnection among the three representative vorticity lines, which intersect at the local maximum Q-value. At time instant t_1, the heights of the three toroidal vortices surrounding the flames follow the descending order of 1-2-3, with Flame 1 exhibiting more prominent stretching and necking than the other two.

By t_2, the vortex associated with Flame 1 has shed, and a new vortex forms at the base of the flame; the height order of the three vortices is now 2-3-1. Following this, as a result of the shedding of the old vortex and the formation of a new vortex from Flame 2, the order changes to 3-1-2 at t_3 and t_4. Finally, following the shedding of the old vortex and the emergence of a new vortex from Flame 3, the arrangement of the vortex

heights returns to 1-2-3 at time instants t_5 and t_6. At this point, a complete cycle of the rotation mode concludes.

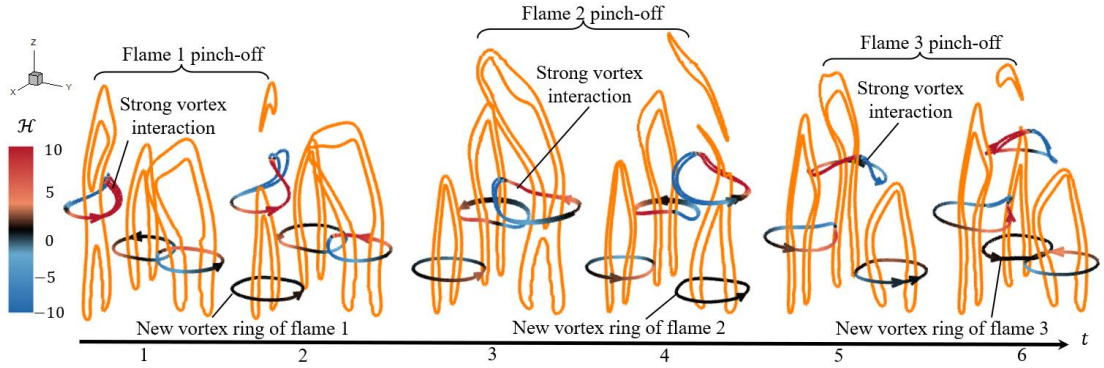

Figure 6-16 The triple flame system at $Re = 100$ and $R/D = 2$. The vorticity lines cross the highest Q-value and are colored by the normalized helicity density $\mathcal{H}$. The flame is represented by the orange isoline of heat release.

To quantify the interaction of vortices in the rotation mode, we plotted the normalized helicity density $\mathcal{H} = h/g$ along each vorticity line, as there is no observable vorticity reconnection, making the normalized $(\Delta^2\omega)_\perp$ an inappropriate metric. In cases of axisymmetric flow, where $\vec{\omega}$ is orthogonal to $\vec{u}$, the helicity density is zero. Thus, a nonzero helicity density indicates the non-orthogonality of $\vec{u}$ and $\vec{\omega}$, which arises from the induced flow around a toroidal vortex due to the influence of the other two vortices.

It is evident that the variation in the $\mathcal{H}$ value along each vorticity line corresponds to the height order of the vortices. For instance, at t_1, the magnitude of the $\mathcal{H}$ value along vortex 1 is the highest (mostly positive), vortex 2 has a middle value (mostly negative), and vortex 3 has the smallest magnitude (around 0). Physically, this indicates that the vortex-induced flow varies around each vortex, with positive $\mathcal{H}$ suggesting that the induced flow promotes vortex growth, while negative $\mathcal{H}$ implies suppression.

Therefore, when old vortex 1 sheds at t_2, it alleviates its suppressive effect on the subsequent vortex 2, which in turn sheds at t_4, relieving its suppression on vortex 3.

The rotation mode is also observable at different flame distances, such as at $Re = 100$ and $R/D = 3$ as shown in Fig. 6.17. In this scenario, the same phenomenon of alternating flame flickering is evident; however, the primary distinction lies in the reduced vortex interaction resulting from the increased separation distance between the flames. This difference is clearly illustrated by the normalized helicity density along each toroidal vortex line.

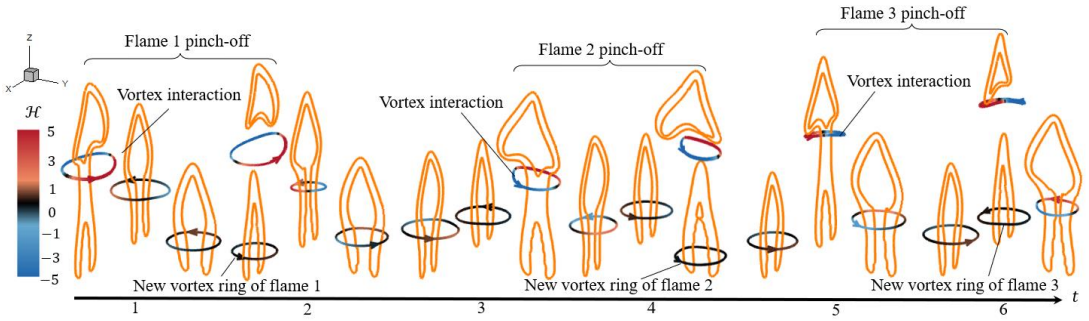

Figure 6-17 The triple flame system at $Re = 100$ and $R/D = 3$. The representative vorticity lines cross the highest Q-value and are colored by the normalized helicity density $\mathcal{H}$.

By further increasing the flame distance to $R/D = 3.6$, we were able to reproduce the partially in-phase mode, illustrated in Fig. 6.18. In this mode, two flames flicker without a phase difference, while the third flame flickers in anti-phase, exhibiting a phase difference of π. As demonstrated in Fig. 6.19, vorticity reconnection takes place between the two toroidal vortices, enabling their flame flicker to achieve in-phase synchronization. It is important to note that, due to the increased R/D, reconnection does not occur between the two representative vorticity lines that intersect at the highest Q-value.

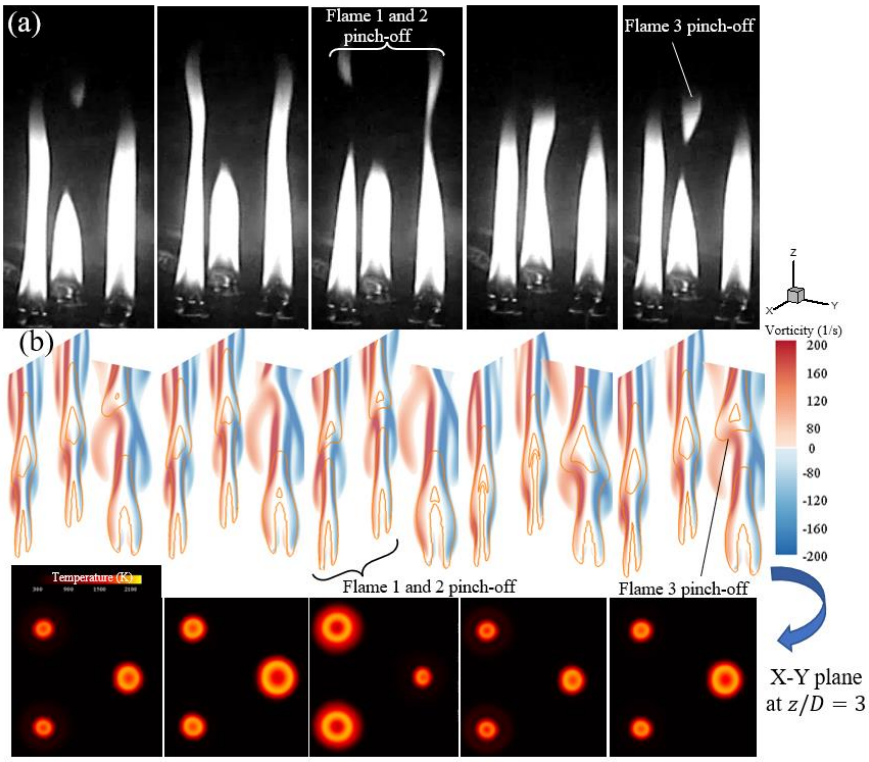

Figure 6-18 Partial in-phase mode of triplet flames observed in (a) candle experiment [80] and in the present simulation for (b) the vorticity field and (c) the temperature profile at the horizontal plane z/D=3.

The reconnection is represented by vorticity lines associated with a lower Q-value. The intertwined "8-shaped" vortex compresses inward, triggering the "necking" effect in the two flames, which leads to the creation of two flame "bubbles." These bubbles eventually break away from the primary flames as a result of the shedding of the "8-shaped" vortex. This shedding process reduces the suppression of vortex-induced flow, promoting the expansion of the toroidal vortex around the third flame. As a consequence, this vortex undergoes further growth and ultimately sheds, giving rise to the anti-phase flickering of the third flame.

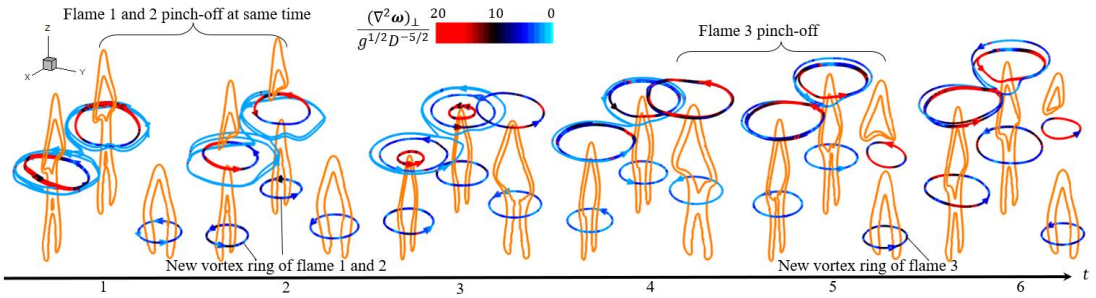

Figure 6-19 The triple flame system at $Re = 100$ and $R/D = 3.6$. The representative vorticity lines cross the highest Q-value and are colored by the normalized $(\Delta^2\omega)_\perp$. The flame is represented by the orange isoline of heat release.

6.3 Summary and Conclusions

In recent years, multiple coupled flickering flames have garnered enhanced interest as a dynamic system of oscillators. We attempted to explore the four unique dynamical modes by focusing on vortex interaction, considering the vital role that buoyancy-driven toroidal vortices have been shown to play in various experimental and theoretical studies. We conducted computational simulations to recreate the four dynamical modes exhibited by the triple flickering buoyant jet diffusion flames of methane, configured in an equilateral triangle at various R/D ratios. The following is a comprehensive summary of how these modes can be understood from a vortex-dynamical perspective.

In the realm of nonlinear dynamics, the interaction among three bodies introduces a significant level of complexity and novelty compared to two-body interactions. This study addresses, for the first time, how the triplet flickering flame system displays four distinct dynamical modes and how the interplay between toroidal vortices provides insights into these modes. Additionally, we offer new vortex-dynamical explanations for the observed behaviors of the triple-flame system, particularly by incorporating the mechanisms of vorticity reconnection, $(\Delta^2\vec{\omega})_\perp$, and vortex-induced flow as characterized by the helicity density $\mathcal{H}$.

Chapter 7. Synchronization of Multiple Flickering Flames

In the chapter, a series of circular arrays of octuple flickering laminar buoyant diffusion flames were investigated in computational and modeling manners to understand their collective behaviours. In the present simulations, five distinct dynamical modes, such as the merged, in-phase mode, rotation, flickering death, partially flickering death, and anti-phase modes, were identified and interpreted from the perspective of vortex dynamics. All the modes were found to be controlled by the three dimensionless parameters, namely the normalized flame frequency f/f_0, the ratio of the flame separation distance to the flame diameter $\alpha = (l - D)/D$, and the Grashof number Gr.

A unified regime diagram was obtained in terms of f/f_0 and of a combined Reynolds-number-like parameter $\alpha Gr^{1/2}$. The bifurcation transition from the in-phase mode and the anti-phase mode to the totally or partially flickering death occurs at $\alpha Gr^{1/2} = 655 \pm 55$. In addition, a toy model of identical Stuart-Landau oscillators with time-delay coupling was utilized to mimic the collective dynamics of multiple flame systems, bringing out a great capability of reproducing the general features and collective modes.

The physical model based on vortex-dynamics mechanisms and the toy model of Stuart-Landau oscillators remain fundamental and novel tools in the study of synchronization and continue to provide valuable insights into the behavior of complex coupled oscillatory systems. This work aims to make a small but firm step toward understanding the complex combustion dynamics of annular combustion systems. The influences of wall confinement and combustion-acoustics interaction [99, 227] in larger-size annular combustion systems merit future works.

7.1 Computational Setups for Circular Arrays of Flickering Flames

The circular systems of octuple flames are studied by simulating eight identical Bunsen-type diffusion flames in circle arrays in a quiescent environment, as shown in Fig. 7.1. The square column of $16D \times 16D \times 24D$ for the present computational domain, where $D = 10$ mm is the characteristic length of the Bunsen burner. The Bunsen burners (the gray square columns of $D \times D \times 3D$) are located with the same gap distance of l along a cycle of $L = \beta D$ diameter and labeled by 1-8 numbers in a clockwise direction.

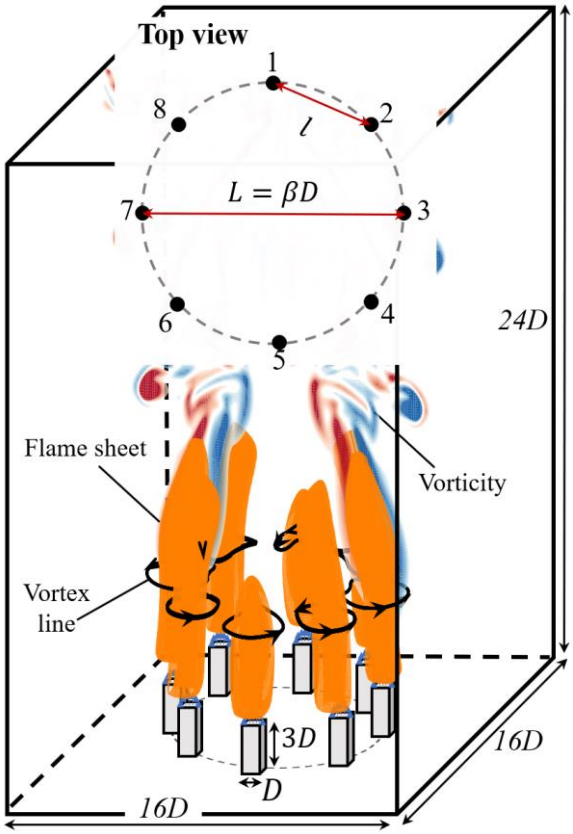

Figure 7-1 Schematic of the three-dimensional simulation and flame arrangement (top view) for circular arrays of octuple identical flickering flames.

The bottom of each burner is an inlet boundary for the gaseous methane jet (density $\rho_F = 0.66$ kg/m^3 and kinematic viscosity $\nu_F = 1.65 \times 10^{-5}$ m^2/s) at the uniform velocity U_0, while the burner wall (grey area) is set as an impermeable, non-

slip, and adiabatic solid boundary. The six sides of the computation domain are set as an open boundary condition (i.e., a simple upwind boundary condition). On these boundaries, the local pressure gradient determines whether gases flow inwards or outwards. When the flow is incoming or outgoing, the temperature and species mass fractions take on their respective exterior values or the respective values in the grid cell adjacent to the boundary. The environment is set as quiescent air (density $\rho_A = 1.20$ kg/m^3 and kinematic viscosity $\nu_A = 1.51 \times 10^{-5}$ m^2/s) under the normal temperature and pressure conditions (20℃ and 1 atm).

For the thermally driven flow of flickering flame, the buoyancy is predominant and the dynamic structures of flames are unaffected by the fast-chemistry assumptions. For simplicity of simulating the buoyancy-dominated diffusion flames, one-step overall methane/air combustion of $CH_4 + 2(O_2 + 3.76N_2) \rightarrow CO_2 + 2H_2O + 7.52N_2$ is adopted, the chemical reaction is a mixing-limited, infinitely fast model, and radiation and soot formation were neglected. The flames of all cases were in a fully developed state as the simulation time was at least 20 times longer than the characteristic time L/U_0. Table 7-1 shows the detailed setups for simulating the flickering phenomenon.

A mesh-independence study is a process used to determine whether the numerical solutions obtained from a simulation are dependent on the grid or mesh size used in the analysis. Our previous mesh-independence study of flickering flames [163] shows that the mesh refinement (each grid has $\Delta x/D = \Delta y/D = \Delta z/D = 10^{-2}$) is sufficient to capture the essential features of the buoyance-induced flicker of single laminar diffusion flame and the various flickering modes of dual- and triple-laminar diffusion flames. In this chapter, we focus on investigating the flickering behaviours of multiple laminar diffusion flames so that it is necessary to examine whether the computational domain and grid sizes are appropriate to capture strong couplings between vortices of

those flames. Further validation helps enhance the credibility of the present simulation outcomes before making the following analyses based on the numerical results.

Therefore, we take the case of $L = 10.2D$ as an example (the flame gap is relatively large to couple weakly) and carry out a domain-independence study. The goal is to ensure that further refinement of the mesh does not significantly affect the results, indicating that the solutions are accurate and reliable. As a result of the domain-independence study, we compare the dynamics mode of flames and flickering frequency of four cases with different domains and grids in Table 7-2. The mode is determined by the phase difference, while the frequency is calculated by the Fast Fourier Transform of flame signals (e.g., the vertical velocity at a fixed point [162]) at $\pm$0.2 Hz error. The flame dynamics of octuple flickering flames will be elaborated.

The present results show that the second domain and grid study can capture well the flame mode and frequency, as the same mode and a small frequency change (about 5%) are simulated by enlarging the domain and refining the mesh. Consequently, we adopted the domain of $16\text{D} \times 16\text{D} \times 24\text{D}$ and the grid of $160 \times 160 \times 240$ for the parametric studies in the following sections to ensure adequate accuracy with reasonable computational cost. According to the thermal diffusivity (about 20-140 mm^2/s at 300-2100 K) and the characteristic time of the present flickering flames (flame frequency about 10 Hz), the diffusion zone of the flame is evaluated to be 1.4-3.7 mm and can be resolved by the present mesh size [162].

Table 7-1 Key parameters of numerical simulations.

Setup	Detailed description
Fuel and oxidizer	Methane gas with kinematic viscosity $\nu_F = 1.65 \times 10^{-5}$ m^2/s is ejected at a uniform inlet velocity $U = 0.165$ m/s from each burner; Environment air with kinematic viscosity $\nu_A = 1.51 \times 10^{-5}$ m^2/s is quiescent under the normal temperature and pressure conditions (20℃ and 1 atm).
Bunsen burner	Identical square burners with $D = 10$ mm length and $3D$ height.
Nondimensional parameter	Reynolds number defined by $Re = UD/\nu_F = 100$ and Froude number defined by $Fr = U^2/gD = 0.28$.
Domain	A square column of $16D \times 16D \times 24D$ with the gravity constant of g=9.8 m/s^2.
Boundary	Open boundary conditions allow airflow in and out freely for six surfaces of the domain; impermeable, non-slip, and adiabatic boundary conditions for solid surfaces of the burners with the central fuel inlet.
Grid	Structured, uniform, and staggered grids of $\Delta x = \Delta y = \Delta z = 10^{-2}D$.
Model	Infinitely fast reaction for one-step overall methane/air combustion; no modeling for radiation and soot formation.
Simulation	Fully developed flows after running at least 20 times longer than (L/U_0).

Table 7-2 The domain and grid-independence studies.

No.	Domain and grid	Flame mode		Frequency
1	$20D \times 20D \times 30D$	Anti-phase: two groups	1-3-5-7 in-phase;	12.2
	$200 \times 200 \times 300$	with π phase difference	2-4-6-8 in-phase	12.2
2	$16D \times 16D \times 24D$	Anti-phase: two groups	1-3-5-7 in-phase;	12.4
	$160 \times 160 \times 240$	with π phase difference	2-4-6-8 in-phase	12.4
3	$16D \times 16D \times 24D$	Anti-phase: two groups	1-3-5-7 in-phase;	12.8
	$240 \times 240 \times 360$	with π phase difference	2-4-6-8 in-phase	12.8
4	$12D \times 12D \times 18D$	Partially flickering death: two groups with different dynamics	2-6 and 4-8 in-phase; 1-3-5-7 flickering death	12.4
	$120 \times 120 \times 180$			15.8

As a benchmark case in Fig. 7.2, the flickering phenomenon i qualitatively reproduced by a diffusion flame of $Re = 100$ and $Fr = 0.28$, in which the evolution of the simulated temperature and vorticity contours during a period of $\tau = 0.1\text{s}$ is illustrated. Fig. 4(a) clearly shows that the flame pinches off within $t = 3\tau/5$ and $4\tau/5$, because the vorticity accumulation inside the toroidal vortex (e.g., vortex ring) reaches a threshold [24], as illustrated by the increasingly spiral streamlines from $0\tau/5$ to $3\tau/5$.

Specifically, the toroidal vortex around the flame induces a high velocity near the center of the flame, contracts the flame sheet, and causes the flame neck. The vortex shedding finally separates the flame top from the base. After the pinch-off of flame at $t = 4\tau/5$, the upper portion of the flame is convected downstream with the toroidal vortex, while a new vortex (denoted by a small spiral streamline) is generated at the flame base. The next cycle of vortex and flame interaction starts at $t = \tau$. Therefore,

flame dynamics is closely associated with vortex evolution. More details on the connection between the vortex shedding and the flame flicker can be referred to [24, 163, 164].

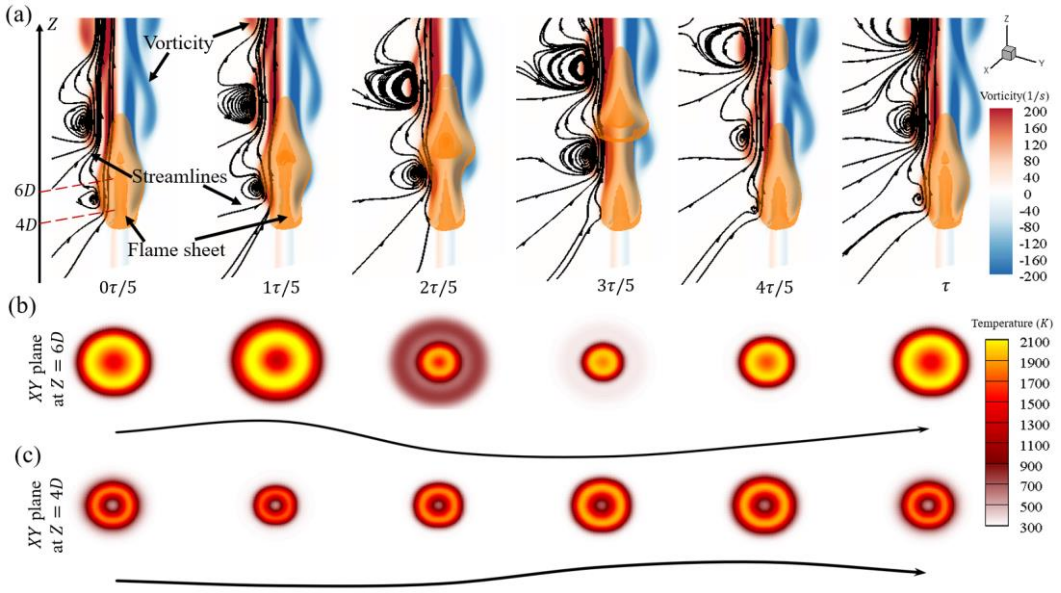

Figure 7- 2 (a) Evolution of single flickering diffusion flame with the flame (denoted by the iso-surface of the heat release rate) and vortex flow (denoted by streamlines and vorticity contour) during a period of τ. (b-c) Time-varying contours of temperature in the transverse planes of $X-Y$ at $z=4D$ and $6D$. The curve lines represent the variance of temperature area with time.

7.2. Dynamical Modes of Circular Systems of Octuple Flames

The interactions of two flames are fundamental to understanding the bifurcation of various dynamical modes of circular arrays of flame oscillators, as illustrated in chapter 5.4. In this chapter, the octuple flame system, consisting of identical flame individuals with the Froude number Fr =0.28 and the flickering frequency $f_0 = 10$ Hz, can create complex collective behaviours. Ten circular arrays of octuple-flickering flames with Fr =0.28 and $\alpha Gr^{1/2} = 152 - 885$ are investigated by increasing the

dimensionless parameter α and correspondingly resulting in the bifurcation of vortex dynamics among the flames, we found five distinct modes for collective behaviours of present circular flame arrays by characterizing their flame frequency and phase difference. Table 7-3 shows the present simulated circular arrays of flame oscillators. To facilitate the notation, the ten cases will be denoted as Case α. Their dimensionless flame-gap distance α varies from 0.6 to 3.5, so these cases cover the range of coupling effects of the dual flame system. For a larger circular array of present flickering flames, the adjacent flames would be weak and render a case of no interest to the present work.

Table 7-3 Main information of simulation cases.

No.	α	$\alpha Gr^{1/2}$	Flame dynamical mode
1	0.6	152	Merged (Me): all flames are merged into a big flame.
2	1.4	354	
3	1.8	455	In-phase (IP): all flames flicker as one group without phase difference.
4	2.0	506	
5	2.1	531	
6	2.4	607	Rotation and flickering death (RFD): all flames are not pinched off and alternatively oscillate in the azimuthal direction.
7	2.5	632	Partially flickering death (PFD): the subgroup of flame 1-2-3 behaves the same as the partially flickering death mode of the triple flame system.
8	2.8	708	
9	3.0	759	Anti-phase (AP): eight flames are divided into two groups (1-3-5-7 and 2-4-6-8) with a constant phase difference of π.
10	3.5	885	

In brief, the relevant observations for those modes can be made as follows: 1) merged (Me) mode indicates that the octuple flames can merge into a bigger one, as they are too close to each other (e.g., α =0.6 and 1.4); 2) in-phase (IP) mode appears as these flames are sufficiently separated but can flicker synchronously without a phase difference (e.g., α =1.8, 2.0, and 2.1); 3) rotation and flickering death (RFD) mode appears as the flames alternatively flicker in the azimuthal direction and the flame flicker is suppressed (e.g., α =2.4); 4) partially flickering death mode (PFD) occurs when the octuple can be divided into several subgroups (e.g., the 1-2-3 flames), behaving behaves like the partially flickering death mode of triple flame system (e.g., α =2.5 and 2.8); 5) anti-phase (AP) mode is that the eight flames are divided into two groups (1-3-5-7 flames and 2-4-6-8 flames) with a constant phase difference of π (e.g., α =3.0 and 3.5). The details of each dynamic mode will be elaborated in later sections.

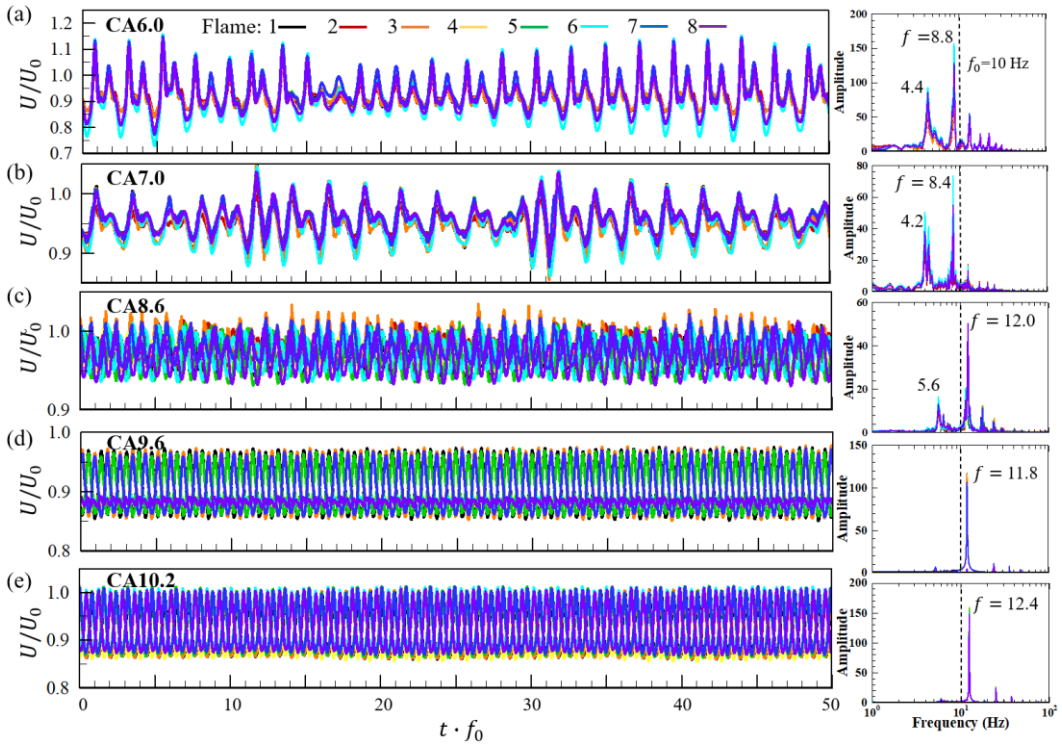

Figure 7-3 Time and frequency domains of the velocity magnitudes at the center of each nozzle in the five cases of α = (a) 1.4, (b) 1.8, (c) 2.4, (d) 2.8, and (e) 3.0.

Furthermore, compared to the self-excited motion of a single flame, collective flames oscillate at different frequencies. The flame frequencies of five representative cases of these distinct modes are calculated from the flame time series, for example, the velocity magnitude at the center of each nozzle, as shown in Fig. 7.3. Same flame frequencies are calculated based on the velocity magnitude at the 3D downstream of each nozzle in Fig. 7.4. Due to the complexity of collective flames, we adopted the time-varying quantity in the transverse section to characterize flame dynamics.

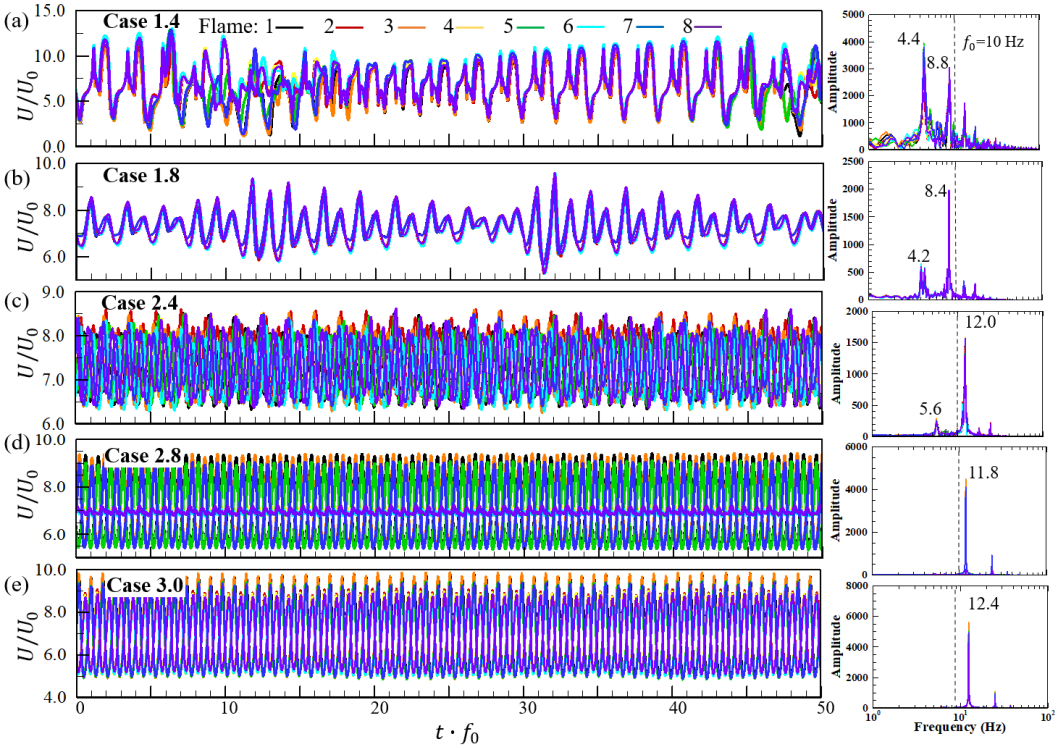

Figure 7- 4 Time and frequency domains of the velocity magnitudes at 3D downstream of each nozzle in Fig 7-3 for α = (a) 1.4, (b) 1.8, (c) 2.4, (d) 2.8, and (e) 3.0.

7.2.1 Merged (Me) Mode and In-phase (IP) Mode

Figure 7.4 shows the representative case for the merged mode of octuple flickering flames. During the periodic process of $\tau = 1/f = 114$ ms, the eight flames can be well recognized according to the time-varying temperature distributions in the horizontal

plane, as shown in Fig. 7.3(a) and Fig. 7.4(a). Particularly, their high temperature ($\geq$ 2000K) can be connected from $2\tau/6$ to $3\tau/6$. The connected zone indicates that the flame sheets are merged and subsequently form a big flame surface.

Besides, Fig. 7.5(b) corresponds to the dynamical behaviours of two flames (flames 3 and 7) in the longitudinal plane. An inner vortex, denoted by curled streamlines, appears inside the flames. The size and location of the recirculation zone evolve with the flames. The vortex grows up when flames are lengthened and deformed. At $5\tau/6$, the flame is pinched off and the vortex shedding occurs. The merged flames flicker like a big one at a primary frequency of 8.8 Hz, smaller than that of a single flickering flame. Also, we noted a lower frequency of 4.4 Hz in Fig. 7.3(a) and conjectured the frequency results from the emergence of the inner vortex, as the vortex has about twice the scale of the buoyance-induced toroidal vortex. Interestingly, the time-varying velocity magnitude waves as an "M" shape with unequal left and right peaks.

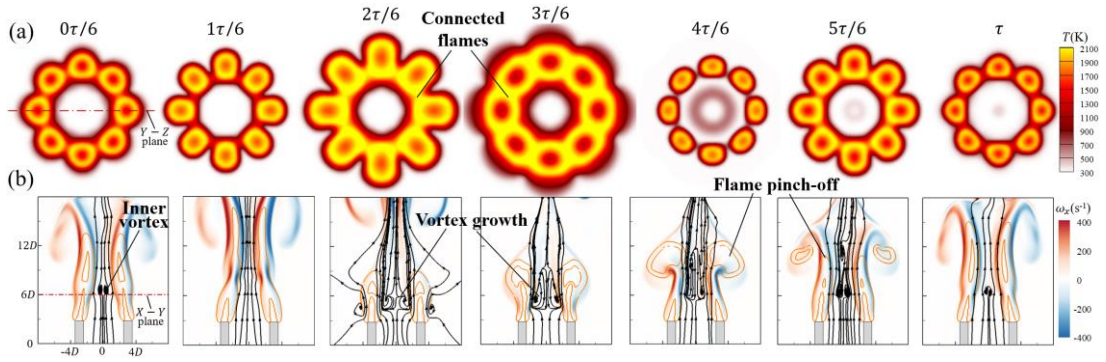

Figure 7- 5 The periodic collective process of the circular array of octuple flickering flames for α =1.4: (a) horizontal $X-Y$ plane and (b) longitudinal $Y-Z$ plane.

Similarly, the collective behaviours of eight flames in the case α =1.8 occur in a flickering way, as shown in Fig. 7.6. As there is no connection to the high-temperature zone in Fig. 7.6(a), these flames are unmerged, but the separated individuals oscillate

with no phase difference. Fig. 7.6(b) clearly shows that the collective flames are affected by the inner vortex and the flame dynamics are closely associated with the vortex evolution.

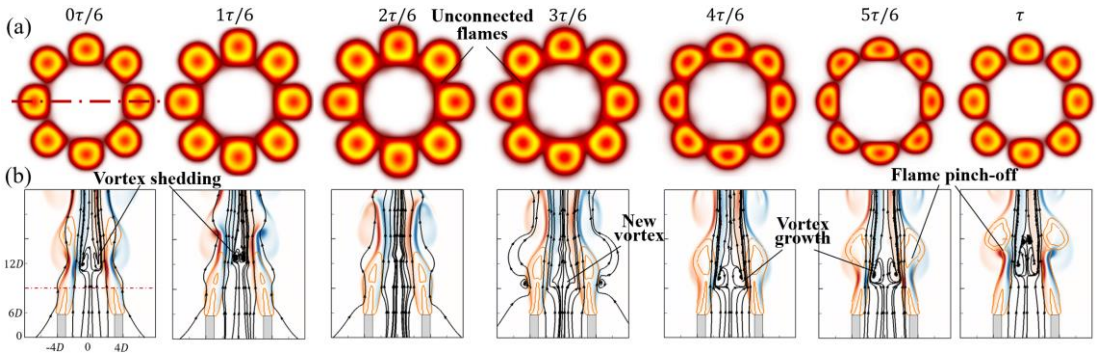

Figure 7-6 The periodic collective process of a circular array of octuple flickering flames for α =1.8: (a) horizontal $X-Y$ plane and (b) longitudinal $Y-Z$ plane.

These synchronized flames exhibit the up-and-down and the back-and-forth deformation, appearing like a "worship" [84]. The vortex reconnection plays an essential role in the collective dynamics, as similarly illustrated in the triple-flame system in our previous work [164]. Besides, their primary and secondary frequencies, 8.4 Hz and 4.2 Hz shown in Fig. 7.3(b) respectively, are a little smaller than those of the case α =1.4, which would be due to the bigger diameter of the circular.

7.2.2 Rotation & Flickering Death (RFD) Mode

When the flame circular becomes bigger, the collective behaviours vary significantly, for example, the case α =2.4 in Fig. 7.7. The most differences have two points: these flames have an azimuthal motion and the pinch-off of each flame vanishes. As shown in Fig. 7.7(a), the transverse temperature shapes of each two diagonal flames deform in opposite directions (denoted by the opposite arrows). The collective flames

regularly form the circumferential motion. The inserted figure specifically shows the three-dimensional pattern of flame sheets (denoted by the heat release iso-surface).

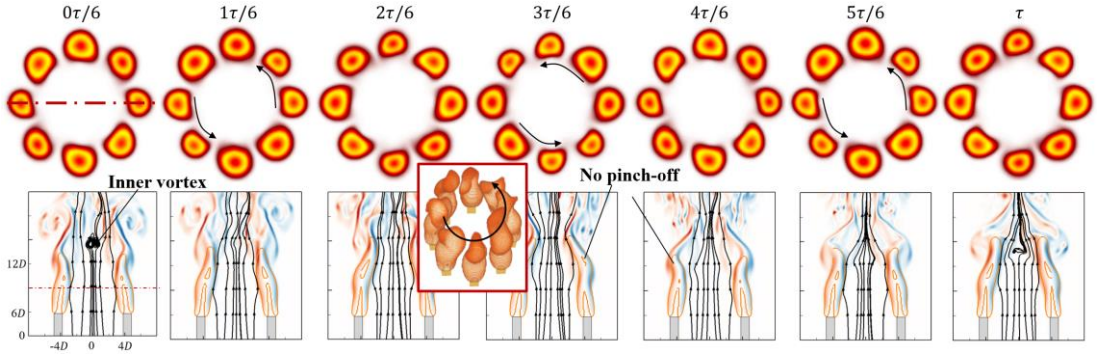

Figure 7-7 The periodic collective process of a circular array of octuple flickering flames for $\alpha = 2.4$: (a) horizontal $X - Y$ plane and (b) longitudinal $Y - Z$ plane.

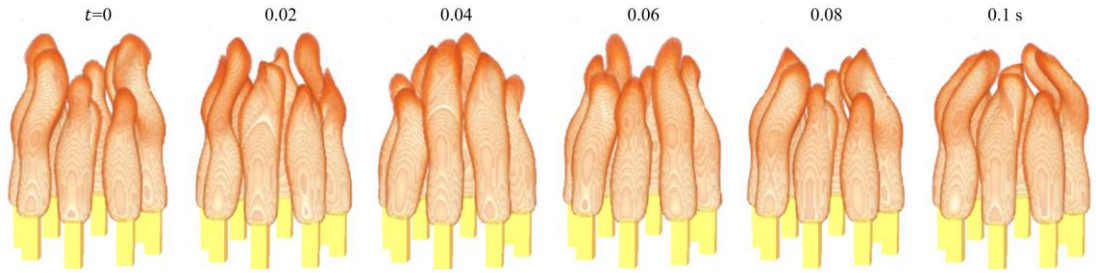

Figure 7-8 Three-dimensional patterns of the case α =2.4. Flames are denoted by the iso-surface of the heat release rate.

A twisting deformation of flames in the anticlockwise direction can be seen. In addition, we noted that the eight flames have no pinch-off during the periodic process of $\tau = 1/f = 83$ ms, as shown in Fig. 7.7(b). It should be noted that the inner vortex plays an insignificant role in collective behavior as the small vortex sometimes occurs near the top part of flames. More three-dimensional details are given in Fig. 7.8. In fact, the primary frequency of f=12 Hz could characterize the swaying of the flame head, instead of the vertical oscillation. This collective behavior is similar to the flickering death mode of a dual- or triple-flame system [78, 102], in which the flicker of one flame is suppressed by the vortex-induced flow of the a djacent flames [164].

7.2.3 Partially Flickering Death (PFD) Mode

In the case α =2.8, the longitudinal diagonal flames (flames 1 and 5) flicker in an in-phase way and so do the horizontal pair of flames 3 and 7. However, these two pairs have a π phase difference, as shown in Fig. 7.9(a). Interestingly, the rest flames (flames 2, 4, 6, and 8) behave in the flickering death mode. If we regard the 1-2-3 flames as a subgroup (encircled by the red dotted line), the triple flame system performs like the partially flickering death (PFD) mode that the left and right flames flicker in an anti-phase way while the middle flame oscillates without the flame flicker, as shown in Fig. 3(c) of [102]. For the collective flicker of 1-3-5-7 flames, its primary frequency is f=11.8 Hz (about a period of τ=85 ms) in Fig. 7.3(d). Interestingly, Fig. 7.9 (b) shows that the inner vortex forms far away from the flames. The no influence of the downstream vortex on the flames may cause the result of no secondary frequency.

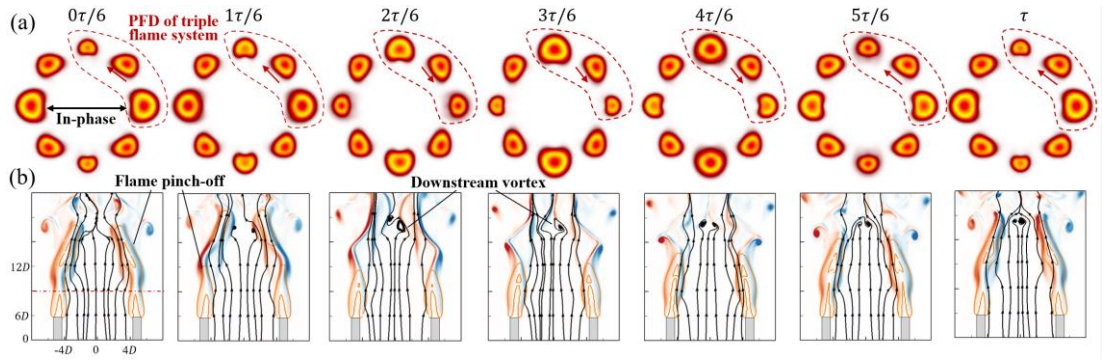

Figure 7-9 The periodic collective process of a circular array of octuple flickering flames for α =2.8: (a) horizontal X-Y plane and (b) longitudinal Y-Z plane.

7.2.4 Anti-phase (AP) Mode

When eight flames are relatively away from each other, for example in the case α =3.0, we can see the flames are separated into two groups of 1-3-5-7 flames and 2-4-6-8 flames in Fig. 7.10(a). In each group, the in-phase mode appears as the four

flames flicker synchronously with no phase difference. The two group flames alternatively flicker with a phase difference of π. The collective behavior of octuple flickering flames is similar to the anti-phase mode of the dual flame system [163], in which the toroidal vortex together with the flow becomes asymmetric, like a von Karman vortex street. Besides, we noted that the inner vortex forms near the flame downstream in Fig. 7.10(b). Thus, the shear layers of adjacent flames in the circular array, exhibiting a distinct asymmetric feature, play an important role in the collective behavior. In this case, the collective motion only has a primary frequency of 12.4 Hz, of which the frequency increase (2.4 Hz higher than f_0) is consistent with the finding of the anti-phase mode of the dual flame system.

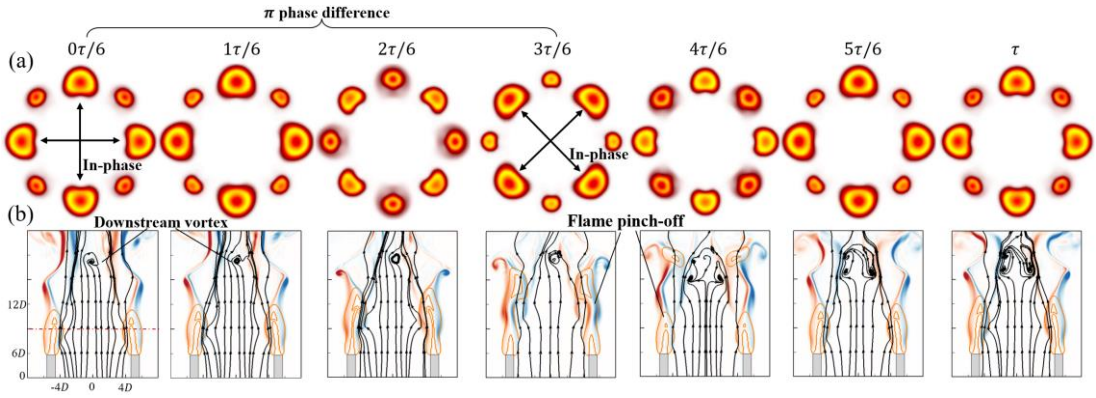

Figure 7-10 The periodic collective process of a circular array of octuple flickering flames for α =3.0: (a) horizontal $X-Y$ plane and (b) longitudinal $Y-Z$ plane.

7.3 Unified Regime Diagram of Dynamical Modes

The non-dimensional frequencies, primary and secondary f/f_0, of circular arrays of octuple flickering flames are plotted against $\alpha Gr^{1/2}$ based on the current simulations in Fig. 7.11. This frequency variation trend shows a bifurcation transition (denoted by the grey zone of $\alpha Gr^{1/2} = 620 \pm 50$) between the in-phase mode (a lower-frequency collective state with secondary frequency) and the anti-phase mode (a higher-frequency

collective state without secondary frequency). It should be noted that the collective effect causes the transition range Re_A to be higher than that of the dual flame system.

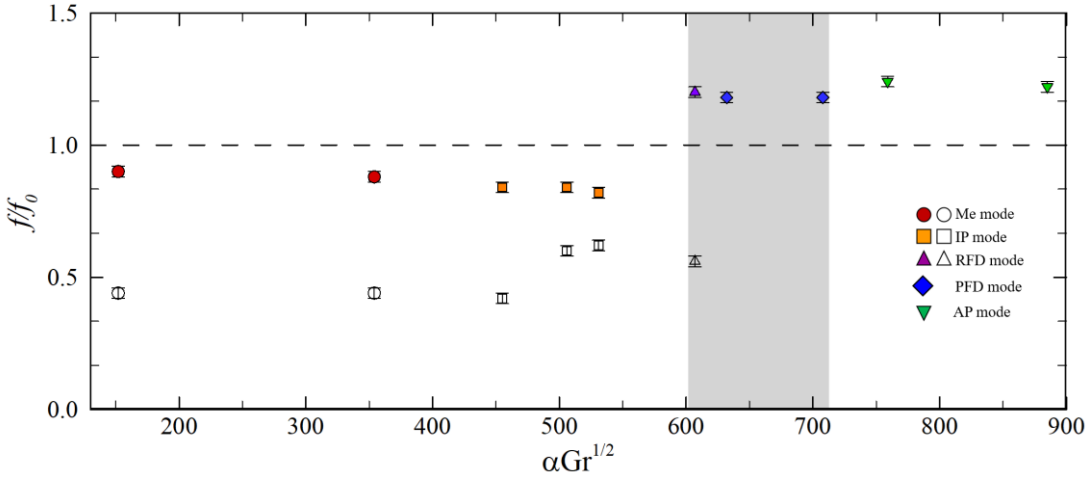

Figure 7-11 Regime diagram of the octuple flame system. The eight identical flickering diffusion flames exhibit five distinct modes with increasing the nondimensional number of $\alpha Gr^{1/2}$[163]. Their frequencies f are normalized by the natural frequency f_0 and small $\alpha Gr^{1/2}$ cases, including the merged, in-phase, rotation & flickering death modes, have secondary frequencies. A transition region of $600 < \alpha Gr^{1/2} < 710$, where the flicker death occurs in some or all flames, distinctly separates the in- and anti-phase modes.

Besides, the transition covers the RFD and PFD modes, in which the flickering amplitudes of collective flames are suppressed totally or partially. Previous experimental observations [78, 102] reported similar phenomena of amplitude death in combustion systems with a few flames (≤ 3). In fact, the death state occurs commonly in various fields, such as neuron and brain cells and prey-predator systems. Particularly, nonflickering flames may weaken the influences of thermoacoustic instability on rocket engines [228] as the noise generation is reduced in a combustion chamber. Different from the moving-burner technique to achieve steady-state combustion [228], the

present study gives a feasible way to design flame layouts in a circular array system for flicker suppression.

7.4 Stuart-Landau Oscillators with Nearest Neighbor Coupling

To simplify the complex interactions among multiple Stuart-Landau (S-L) oscillators, we utilized the nearest neighbor coupling model, considering the oscillator's local interplay, where each oscillator is coupled only to its nearest neighbor. For multiple interacting bodies distributed uniformly along a ring, the extension of Eq. (5.5) can be approximated to just two coupling terms and the model has the form

$$\frac{dZ_j}{dt} = \left(1 + 10i - \left|Z_j\right|^2\right) Z_j + K\left(Z_{j+1}(t-\tau_d) - Z_j(t)\right) + K\left(Z_{j-1}(t-\tau_d) - Z_j(t)\right) \tag{7.1}$$

where all oscillators are identical with a =1 and ω =10 and arranged in a closed ring, forming a local coupling unite of $j-1$, j, and $j+1$ oscillators, for example, 8-1-2, 1-2-3, 2-3-4, 3-4-5, 4-5-6, 5-6-7, 6-7-8 in the present problem. Similarly, Biju et al.'s work [229] employed periodic boundary conditions to enforce the ring topology of an oscillator network. It's noteworthy that the nearest neighbor coupling is unlike the situation where the coupling has a global dependence on the geometrical arrangement of the oscillators.

In the present study, Eq. (7.1) is used as a toy model to study the collective states of multiple flame oscillators. Figure 7.12 shows the results of the present model within $10 < K < 30$ and $0.01 < \tau_d < 0.4$ for octuple S-L oscillator systems. In the regime diagram, the in-phase, death, and anti-phase modes are reproduced with increasing τ_d, while the death mode is absent when K is relatively large. In general, the frequency trend of ω_d/ω has a jump variation within the transition region of $0.10 < \tau_d < 0.18$.

Like the dual oscillator system, the eight oscillators in the in-phase state have lower frequencies than the natural frequency, while the frequencies of those in the anti-phase state are higher. Interestingly, those results are basically consistent with the observations in the octuple flickering flame systems in Fig. 7.11.

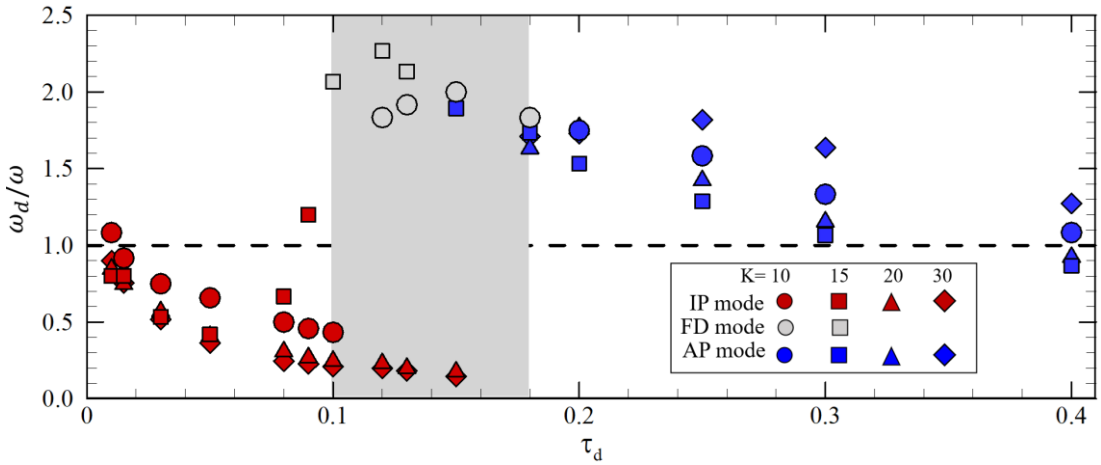

Figure 7-12 Regime diagram of octuple identical S-L oscillators with time-delay coupling. Using the nearest neighbor coupling for the oscillator interactions, Eq. (7.1) is solved to obtain three modes and their ω_d/ω at different K and τ_d.

Specially, the small $\tau_d = 0{\sim}0.1$ region roughly corresponds to the region of merged and in-phase states, where $\alpha Gr^{1/2}$ is smaller than 600; the situation that the death mode occurs at the appropriate τ_d and K is similar to those cases of rotation & death and partial death modes in a narrow region of $\alpha Gr^{1/2} = 600 - 710$; big τ_d causing the eight oscillators to divide into two anti-phase clusters (i.e., four oscillators are in-phase in each cluster but anti-phase with the other four) is like big $\alpha Gr^{1/2}$, at which eight flames are synchronized in anti-phase mode. Therefore, the toy model used here has brought out a great capability of reproducing the general features and collective modes of flickering flame in circular arrays.

However, a few modes with specific characteristics, such as all flames in the merged state, all flames possessing an azimuthal motion, and partial flames in the death state, are not presented. The limits of Eq. (7.1) may be due to two potential causes:

First, the S-L model is represented by a limit cycle oscillator, consisting of amplitude and frequency, while the flame is a high-dimensional system, in which spatiotemporal interactions could be multimodal. Increasing flame numbers or varying flame layouts is likely to make the flame and vortex interactions complicated, thereby forming distinct dynamical behaviours from the collective perspective.

Second, the nearest neighbor coupling of S-L oscillators is an approximate model to mimic the interaction between adjacent flames. Collective states and essential characteristics of oscillators apparently rely on coupling scenarios, for example, all-to-all (global) coupling and spatially varying (non-local) coupling. The additional dimension is required for the global or nonlocal coupled terms and accordingly introduces new equilibrium states in the system such as traveling waves and in higher dimensions spiral patterns or scroll waves [184]. The influences of the global coupling on the collective behaviours of multiple oscillators merit future work.

7.4 Summary and Conclusions

In nature, local interactions between individual entities give rise to patterns or collective behaviours in groups. The flickering flame, as a flame oscillator, has been used widely in recent years to study the nonlinear dynamics of complex systems. In this study, we computationally investigated the emergence of synchronization events in circular arrays of octuple identical flame oscillators (i.e., small-scale flickering buoyant diffusion flames of Re=100). A parametric study was carried out in the range of a bifurcation parameter $\alpha Gr^{1/2} = 100\sim900$.

Five distinct dynamical modes were identified by comparing their frequencies and phase differences, namely the merged mode (all flames are merged into a big one with a lower flickering frequency), in which an inner vortex forms in the circle array and coexists with the outer buoyance-induced toroidal vortex; the in-phase mode (all separated flame individuals flicker synchronously without phase difference), in which the vortex reconnection keeps all flames in same manner; the rotation & flickering death mode (the flicker of all flames is suppressed and they collectively form an azimuthal motion), in which the flame flicker is suppressed by the vortex-induced flow of other flames; partially flickering death mode (a part of the eight identical flames is flickering death and the rest flames flicker in an in-phase or anti-phase synchronization), in which the inner vortex occurs far away from the flames and the vortex-induced flow causes the flickering death of some flames; anti-phase mode (flames are separated into two groups with a π phase difference, but flames flicker synchronously without phase difference in each group), in which the shear layers of adjacent flames exhibit a distinct asymmetric feature. Understanding such a switching of phenomena between various dynamical modes helps us to evade their undesirable occurrences.

In the regime diagram of flame circular arrays, we found a bifurcation transition of $\alpha Gr^{1/2} = 620 \pm 50$ between the in-phase mode and the anti-phase mode. The transition separates lower-frequency collective states with a secondary frequency and higher-frequency collective states without a secondary frequency. Those secondary frequencies could be due to the formation of a big-scale inner vortex in circle arrays. In the transition, the collective effect can suppress the flame flicker totally or partially (i.e., the flickering death). Thus, designing a circular array system with a suitable $\alpha Gr^{1/2}$ is a feasible way to generate a death mode, thereby reducing noise generation and possibly relieving thermoacoustic instability that usually occurs in annular combustors.

Part 2

Droplet Splash and Rebound on Surface

Chapter 8. Droplet Splash on Smooth and Heated Surfaces

In this chapter, droplet impact on a smooth solid surface at atmospheric pressure is physically interpreted in the relevant experiments carried out by coworkers. The main contributions of the PhD candidate are the establishment of theoretical analyses and physical pictures for the scaling laws and underlying mechanisms. A particular emphasis of the study is on the effects of liquid viscosity on the transition between droplet deposition (or droplet spreading without breakup) and droplet disintegration (including droplet splash and receding breakup). Specifically, the critical Weber number separating We droplet deposition from droplet disintegration decreases and then increases with increasing the Ohnesorge number Oh. The splash in low-Oh region and the receding breakup in high-Oh region were analyzed qualitatively based on the unbalanced forces acting on the rim of the spreading or receding liquid film. A semi-empirical correlation of droplet deposition/disintegration thresholds is proposed and well fits the experimental results over a wide range of liquid viscosity.

In addition, following the previous work identifying three subpatterns of a thin-sheet splash on a smooth wall at room temperature (T_0), we show that subpatterns of a thin-sheet splash at a high temperature (T_W) surface can be unified in the three-dimensional phase diagram of $Oh-We-T_\mathrm{W}$. As T_W is sufficiently high, the Leidenfrost effect becomes so prominent that both deposition and thin-sheet splash make the transition to Leidenfrost breakup. For the transition surface temperature $T_\mathrm{W,cr}$ from thin-sheet splash to deposition, a scaling correlation of $T_\mathrm{W,cr}/T_0 \sim We^{3/2}$ is derived based on the analysis of the temperature-dependent destabilizing force on the levitated lamella and agrees well with the experimental data.

8.1 Droplet Splash and Receding Breakup on a Smooth Surface

Two distinct patterns of droplet splash are clearly identified by examining the disintegration of the liquid film at different stages. For instance, with a Weber number We of approximately 453, as shown in Fig. 8.1, splashing is observed in all cases, but two different patterns emerge for droplet separation [124]. Specifically, low Ohnesorge number Oh liquids, such as 30%, 45%, and 60% glycerol solutions, exhibit splashing during the spreading phase, whereas high Oh liquids, like 75% and 85% glycerol solutions, only experience breakup during the retracting phase.

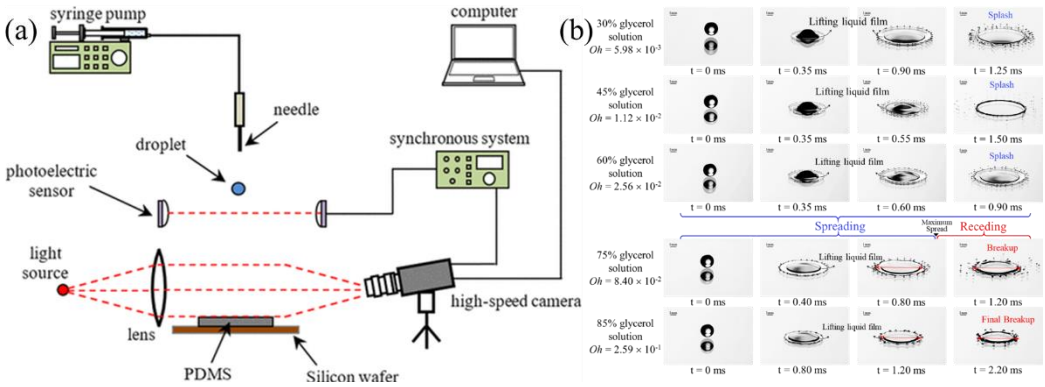

Figure 8-1 Experimental (a) setups and (b) snapshots of droplet impact on a solid surface. The experiments are from the work [124].

Yang et al. [124] experimentally presented deposition, splash, and receding breakup as a regime nomogram of Oh-We in Fig. 8.2. The critical boundaries of splashing and non-splashing show that no splashing occurs regardless of the value of Oh in the relatively low We range; droplet splashing varies non-monotonically with Oh in the intermediate range of We (250~500).

The mechanisms of droplet splash in low and high Ohnesorge number Oh regimes have been separately illustrated through the lens of flow instabilities [230, 231]. We acknowledge that a purely flow instability approach does not capture all facets of the phenomena [121, 232-236]. Nonetheless, the criteria used within the instability

framework typically involve comparing characteristic lengths, such as the thickness of the liquid film and the wavelength of the neutrally unstable mode. While these length-based criteria align well with those derived from an analysis of unbalanced forces [116, 237, 238], their fundamental distinction lies in how characteristic lengths or forces are estimated.

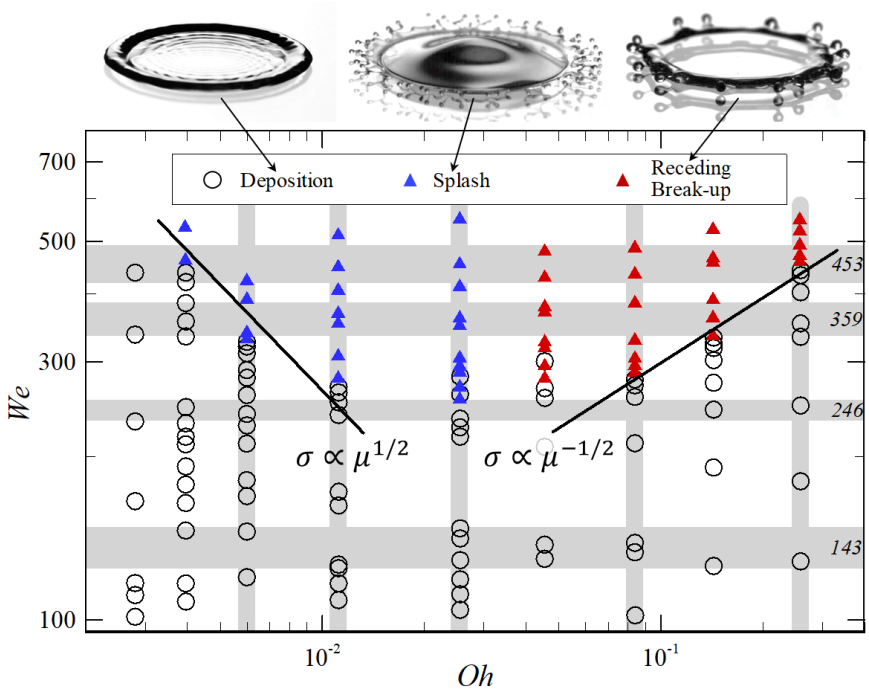

Figure 8-2 Regime nomogram of three impact patterns, namely the deposition, the splash, and the receding break-up, in the $Oh - We$ subspace of We and Oh. The experimental data are from the work [124].

8.1.1 Scaling Laws for Non-monotonic Droplet Splash on Liquid Viscosity

The promotion of droplet splashing by viscosity has been observed and interpreted in previous studies [230, 231, 239-241]. Figure 8.3(a) illustrates that droplet splashing is considered to occur when the stabilizing capillary pressure of the spreading liquid film, denoted as Σ_L, is surpassed by the destabilizing stress of the gas film, referred to

as Σ_G. The capillary pressure is expressed as $\Sigma_L = \sigma/d$, where the thickness d of the liquid film formed during the spreading process is approximated by $d \sim \sqrt{\mu t/\rho}$, based on previous studies [116, 240, 242]. On the other hand, the destabilizing stress is estimated as $\Sigma_G \sim \rho_g u_s u_e$ for air compressibility [116], which is related to the expanding velocity u_e, the gas density ρ_g and the sound speed u_s, but does not depend on the surface tension or viscosity of the liquid.

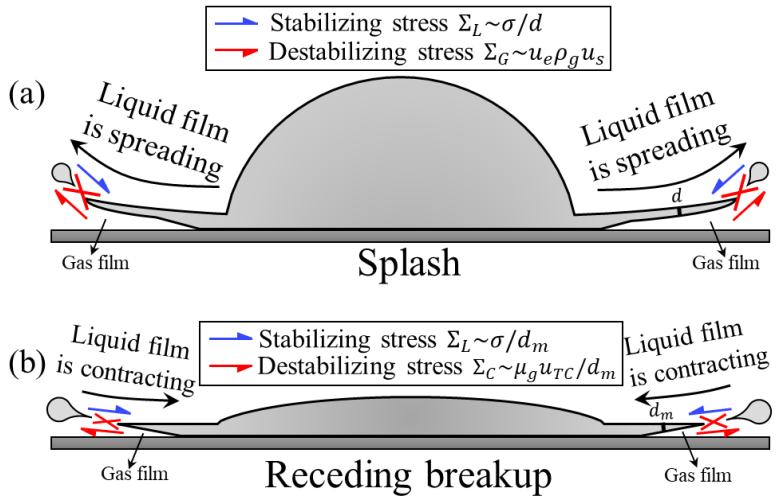

Figure 8-3 Schematic diagrams of a droplet splash (a) and receding breakup (b) on a smooth surface as their liquid film is spreading outwards and contracting inwards, respectively.

Secondary droplets detach from the parent liquid at the red cross when the destabilizing stress exceeds the stabilizing stress. By drawing an analogy with the "water hammer" phenomenon [243], an approximation of the expanding velocity is typically expressed as $u_e \sim \sqrt{DU/t}$ was usually used [116]. Hence, we can establish the critical condition for film disintegration as:

$$\frac{\sum_G}{\sum_L} \propto \mu^{1/2} \sigma^{-1} \propto We^{3/4} Oh^{1/2} \sim O(1) \tag{8.1}$$

This correlation indicates that droplet splashing becomes more likely with an increase in viscosity μ, as the destabilizing stress becomes stronger. Consequently, if we represent $\sigma \propto \mu^{1/2}$ within the parameter space of Weber number (We) and Ohnesorge number (Oh), as illustrated in Fig. 8.2, it is evident that this relationship effectively separates the experimental results in the low-Oh range into two distinct regimes: deposition and splash. This observation supports the earlier hypothesis that a low-viscosity liquid film is stabilized by surface tension, while also suggesting that a reduction in viscosity leads to a thinner and more unstable liquid film.

For high-viscosity liquids, experimental observations clearly indicate that film disintegration occurs during the retraction of the liquid film. While several mechanisms have been proposed to explain the breakup of tiny droplets from a retracting liquid rim [233, 234, 242, 244], we offer a qualitative interpretation based on force-balance analysis. As the liquid film retracts due to surface forces, the initial acceleration of the liquid rim is typically substantial until it reaches the equilibrium Taylor-Culick velocity.

Drawing inspiration from the findings [244], we can postulate that the breakup of droplets during retraction in the present experiments is influenced by surface-tension-driven Rayleigh Plateau instability. Consequently, the destabilizing stress is estimated as $\Sigma_C \sim \mu_g u_{TC}/d_m$, which accounts for the viscous drag force exerted by the gas film. Here, μ_g represents the viscosity of the gas, and $u_{TC} \sim \sqrt{\sigma/\rho d_m}$ denotes the Taylor-Culick velocity [245-247]. It is important to note that while d_m and d are comparable, they represent the thickness of the liquid film at different stages of the process.

As shown in Figure 8.3(b), it is thought that the liquid film begins to break apart when the destabilizing forces Σ_C surpass the stabilizing capillary pressure Σ_L. Consequently, the critical threshold for the film's disintegration can be described as follows:

$$\frac{\sum_C}{\sum_L} \propto \mu^{-1/4}\sigma^{-1/2} \propto We^{5/8}\, Oh^{-1/4} \sim O(1) \tag{8.2}$$

When we map the correlation $\sigma \propto \mu^{-1/2}$ within the $We - Oh$ space depicted in Fig. 8.2, the experimental data in the high-Oh range can be distinctly categorized into two regions: deposition and receding breakup. This observation suggests that as the liquid's viscosity increases, droplet breakup becomes more challenging. This is because higher viscosity decreases $u_{TC} \propto \mu^{-1/4}$, thereby reducing the destabilizing force $\Sigma_C \propto u_{TC}$. However, the viscosity must be sufficiently high to prevent splashing during the droplet's spreading phase. Notably, our splash criterion $\sum_C/\sum_L \sim \mu_g u_{TC}/\sigma$ for high-viscosity liquids shares a similar functional form with the approximate splash criterion proposed $\mu_g u_t/\sigma \propto constant$ [237]. In both cases, u_{TC} and u_t represents the velocity of the liquid film, though it is calculated differently. The scaling law for $We \propto Oh^{2/9}$ can be derived from Riboux and Gordillo's splash criterion in the high-Oh limit, and it closely aligns with our expression for $We \propto Oh^{2/5}$ from Eq. (8.2).

The above physical interpretations for the influence of liquid viscosity on the droplet splash are mostly phenomenological. Equations (8.1) and (8.2) cannot serve as predictive scaling laws because they lack a comprehensive set of dimensionless parameters necessary to fully capture flow similarity. To develop physically robust scaling laws, it is essential to analyze both the viscous liquid film and the underlying gas film. This comprehensive approach will be the focus of our future research.

8.1.2 Empirical Correlations for Splash Threshold

Earlier research [116, 123, 237, 248-251] has introduced numerous correlations for splashing, utilizing various combinations of parameters, such as Oh, We, and Re. Mundo et al. [248] gave the scaling law of $OhRe^{5/4} = 57.5$ for a viscosity dependence

($\propto \mu^{-1/4}$). As a result, it fails to capture the nonmonotonic effects of viscosity on droplet splashing. In Stevens' study [252] on droplet splashing under varying ambient pressures, two distinct regimes were identified, with the threshold pressure showing an inflection point as the impact velocity increased. Since Stevens' experiments only involved low-viscosity fluids, the parameters We and Re in her fitting formula consistently showed a positive correlation. In the theoretical model of drop splash by Riboux and Gordillo [237], the splashing criteria are categorized into low-Oh and high-Oh regimes, with the scaling relations being $t_{e,crit} \propto Re^{-1/2}$ and $t_{e,crit} \propto We^{-2/3}$, respectively, where $t_{e,crit}$ represents the dimensionless ejection time of the thin liquid sheet. This model implicitly confirms the nonmonotonic effects of viscosity and aligns with current experimental observations. Palacios et al. [249] introduced a splashing threshold as follows:

$$We = 5.8Re^{1/2} + 4.01 \times 10^{7} Re^{-1.97} \tag{8.3}$$

As the experimental liquids were confined to low-viscosity liquids, Eq. (8.3) exhibits deviations when applied for higher viscosity droplets.

A similar splash criterion was identified in [253] and it is expressed as

$$We/Re - 6762Re^{-3/2} = C \tag{8.4}$$

where the C is constant depending on surface wettability. It works well for $Re > 300$ but not from $Re \approx 2000$. Although they investigated a broad range of liquid viscosities ($1\sim100\ cSt$) ,there were few instances of splash or breakup for highly viscous droplets. This scarcity might be due to the infrequent occurrence of cases where the liquid viscosity exceeds a certain threshold of $10\ cSt$. Recently, Zhang et al. [254] experimentally found that increasing liquid viscosity can reduce the lifting angle of the liquid film, consistent with our observations regarding the wedged angle. Based on this, they adjusted the splashing angle and aerodynamic forces used in [237] and proposed

splash criteria for both low-viscosity ($Oh < 0.007$) and high-viscosity ($Oh > 0.007$) regions. These criteria were validated with experimental results within the range of $0.002 \lesssim Oh \lesssim 0.05$ and $400 \lesssim Re \lesssim 17000$. However, their maximum liquid viscosity was 25.1 mPa·s, which is about a quarter of the maximum viscosity used in our current study.

We propose a new semi-empirical correlation for deposition and splashing threshold as

$$We = 5Re^{1/2} + 10^4 Re^{-3/4} \tag{8.5}$$

where the data for receding breakup is considered equivalent to droplet splashing. It's important to note that the coefficients and exponents in Eq. (8.5) may vary slightly, as they are influenced by the properties of the ambient gas and the substrate. By comparing Eq. (8.5) with various experimental datasets and existing criteria from the literature[248, 249, 253, 255] in Fig. 8.4, we can gain further insights.

The current formula, Eq. (8.5), aligns well with both previous and current experimental data in the range of $Re = 200 - 20000$. In contrast, other formulas exhibit discrepancies and limitations, particularly in either the lower or higher Re regimes.

Palacios et al.'s formula [249], $5.75 = WeRe^{-1/2} = (ReOh^{4/3})^{3/2}$, agrees well for low viscosity droplets ($Oh < 0.01$), which is almost same with the splash criterion of $ReOh^{1.3} = 3.8$ at $Oh < 0.007$ given by Zhang et al. [254]. Interestingly, the combination of $ReOh^{4/3}$ can also been derived from the Eq. (13) in de Goede et al. [256], which is simplified from Riboux and Gordillo's splashing model [237] for low-Oh liquids, accompanied by the finding [254] that splashing angle's tangent is proportional to $\sqrt{\mu_g/\mu}\, Re^{-1/6}$. From Eq. (8.1), we can obtain the same exponents of We and Re as $\sqrt{\mu}/\sigma \propto \mathrm{We}Re^{-1/2}$. This boundary aligns with the relationship between

the first and second terms in Eq. (8.5), further supporting the notion that the current physical interpretation effectively captures the fundamental physics of splashing in low-viscosity droplets. While the threshold correlation in Eq. (8.3) by Palacios et al. [249] shares a similar form with our Eq. (8.5), it does not align with the high-viscosity data from Mundo et al. [248] or the present cases of receding breakup.

Mundo et al.'s formula [248] works for high-viscosity droplets ($Oh > 0.04$), $OhRe^{5/4}$ of which is reproduced by the splash criterion of Riboux and Gordillo [237] in the high-Oh limit under the condition $\sqrt{\rho\sigma D}\sim constant$. The present threshold splash Eq. (8.5) is close to the scaling $OhRe^{5/4}\sim constant$ for high viscosity liquids.

It is noted that the splashing of mercury droplets in Schmidt and Knauss [255], used by Mundo et al. [248] for supporting their splash criterion $57.7 = OhRe^{5/4}$, are distinctly non-gregarious compared to other liquids. This implies that additional factors, such as liquid volatility, might influence the impact behavior of mercury droplets.

It's important to note that threshold splashing data from various experiments show some moderate discrepancies in the transition region of $Oh = 0.01\sim0.0$, likely due to differing experimental conditions, especially surface roughness. The surface roughness in these experiments are listed here: 2.8 μm and 78 μm in Mundo et al. [248], $0.1\sim0.5$ nm in Palacios et al. [249], about $10nm$ in Almohammadi and Amirfazli [253] and Zhang et al. [254], and about $1nm$ in the present study.

The splashing threshold for droplets examined in this study falls within a moderate $We = 100\sim600$ range, distinguishing it from the transition from splashing to spreading observed at very high $We \approx 1000$. These latter scenarios typically happen when droplets impact at high velocity [253], where the thickness of the ejected liquid film becomes comparable to the mean free path of gas molecules, thereby suppressing splashing [257].

Thoraval et al. recently discovered that splashing can be suppressed at certain conditions (such as $We \approx 500$) due to the dispersion of silver nanoparticles. This likely affects non-Newtonian flow or the behavior of particle/liquid two-phase flows, necessitating additional parameters for accurate phenomenological characterization. In our current study, we utilized pure Newtonian fluids, specifically water-glycerol solutions, with only We and Oh as the varying parameters, while other parameters remained constant.

It is important to note that Eq. (8.5) is a practically useful semi-empirical formula that accounts for the effect of liquid viscosity on droplet impact at atmospheric pressure. However, it is not a rigorous scaling theory or a universal correlation for droplet splashing under varying ambient conditions [116, 252]. The impact of the surrounding gas, including its pressure and composition, cannot be fully captured within the current framework and is beyond the scope of this study. These factors will be addressed in our future research.

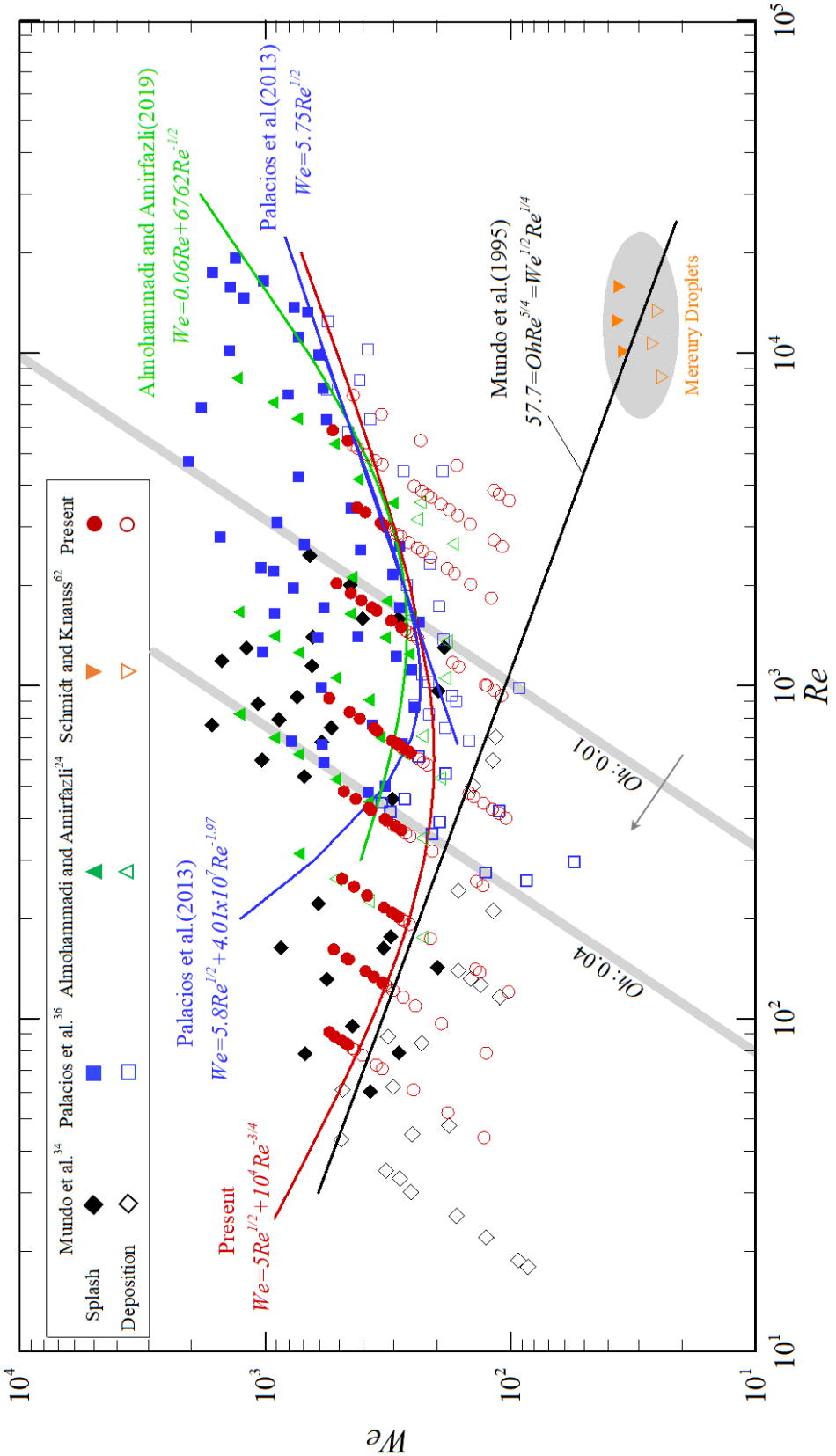

Figure 8-4 Comparison in the $We - Re$ plane between a few threshold correlations with experimental data [124, 248, 249, 253, 255].

8.2 Droplet Splash on a Smooth Heated Surface

Previous studies demonstrated that the wall temperature has significant influences on various outcomes of the droplet-wall interaction [127, 258, 259], but very little attention is paid to different splashing patterns on a heated smooth surface. Qin et al. [122] first explored the occurrence of different subpatterns of thin-sheet splash on unheated surfaces [121] can be observed on surfaces with high temperature, as shown in Fig. 8.5. Furthermore, regimes of five distinct outcomes (TSP2, TSP1, TSP3, deposition, and Leidenfrost breakup) for droplet impact in the parametric space of $We - T_{\mathrm{W}}$ were identified in Fig. 8.6. Comparing the regime maps of droplet impact on an unheated surface and a heated surface, they found that the distributions of thin-sheet splash patterns and deposition have some general features: the sufficiently high Oh or T_{W} can result in the vanishment of a splash; the higher We, the more likely a thin-sheet splash occurs; TSP3 usually occurs at a relatively higher We.

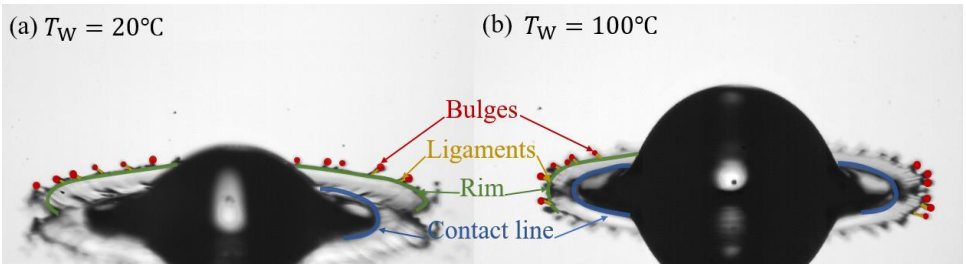

Figure 8-5 Comparison between the thin-sheet splash on (a) unheated and (b) heated surfaces. The experimental images come from the work [122].

Particularly, the deposition regime is neighbouring to the Leidenfrost breakup regime at relatively low We, but deposition does not occur for high We and TSP3 can directly transition into Leidenfrost breakup. The striking discontinuity was considered by Staat et al. [131] as a non-monotonic inflexion point for the critical splash of droplet impact because they regarded the Leidenfrost breakup as a special splash. For the three

subpatterns of the thin-sheet splash, the experimental results in Fig. 8.6 show that the TSP1/TSP3 transition is divided by a fixed We (about 530) and slightly different from Qin et al.'s observation [121], while the TSP2/TSP1 and TSP2/TSP3 transitions are both affected by We and T_W.

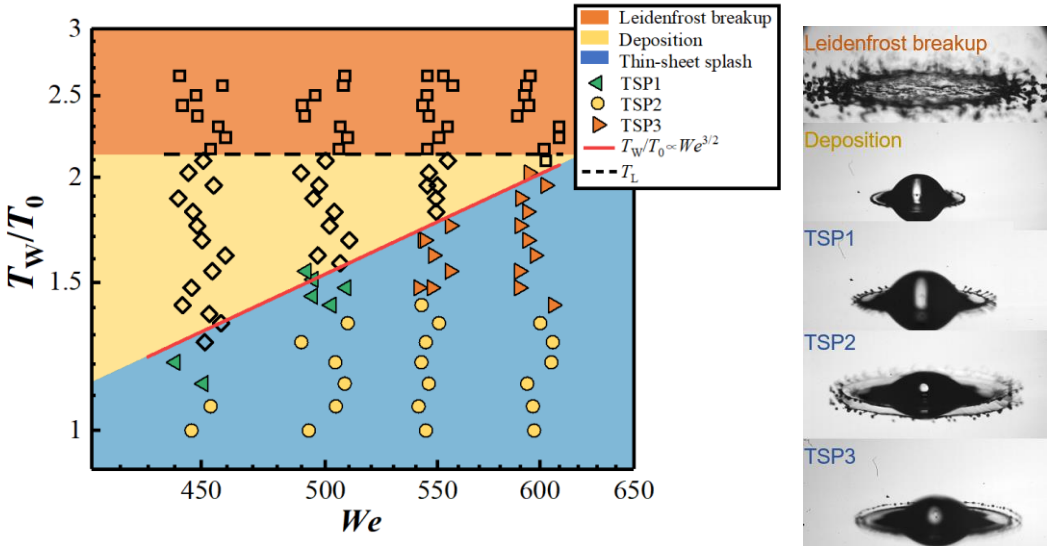

Figure 8-6 Phase diagram of five distinct outcomes (TSP2, TSP1, TSP3, deposition, and Leidenfrost breakup) for droplet impact in the space of $We - T_W$. The experimental data and images come from the work [122].

Consequently, according to the phase diagram of thin-sheet splash patterns, we attempt to interpret qualitatively those transitions by considering the influences of the preheated gas near the surface on the levitated lamella of droplets. The following will be focused on these transitions among TSP1, TSP2, and TSP3 by increasing We and T_W.

8.2.1 Transition from Thin-sheet Splash to Deposition

The thin-sheet splash of high-We droplet impact on smooth surfaces can transition into deposition by increasing T_W or decreasing We. It was reported previously that the

splash on a heated surface is considerably suppressed due to the change in the physical properties of both the liquid and the air[131]. Similarly, a recent study[260] suggested that the suppression of droplet splash on the heated surface is due to the near-wall air that has temperature-dependent gas viscosity. It is well known that splash can be weakened and even completely suppressed in a low-pressure gas [116]. Based on previous studies [261, 262], there are two competing stresses on the thin-sheet splash of the low-viscosity droplet impacting on a smooth surface: the destabilizing stress $\Sigma_{\mathrm{G}}\sim\rho_{\mathrm{G}}U_{\mathrm{G}}U_{\mathrm{e}}$ of the gas (ρ_{G} is the gas density; U_{G} is the speed sound in the gas; U_{e} is the expanding velocity of the thin sheet and can be approximated as $U_{\mathrm{e}}\sim\sqrt{DU/t}$) and the stabilizing stress $\Sigma_{\mathrm{L}}\sim\sigma/d$ due to the surface tension (d is the liquid film thickness and approximated as $\sqrt{\mu t/\rho}$).

Therefore, the threshold between droplet splash and deposition is given by the balance of these two stresses $\Sigma_{\mathrm{G}}/\Sigma_{\mathrm{L}}\sim1$ yielding

$$\frac{\rho_{\mathrm{G}}U_{\mathrm{G}}}{\rho U}We^{3/4}Oh^{1/2}\sim1 \tag{8.6}$$

which agrees well with the experimental data of Yang et al.[262] on a smooth surface at atmospheric pressure. It is noted that the critical condition of $\Sigma_{\mathrm{G}}/\Sigma_{\mathrm{L}}\sim1$ has been confirmed in the previous and present studies as it is about 0.45 for the unheated cases[116], 0.8 for the unheated and heated cases[131], $0.74-1.33$ for the heated cases[260], and around 1.6 for the data in this study.

By considering the dependence of ρ_{G} and U_{G} on the temperature, the scaling law can be generalized for the transition between thin-sheet splash and deposition on a heated smooth surface. We assumed that the gas temperature T_{G} nearby the heated wall is close to T_{W} because in the present experiment, a sufficient time (>1 minute) is given to heat the surface to a specified temperature. The density of the heated gas is

determined by the relation of $\rho_G = \rho_{G,0} T_0/T_G$, where the subscript 0 means the normal atmosphere condition ($\rho_{G,0} = 1.20$ kg/m^3 at $T_0 = 293$ K) Besides, the sound speed of gas depends on the temperature as $U_G = U_{G,0}\sqrt{T_G/T_0}$, where $U_{G,0}$ is 343.32 m/s. Therefore, we have a modified Eq. (8.6) by taking into account the temperature effects:

$$C\left(\frac{T_0}{T_G}\right)^{1/2} We^{3/4} Oh^{1/2} \sim 1 \tag{8.7}$$

where $C = \rho_{G,0} U_{G,0}/\rho U$ is about $0.16 - 0.19$ for the present experiments. By using the approximation of $T_G \approx T_W$, we obtain a scaling law for the threshold splash on the heated surface: $T_{W,cr}/T_0 \propto We^{3/2}$, which delimits very well the regimes of the thin-sheet splash and the deposition as shown in Fig. 8.7.

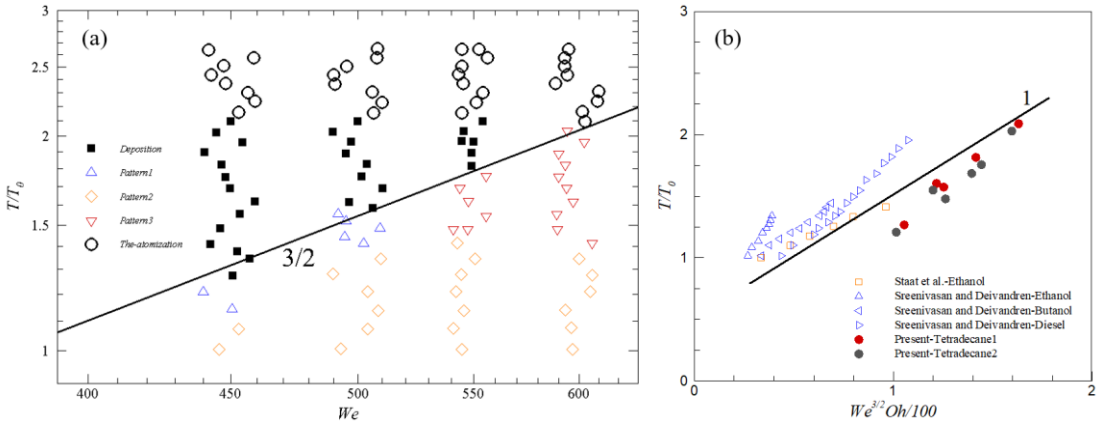

Figure 8-7 Comparison between the previous experimental data and the present scaling law of Eq. (8.7): (a) Data are from Fig. 8-6 and (b) Critical splash from Staat et al. [131], Sreenivasan and Deivandren [260], and Qin et al. [122].

To understand the scaling law in physics, the near-wall gas beneath the liquid thin sheet gets the heat transfer from the heated surface. The density ρ_G decreases and the sound speed U_G increases while their product $\rho_G U_G$ is proportional to $T_G^{-1/2}$. Therefore, the spreading thin sheet becomes more stable due to the smaller Σ_G caused by the temperature increase. Besides, the droplet surrounded by the heated gas suffers from

evaporation around the liquid surface, but our present results show that its influence seems to be insufficient for the transition from thin-sheet splash to deposition.

8.2.3 Transitions among Thin-sheet Splash by Increasing We and T_W

Many previous studies observed that the temperature difference between gas and liquid is a significant influencing factor for the threshold splash. However, the transitions among various splashing patterns induced by the temperature difference have not been illustrated yet. The schematic diagrams of three thin-sheet splash subpatterns (TSP1, TSP2, and TSP3) are presented respectively in Fig. 8.8(a-c).

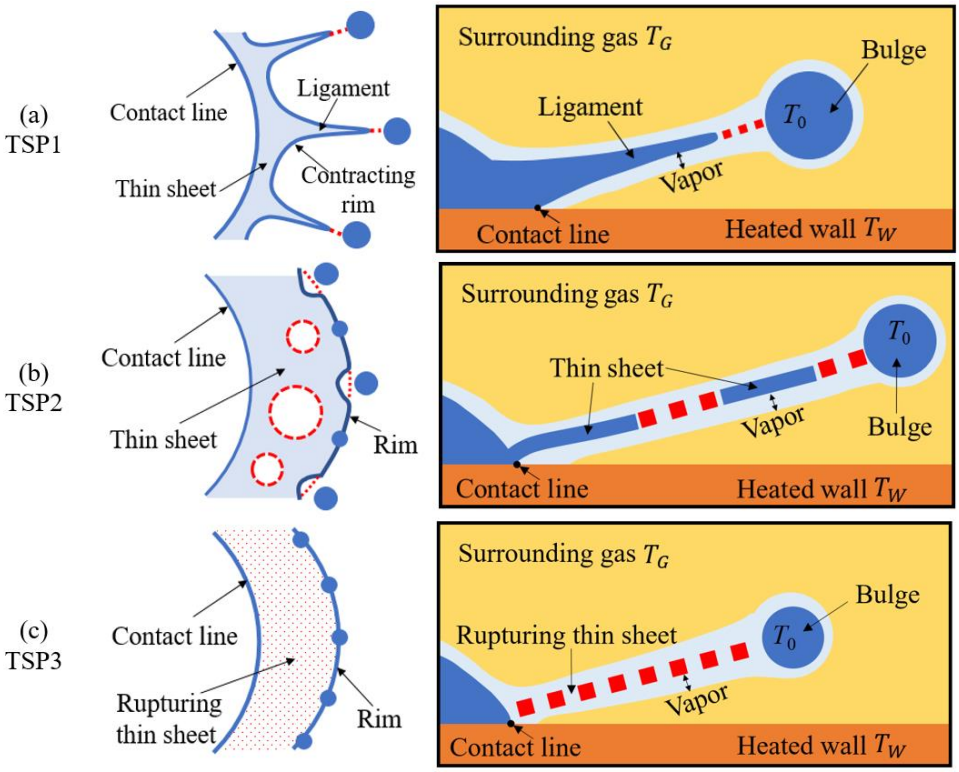

Figure 8-8 Schematic diagrams of three thin-sheet splash patterns, including (a) TSP1, (b) TSP2, and (c) TSP3 on the heated smooth surface. The surrounding gas has a temperature $T_G \approx T_W$ as the gas is very close to the surface and heated for a sufficient time.

Here, a basic fact should be noted that during the impact process on the heated surface, the droplet surface (its temperature is $T_0 = 20\,℃$) is heated up by the surrounding gas (temperature at $T_G \approx T_W$), and subsequently a vapor layer forms and covers the droplet. The thickness of the layer has the same order as that of the thin-sheet and the temperature of the layer is larger than T_0 but smaller than T_G. Therefore, the influences of the heated gas on different types of thin-sheet disintegration are illustrated qualitatively, in combination with our understanding of thin-sheet splash on the unheated surface.

First, the ligament breakup and the thin-sheet disintegration of TSP2 can be observed in the droplet impact with a high We and a relatively low T_W. Some broken holes in the thin sheet and grow-out droplets at the rim are clearly shown in Fig. 8.8(b). This means that the droplet inertia is highly predominant over the surface tension and the small influence of the gas temperature increase.

Second, on a slightly higher temperature surface ($T_W \approx 100℃$), TSP2 transitions into TSP1 with the ligament breakup at $We \approx 450 - 500$ or into TSP3 with the thin-sheet disintegration at $We \approx 550 - 600$. The splashing behaviours of TSP1 and TSP3 are completely different as shown by Fig. 8.8(a) and Fig. 8.8(c), respectively.

In the TSP2 regime, surface tension and inertia forces are comparable, and both can make the droplet splash. The heat transferred from the high-temperature surface to the near-wall gas causes the bifurcation of the TSP2 regime into the TSP1 regime for the surface-tension-driven ligament breakup, or into the TSP3 regime for the inertia-driven thin-sheet disintegration. The destabilizing stress $\Sigma_G \sim \rho_G U_G U_e$ increases with U but decreases with T_W, as $\rho_G C_G$ is proportional to $T_W^{-1/2}$ while U_e to $U^{1/2}$. The thin-sheet liquid tends to be stable on the heated surface while unstable at the high We (Σ_G is proportional to $\sqrt{U/T_W}$). For all thin-sheet splash, Σ_G is enough high over Σ_L to

cause the formation of secondary droplets. At relatively low U, Σ_G from the higher temperature gas is insufficiently strong to break the thin-sheet. Thus, the rim is pulled back to the contact line by the surface tension and secondary droplets are ejected due to the ligament breakup. In contrast, at relatively high U, Σ_G from the higher temperature gas is sufficiently strong to burst the thin-sheet liquid promptly. Thus, the rim flees outwardly from the thin sheet in an intact ring and finally breaks up into many secondary droplets.

8.3 Summary and Conclusions

This chapter includes two parts of droplet splash on surfaces:

In the first part, an experimental study of water-glycerol droplets impacting on a solid smooth surface at atmospheric pressure was conducted in the range of $Oh = 0.002\sim0.3$ and $We = 20\sim550$, with particular emphasis on clarifying the effects of viscosity on the splashing process. The most important observation in the experiment is the non-monotonic dependence of droplet disintegration (including droplet splash and receding breakup) on the liquid viscosity. The parametric characterization of the phenomenon is that, for intermediate *We*, the droplet splashing appears in the intermediate Oh but is absence at relatively small and large Oh.

To interpret the non-monotonic phenomenon, we adopted a perspective based on unbalanced forces acting on the liquid film. The splashing occurring in the small Oh range favors larger liquid viscosity because a less viscous liquid will cause a thinner liquid film and therefore a stronger stabilizing capillary force. The receding breakup occurring in the large Oh range favors smaller liquid viscosity (which however cannot be too small to cause droplet splash during the droplet spreading stage) because a larger viscosity will cause a smaller retraction velocity and hence a smaller destabilizing force

due to the viscous drag of gas film. Based on experimental observations, a new semi-empirical splashing correlation is proposed by fitting experimental data in a wide viscosity range. The underlying physics of droplet splashing, particularly the effect of ambient gas and pressure merits future investigation and validation.

In the second part, experimental observations reported that three subpatterns of thin-sheet splash (TSP1, TSP2, and TSP3) of tetradecane droplet impact on a heated smooth stainless-steel surface at varied surface temperature T_{W} and Weber number We are investigated. According to the experiment results [122], we conceptualized the phase diagram of TSP1, TSP2, and TSP3 in the three-parametric space $Oh - We - T_{\mathrm{W}}$. When T_{W} is increased, these subpatterns vanish and the impacting droplet just deposits due to the suppressing effect of near-wall gas. The transition of thin-sheet splash and deposition is delimited well by the scaling law of $T_{\mathrm{W,cr}}/T_0 \sim We^{3/2}$. When T_{W} is further increased to above the dynamics Leidenfrost temperature T_{L}, the impact outcomes transitions from deposition or TPS3 to Leidenfrost breakup. The transitions among different impact outcomes are qualitatively interpreted by considering the temperature-dependent physical properties of the near-wall gas heated by the hot surface.

The vapor layer on the droplet needs to be shown in detail. The above analysis hitherto has qualitatively accounted for the suppressing effect of the heated surface on the thin-sheet splash.

Chapter 9. Theoretical Model of Splash Threshold

In this chapter, two combinations, Π_L and Π_G, in four dimensionless numbers regime (Re, Oh, Kn and μ_G/μ_L) are utilized to characterize the threshold between deposition and splash of droplets impacting on a smooth solid surface. Based on hydrodynamics instability analysis (i.e., the Kelvin-Helmholtz and Rayleigh-Taylor instabilities), a scaling law of the splash threshold comprising both physical properties of the impacting liquid and the surrounding gas is derived from the balance between the thickness of the spreading liquid sheet and the most unstable wavelength of entrapping air film.

The correlation between $\Pi_L = Re^{1/2}Oh^2$ and $\Pi_G = (\mu_G/\mu_L)Kn^{-1}$ distinguishes out the disintegration of impacting droplets, which is verified by several sets of experimental data including the variance of ambient gases. Interestingly, we note there are some underlying influences of other factors, such as the capillary length of droplets, density ratio of the gas and liquid, and time ratio of the splash and the critical thin-sheet ejection on the splashing threshold.

9.1 Limitations of Current Splash Criteria

To facilitate comparison for splash criteria limitations, the undermentioned criteria of droplet splash are briefly summarized in Table 9-1. Before presenting the splash criteria, it is necessary to have a clear definition of the droplet splash, namely, the disintegration of a droplet resulting from the breakthrough of inertia upon the interfacial tension and the viscous stress. Therefore, the droplet splash directly depends on what characteristics the liquid has [103, 106], such as droplet diameter, D, liquid density, ρ_L, viscous force, μ_L, interfacial tension, σ, and impacting velocity, U. The early correlations were mostly formulated based on the three non-dimensional parameters of

impinging liquids: the Ohnesorge number $Oh = \mu_L/\sqrt{\rho_L \sigma D}$, the Reynold number$Re = \rho_L DU/\mu_L$ and the Webber number $We = \rho_L DU^2/\sigma$ [106].

Mundo et al. [248] empirically established the correlation $OhRe^{5/4} = K$ based on experimental results, where the constant $K \approx 57.7$ depends on the surface roughness, R_a. On the basis of empirical data for droplets impinging on a dry surface, Vander Wal et al. [251] proposed the splashing threshold of $\sqrt{Ca} = \sqrt{Re}Oh = 0.35$, where $Ca = U\mu_L/\sigma$ is the capillary number. Similarly, a power-law form of $OhRe^{\alpha} = const.$ has often been found to delineate the splash and non-splash regions on dry surfaces and the exponent α varies around 1 in different studies [263, 264].

However, the scaling law is no longer monotonous with the increase of liquid viscosities. Palacios et al. [249] reported that the critical We number of droplets splashing shows a non-monotonic trend as their fitting relation of $We = 5.8Re^{0.5} + 4.01 \times 10^7 Re^{-1.97}$ has a turnover point at about $Re = 1000$ among the 400~2000 range. Above the transitional region (Re~1000), the tensional force dominates the viscous force, while the opposite is true below that. For the drop splashing on surfaces with different wettability, Almohammadi and Amirfazli [253] proposed a similar criterion of $We/Re - 6762Re^{-3/2} = C$, where the constant C is about 0.06 and insignificantly related to the surface wettability. Also, they identified two distinct regions to characterize the nonmonotonicity of viscosity effect [253], which is similar to the inviscid and viscous models [240]. Xu [240] believed that the inertia force needs to break through the restraint of surface tension in the inviscid regime, while the viscosity plays a key role in the splashing of viscous droplets. Mandre & Brenner [117] interpreted the non-monotonic dependence of the splashing threshold on liquid viscosity as the viscosity could sufficiently affect the development of the boundary layer at the surface and make the thin sheet deflect. For the non-monotonic effect in a

wide range of liquid viscosities ($Oh\sim$ 10^{-3}-10^{-1}), Yang et al. [124] proposed a more applicable correlation and employed Kelvin-Helmholtz and Rayleigh-Taylor instabilities to qualitatively account for the trends of splash threshold in low and high viscous regions, respectively.

Physical properties of ambient gas, such as density ρ_G, viscosity μ_G, and pressure P, have been focused greatly, as Xu et al. [116] first pointed out that low pressures can suppress the occurrence of droplet splashing. They estimated two stresses (Σ_G and Σ_L) from the gas film and the liquid sheet respectively and found the boundary between the non-splashing and splashing data stays around $\Sigma_G/\Sigma_L = 0.45$ [116]. Rein and Delplanque [123] transformed the stress criterion into the correlation of $OhRe^{3/4} \approx 3.6$ and found the threshold is appropriate for low viscosity and smooth cases [265]. Later, Xu [240] experimentally reported the threshold pressures vary nonmonotonically with the liquid viscosity. Therefore, the compressible effect of ambient gas on the splashing is thought of as a pivotal role, as well as the physical characteristics of liquids, the droplet size, and the impacting velocity.

To reveal the underlying mechanism of droplet splashing, Liu et al. [250] experimentally illustrated that the ultrathin air film trapped under the expanding liquid front triggers splashing. Based on an assumption of a spatial "resonance" in length scales, they proposed a resonance mode of $k_m^{-1} = d$, that is, the length of the most unstable wave of the entrapped air film k_m^{-1}, obtained based on the K-H instability, may match the thickness of the liquid sheet d [250]. It should be noted that the splashing model was verified by their experimental data within the low-viscosity regime, but its feasibility for more viscous liquids needs to be further validated.

Table 9-1 Previous scaling laws of droplet splashing on solid surfaces.

No.	Authors	Parameters and Correlations	Ranges
1	Mundo et al. (1995)	Oh, Re; $OhRe^{5/4} = 57.7$	$20 < Re < 20000$ $0.3 < 10^3 Oh < 500$
2	Vander Wal et al. (2006)	Oh, Re; $OhRe^{1/2} = \sqrt{Ca} = 0.35$	$1 < 10^3 Re < 14$ $2 < 10^3 Oh < 22$
3	Palacios et al. (2013)	We, Re; $We = 5.8Re^{0.5} + 4.01 \times 10^7 Re^{-1.97}$	$0.4 < 10^3 Re < 20$ $2 < 10^3 Oh < 41$
4	Almohammadi & Amirfazli (2019)	We, Re; $WeRe^{0.5} \sim const.$ for $Re < 2000$ $We/Re \sim const.$ for $Re > 2000$	$300 < Re < 10000$ $300 < We < 700$
5	Yang et al. (2021)	We, Re; $We = 5Re^{0.5} + 10^4 Re^{-0.75}$	$40 < Re < 7500$ $2 < 10^3 Oh < 300$
6	Xu et al. (2005)	P, U, σ, ν_L; $\Sigma_G/\Sigma_L \sim P\sqrt{\gamma M_G D U \nu_L / 4k_B T}/\sigma \approx 0.45$	$U > U^* \approx 2m/s$
7	Liu et al. (2015)	k_m^{-1}, d; $k_m^{-1} = d$	Low Oh region
8*	Stevens (2014)	Kn,We, Re $We^{1.5}/(Re^{1.1}Kn^{0.5}) \approx 140$ at low U $We^{0.2}/(Kn^{0.5}Re^{0.35}) \approx 28$ at high U	low viscosity region
9#	Riboux & Gordillo (2014)	μ_L/μ_G, Oh, Re; $\mu_L/\mu_G \propto (ReOh_G^{8/5})^{-\alpha}$, $\alpha = 1$ and $5/4$ for low and high Oh limits	$10 < \mu_L/\mu_G < 1000$ $0.1 < 10^3 ReOh_G^{8/5} < 10$
10+	Riboux & Gordillo (2017)	μ_L/μ_G, Oh, Re; $\mu_L/\mu_G \propto (ReOh_G^{8/5})^{-1}$ and $(ReOh_G^{12/7})^{-7/6}$ for low and high Oh limits	$Re^{1/6}Oh^{2/3} > 0.28$ $Re^{1/6}Oh^{2/3} < 0.28$

*The mean free path of gas and the droplet diameter are substituted by $\boldsymbol{Kn}$.

#The radius of the droplet is used as the characteristic length in $\boldsymbol{Oh_G = (\mu_G/\mu_L)Oh}$.

+The criterion for high oh is deduced by new $\boldsymbol{\tau_e}$ approximation.

In terms of the relation between the mean free path λ and the pressure P, Stevens [252] used the Knudsen number $Kn = \lambda/D$ to consider the effect of the gas pressure and specie. For the critical boundaries of splash, the combination of Re, We, and Kn

was found to exhibit a good collapse of all data under different ambient conditions [252]. Therefore, Kn has been used widely in modelling the droplet splash under various ambient conditions. Besides, the gas viscosity was found to play an important role in the droplet splashing. Riboux and Gordillo [237] used the ratio of the liquid and gas viscosities μ_L/μ_G to reflect the aerodynamic effect in the theoretical model (refer to R&G model). It should be noted that their splash criteria were divided by high-Oh and low-Oh limits for approximation and simplification. However, the two limits' scope was not given and explained. Subsequently, they noted the influence of boundary-layer on the ejection time in the droplet splashing and improved the two scaling relations of τ_e in Oh limits [266]. In their new criteria, the ejection time τ_e, is proportionable to $Re^{-1/3}$ and $Re^{-4/3}Oh^{-4/3} = We^{-2/3}$ in the regions of $Re^{1/6}Oh^{2/3}$ larger and smaller than 0.28, respectively.

9.2 Theoretical Modeling on Splash Criteria

In many previous studies, either their valid scopes are limited, or they are expressed in piecewise approximations. The predicament may mainly result from the nonmonotonic effect of liquid viscosity and the influence of the surrounding gas, which need to be settled in a multiple-parameters phase space. The most challenging is how to present a multiple-parameter-relied scaling law replying in a two-dimensional space. A unified splash criterion performing well in a wide viscosity regime merits further study. In this work, the key features of droplets splashing on a dry and smooth wall will be first illustrated and clarified. Then, two combinations of multiple dimensionless numbers for the splashing criterion will be derived from the analyses of K-H instability. Finally, the new criterion will be validated by experimental data in the literature and discussed with its merits.

To acquire a unified scaling law of droplet splashing, its physical process should be depicted clearly. Extensive studies have attempted to elucidate the droplet impact on a surface. The phenomenon of the droplet/wall impact is perplexing due to the complicated interplay among the liquid droplet, the surrounding gas, and the solid surface [106, 267]. As a droplet spreads on the smooth wall, as shown in Fig. 9.1(a), the liquid lamella is formed subsequently and affects the impact outcome, such as deposition, bounce-off, and self-separation. Fig. 9.1(b) shows that the front of the liquid lamella detaches from the surface to form the air entrainment, that is, a gas film is filled with the liquid /solid gap as shown in the zoom sketch of Fig. 9.1.

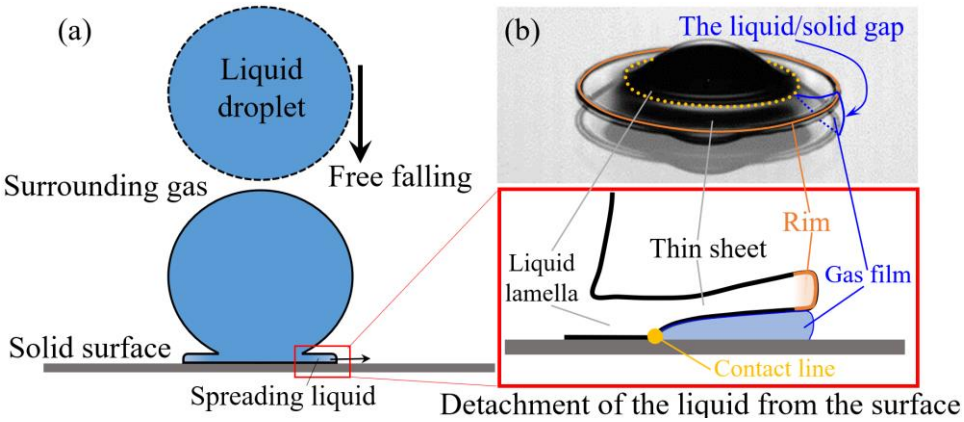

Figure 9-1 (a) Schematic diagram of a droplet impacting on a solid surface. (b) Snapshot of the spreading droplet [124]. The zoom sketch for the front of liquid lamella surfing on the gas film.

The lamella detachment is a precursory process for the formation of secondary droplets, while it is a necessary condition but not a sufficient condition for the occurrence of droplet splash. In previous experimental observations [237, 268], the lamella could also detach at the front and then reattach to the surface, instead of splitting out a liquid globule, when the impacting velocity or the ambient pressure is slightly below the threshold value.

9.2.1 Effects of Air Entrainment on Droplet Splash

Previous studies [123, 237, 269] noticed a similar scenario in the spreading liquid lifts off the surface, as sketched in Fig. 9.1. Specifically, the liquid lamella wets outwardly the surface, and a thin sheet can protrude partially from the lamella [125, 239, 268]. As a result, the thin sheet levitates in the gas so that a gas film is entrapped beneath [250]. The detaching behavior, also called the de-wetting by Riboux and Gordillo [237], leads to a dynamics three-phase contact line [118, 270], of which moving velocity is closely related to the critical velocity for air entrainment in dynamic wetting of coating flow [123]. Therefore, the focus of this study is the rupture of the thin sheet, which finally causes the droplet disintegration at the rim (i.e., the droplet splashing), without considering that the early-stage process of droplet impact may affect the formation of the thin sheet.

Although the splash criterion can be characterized by the balance of stresses or the ratio of length scales from the liquid and gas, respectively, there are few attempts to correlate it with the fundamental parameters, such Oh, Re, μ_L/μ_G, etc. For the effects of liquids, a splash criterion can be characterized by Oh, Re, or their combinations based on the surface tension, the viscous force, and the inertial force. Regarding the effects of ambient gas, the pressure plays a crucial role in the droplet impact, but there are no unified parameters to normalize it. Mandre et al. [271] introduced a compressibility parameter for the gas effect in the precursory process of droplet splash, where the ambient pressure is normalized by four parameters ρ_L, U, D and μ_G. Interestingly, Driscoll et al. [125] scaled the pressure of ambient gas to universally collapse experimental data by the parameters μ_L/ρ_L, U and M_G, while the five μ_L, D, ρ_L, σ and M_G were used in Stevens [252]. However, Zhang et al. [272] found μ_G correlates with the splashing threshold of drop impact into a deep pool, but not ρ_G. To

estimate the gas effect, a new Webber number We_λ was defined by replacing the droplet diameter by the mean free path λ, a length scale associated with the ambient pressure [257, 266, 273]. Thus, it is rather necessary to figure out representative parameters of the gas effect in droplet splashing.

9.2.2 Instability Analyses for Splash Criteria

In this work, the physical picture of a droplet splashing on the solid substrate is basically depicted in Figure 3. The instability model of the ejected liquid lamella and the ultra-thin gas film is adopted here. Therefore, to splash or not (i.e., whether the rim of liquid lamella is pinched off) is determined by the scale ratio between the thickness of liquid lamella d, proportional to the viscous length $\sqrt{\mu_L t/\rho_L}$ [274], and the length of the gas film, inverse to the most unstable wavenumber k_m. We believe the resonant undulation leads to the shed-off of secondary drop at the rim of liquid lamella, as depicted by the dash lines.

Firstly, we apply the relation for the wavenumber of the fastest-growing mode, $k_m \sim \Sigma_G/\sigma$, in KH instability [240, 250], where Σ_G denotes the destabilizing stress from the ambient gas. Similar to the development of the boundary layer, the diffusion of vorticity affects the thickness of liquid lamella d during the spreading. Eggers et al. [242] used the approximation of $d \sim \sqrt{\mu_L t/\rho_L}$. Hereto, we have

$$\frac{d}{k_m^{-1}} \sim \Sigma_G \sqrt{\frac{t}{\rho_L}} \frac{\sqrt{\mu_L}}{\sigma} = \Sigma_G \sqrt{\frac{t}{\rho_L}} \frac{We^{3/4} Oh^{1/2}}{\sqrt{\rho_L D U^3}} \tag{9.1}$$

After plugging the estimation of $\Sigma_G = \rho_G c U_e/\sqrt{2\pi\gamma}$ [116] into Eq. (9.1), we have

$$\frac{d}{k_m^{-1}} \sim \frac{1}{\sqrt{2\pi\gamma}} \frac{\rho_G c}{\rho_L U} \sqrt{\frac{U_e t}{D} \frac{U_e}{U}} We^{3/4} Oh^{1/2} \sim O(1) \tag{9.2}$$

where c is the sound speed of the ambient gas, γ is the adiabatic constant, and U_e is the expanding velocity of the ejected liquid lamella.

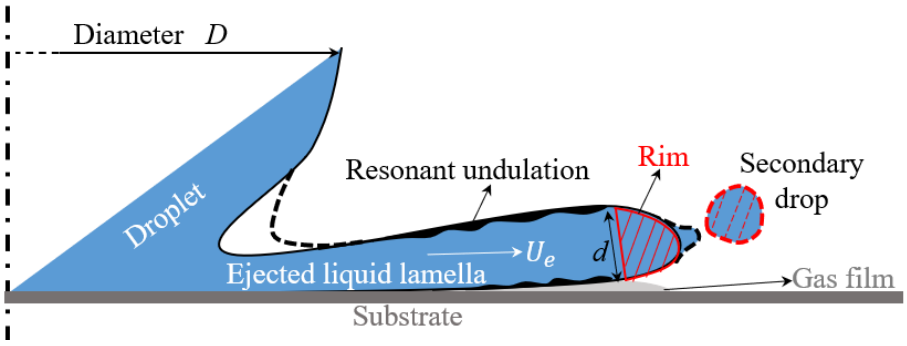

Figure 9-2 Schematic diagram of the interaction between the liquid lamella and the gas film on a smooth substrate (the prototype of our physical mode is inspired by Fig. 4(a) in Riboux & Gordillo [237] and Fig. 2(d) in Liu et al. [250]). The solid lines denote the onset of droplet splash, and the dashed lines denote the formation of secondary drop at t_{sp} succeeded by the resonance of the liquid and the gas.

Assuming the similarity of the droplet impact with the "water hammer" impact, Xu et al. [116] approximated $U_e \sim \sqrt{DU/t}$. We accept the assumption here and set $\Phi = \sqrt{(U_e t/D)(U_e/U)}$ as $O(1)$. This simplification is admissible for the study and we will quantitatively evaluate it later. Besides, considering the speed of sound in an ideal gas, if we put $c = \sqrt{\gamma kT/m_G}$ into Eq. (9.2), we have

$$\frac{1}{4}\frac{\rho_G \bar{U}_G}{\rho_L U} We^{3/4} Oh^{1/2} \sim O(1) \tag{9.3}$$

where γ is the adiabatic index; k is the Boltzmann constant; T and m_G are the temperature and the single molecular weight of ambient gas, respectively; $\bar{U}_G = \sqrt{8kT/\pi m_G}$ is the average speed of a gas molecule. In this way, the ratio $\eta = \rho_G \bar{U}_G / \rho_L U$ represents the momentum relationship of the free-falling droplet and expelled gas with the same volume, calculated about $1/3$ (refer to the $1\ mm$ ethanol

droplet with $2.19m/s$ threshold velocity at atmosphere condition in Fig. 1 of Riboux & Gordillo [237]). Actually, $\eta/4$ in Eq. (9.3) is close to $(1/3.6)^2$, where 3.6 is the derived constant in Rein and Delplanque [123].

However, η will decrease at sub-atmospheric pressures due to the lower gas density but higher threshold velocity. In view of the importance of ambient pressure, our derivation should have it explicitly. Therefore, we put $c = \sqrt{\gamma P/\rho_G}$ into Eq. (9.2)

$$\frac{1}{\sqrt{2\pi}}\eta' We^{3/4} Oh^{1/2} \sim O(1) \tag{9.4}$$

where $\eta' = \sqrt{(P/\rho_L U^2)(\rho_G/\rho_L)}$ contains the scale of the gas pressure and the droplet's kinetic energy per unit volume, as well as the density ratio of the ambient gas to the impacting liquid. Driscoll et al. [268] studied the former and found that the threshold pressure is almost fixed when the kinetic energy is above a threshold value. The latter is not only related to the ambient pressure and temperature, but also is determined by gas components (i.e., the molecular weight). Those relations are consistent with experimental results in Xu et al. [116].

Equations (9.3) and (9.4) both confirm that the physical properties of ambient gas should be involved in modelling the droplet splash, in other words, the competition between the pressure of ambient gas and the impacting kinetic energy of the droplet must be seriously taken account of the formulating of a splash criterion. Combined with the ideal gas law, $P = \rho_G RT/M_G$, η is transferred into $(P\sqrt{M_G}/U)/(\rho_L\sqrt{RT})$, where R is the ideal gas constant, and M_G is the molecular weight of ambient gas. The numerator term was first validated by the experimental results of Xu et al. [116], but they ignored the liquid density because all experimental drops are alcohols with a similar density. This issue was found by Driscoll et al. [268] and Stevens [252], however, the inconsistency of their pressure-scaled parameters owes to that they were

not able to peel the gas effect with that of the droplet itself. Even in the R&G model [237], the pressure effect was hinted in the lubrication coefficients, $K_l = f(\alpha, \lambda, D, t_e)$, where the wedge angle α~60° is confirmed by De Goede et al. [256] but asserted not suitable for high-Oh liquids [254]. Gordillo & Riboux [273]attempted to simplify the unfathomable expression of K_l in two functions of We_λ.

There is no doubt that the pressure effect should be manifested in a splash criterion, as we discuss above. Meanwhile, we note that the pressure is straight associated with the mean free path of gas [275], expressed as $P = (\mu_G/\lambda)\sqrt{RT/2M_G}$. Therefore, by means of the relation of the gas viscosity $\mu_G = \lambda\rho_G c\sqrt{2/\pi\gamma}$ in kinetic theory, the length scale of the Knudsen number $Kn = \lambda/D$ [252], and the viscosity ratio between the gas and the liquid μ_G/μ_L [237], Eq. (9.2) can be rewritten as

$$\frac{1}{2}\underbrace{(D/\lambda)(\mu_G/\mu_L)}_{\Pi_G}\Phi\underbrace{Re^{-1}We^{3/4}Oh^{1/2}}_{\Pi_L} \sim O(1) \tag{9.5}$$

where an additional Re^{-1} is obtained due to Kn and μ_G/μ_L. Consequently, we define two new dimensionless combinations $\Pi_G = (\mu_G/\mu_L)Kn^{-1}$ and $\Pi_L = Re^{-1}We^{3/4}Oh^{1/2} = Re^{1/2}Oh^2$ to discuss the impacts of gas and liquid phases on the threshold splash, respectively. Besides the term Φ, related to the splashing time t_{sp} and the expanding velocity U_e, will be illustrated in the next section.

Secondly, we try to analyze, for instance, the suitability of R-T instability for the mechanism of droplet splashing. Xu [240] mentioned that R-T instability could not respond appreciably to different gas pressures. Yoon et al. [232] reported the R-T theory failed to explain some observations under conditions of low air density as well as the droplet-pool impact of equal-density fluid. However, it was used to account reasonably for the viscous effect in high-Oh region in the normal atmosphere [124]. Here, we accomplish a brief discussion mainly focusing on the effects of high liquid viscosity on

receding break-up behavior. According to Yang et al.'s hypothesis [124], the outer rim breaks up as the thickness of ejected liquid lamella, d, is comparable with the reciprocal of the wavenumber of the most dangerous R-T mode $k_{m,RT}^{-1}$, that is

$$\frac{d}{k_{m,RT}^{-1}} \sim d\sqrt{\frac{\rho_L a(1-\rho_G/\rho_L)}{\sigma}} \sim O(1) \tag{9.6}$$

where a is the acceleration of the interface from gas to liquid and the density ratio $\rho_G/\rho_L \ll 1$ is small enough to be neglected. We estimate the acceleration by $a \sim u_{TC}/t_{TC}$, where $u_{TC} = \sqrt{2\sigma/\rho_L d}$ is the Taylor-Culick velocity and $t_{TC} = \mu_L d/2\sigma$ is the viscous relation time to achieve the velocity u_{TC} [246]. Consequently, we have

$$a \sim \sqrt{8} d^{-3/2} \sigma^{3/2} \rho_L^{-1/2} \mu_L^{-1} \tag{9.7}$$

Substituting Eq. (9.7) and $d \sim \sqrt{\mu_L t_m/\rho_L}$ into Eq. (9.6), we get

$$\frac{d}{k_{m,RT}^{-1}} \sim (8\sqrt{\rho_L t_m}\sigma/\mu_L^{3/2})^{1/4} = 8^{1/4}(Ut_m/D)^{1/8}(WeOh^6)^{-1/16} \tag{9.8}$$

where t_m means the break-up time when the liquid lamella spreads to the maximum. The normalized time $\tau_{max} = Ut_m/D$ approximates to 4 and 2 for low-Oh and high-Oh liquids respectively, as reported in [276].

As we neglect the small-term ρ_G/ρ_L, there are no variables relative to the gas effect in Eq. (9.8). Actually, the density ratio is a useful correction factor for the splash criterion, as shown later. It should be noted that the group of $WeOh^6$ reflecting the liquid part of droplet splash is the biquadrate of Π_L. Intriguingly, the group of $Re^{1/6}Oh^{2/3}$ used in Riboux and Gordillo [266], of which the value is equal to 0.25 for identifying the effect of the boundary layer, is the cube root of Π_L. Moreover, the Riboux and Gordillo's point $Re^{1/6}Oh^{2/3} = 0.28$ locates in the transition between low- and high-viscosity regions, spanning $350 < Re < 1600$ and $1 < 100Oh < 4$ as shown in Yang et al. [124].

In this section, four parts have been studied mainly. First, the precursory process of the formation of secondary droplets, the take-off of the thin sheet, is described in detail. Then, we emphasize the importance of air entrainment on droplet splashing and realize that it is the precondition of modelling the splash criterion. Intuitively, we accept the assumption that the length scales of the liquid lamella and the gas film are comparable. Next, a correlation of splashing criterion consisted of Π_L and Π_G of four dimensionless numbers (Re, Oh, Kn and μ_G/μ_L) as well as ε, is derived based on the K-H instability. Last, the R-T theory comes out Π_L, ρ_G/ρ_L and τ_{max}, although the order of the second term is $O(10^{-3})$ for most liquids in the air, and the last term is estimated roughly as a constant of around 3.

9.3. Validation of Present Splash Criterion

It is well known that the droplet impact involves the complicated dynamics among three-phase mediums: the liquid droplet, the surrounding gas, and the solid surface. By investigating the effects of surface roughness and gas pressure, Xu [240]and Latka et al. [125] both pointed out that the compressible effect on droplet splash might be contaminated by nonzero roughness surfaces. Previous studies also have found that the properties of solid surfaces, such as the heating [121, 122], stiffness [277], and wettability [278, 279], affect the outcomes from a drop impact. However, many recent studies [119, 132, 254, 280, 281] have reported that some basic mechanisms or empirical correlations could be effectively utilized to account for the droplet splashing in more complex situations.

Although the study pays great attention to some physical mechanisms of the droplet splashing on a dry, smooth, and rigid surface in the isothermal condition, many forward-looking insights provided here, we suppose, are conducive to future studies.

Next, we will focus influences of those terms ε, Π_L and Π_G in Eq. (9.5) as well as ρ_G/ρ_L in Eq. (9.8) on the droplet splashing. Particularly, a regime on the ground of the two combinations Π_L and Π_G will be validated and clarified with experimental results of the splash threshold.

9.3.1 Analysis of the Characteristic Times on Droplet Splash

Following the "water hammer" assumption, the order of $\Phi = \sqrt{(U_e t/D)(U_e/U)}$ is $O(1)$. To precisely simplify it, the ejection velocity U_e should be formulated first. As our physical picture is developed from the R&G model [237], here we resort to the estimation of liquid lamella velocity, $U_e \cong \sqrt{3}U\tau_e^{-1/2}/2$. Therefore, Φ can be approximated to $\sqrt{3(Ut_{sp}/D)/4\tau_{e,crit}} = \sqrt{3\tau_{sp}/4\tau_{e,crit}}$, where t_{sp} denotes the moment of droplet splashing and $\tau_{e,crit} = Ut_e/D$ is the critical time for sheet ejection, which is calculated from

$$c_1 Re^{-1}\tau_e^{-1/2} + \sqrt{2}Re^{-2}Oh^{-2} = c^2\tau_e^{3/2} \tag{9.9}$$

where $c_1 = \sqrt{3}/2$ and $c^2 = 2.42$ are constants adjusted experimentally. For a high or low viscous droplet splash, the time ratio $t_{sp}/t_{e,crit}$ was measured experimentally 5 (referring to the Fig.4 in De Goede et al. [256]) or about 3 (referring to the Fig. 4 in Zhang et al. [254]). Thus, Φ can be valued at $1\sim2$, which is the order of 1 and agrees with the assumption used above. In a general way, Eq. (9.5) based on the K-H instability can get rid of the characteristic time, besides τ_{max}, a time value of $O(1)$ estamated above, in Eq. (9.8) based on the R-T instability.

Alternatively, based on the threshold condition that the vertical lift force F_G, imparted by the gas on the rim, just breaks through the interfacial tension, Riboux & Gordillo [237] formulated the splash criterion as

$$\beta = \sqrt{F_G/2\sigma} \simeq 0.14;\ F_G = K_l \mu_G U_e + K_u \rho_G U_e^2 d \tag{9.10}$$

where K_l and K_u are lubrication and suction coefficients, respectively; the velocity and thickness of the liquid lamella are calculated as $U_e \cong \sqrt{3}/2 U \tau_{e,crit}^{-1/2}$ and $d \cong \sqrt{3} D/\pi \tau_{e,crit}^{3/2}$.

Although the criterion of Eq (9.10) is widely verified for the splash condition, it still needs to be solved numerically in combination with Eq (9.9). To obtain power law expressions, Eq. (9.10) is approximated as $(\mu_G U/\sigma)\tau_{e,crit}^{-1/2} \propto const$ under two simplified conditions that the lubrication force $K_l \mu_G U_e$ is dominant and the lubrication coefficient is approximately constant. Besides, $\tau_e \propto Re^{-1/2}$ and $\tau_e \propto Re^{-4/3} Oh^{-4/3}$ are the reduced form of Eq. (9.9) in high-Oh and low-Oh limits respectively, when the diffusion effect (the first term in LHS) is leading or else the capillary pressure (the second term in LHS) for the ejection of thin sheet. Some previous studies [254, 256] have attempted to simplify and promote it. Besides, it should be noted that $\tau_{e,crit}$ has been identified as a function of Re and Oh in the R&G model [237] as well as the ambient pressure [239, 268]. Also, the instability onset, closely relative with τ_{sp}, was proportional to μ_L/P^2 [230]. To examine whether $\Phi \approx \sqrt{\tau_{sp}/\tau_{e,crit}}$ could be estimated $O(1)$ under different pressure conditions merits future study.

The approximate splash criteria listed in No. 9 of Table 9-1 are well acknowledged and facilitated to use, where Oh_G is defined as $\mu_G/\sqrt{\rho_L \sigma D} = (\mu_G/\mu_L)Oh$. Comparing the criteria with several experimental results, in Fig. 9.3, it is easy to note that the mathematical approximations of Eq. (9.9) work well in the two Oh limits but not in the intermediate region. Although the prediction of the criteria is not bad in the wide range of $-5 < \log_{10} ReOh_G^{8/5} < -2$, there is no clear border between the low and high limits. Later, a critical point of $Re^{1/6} Oh^{2/3} = 0.28$ is derived from boundary-layer effects in

droplet splashing in Riboux and Gordillo [266]. However, their criteria, as listed in No. 10 of Table 9-1, are still piecewise and cannot be unified in a regime nomogram of the normalized viscosity, μ_L/μ_G, versus a characteristic group of Re and Oh_G.

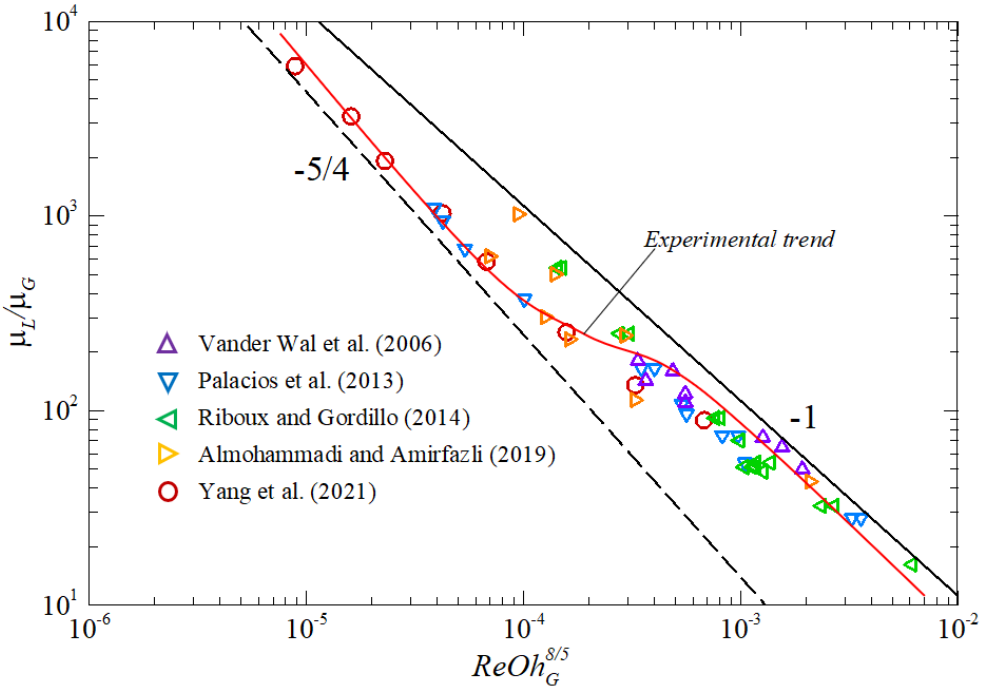

Figure 9-3 Comparison of the splash criteria with experimental data of splash threshold under atmospheric conditions. The red curve basically outlines the trend of those experiment results. The solid line denotes $\mu_L/\mu_G \propto (ReOh_G^{8/5})^{-1}$for low Oh liquids, while the dashed line denotes $\mu_L/\mu_G \propto (ReOh_G^{8/5})^{-5/4}$ for high Oh liquids. Experimental conditions of droplet splash refer to Table 9-2.

In Figure 9.3, the same experimental data in the regime of $\Pi_G = (\mu_G/\mu_L)Kn^{-1}$ and $\Pi_L = Re^{1/2}Oh^2$ are aligned along the correlation, $\Pi_G{\Pi_L}^{3/4} \approx 4$. The splash threshold region, coloured by the grading orange, directly delimits the boundary of splash (the top right side) and deposition (the down left side) in a wide Oh range. The nonmonotonic-viscosity transition region ($0.4 < 100\Pi_L < 3$), coloured by the grey, contains the R&G point and separates low- and high-Oh regions. As the core task of

this study, the dimensionless groups Π_G and Π_L are first found based on instability analyses and proposed to be responsible for the contributions of the gas and the liquid to the droplet splashing, respectively.

Table 9-2 Basic information of previous experiments.

Experiment	Symbol	Liquid	Gas	Substrate material	Surface roughness
Vander et al.	△	water,methanol,ethanol,butanol, n-propanol,heptane,nonane, decane,dodecane,tetradecane, hexadecane,glycerol-water,	Normal atmosphere(air and 101 kPa)	aluminum	<10nm
Palacios et al.	▽	glycerol-water mixtures, water, methanol, ethanol,butanol, isopropanol		glass	0.1~0.5nm
Riboux & Gordillo	◁	acetone,water,methanol,ethanol,decamethyltetrasiloxane,dodecamethylpentasiloxane,polydimethylsiloxane,silicone oil		galss	---
Almohammadi & Amirfazli	▷	water,glycerol-water mixtures silicone oils		glass, PMMA, teflon	~10nm
Yang et al.	○	water,glycerol-water mixtures		PDMS	1.04nm
Xu et al.	■	methanol,ethanol,2-propanol	He,air, Kr,SF_6 < 101 kPa	glass	----
Stevens	◆	ethanol,fluorinert, glycerol-water mixtures,siliconeoils	He,air, SF_6	glass	~5nm

Particularly, the coordinates of our splash criterion are seemingly similar but different with μ_L/μ_G and $ReOh_G^{8/5}$ obtained from the mathematical approximation of Eq. (9.9). More details refer to Appendix III. Taking two examples of Palacios et al. [249] and Yang et al. [124] in Fig. 9.3 and Fig. 9.4, the data of the two groups follow the same trend with different scaling laws for low and high viscosity liquids, while they both agree with our correlation. The good performance of the scaling law $\Pi_G \sim {\Pi_L}^{-3/4}$ indicates that our theory is capable of modelling the critical condition for droplet

splashing on a solid surface, although ambient conditions of experimental data referred to in Fig. 9.3 and Fig. 9.4 are air at the atmospheric pressure and the room temperature.

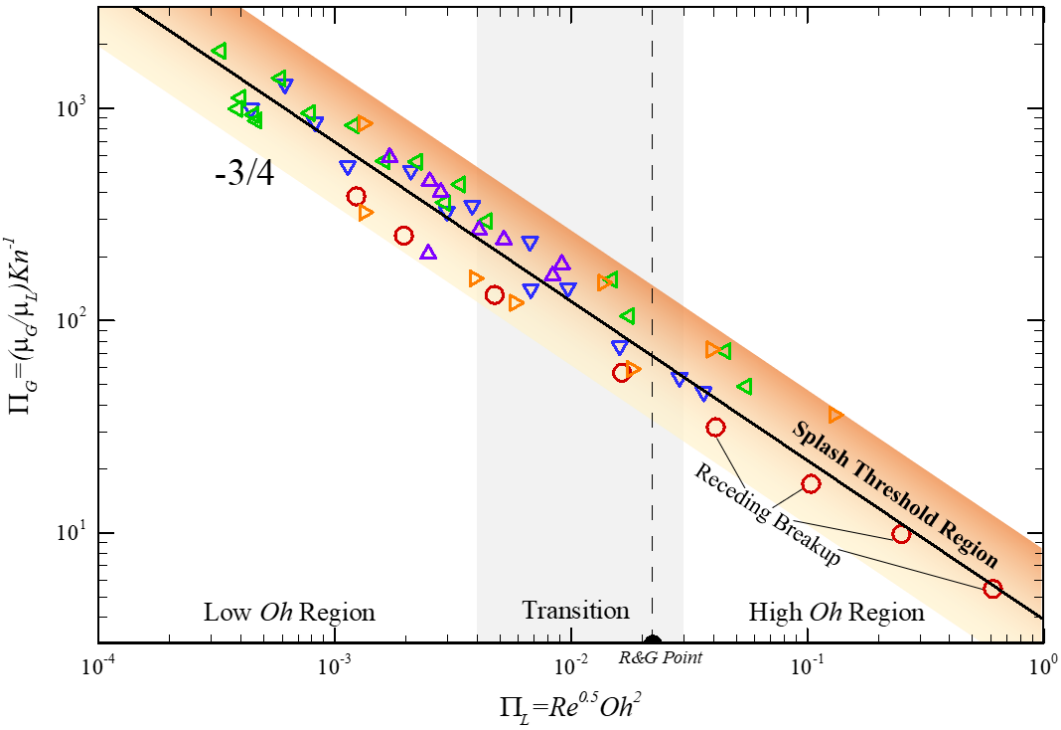

Figure 9-4 $\Pi_G - \Pi_L$ regime of droplet splashing threshold under atmospheric conditions. Experimental data is the same as those in Fig. 9.3.

Also notice that, while some experiments stand in a line very well, particularly the cases of Palacios et al. [249], the scattering of data used in Fig. 9.4 might well result from different experimental conditions, particularly the material and roughness of solid surfaces listed in Table 9-2. In addition, while the ratio of two fluids, ρ_G/ρ_L is thought as a negligible term, we speculate that the densities of two fluids, ρ_L and ρ_G, should be involved in the gas contribution on the droplet splash, because the data scattering of a critical splash in the orange strap is noticed. Particularly we notice the gas density ρ_G has been focused on the suction contribution of lift force, formulated as $K_u\rho_G U_e^2 d$, in Riboux & Gordillo [237]. To obtain a refined splash criterion, therefore ρ_G/ρ_L should

be tried to correct our Π_G, which will be varied in different pressures and gases for same liquids.

9.3.2 Effects of Ambient Pressure and Gas on Π_G

Here, we examine our theory on the effects of ambient gas, mainly focusing on the influences of the pressure and the gas medium. Therefore, we adopt experimental data of splash thresholds at varied pressures ($< 101kPa$) and in four gas mediums (Air, SF_6, He, and Kr). As shown in Figure 9.5, most data from previous experiments collapse to the correlation $\Pi_G\Pi_L \approx 0.66$. The results suggest that the $\Pi_G - \Pi_L$ the regime still agrees with the droplet splashing, which μ_G/μ_L represents reasonably for gas effects as well as $Kn = \lambda/D$ for the pressure effect. Particularly, the viscosity change of gases and liquids at room temperature and different pressures is ignored.

It should be noted that there exists a small deviation of orders between $\Pi_G \sim {\Pi_L}^{-3/4}$ and $\Pi_G \sim {\Pi_L}^{-1}$ in the 3.2 and 3.3 sections, respectively. While the latter agrees with the data under varied gas conditions, the former fits the experiment in the atmosphere. We speculate the deficiency is probably caused by ignoring the Φ effect if the surface differences of experiments are not important enough. In chapter 9.3.1, Φ is estimated close to a constant by using $U_e \propto U\tau_{e,crit}^{-1/2}$. The correlation of U_e is derived by adopting the potential flow theory. Accordingly, the capillarity and viscosity of fluids are neglected in the sheet ejection of the R&G model. Also, Vu et al. [269] found that adhesive force has an influence on the threshold requirements for lamella lift, which is closely relative to liquid/solid wettability. Therefore, $\Phi = \sqrt{(U_e t/D)(U_e/U)}$ may have an underlying correlation with Π_G or Π_L, intriguingly and particularly for the droplet splashing under the atmospheric condition.

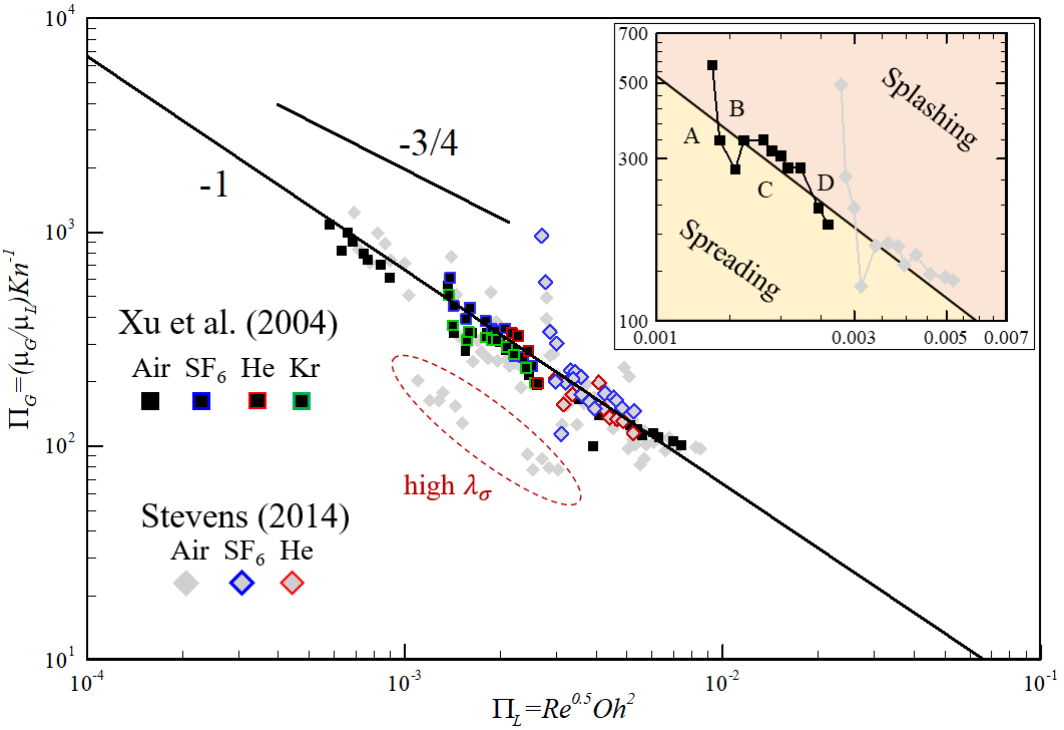

Figure 9-5 $\Pi_G - \Pi_L$ regime of droplet splashing thresholds under different pressure and gas conditions. (inset) The zoom details show the threshold line goes through A(spreading)-B(splashing)-C(spreading)-D(splashing) points. Experimental conditions of droplet splash refer to Table 9-2. Different colour borders of the same symbols denote different gas components.

In the zoom of Fig. 9.5, we observed the spreading–splashing–spreading–splashing transition a fixed (low) value of the gas pressure as the drop impact velocity increases in Gordillo & Riboux [273]. They tried to introduce $We_\lambda = \rho\lambda U^2/\sigma = WeKn$ for the consideration of the effect of Knudsen layer at the gas-liquid interface, where the critical relationship of two slip lengths, specifically expressed as $We_\lambda \sim 3(\mu_G/\mu_L)^{3/4} Oh^{1/4}$, determines the expressions of the coefficient of lubrication force K_l. Recently, Usawa et al. [257] reported that the splashing of micron-sized droplets is inhibited by large impact velocities, when $We_\lambda \geq 0.5$.

9.4 Other Factors on Droplet Splash

To determine the splash threshold on general surfaces (non-dry, non-smooth, non-solid), these factors should be considered for future extensions of the present model:

1. Splashing depends on the surface wettability, but its influence on the splashing criteria is limited. For a variety of wetting substrates with hydrophilic to superhydrophobic properties, Quetzeri-Santiago et al. [118] found that the maximum advancing contact angle plays an important role in parameterizing the splashing behaviour over smooth substrates. However, when static contact angles of these substrates widely range from 0 to 160°, the splashing ratio β has a small change from 0.06 to 0.13. In contrast, β is regarded as constant about 0.11-0.14 in previous works with neglecting the wettability effect on splashing.

2. The surface roughness plays a pivotal role in splashing. Goede et al. [282] showed that the roughness is large enough to disrupt the spreading droplet lamella and change the droplet splashing mechanism from corona to prompt splashing. Based on the R&G model for smooth substrate, García-Geijo et al. [119] effectively introduced the ratio of the substrate roughness and the initial lamella thickness for classifying the transition from spreading to splashing.

3. Substrate stiffness also affects the splashing threshold. Howland et al. [283] found that splashing is reduced or even eliminated: droplets on the softest substrates need over 70% more kinetic energy to splash than they do on rigid substrates. Pegg et al. [284] presented a splashing mechanism induced by the elastic deformation of the substrate. Langley et al. [285] experimentally observed that the soft solid can delay the effects of gas compressibility.

4. Droplet splash can be entirely suppressed by increasing the inclination angle between the droplet and the surface. Hao et al. [286] found that the threshold angle varies the velocity of the lamella tip determining the splash onset.

9.5 Summary and Conclusions

Droplet/wall impact is a ubiquitous phenomenon both in nature and industrial applications. Many previous splashing criteria of droplet impact are either limited to valid scopes or expressed in piecewise approximations. In this work, a new splash threshold of droplets impacting on a smooth solid surface is established by considering both the physical properties of the impacting liquid and the surrounding gas in a wide range. Based on the understanding of the precursory process and physical picture of the droplet splash, we established a K-H-instability-based criterion by adopting previous models and correlations, proposed by Xu et. al [116] and Gordillo and Riboux [237].

Specifically, derived from the balance between the thickness of the spreading liquid sheet and the most unstable wavelength of entrapping air film, two new parameters of Π_L and Π_G, which combines the four dimensionless numbers of Re, Oh, Kn, and μ_G/μ_L, are utilized to characterize the threshold between deposition and splash. New correlations between $\Pi_L = Re^{1/2}Oh^2$ and $\Pi_G = (\mu_G/\mu_L)Kn^{-1}$ can distinguish the splashing and non-splashing cases of various experiments with different liquids and gases. Insights of the present work could be especially useful for the study of the formation of deposits and wall combustion in engine cylinders. Also, we discussed some underlying influences of other factors on the splashing threshold.

Chapter 10. Droplet Complete Rebound on Soft Smooth Surfaces

In this chapter, the experimental finding that the recovery coefficient of oscillating droplets rebounding completely from soft smooth surfaces (polydimethylsiloxane, PDMS) has an overall trend of decrease but in a fluctuating manner with increasing the droplet impact Weber numbers We as theoretically interpreted. Physically, a sufficiently large droplet freely falling under gravity has an inevitable oscillation, which makes the impacting droplet shape slightly deviate from being spherical and in turn affects the interaction between the droplet and the surface. The fluctuating recovery coefficient is the result of the periodically varying phase of droplet oscillation with increasing We. A theoretical model of oscillating droplet rebound is proposed and well fits the present experiments over a wide range of We.

10.1 Effects of Droplet Oscillation on Rebound

The deformation or oscillation of a droplet upon impacting a surface has a potential influence on the impact dynamics. Liu et al. [287] showed that different droplet shapes produce large variations in spreading dynamics, splash onset, and splash amount. Yun and Lim's experimental and numerical results [288] showed that a high geometric aspect ratio (big shape distortion) is prone to induce alternate expansion and contraction of drop during retraction, thereby preventing drop from rebounding. Zhang et al. [289] studied the impact behavior of ellipsoidal droplets and found that decreasing the droplet aspect ratio enhances the viscous dissipation during impact. The oscillation phase and shape change of droplets can significantly alter the impact dynamics and weaken the bounce magnitude [290].

Recently, Wang et al. [148] reported that the oscillation of droplets before impact can affect the droplet spreading and the recovery coefficients e of bouncing droplets fluctuate visibly with We. Similar fluctuating curves of e and We are also found in previous experimental results [149, 291]. As shown in Fig 10.1, the recovery coefficients seem to be related to the ratio between the droplet radial lengths, with increasing We.

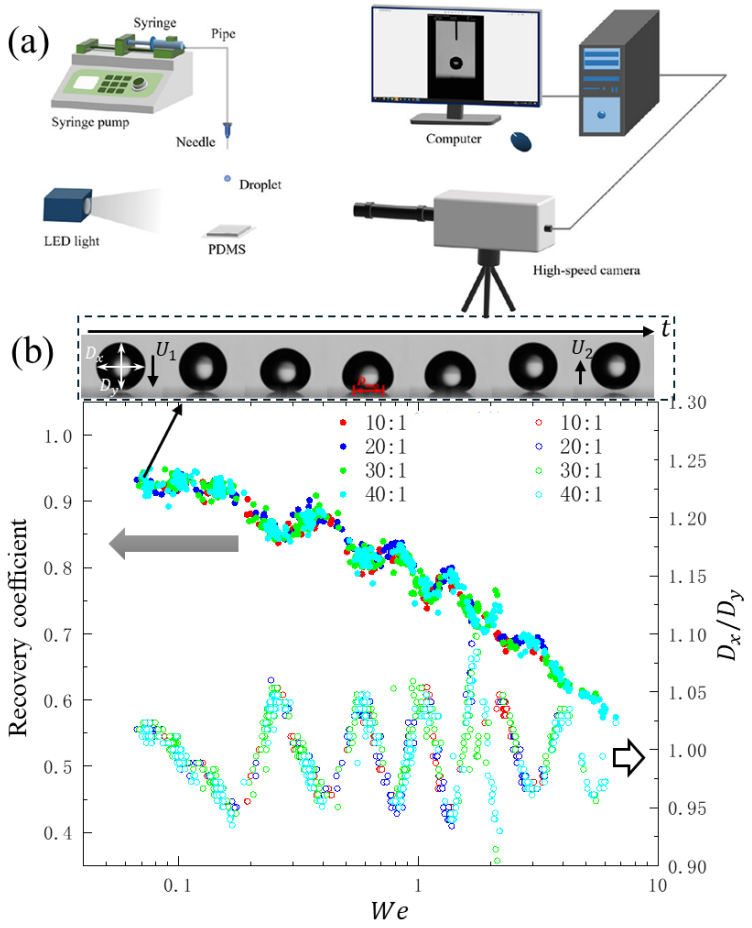

Figure 10-1 Experimental (a) setups and (b) results for the recovery coefficient and diameter ratio of droplet vs. the droplet impact Weber number. The experiments come form the work [292].

Little attention has been paid to the influence of the shape variation due to droplet oscillation on the recovery coefficient e of rebounding drop at different We. For droplets completely rebounding from a flexible solid surface, the experimental results

on the recovery coefficient in a large range of We are relatively limited. It is valuable to explore whether the surface oscillation of a free-falling drop in the air has a significant effect on the drop rebound.

10.2 Recovery Coefficient of Droplet Rebound

Generally, the energy loss for such droplet rebounds can be quantified by the recovery coefficient

$$e = U_1/U_0 \tag{10.1}$$

where U_0 and U_1 are the velocities of droplet centroid before impacting and after rebounding, respectively. Figure 10.2 shows that e decreases in an oscillatory way with increasing We for DI water droplets ($Oh \simeq 2.6 \times 10^{-3}$) impacting the 10:1, 20:1, 30:1, and 40:1 PDMS surfaces. The scattered points of different surfaces seem to follow the same oscillatory trend. Likewise, the data of Mix-1 or Mix-2 droplets on different solid surfaces fall along the same curve of e and We.

A similar decreasing trend in the high-Weber number regime was reported by Wang et al. [148] ($We \gtrsim 0.4$) and Thenarianto et al. [149] ($We \gg 1$). However, previous studies [145, 147-149] found that the droplet rebound is dominated by two distinct regimes and e varies nonmonotonously with increasing We. Specifically, the rapid increase of e in the low-Weber regime is due to the contact-line pinning, while the gradual decrease of e in the high-Weber regime is due to the inertial-capillary effects [149]. Based on scaling analyses, Wang et al. [148] proposed the best fit of their experimental data using $e^2 = 1 - aWe^{-1/2} - bWe^{1/2}$, where a and b are the fitted parameters. Thenarianto et al. [149] proposed a scaling law of $e \propto We^{-1/4}$ for the inertial-capillary regimes ($We \gg 1$). Remarkably, Figure 10.2 shows that the two correlations of e and We do not agree with the experiments.

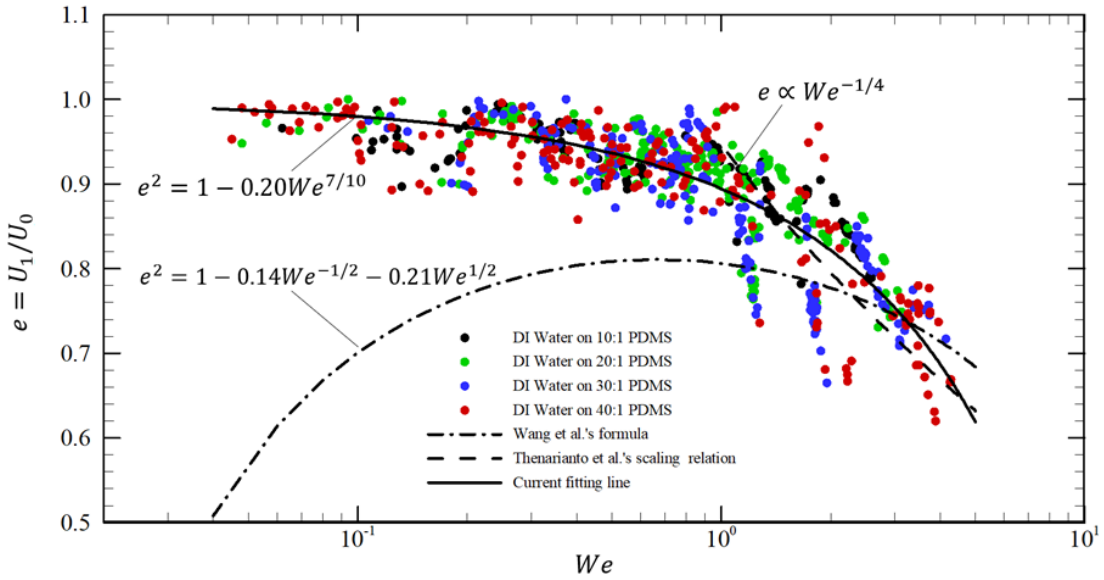

Figure 10-2 Recovery coefficient e of rebounding droplets as a function of Weber number We. The colored circles correspond to droplets impacting the PDMS surfaces. Previous correlations of e and We in Wang et al. [148] and Thenarianto et al. [149] are compared with the experiments in Fig 10.1.

Specifically, the substrates in the present work are non-superhydrophobic smooth surfaces without micro- or nano-scale features and very different from those with excellent water repellence used by Wang et al. [148] and Thenarianto et al. [149]. According to the present results of DI water droplets rebounding on four PDMS surfaces, we can obtain a fitting relation

$$e^2 = 1 - 0.20We^{7/10} \tag{10.2}$$

Interestingly, it is similar to the previous empirical formula of $e^2 = 1 - 0.21We^{1/2}$ for $We \gtrsim 0.2$ droplets impacting the superhydrophobic surface [149]. The present results indicate that the droplet viscosity μ should play an important role in the recovery coefficient. In particular, the scattering points of e seem to follow a period-like trend.

10.3 Model of Droplet Deformation

According to previous studies [293-295], small-scale disturbances (about 0.1– 0.3 mm) are observed on the surface of a millimetric droplet. The droplets oscillate regularly with a small amplitude (less than 10%), similar to a sinusoidal wave. It is understandable that different We droplets have the phase difference of droplet oscillation (i.e., D_x/D_y variation) upon touching the surfaces, as different initial heights cause different oscillation times in the air.

Under the action of surface tension forces, a droplet without any disturbances is spherical. In a disturbed state, droplet deformation can be treated as surface oscillations caused by the action of capillary forces and as volume oscillations [296, 297]. According to the Rayleigh theory [298], the naturally self-oscillating time of droplets is $t_{osc} = (\pi/4)\sqrt{\rho D^3/\sigma} = 5{\sim}9$ ms for 0, 30, and 60% water–glycerol solutions. In a small oscillation, the deformation of the liquid surface can be in general expressed as $D_0(t,\theta,\varphi) = \bar{D}_0\left[1 + \sum_{l,m} \epsilon_{l,m}(t) Y_l^m(\theta,\varphi)\right]$, where $\bar{D}_0$ is the diameter of the sphere, $\epsilon_{l,m}(t) \ll 1$ is a time-varying small parameter, and $Y_l^m(\theta,\varphi)$ is the spherical harmonic function [297]. In the absence of viscosity, the frequencies of oscillation are $f_{osc} = \sqrt{l(l-1)(l+2)\sigma/8\rho D^3}$ for different mode numbers l [296]. For low-viscosity liquids and relatively large droplets in dynamically inactive surroundings, Lamb [296] gave the oscillation frequency as $f_{osc}^* = f_{osc}\sqrt{1-\zeta Oh^2}$, where ζ is a constant relying on the mode number l. Therefore, the oscillating frequency of the droplet has the damping effect of viscosity. The higher Oh is, the lower f_{osc}^* is.

Considering the axially symmetric oscillation that corresponds to $m = 0$, we can simplify the droplet deformation as $D_0(t,\theta) = \bar{D}_0\left[1 + \sum_{l=0}^{\infty} \epsilon_l(t) P_l(cos\theta)\right]$, where $\epsilon_l(t) = \epsilon_0 e^{-\omega t}$ ($\epsilon_0 \ll 1$) is a small time-varying quantity and $P_l(cos\theta)$ are the Legendre polynomials. According to the Eq. (21) in [297], ω is a complex number as

$\omega = \omega_r + i\omega_i$. Consequently, $\epsilon_l(t)$ can be rewritten as $\epsilon_0 e^{-\omega_r t} e^{-i\omega_i t}$, where the first exponential term is related to viscous damping and the second exponential term can be expressed by a trigonometric function. According to these results, the axially symmetric oscillation at the impact point ($\theta = \pi$) can be given by:

$$D_0(t, \theta = \pi) = \overline{D}_0[1 + \epsilon(t) sin(\alpha t / t_{osc} + \varphi_0)] \tag{10.3}$$

where $\overline{D}_0$ is the average diameter of a droplet, and $\epsilon(t) sin(\alpha t / t_{osc} + \varphi_0)$ is the small droplet perturbation like a sine wave of amplitude ϵ, frequency α / t_{osc}, and the initial phase φ_0. Particularly, the viscosity damping is introduced by $\epsilon(t) = \epsilon_0 e^{-\beta \nu t / \overline{D}_0^2}$, where ϵ_0 and β are fitting constant parameters and $\nu = \mu / \rho$ is the kinematic viscosity coefficient of liquid.

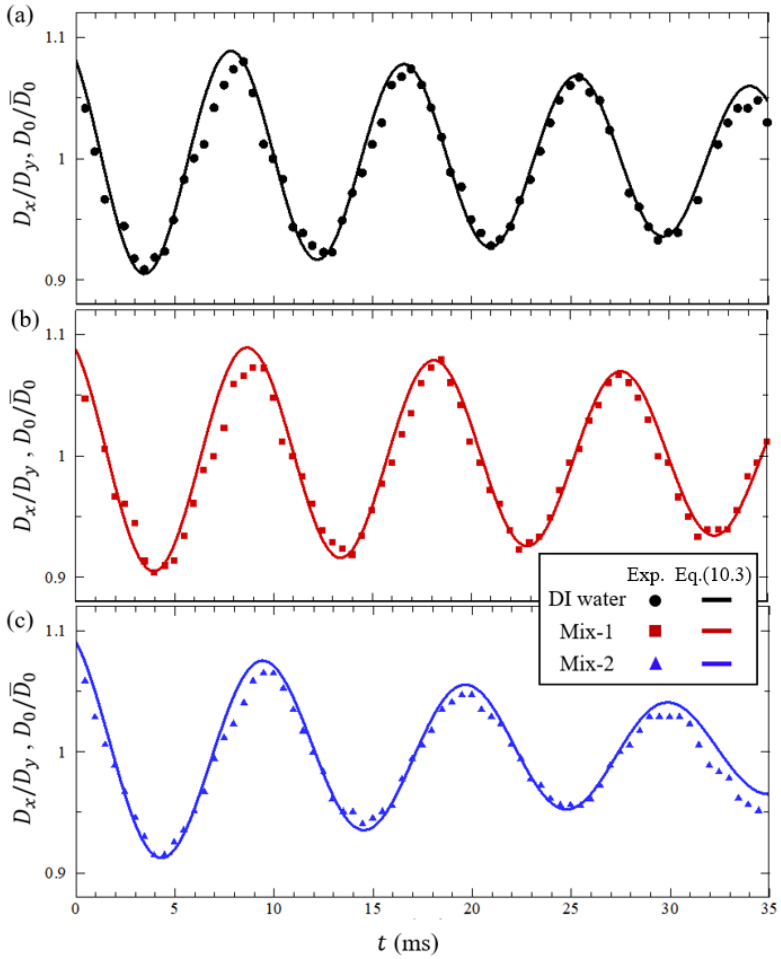

Figure 10-3 Comparison between experimental and modeled results.

Consequently, the aspect ratio of the droplet D_x/D_y can be modeled by Eq. (10.3). Figure 10.3 shows that the model variation of droplet diameter $D_0(t)/\overline{D}_0$ has a good performance in predicting the present experimental results. The parameters of $\epsilon_0 = 0.1$; $\alpha = 0.79$, 0.71, and 0.69; $\beta = 0.060$, 0.022, and 0.013; $\varphi_0 = 0.70\pi$, 0.66π, and 0.64π in Eq. (10.3) can be obtained by fitting the experimental data, respectively.

10.4 Theoretical Modeling for Recovery Coefficient

In the present work, the change of gravitational potential energy of the millimetric droplet before and after the impact is sufficiently small to be negligible. In addition, Chen and Li [143] demonstrated that the droplet at a certain We (generally larger than a lower limit) can rebound on the non-superhydrophobic substrates (PDMS surfaces) because an air film forms beneath the droplet during the whole impact process so that no energy loss is due to wetting.

Therefore, the impacting and rebounding behaviours of droplets from contacting to leaving the solid surface are mainly influenced by the synergistic actions of inertia force, viscous force, and surface tension force. To facilitate theoretically interpreting the present observations, we consider the droplet at the pre- and post-impact states and neglect the dynamic process during the impact. In this way, for droplets impacting the present smooth solid surfaces, the energy conservation equation can be written as

$$E_{k0} + E_{s0} = E_{k1} + E_{s1} + \Phi \tag{10.4}$$

where E_k, E_s are the kinetic energy and surface energy of the droplet, respectively. The left-hand terms with "0" index denote the initial total energy of the system when the droplet touches the substrate, while the right-hand terms with "1" index are the total energy of the system at the moment that the droplet goes away from the substrate. Φ is

the viscous energy dissipation within the droplet and is related to liquid viscosity, droplet diameter, and impact velocity [299].

Based on the energy conservation, a theoretical model of oscillating droplet rebound is established. Next, each term of Eq. (10.4) will be estimated. First, for the pre-impact state "0", we have

$$E_{k0} = \frac{\pi}{12}\rho D_0^3 U_0^2 \tag{10.5}$$

$$E_{s0} = \sigma\pi D_0^2 \tag{10.6}$$

where D_0 and U_0 are the droplet diameter and the impacting velocity before touching the surface, respectively. Second, the post-impact state "1" can be estimated as

$$E_{k1} = \frac{\pi}{12}\rho D_1^3 U_1^2 \tag{10.7}$$

$$E_{s1} = \sigma\pi D_1^2 \tag{10.8}$$

where D_1 and U_1 are the equivalent diameter and the rebounding velocity, respectively. Previous studies [106, 291, 299, 300] showed that Φ is proportionate to the viscous dissipation function of $\phi \sim \mu(U_0/D_0)^2$. Thus, Φ is a function of μ, D_0, and U_0. Finally, by substituting Eq. (10.5-10.8) into Eq. (10.4), we can obtain

$$\frac{\pi}{12}\rho D_0^3 U_0^2 + \sigma\pi D_0^2 = \frac{\pi}{12}\rho D_1^3 U_1^2 + \sigma\pi D_1^2 + \Phi(\mu, D_0, U_0) \tag{10.9}$$

The small droplet oscillation presents that D_0 is a small change around the average diameter $\overline{D}_0$. Similar to Eq. (10.3), we modelled the droplet diameter by $D_0 = [1 + \epsilon sin(\psi)]\overline{D}_0$. The amplitude ϵ and phase ψ can be calculated according to the model of droplet oscillation. ϵ is much smaller than 1 due to the small droplet deformation. Considering this observation that almost identical shapes for different droplets in the post-impact state and to facilitate modeling, we approximate the droplet shape to be non-spherical. Due to the volume conservation of the droplet, the equivalent diameter

D_1 can be estimated as $\zeta\overline{D}_0$. The experimental results show ζ is a constant about 1.0~1.3 by calculating D_1 as the vertical height of the droplet at the bouncing moment.

To normalize the energy relation for a droplet rebounding, we divide Eq. (10.9) by the $\overline{D}_0$-based kinetic energy of $\frac{\pi}{12}\rho\overline{D}_0^3U_0^2$. Also, considering $D_0 = [1 + \epsilon sin(\psi)]\overline{D}_0$ and $D_1 = \overline{D}_0$, we have

$$\varepsilon^3 + \frac{12}{We}\varepsilon^2 = \zeta^3\left(\frac{U_1}{U_0}\right)^2 + \zeta^2\frac{12}{We} + \widehat{\Phi} \tag{10.10}$$

where $\varepsilon = D_0/\overline{D}_0$ denotes the droplet deformation, $We = \rho U_0^2\overline{D}_0/\sigma$ is the Weber number of the impacting droplet, and $\widehat{\Phi} = \pi\Phi/(12\rho\overline{D}_0^3U_0^2)$ is the normalized viscous energy dissipation depending on μ, D_0, $\overline{D}_0$, and U_0. The energy dissipation during the droplet impact is a complex process. Modeling this process is a challenging task [300, 301] and is beyond the scope of the present study. Instead, we are interested in modeling the influence of droplet non-sphericity (at the moment of droplet impact) on viscous dissipation. Consequently, we define a reference $\widehat{\Phi}_{ref}$ for the normalized viscous energy dissipation for an ideal spherical shape at the impact moment.

In view of the viscous dissipation function of $\phi \propto D_0^{-2}$ and the scaling relation of $\Phi \propto \phi$, the normalized viscous energy dissipation can be estimated as

$$\widehat{\Phi} = \widehat{\Phi}_{ref}\left(\frac{D_0}{\overline{D}_0}\right)^2 = \varepsilon^2\widehat{\Phi}_{ref} \tag{10.11}$$

where $\widehat{\Phi}_{ref}$ can be determined by fitting the experimental data. To obtain the recovery coefficient, we use the relation of Eq. (10.11) and the linear approximation relations of $\varepsilon^3 = [1 + \epsilon sin(\psi)]^3 \approx 1 + 3\epsilon sin(\psi)$ and $\varepsilon^2 \approx 1 + 2\epsilon sin(\psi)$. Thus, Eq. (10.10) is

$$\begin{aligned}\left(\frac{U_1}{U_0}\right)^2 &= \left[\varepsilon^3 + \frac{12}{We}(\varepsilon^2 - \zeta^2) - \varepsilon^2\widehat{\Phi}_{ref}\right]\zeta^{-3} \\ &\approx 1 - \widehat{\Phi}_{ref} + (3 + \frac{24}{We} - 2\widehat{\Phi}_{ref})\epsilon sin(\psi)\end{aligned} \tag{10.12}$$

As ζ is a constant close to 1.0, we approximate ζ^2 and ζ^{-3} to a prefactor of about 1.0. Hereto, two factors can affect U_1/U_0 of a droplet impacting at We, including the viscous dissipation of $\widehat{\Phi}_{ref}$ and the droplet perturbation of $\epsilon sin(\psi)$. When there is no droplet oscillation before impacting the surface (i.e., $\epsilon sin(\psi) = 0$ and $\varepsilon = 1$), the recovery coefficient $e = U_1/U_0$ is approximated by $1 - \widehat{\Phi}_{ref}$. As the droplet deformation is small (i.e., $\epsilon \ll 1$ and $|sin(\psi)| \leq 1$), the last term in Eq. (10.12) should be smaller than $1 - \widehat{\Phi}_{ref}$. Thus, we use the binomial approximation of $(1 + x)^{1/2} \approx 1 + x/2$ and obtain

$$e = \frac{U_1}{U_0} \approx \left(1 - \widehat{\Phi}_{ref}\right)^{1/2}[1 + \gamma\epsilon sin(\psi)] \tag{10.13}$$

where $\gamma = (1/2 + 12/We)/\left(1 - \widehat{\Phi}_{ref}\right) + 1$ is a prefactor depending on We and $\widehat{\Phi}_{ref}$. In the present study, γ is calculated by $We = (\rho U_0^2 \overline{D}_0)/\sigma$ and the fitting results of $\widehat{\Phi}_{ref}$.

Equation 10.13 shows that the recovery coefficient depends on two terms. The first multiplicative factor $\left(1 - \widehat{\Phi}_{ref}\right)^{1/2}$ determines the overall trend and decreases with increasing W. Specifically, for the complete rebound of DI water droplets in the present study, the dissipation energy term $\widehat{\Phi}_{ref}$ of bouncing droplets is equal to $0.20We^{7/10}$ according to Eq. (10.2) and the exponent of We can be derived by evaluating $\widehat{\Phi}_{ref}$. In physics, a higher-We droplet (higher impacting velocity) has more viscous dissipation (more energy loss leads to lower rebounding velocity). Based on Eq. (10.6) of Wang et al.'s work [148], we have $\widehat{\Phi}_{ref} \propto Re_\mu^{-1}We^{1/2}$, where Re_μ=$\rho D(L_v/\tau_C)/\mu$, L_v is the characteristic dissipation length scale, and τ_C is the rebound time from the impact to the take-off. To quantify the exponent of We, we need to obtain a characteristic velocity for viscous dissipation L_v/τ_C, particularly its relationship with

We. It deserves future work on precisely characterizing the flow dynamics of the droplet and the air film. The second multiplicative factor $[1+\gamma\epsilon sin(\psi)]$ is to delineate the fluctuating change of e with increasing We, because the phase ψ, the prefactor γ, and the amplitude ϵ are all related to the impacting velocity U_0.

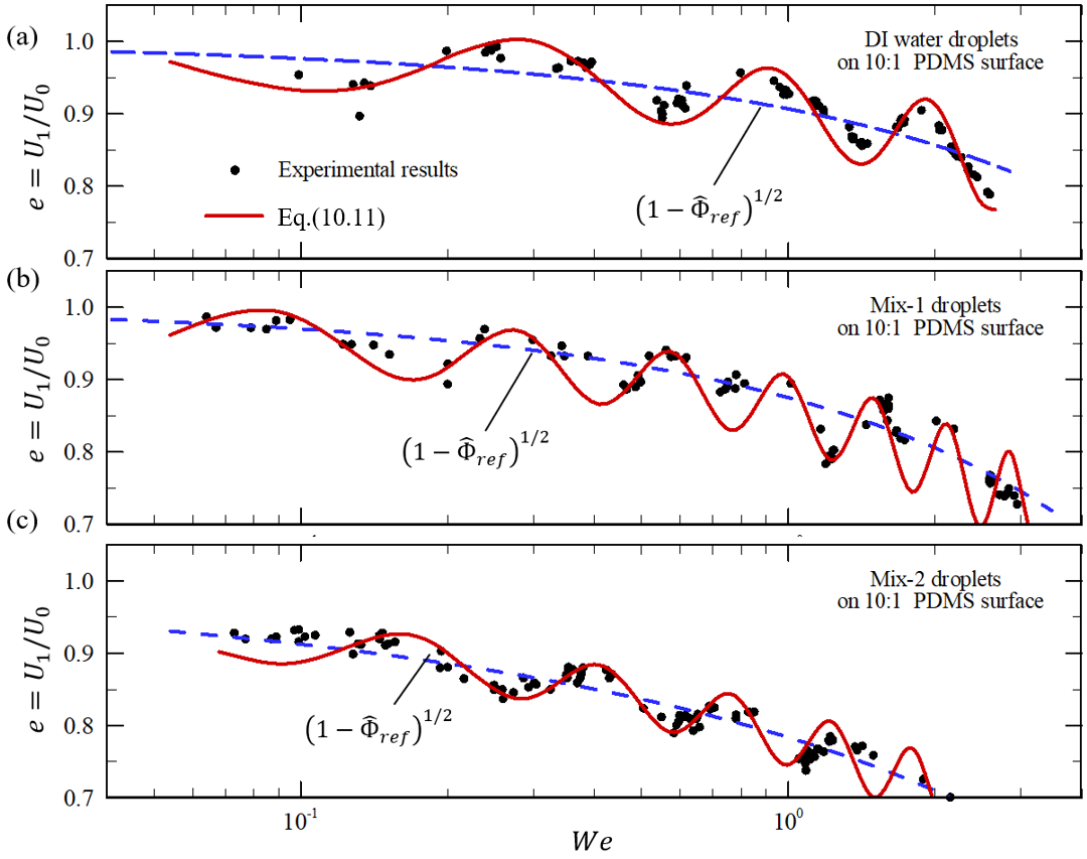

Figure 10-4 Comparisons between the present experimental results (cycles) of (a) DI water, (b) Mix-1, and (c) Mix-2 droplets on the 10:1 PDMS surface and the theoretical predictions (solid red lines) of Eq. (10.13). The dotted blue lines are the first multiplicative factor $\left(1-\hat{\Phi}_{ref}\right)^{1/2}$ and obtained by fitting the present experiments. The fluctuating trend of the solid line is delineated by the second multiplicative factor $[1+\gamma\epsilon sin(\psi)]$, which is caused by the effect of droplet oscillation.

In Fig. 10.4, Eq. (10.13) is plotted and compared with the recovery coefficient e of DI water, Mix-1, and Mix-2 droplets on the 10:1 PDMS surface, where

$\left(1-\widehat{\Phi}_{ref}\right)^{1/2}$ is obtained by fitting the present data. It is shown that the effect of droplet oscillation on e can be captured by introducing the sinusoidal change of $\gamma\epsilon sin(\psi)$ around the overall trend. It should be noted that a few parameters (i.e., β in ϵ and α and φ_0 in ψ) need to be adjusted according to experimental results. In general, the present theoretical predictions perform well in agreement with the experimental results. Comparing the predicted lines in Fig. 10.4(a-c), we also noticed that the recovery coefficient e decreases rapidly and the fluctuating period has a distinct shortness when the droplet viscosity increases. These features of theoretical predictions are consistent with physical observations.

10.5 Summary and Conclusions

Theoretical interpretation for the droplet rebound of DI water, Mix-1, and Mix-2 liquids on the non-superhydrophobic surface (PDMS) was conducted, with particular emphasis on clarifying the effects of droplet oscillation on the rebounding process. Specifically, the oscillation of a freely falling droplet is modeled by using the spherical harmonic function and predicted well by Eq. (10.3). The experimental observation is that the recovery coefficient e, defined as the ratio of the rebounding velocity to the impact velocity, exhibits a fluctuating decrease as We increases.

Considering the inherent oscillation of the freely falling droplet, we hypothesized that the fluctuation of the recovery coefficient could be attributed to the shape deformation of the droplet before impacting the surface. Specifically, the increase of We by increasing the initial height of the droplet is accompanied by the periodical phase variation of the droplet oscillation, leading to the fluctuating recovery coefficient. Increasing the droplet viscosity (Oh) can effectively suppress the droplet oscillation and correspondingly mitigate the fluctuation amplitude of the recovery coefficient.

These findings suggest that the droplet's physical properties play a crucial role in the rebound behavior. To provide a comprehensive understanding of the oscillating droplet rebound phenomenon, a theoretical model is proposed and performs well with present experimental results.

Chapter 11. Concluding Remarks and Future work

11.1 Concluding Remarks

The thesis mainly contains the theoretical and computational studies on flame stability and the theoretical modelling of droplet impact, aiming to gain a fundamental understanding of spray flames. First, the vortex-dynamics interactions and synchronization modes of different flickering diffusion flames, including single, dual, triple, and octa-flickering flames have been investigated computationally and theoretically. Second, the splash and complete rebound models of droplets impinging on smooth solid surfaces have been established based on previous experimental observations. In the thesis, the main conclusions could be obtained:

To explore collective dynamical behaviours of annular combustion systems of gas-turbine engines for making a fundamental breakthrough of flame instability, present studies in Part I successfully capture flickering behaviours of single buoyant diffusion flames in weakly rotatory flows, flickering modes of various coupled flame systems through computationally and theoretically investigating the vortex interaction. Through these works, we have brought a refreshing understanding of flickering flames from the perspectives of vortex dynamics and nonlinear dynamics, which are beneficial to the combustion community.

For modeling the dynamical behaviours of droplet impact on smooth solid surfaces, present studies in Part II successfully established splash criteria of droplets on the unheated and heated surfaces, with a focus on the effect of ambient gas on the thin-sheet instability, and fluctuating recovery coefficient of complete rebound of droplet on the soft non-superhydrophobic surfaces, with emphasis on the effect of droplet deformation before touching surface. Through these works, we have brought a

refreshing understanding of droplet impact dynamics, which are beneficial to the spray community.

Specifical summaries and conclusions on what has been carried out in the thesis can be referred to in the last section of each chapter.

11.2 Future work

Perfection is impossible to achieve in the present works. Below are some of these potential avenues that could be worthwhile to investigate further.

11.2.1 Flickering Flames

While the present works provide an understanding of various dynamical modes of dual-, triple-, and octa-flame systems, we fully recognized that the present study barely addresses the questions of what dynamical modes of various flame systems with symmetry-breaking and how these modes transition between each other. Future works to address these remaining questions will gain us a deeper understanding of the physical origin and transition of the dynamical modes in the system of multiple flickering flames. In addition, turbulent flames should be studied as turbulence occurs in many industrial applications, in which detailed combustion mechanisms, radiation model, and heat transfer of confined walls are significant in numerical simulations.

To facilitate theoretical modeling while retaining some essential features of annular combustion systems, the present work is mainly focused on unconfined, coupled, periodic-oscillator systems of laminar methane diffusion flames to minimize the complexity of turbulent fluctuations, combustion chemistry, and flame acoustics interaction. Therefore, we fully recognized that they hardly address the challenging problem of turbulent flames and their dynamical origin and transition in a wider

parameter space formed by the swirling intensity, the swirling angle, and the coupled flame number.

11.2.2 Droplet Splash and Complete Rebound

Being fully aware of the limitations of the present droplet impact models on smooth surfaces, we need to investigate the underlying influences of other factors, such as surface roughness, wettability, and high pressure of ambient gas on the splashing threshold and the complete rebound. For example, as the thin-sheet splash on heated surfaces, Eq. (8.6) is only applicable to the low-Oh droplet splash, a more general scaling law should consider the non-monotonic effects of liquid viscosity, the volatility of liquids (methanol, ethanol, propanol, etc.), and the heat conduction of materials. Also, more complex physics of droplet rebounding, particularly the gas film dynamics during the impact, merits future study.

11.2.3 Machine Learning for Flame and Droplet Dynamics

To identify and understand complex spray combustion systems, machine learning-based approaches may provide new perspectives by analyzing and interpreting the spatiotemporal variables in spray, droplet, flame, and flow fields, compared to conventional approaches based on fluid mechanics, vortex dynamics, thermodynamics nonlinear dynamic analysis, etc. This can facilitate providing insights into the underlying physics of these systems.

For various spatiotemporal patterns of complex combustion systems, dimensionality reduction (i.e., Convolutional Neural Network (CNN), variational autoencoder (VAE)) and time-series analysis (i.e., Recurrent Neural Network (RNN) or Long Short-Term Memory (LSTM)) of deep learning approaches could provide new

ways of monitoring and controlling complex combustion systems. Furthermore, utilizing various supervised and unsupervised methods developed in the deep learning field can facilitate establishing a robust and comprehensive framework for dynamical mode recognition in real combustion systems, especially larger and more complicated systems with richer dynamical phenomena.

For spray and droplet dynamics, machine learning can be used to analyze large sets of experimental data to identify patterns, correlations, and dependencies in spray and droplet behavior. For example, random forest (RF) and gradient boost (GB) could be utilized to assess previous empirical scaling laws and analytical models of droplet impact; Through neural network approaches, like CNN and VAE, feature extraction and prediction could be convenient and efficient for analyzing spray and droplet dynamics; Generative models, such as generative adversarial network (GAN) and diffusion model, is employed to reconstruct and predict the morphological evolution of spray atomization and droplet impact.

Reference

[1] Kuo K. K., *Recent advances in spray combustion: Spray atomization and drop burning phenomena*. 1996.

[2] Stiesch G., *Modeling engine spray and combustion processes* (Springer Science & Business Media, 2013).

[3] Williams A., *Combustion of liquid fuel sprays* (Butterworth-Heinemann, 2013).

[4] Luo K., Shao C., Chai M., and Fan J., *Level set method for atomization and evaporation simulations*. Progress in Energy and Combustion Science, 2019. **73**: 65-94.

[5] Vignat G., Durox D., Schuller T., and Candel S., *Combustion dynamics of annular systems*. Combustion Science and Technology, 2020. **192** (7): 1358-1388.

[6] Barlow R. S., *International workshop on measurement and computation of turbulent nonpremixed flames*. h ttp://www. ca. sandia. gov/TNF/abstract. html, 2003.

[7] Network E. C., *'Spray G'Operating Condition*. Last update, December, 2014. **3**.

[8] Matalon M., *Intrinsic flame instabilities in premixed and nonpremixed combustion*. Annu. Rev. Fluid Mech., 2007. **39**: 163-191.

[9] Moreira A., Moita A. S., and Panao M. R., *Advances and challenges in explaining fuel spray impingement: How much of single droplet impact research is useful?* Prog. Energy Combust. Sci., 2010. **36** (5): 554-580.

[10] Burke S., and Schumann T., *Diffusion flames*. Industrial & Engineering Chemistry, 1928. **20** (10): 998-1004.

[11] Linán A., Vera M., and Sánchez A. L., *Ignition, liftoff, and extinction of gaseous diffusion flames*. Annual Review of Fluid Mechanics, 2015. **47**: 293-314.

[12] Chamberlin D. S., and Rose A., *The flicker of luminous flames*. Proceedings of the Combustion Institute, 1948. **1-2**: 27-32.

[13] Barr J., *Diffusion flames*. Proceedings of the Combustion Institute, 1953. **4** (1): 765-771.

[14] Byram G. M., and Nelson R. M., *The modeling of pulsating fires*. Fire Technology, 1970. **6** (2): 102-110.

[15] Chen L.-D., Seaba J., Roquemore W., and Goss L., *Buoyant diffusion flames*. Proceedings of the Combustion Institute, 1989. **22** (1): 677-684.

[16] Cetegen B. M., and Ahmed T. A., *Experiments on the periodic instability of buoyant plumes and pool fires*. Combustion and Flame, 1993. **93** (1-2): 157-184.

[17] Davis R., Moore E., Chen L.-D., Roquemore W., Vilimpoc V., and Goss L., *A numerical/experimental study of the dynamic structure of a buoyant jet diffusion flame*. Theoretical and Computational Fluid Dynamics, 1994. **6**: 113-123.

[18] Malalasekera W., Versteeg H. K., and Gilchrist K., *A review of research and an experimental study on the pulsation of buoyant diffusion flames and pool fires*. Fire and Materials, 1996. **20** (6): 261-271.

[19] Jiang X., and Luo K., *Combustion-induced buoyancy effects of an axisymmetric reactive plume*. Proceedings of the combustion institute, 2000. **28** (2): 1989-1995.

[20] Tieszen S. R., *On the fluid mechanics of fires*. Annual Review of Fluid Mechanics, 2001. **33** (1): 67-92.

[21] Hostikka S., McGrattan K. B., and Hamins A., *Numerical modeling of pool fires using LES and finite volume method for radiation*. Fire Safety Science, 2003. **7**: 383-394.

[22] Sahu K., Kundu A., Ganguly R., and Datta A., *Effects of fuel type and equivalence ratios on the flickering of triple flames*. Combustion and Flame, 2009. **156** (2): 484-493.

[23] Carpio J., Sánchez-Sanz M., and Fernández-Tarrazo E., *Pinch-off in forced and non-forced, buoyant laminar jet diffusion flames*. Combustion and flame, 2012. **159** (1): 161-169.

[24] Xia X., and Zhang P., *A vortex-dynamical scaling theory for flickering buoyant diffusion flames*. Journal of Fluid Mechanics, 2018. **855**: 1156-1169.

[25] Vadlamudi G., Thirumalaikumaran S., and Basu S., *Insights into the dynamics of wake flame in a freely falling droplet*. Phys. Fluids, 2021. **33** (12): 123306.

[26] Zhang Y., Yang Y., Wei Y., and Liu S., *Vortex shedding controlled combustion of the wake flame of an n-heptane wetted porous sphere*. AIP Adv., 2022. **12** (10): 105216.

[27] Sitte M. P., and Doan N. A. K., *Velocity reconstruction in puffing pool fires with physics-informed neural networks*. Phys. Fluids, 2022. **34** (8): 087124.

[28] Sayed-Kassem A., Gillon P., Idir M., and Gilard V., *Flickering of a diffusion flame: An innovative way of stabilization by a mechanical actuator*. International Communications in Heat and Mass Transfer, 2022. **139**: 106475.

[29] Yang X., Ma S., Gao J., Du Q., Zhang Y., Dong H., Wu S., and Qin Y., *Mechanism and effect assessment of sub-atmospheric pressure and co-flow air to suppress the flicker of buoyancy-driven methane laminar diffusion flame*. Fuel Processing Technology, 2023. **242**: 107649.

[30] Cetegen B. M., and Kasper K. D., *Experiments on the oscillatory behavior of buoyant plumes of helium and helium‐air mixtures*. Phys. Fluids, 1996. **8** (11): 2974-2984.

[31] Pasumarthi K. S., and Agrawal A. K., *Schlieren measurements and analysis of concentration field in self-excited helium jets*. Phys. Fluids, 2003. **15** (12): 3683-3692.

[32] Wimer N. T., Lapointe C., Christopher J. D., Nigam S. P., Hayden T. R., Upadhye A., Strobel M., Rieker G. B., and Hamlington P. E., *Scaling of the puffing Strouhal number for buoyant jets and plumes*. J. Fluid Mech., 2020. **895**: A26.

[33] Gergely A., Paizs C., Tötös R., and Néda Z., *Oscillations and collective behavior in convective flows*. Physics of Fluids, 2021. **33** (12): 124104.

[34] Pandey K., Basu S., Krishan B., and Gautham V., *Dynamic self-tuning, flickering and shedding in buoyant droplet diffusion flames under acoustic excitation*. Proceedings of the Combustion Institute, 2021. **38** (2): 3141-3149.

[35] Thirumalaikumaran S., Vadlamudi G., and Basu S., *Insight into flickering/shedding in buoyant droplet-diffusion flame during interaction with vortex*. Combust. Flame, 2022. **240**: 112002.

[36] Papadopoulos G., Bryant R., and Pitts W., *Flow characterization of flickering methane/air diffusion flames using particle image velocimetry*. Experiments in Fluids, 2002. **33** (3): 472-481.

[37] McCamy C., *A five-band recording spectroradiometer*. Journal of Research of the National Bureau of Standards, 1956. **56** (5): 293.

[38] Portscht R., *Studies on characteristic fluctuations of the flame radiation emitted by fires*. Combustion Science and Technology, 1975. **10** (1-2): 73-84.

[39] Sibulkin M., and Hansen A. G., *Experimental study of flame spreading over a horizontal fuel surface*. Combustion Science and Technology, 1975. **10** (1-2): 85-92.

[40] Detriche P., and Lanore J., *An acoustic study of pulsation characteristics of fires*. Fire Technology, 1980. **16** (3): 204-211.

[41] Zukoski E., Cetegen B., and Kubota T., *Visible structure of buoyant diffusion flames*. Symposium (International) on Combustion, 1985. **20** (1): 361-366.

[42] Buckmaster J., and Peters N., *The infinite candle and its stability—a paradigm for flickering diffusion flames*. Symposium (International) on Combustion, 1988. **21** (1): 1829-1836.

[43] Moreno-Boza D., Coenen W., Sevilla A., Carpio J., Sánchez A., and Liñán A., *Diffusion-flame flickering as a hydrodynamic global mode*. Journal of Fluid Mechanics, 2016. **798**: 997-1014.

[44] Moreno-Boza D., Coenen W., Carpio J., Sánchez A. L., and Williams F. A., *On the critical conditions for pool-fire puffing*. Combustion and Flame, 2018. **192**: 426-438.

[45] Chen L.-D., Seaba J. P., Roquemore W. M., and Goss L. P., *Buoyant diffusion flames*. Proceedings of the Combustion Institute, 1989. **22** (1): 677-684.

[46] Durox D., Yuan T., and Villermaux E., *The effect of buoyancy on flickering in diffusion flames*. Combustion science and technology, 1997. **124** (1-6): 277-294.

[47] Jiang X., and Luo K. H., *Combustion-induced buoyancy effects of an axisymmetric reactive plume*. Proceedings of the Combustion Institute, 2000. **28** (2): 1989-1995.

[48] Finney M. A., Cohen J. D., Forthofer J. M., McAllister S. S., Gollner M. J., Gorham D. J., Saito K., Akafuah N. K., Adam B. A., and English J. D., *Role of buoyant flame dynamics in wildfire spread*. Proceedings of the National Academy of Sciences, 2015. **112** (32): 9833-9838.

[49] Gharib M., Rambod E., and Shariff K., *A universal time scale for vortex ring formation*. Journal of Fluid Mechanics, 1998. **360**: 121-140.

[50] Dabiri J. O., and Gharib M., *Starting flow through nozzles with temporally variable exit diameter*. Journal of Fluid Mechanics, 2005. **538**: 111-136.

[51] Krueger P. S., Dabiri J. O., and Gharib M., *The formation number of vortex rings formed in uniform background co-flow*. Journal of Fluid Mechanics, 2006. **556**: 147-166.

[52] Lawson J. M., and Dawson J. R., *The formation of turbulent vortex rings by synthetic jets*. Physics of Fluids, 2013. **25** (10): 105113.

[53] Xia X., and Mohseni K., *Far-field momentum flux of high-frequency axisymmetric synthetic jets*. Physics of Fluids, 2015. **27** (11): 115101.

[54] Emmons H. W., and Ying S.-J., *The fire whirl*. Proc. Combust. Inst., 1967. **11** (1): 475-488.

[55] Battaglia F., Rehm R. G., and Baum H. R., *The fluid mechanics of fire whirls: An inviscid model*. Phys. Fluids, 2000. **12** (11): 2859-2867.

[56] Lei J., Liu N., and Satoh K., *Buoyant pool fires under imposed circulations before the formation of fire whirls*. Proceedings of the Combustion Institute, 2015. **35** (3): 2503-2510.

[57] Tohidi A., Gollner M. J., and Xiao H., *Fire whirls*. Annual Review of Fluid Mechanics, 2018. **50**: 187-213.

[58] Coenen W., Kolb E. J., Sánchez A. L., and Williams F. A., *Observed dependence of characteristics of liquid-pool fires on swirl magnitude*. Combustion and Flame, 2019. **205**: 1-6.

[59] Yang Y., Zhang H., Xia X., Zhang P., and Qi F., *An experimental study of the blue whirl onset*. Proc. Combust. Inst., 2022. **39** (3): 3705-3714.

[60] Ju X., Mizuno M., Matsuoka T., Yamazaki T., Kuwana K., and Nakamura Y., *Effect of circulation on flame heights over liquid fuel pools*. Combust. Flame, 2022. **246**: 112435.

[61] Candel S., Durox D., Schuller T., Bourgouin J.-F., and Moeck J. P., *Dynamics of swirling flames*. Annu. Rev. Fluid Mech., 2014. **46**: 147-173.

[62] Wang S., Zheng J., Xu L., An Q., Han X., Zhang C., Li L., Xia X., and Qi F., *Experimental investigation of the helical mode in a stratified swirling flame*. Combust. Flame, 2022. **244**: 112268.

[63] Emmons H. W., and Ying S.-J., *The fire whirl*. Symposium (international) on Combustion, 1967, 475-488.

[64] Muraszew A., Fedele J., and Kuby W., *The fire whirl phenomenon*. Combustion and Flame, 1979. **34**: 29-45.

[65] Hassan M. I., Kuwana K., Saito K., and Wang F., *Flow structure of a fixed-frame type fire whirl*. Fire Safety Science, 2005. **8**: 951-962.

[66] Zhou R., and Wu Z.-N., *Fire whirls due to surrounding flame sources and the influence of the rotation speed on the flame height*. Journal of Fluid Mechanics, 2007. **583**: 313-345.

[67] Kuwana K., Morishita S., Dobashi R., Chuah K. H., and Saito K., *The burning rate's effect on the flame length of weak fire whirls*. Proceedings of the Combustion Institute, 2011. **33** (2): 2425-2432.

[68] Xiao H., Gollner M. J., and Oran E. S., *From fire whirls to blue whirls and combustion with reduced pollution*. Proceedings of the National Academy of Sciences, 2016. **113** (34): 9457-9462.

[69] Chuah K. H., and Kushida G., *The prediction of flame heights and flame shapes of small fire whirls*. Proc. Combust. Inst., 2007. **31** (2): 2599-2606.

[70] Gotoda H., and Ueda T., *Transition from periodic to non-periodic motion of a bunsen-type premixed flame tip with burner rotation*. Proceedings of the Combustion Institute, 2002. **29** (2): 1503-1509.

[71] Gotoda H., Maeda K., Ueda T., and Cheng R. K., *Periodic motion of a Bunsen flame tip with burner rotation*. Combustion and flame, 2003. **134** (1-2): 67-79.

[72] Gotoda H., and Ueda T., *Orbital instability and prediction of a Bunsen flame tip motion with burner rotation*. Combustion and flame, 2005. **140** (4): 287-298.

[73] Gotoda H., Ueda T., Shepherd I. G., and Cheng R. K., *Flame flickering frequency on a rotating Bunsen burner*. Chemical engineering science, 2007. **62** (6): 1753-1759.

[74] Gotoda H., Asano Y., Chuah K. H., and Kushida G., *Nonlinear analysis on dynamic behavior of buoyancy-induced flame oscillation under swirling flow*. International Journal of Heat and Mass Transfer, 2009. **52** (23-24): 5423-5432.

[75] Gotoda H., Asano Y., Chuah K. H., Kushida G., and Miyano T., *Dynamic behavior of buoyancy-induced flame oscillation under swirling flow by a use of nonlinear time series analysis in combination with surrogate data method*. Combustion science and technology, 2010. **182** (11-12): 1820-1840.

[76] Lei J., Liu N., Jiao Y., and Zhang S., *Experimental investigation on flame patterns of buoyant diffusion flame in a large range of imposed circulations*. Proc. Combust. Inst., 2017. **36** (2): 3149-3156.

[77] Kuramoto Y., and Battogtokh D., *Coexistence of coherence and incoherence in nonlocally coupled phase oscillators*. Nonlinear Phenomena in Complex Systems, 2002. **5** (4): 380-385.

[78] Manoj K., Pawar S. A., and Sujith R., *Experimental evidence of amplitude death and phase-flip bifurcation between in-phase and anti-phase synchronization*. Scientific Reports, 2018. **8** (1): 1-7.

[79] Chen T., Guo X., Jia J., and Xiao J., *Frequency and phase characteristics of candle flame oscillation*. Scientific Reports, 2019. **9** (1): 1-13.

[80] Okamoto K., Kijima A., Umeno Y., and Shima H., *Synchronization in flickering of three-coupled candle flames*. Scientific Reports, 2016. **6** (1): 1-10.

[81] Baldwin R., *Flame merging in multiple fires*. Combustion and Flame, 1968. **12** (4): 318-324.

[82] Weng W. G., Kamikawa D., Fukuda Y., Hasemi Y., and Kagiya K., *Study on flame height of merged flame from multiple fire sources*. Combustion Science and Technology, 2004. **176** (12): 2105-2123.

[83] Kitahata H., Taguchi J., Nagayama M., Sakurai T., Ikura Y., Osa A., Sumino Y., Tanaka M., Yokoyama E., and Miike H., *Oscillation and synchronization in the combustion of candles*. The Journal of Physical Chemistry A, 2009. **113** (29): 8164-8168.

[84] Forrester D. M., *Arrays of coupled chemical oscillators*. Scientific Reports, 2015. **5** (1): 1-7.

[85] Dange S., Pawar S. A., Manoj K., and Sujith R., *Role of buoyancy-driven vortices in inducing different modes of coupled behaviour in candle-flame oscillators*. AIP Advances, 2019. **9** (1): 015119.

[86] Fujisawa N., Imaizumi K., and Yamagata T., *Synchronization of dual diffusion flame in co-flow*. Experimental Thermal and Fluid Science, 2020. **110**: 109924.

[87] Bunkwang A., Matsuoka T., and Nakamura Y., *Mode transition of interacting buoyant non-premixed flames*. Journal of Thermal Science and Technology, 2020. **15** (1): 1-11.

[88] Bunkwang A., Matsuoka T., and Nakamura Y., *Similarity of dynamic behavior of buoyant single and twin jet-flame (s)*. Journal of Thermal Science and Technology, 2020. **15** (3): 1-14.

[89] Gergely A., Sándor B., Paizs C., Tötös R., and Néda Z., *Flickering candle flames and their collective behavior*. Scientific Reports, 2020. **10** (1): 1-13.

[90] Manoj K., Pawar S. A., and Sujith R., *Experimental investigation on the susceptibility of minimal networks to a change in topology and number of oscillators*. Physical Review E, 2021. **103** (2): 022207.

[91] Manoj K., Pawar S. A., Dange S., Mondal S., Sujith R., Surovyatkina E., and Kurths J., *Synchronization route to weak chimera in four candle-flame oscillators*. Physical Review E, 2019. **100** (6): 062204.

[92] Abrams D. M., and Strogatz S. H., *Chimera states for coupled oscillators*. Physical Review Letters, 2004. **93** (17): 174102.

[93] Staffelbach G., Gicquel L., Boudier G., and Poinsot T., *Large Eddy Simulation of self excited azimuthal modes in annular combustors*. Proceedings of the Combustion Institute, 2009. **32** (2): 2909-2916.

[94] Bauerheim M., Nicoud F., and Poinsot T., *Progress in analytical methods to predict and control azimuthal combustion instability modes in annular chambers*. Physics of Fluids, 2016. **28** (2): 021303.

[95] Faure-Beaulieu A., Indlekofer T., Dawson J. R., and Noiray N., *Imperfect symmetry of real annular combustors: beating thermoacoustic modes and heteroclinic orbits*. Journal of Fluid Mechanics, 2021. **925**.

[96] Nygård H. T., Ghirardo G., and Worth N. A., *Azimuthal flame response and symmetry breaking in a forced annular combustor*. Combustion and Flame, 2021. **233**: 111565.

[97] Peake N., and Parry A. B., *Modern challenges facing turbomachinery aeroacoustics*. Annual Review of Fluid Mechanics, 2012. **44**: 227-248.

[98] Moon K., Choi Y., and Kim K. T., *Experimental investigation of lean-premixed hydrogen combustion instabilities in a can-annular combustion system*. Combustion and Flame, 2022. **235**: 111697.

[99] Buschmann P. E., Worth N. A., and Moeck J. P., *Thermoacoustic oscillations in a can-annular model combustor with asymmetries in the can-to-can coupling*. Proceedings of the Combustion Institute, 2023. **39** (4): 5707-5715.

[100] Liu X., Zhao D., Guan D., Becker S., Sun D., and Sun X., *Development and progress in aeroacoustic noise reduction on turbofan aeroengines*. Progress in Aerospace Sciences, 2022. **130**: 100796.

[101] Pikovsky A., Rosenblum M., and Kurths J., (American Association of Physics Teachers, 2002).

[102] Chi Y., Yang T., and Zhang P., *Dynamical mode recognition of triple flickering buoyant diffusion flames in Wasserstein space*. Combustion and Flame, 2023. **248**: 112526.

[103] Josserand C., and Thoroddsen S. T., *Drop impact on a solid surface*. Annu. Rev. Fluid Mech., 2016. **48**: 365-391.

[104] Park B. K., Kim D., Jeong S., Moon J., and Kim J. S., *Direct writing of copper conductive patterns by ink-jet printing*. Thin Solid Films, 2007. **515** (19): 7706-7711.

[105] Worthington A. M., *On the forms assumed by drops of liquids falling vertically on a horizontal plate*. Proc. R. Soc. London, 1877. **25** (171-178): 261-272.

[106] Yarin A. L., *Drop impact dynamics: splashing, spreading, receding, bouncing…*. Annu. Rev. Fluid Mech., 2006. **38**: 159-192.

[107] Wang H., Lu H., and Zhao W., *A review of droplet bouncing behaviors on superhydrophobic surfaces: Theory, methods, and applications*. Phys. Fluids, 2023. **35** (2).

[108] Hu Z., Chu F., Shan H., Wu X., Dong Z., and Wang R., *Understanding and utilizing droplet impact on superhydrophobic surfaces: phenomena, mechanisms, regulations, applications, and beyond*. Adv. Mater., 2024. **36** (11): 2310177.

[109] Rioboo R., Tropea C., and Marengo M., *Outcomes from a drop impact on solid surfaces*. Atomization and sprays, 2001. **11** (2).

[110] Ma T., Feng L., Wang H., Liu H., and Yao M., *A numerical study of spray/wall impingement based on droplet impact phenomenon*. Int. J. Heat Mass Transf., 2017. **112**: 401-412.

[111] Liu H., Ma S., Zhang Z., Zheng Z., and Yao M., *Study of the control strategies on soot reduction under early-injection conditions on a diesel engine*. Fuel, 2015. **139**: 472-481.

[112] Chen B., Feng L., Wang Y., Ma T., Liu H., Geng C., and Yao M., *Spray and flame characteristics of wall-impinging diesel fuel spray at different wall temperatures and ambient pressures in a constant volume combustion vessel*. Fuel, 2019. **235**: 416-425.

[113] Tang Q., Liu H., Li M., and Yao M., *Optical study of spray-wall impingement impact on early-injection gasoline partially premixed combustion at low engine load*. Appl. Energy, 2017. **185**: 708-719.

[114] Rein M., *Phenomena of liquid drop impact on solid and liquid surfaces*. Fluid Dyn. Res., 1993. **12** (2): 61.

[115] Harlow F. H., and Shannon J. P., *The splash of a liquid drop*. J. Appl. Phys., 1967. **38** (10): 3855-3866.

[116] Xu L., Zhang W. W., and Nagel S. R., *Drop splashing on a dry smooth surface*. Phys. Rev. Lett., 2005. **94** (18): 184505.

[117] Mandre S., and Brenner M. P., *The mechanism of a splash on a dry solid surface*. J. Fluid Mech., 2012. **690**: 148.

[118] Quetzeri-Santiago M. A., Yokoi K., Castrejón-Pita A. A., and Castrejón-Pita J. R., *Role of the dynamic contact angle on splashing*. Phys. Rev. Lett., 2019. **122** (22): 228001.

[119] García-Geijo P., Quintero E., Riboux G., and Gordillo J., *Spreading and splashing of drops impacting rough substrates*. J. Fluid Mech., 2021. **917** (A50): 1-29.

[120] Tang C., Qin M., Weng X., Zhang X., Zhang P., Li J., and Huang Z., *Dynamics of droplet impact on solid surface with different roughness*. Int. J. Multiph. Flow, 2017. **96**: 56-69.

[121] Qin M., Tang C., Guo Y., Zhang P., and Huang Z., *Subpatterns of Thin-Sheet Splash on a Smooth Surface*. Langmuir, 2020. **36** (18): 4917-4922.

[122] Qin M., Yang T., Song Y., Tang C., and Zhang P., *Subpatterns of Thin-Sheet Splash of a Droplet Impact on a Heated Surface*. Langmuir, 2021. **38** (2): 810-817.

[123] Rein M., and Delplanque J.-P., *The role of air entrainment on the outcome of drop impact on a solid surface*. Acta Mechanica, 2008. **201** (1): 105-118.

[124] Yang L., Li Z., Yang T., Chi Y., and Zhang P., *Experimental study on droplet splash and receding breakup on a smooth surface at atmospheric pressure*. Langmuir, 2021. **37** (36): 10838-10848.

[125] Latka A., Strandburg-Peshkin A., Driscoll M. M., Stevens C. S., and Nagel S. R., *Creation of prompt and thin-sheet splashing by varying surface roughness or increasing air pressure*. Phys. Rev. Lett., 2012. **109** (5): 054501.

[126] Ashida T., Watanabe M., Kobayashi K., Fujii H., and Sanada T., *Hidden prompt splashing by corona splashing at drop impact on a smooth dry surface*. Phys. Rev. Fluids, 2020. **5** (1): 011601.

[127] Liang G., and Mudawar I., *Review of drop impact on heated walls*. Int. J. Heat Mass Transf., 2017. **106**: 103-126.

[128] Bertola V., *An impact regime map for water drops impacting on heated surfaces*. Int. J. Heat Mass Transf., 2015. **85**: 430-437.

[129] Liang G., Shen S., Guo Y., and Zhang J., *Boiling from liquid drops impact on a heated wall*. Int. J. Heat Mass Transf., 2016. **100**: 48-57.

[130] Tran T., Staat H. J., Prosperetti A., Sun C., and Lohse D., *Drop impact on superheated surfaces*. Phys Rev Lett, 2012. **108** (3): 036101.

[131] Staat H. J. J., Tran T., Geerdink B., Riboux G., Sun C., Gordillo J. M., and Lohse D., *Phase diagram for droplet impact on superheated surfaces*. J Fluid Mech, 2015. **779**.

[132] Staat H. J., Tran T., Geerdink B., Riboux G., Sun C., Gordillo J. M., and Lohse D., *Phase diagram for droplet impact on superheated surfaces*. J. Fluid Mech., 2015. **779**: R3.

[133] Chen K., Xu R. N., and Jiang P. X., *Evaporation Enhancement of Microscale Droplet Impact on Micro/Nanostructured Surfaces*. Langmuir : the ACS journal of surfaces and colloids, 2020. **36** (41): 12230-12236.

[134] Hesamaldin, Jadidbonab, Nicholas, Mitroglou, Ioannis, Karathanassis, Manolis, and Gavaises, *Experimental Study of Diesel-Fuel Droplet Impact on a Similarly Sized Polished Spherical Heated Solid Particle*. Langmuir: The ACS Journal of Surfaces and Colloids, 2018.

[135] Tran T., Staat H. J. J., Susarrey-Arce A., Foertsch T. C., van Houselt A., Gardeniers H. J. G. E., Prosperetti A., Lohse D., and Sun C., *Droplet impact on superheated micro-structured surfaces*. Soft matter, 2013. **9** (12): 3272-3282.

[136] Zhang W., Yu T., Fan J., Sun W., and Cao Z., *Droplet impact behavior on heated micro-patterned surfaces*. J. Appl. Phys., 2016. **119** (11): 114901.

[137] Jadidbonab H., Malgarinos I., Karathanassis I., Mitroglou N., and Gavaises M., *We -T classification of diesel fuel droplet impact regimes*. Proc. R. Soc. A, 2018. **474** (2215): 20170759.

[138] Chen L., Bonaccurso E., Deng P., and Zhang H., *Droplet impact on soft viscoelastic surfaces*. Phys. Rev. E, 2016. **94** (6): 063117.

[139] Antonini C., Villa F., Bernagozzi I., Amirfazli A., and Marengo M., *Drop rebound after impact: The role of the receding contact angle*. Langmuir, 2013. **29** (52): 16045-16050.

[140] Bartolo D., Bouamrirene F., Verneuil E., Buguin A., Silberzan P., and Moulinet S., *Bouncing or sticky droplets: Impalement transitions on superhydrophobic micropatterned surfaces*. EPL, 2006. **74** (2): 299.

[141] Okumura K., Chevy F., Richard D., Quéré D., and Clanet C., *Water spring: A model for bouncing drops*. EPL, 2003. **62** (2): 237.

[142] Sanjay V., Chantelot P., and Lohse D., *When does an impacting drop stop bouncing?* J. Fluid Mech., 2023. **958**: A26.

[143] Chen L., and Li Z., *Bouncing droplets on nonsuperhydrophobic surfaces*. Phys. Rev. E, 2010. **82** (1): 016308.

[144] Chen L., Wu J., Li Z., and Yao S., *Evolution of entrapped air under bouncing droplets on viscoelastic surfaces*. Colloids Surf. A: Physicochem. Eng., 2011. **384** (1-3): 726-732.

[145] Richard D., and Quéré D., *Bouncing water drops*. EPL, 2000. **50** (6): 769.

[146] Biance A.-L., Chevy F., Clanet C., Lagubeau G., and Quéré D., *On the elasticity of an inertial liquid shock*. J. Fluid Mech., 2006. **554**: 47-66.

[147] Aboud D. G., and Kietzig A.-M., *On the oblique impact dynamics of drops on superhydrophobic surfaces. Part II: Restitution coefficient and contact time*. Langmuir, 2018. **34** (34): 9889-9896.

[148] Wang Y., Zhao Y., Sun L., Mehrizi A. A., Lin S., Guo J., and Chen L., *Successive rebounds of impinging water droplets on superhydrophobic surfaces*. Langmuir, 2022. **38** (12): 3860-3867.

[149] Thenarianto C., Koh X. Q., Lin M., Jokinen V., and Daniel D., *Energy loss for droplets bouncing off superhydrophobic surfaces*. Langmuir, 2023. **39** (8): 3162-3167.

[150] Mell W. E., McGrattan K. B., and Baum H. R., *Numerical simulation of combustion in fire plumes*. Proceedings of the Combustion Institute, 1996, 1523-1530.

[151] McGrattan K., Hostikka S., McDermott R., Floyd J., Weinschenk C., and Overholt K., *Fire dynamics simulator user's guide*. NIST Special Publication, 2013. **1019** (6): 1-339.

[152] Beji T., Zhang J., Yao W., and Delichatsios M., *A novel soot model for fires: validation in a laminar non-premixed flame*. Combustion and Flame, 2011. **158** (2): 281-290.

[153] Battaglia F., McGrattan K. B., Rehm R. G., and Baum H. R., *Simulating fire whirls*. Combustion Theory and Modelling, 2000. **4** (2): 123.

[154] Yuen A., Yeoh G. H., Cheung S. C., Chan Q., Chen T. B. Y., Yang W., and Lu H., *Numerical study of the development and angular speed of a small-scale fire whirl*. Journal of computational science, 2018. **27**: 21-34.

[155] Xin Y., Gore J., McGrattan K., Rehm R., and Baum H., *Large Eddy Simulation of buoyant turbulent pool fires*. Proceedings of the Combustion Institute, 2002. **29** (1): 259-266.

[156] Xin Y., Gore J. P., McGrattan K. B., Rehm R. G., and Baum H. R., *Fire dynamics simulation of a turbulent buoyant flame using a mixture-fraction-based combustion model*. Combustion and Flame, 2005. **141** (4): 329-335.

[157] Xin Y., Filatyev S., Biswas K., Gore J., Rehm R., and Baum H., *Fire dynamics simulations of a one-meter diameter methane fire*. Combustion and Flame, 2008. **153** (4): 499-509.

[158] Takagi K., Gotoda H., Tokuda I. T., and Miyano T., *Nonlinear dynamics of a buoyancy-induced turbulent fire*. Physical Review E, 2017. **96** (5): 052223.

[159] Takagi K., and Gotoda H., *Effect of gravity on nonlinear dynamics of the flow velocity field in turbulent fire*. Physical Review E, 2018. **98** (3): 032207.

[160] Tokami T., Toyoda M., Miyano T., Tokuda I. T., and Gotoda H., *Effect of gravity on synchronization of two coupled buoyancy-induced turbulent flames*. Physical Review E, 2021. **104** (2): 024218.

[161] Hietaniemi J., Hostikka S., and Vaari J., *FDS simulation of fire spread œ comparison of model results with experimental data*. VTT building and Transfor, 2004. **4**.

[162] Yang T., and Zhang P., *Faster flicker of buoyant diffusion flames by weakly rotatory flows*. Theoretical and Computational Fluid Dynamics, 2023. 1-18.

[163] Yang T., Xia X., and Zhang P., *Vortex-dynamical interpretation of anti-phase and in-phase flickering of dual buoyant diffusion flames*. Physical Review Fluids, 2019. **4** (5): 053202.

[164] Yang T., Chi Y., and Zhang P., *Vortex interaction in triple flickering buoyant diffusion flames*. Proceedings of the Combustion Institute, 2023. **39** (2): 1893-1903.

[165] Katta V. R., Goss L., and Roquemore W. M., *Effect of nonunity Lewis number and finite-rate chemistry on the dynamics of a hydrogen-air jet diffusion flame*. Combust. Flame, 1994. **96** (1-2): 60-74.

[166] Yang T., Ma Y., and Zhang P., *Dynamical behavior of small-scale buoyant diffusion flames in externally swirling flows*. Symmetry, 2024. **16** (3): 292.

[167] McGrattan K., Hostikka S., McDermott R., Floyd J., Weinschenk C., and Overholt K., *Fire dynamics simulator technical reference guide volume 1: mathematical model*. NIST special publication, 2013. **1018** (1): 175.

[168] Magnussen B. F., *The eddy dissipation concept: A bridge between science and technology*. ECCOMAS thematic conference on computational combustion, 2005, 24.

[169] Law C. K., *Combustion physics* (Cambridge university press, 2010).

[170] Viskanta R., and Mengüç M., *Radiation heat transfer in combustion systems*. Progress in Energy and Combustion Science, 1987. **13** (2): 97-160.

[171] Schönbucher A., Arnold B., Banhardt V., Bieller V., Kasper H., Kaufmann M., Lucas R., and Schiess N., *Simultaneous observation of organized density structures and the visible field in pool fires*. Symposium (International) on Combustion, 1988, 83-92.

[172] Maynard T., *Fire interactions and pulsation-theoretical and physical modeling* (UC Riverside, 2013).

[173] Fang J., Tu R., Guan J.-f., Wang J.-j., and Zhang Y.-m., *Influence of low air pressure on combustion characteristics and flame pulsation frequency of pool fires*. Fuel, 2011. **90** (8): 2760-2766.

[174] Fang J., Wang J.-w., Guan J.-f., Zhang Y.-m., and Wang J.-j., *Momentum-and buoyancy-driven laminar methane diffusion flame shapes and radiation characteristics at sub-atmospheric pressures*. Fuel, 2016. **163**: 295-303.

[175] Drysdale D., *An introduction to fire dynamics* (John Wiley & Sons, 2011).

[176] Durox D., Yuan T., Baillot F., and Most J., *Premixed and diffusion flames in a centrifuge*. Combustion and flame, 1995. **102** (4): 501-511.

[177] Hamins A., Yang J., and Kashiwagi T., *An experimental investigation of the pulsation frequency of flames*. Proceedings of the Combustion Institute, 1992. **24** (1): 1695-1702.

[178] Carpio J., Coenen W., Sánchez A., Oran E., and Williams F., *Numerical description of axisymmetric blue whirls over liquid-fuel pools*. Proceedings of the Combustion Institute, 2021. **38** (2): 2041-2048.

[179] Strogatz S. H., *Nonlinear dynamics and chaos: with applications to physics, biology, chemistry, and engineering* (CRC Press, 2018).

[180] Kuramoto Y., *Chemical oscillations, waves, and turbulence* (Springer Science & Business Media, 2012).

[181] Kuramoto Y., *Self-entrainment of a population of coupled non-linear oscillators*. International Symposium on Mathematical Problems in Theoretical Physics: January 23–29, 1975, Kyoto University, Kyoto/Japan, 1975, 420-422.

[182] Acebrón J. A., Bonilla L. L., Vicente C. J. P., Ritort F., and Spigler R., *The Kuramoto model: A simple paradigm for synchronization phenomena*. Reviews of modern physics, 2005. **77** (1): 137.

[183] Chi Y., Hu Z., Yang T., and Zhang P., *Synchronization modes of triple flickering buoyant diffusion flames: Experimental identification and model interpretation*. Physical Review E, 2024. **109** (2): 024211.

[184] Atay F. M., *Complex time-delay systems: theory and applications* (Springer, 2010).

[185] Yifan Yang H. Z., Xi Xia, Peng Zhang, Fei Qi, *An experimental study of the blue whirl onset*. Proceedings of the Combustion Institute, 2022. (in press).

[186] Kundu P. K., Cohen I. M., and Dowling D. R., *Fluid mechanics* (Academic press, 2015).

[187] Yang T., Chi Y., and Zhang P., *Vortex interaction in triple flickering buoyant diffusion flames*. Proceedings of the Combustion Institute, 2022. (in press).

[188] Sato H., Kushida G., Amagai K., and Arai M., *Numerical analysis of the gravitational effect on the buoyancy-driven fluctuations in diffusion flames*. Proceedings of the Combustion Institute, 2002. **29** (2): 1671-1678.

[189] Sato H., Amagai K., and Arai M., *Diffusion flames and their flickering motions related with Froude numbers under various gravity levels*. Combustion and Flame, 2000. **123** (1-2): 107-118.

[190] Gotoda H., Kawaguchi S., and Saso Y., *Experiments on dynamical motion of buoyancy-induced flame instability under different oxygen concentration in ambient gas*. Experimental Thermal and Fluid Science, 2008. **32** (8): 1759-1765.

[191] Aravind M., Tiwari I., Vasani V., Cruz J.-M., Vasquez D. A., and Parmananda P., *Ethanol lamp: a simple, tunable flame oscillator and its coupled dynamics*. The European Physical Journal Special Topics, 2021. 1-6.

[192] Chang C., and Smith S. G. L., *The motion of a buoyant vortex filament*. Journal of Fluid Mechanics, 2018. **857**.

[193] Chung J. D., Zhang X., Kaplan C. R., and Oran E. S., *The structure of the blue whirl revealed*. Science Advances, 2020. **6** (33): eaba0827.

[194] Wu J.-Z., Ma H.-Y., and Zhou M.-D., *Vorticity and vortex dynamics* (Springer Science & Business Media, 2007).

[195] Didden N., *On the formation of vortex rings: rolling-up and production of circulation*. Journal of Applied Mathematics and Physics, 1979. **30** (1): 101-116.

[196] Mullen J. B., and Maxworthy T., *A laboratory model of dust devil vortices*. Dynamics of Atmospheres and Oceans, 1977. **1** (3): 181-214.

[197] Kolb E. J., *An Experimental Approach to the Blue Whirl* (University of California, San Diego, 2018).

[198] Zhang H., Xia X., and Gao Y., *Instability transition of a jet diffusion flame in quiescent environment*. Proceedings of the Combustion Institute, 2021. **38** (3): 4971-4978.

[199] Sato H., Amagai K., and Arai M., *Flickering frequencies of diffusion flames observed under various gravity fields*. Proc. Combust. Inst., 2000. **28** (2): 1981-1987.

[200] Cetegen B., and Dong Y., *Experiments on the instability modes of buoyant diffusion flames and effects of ambient atmosphere on the instabilities*. Experiments in Fluids, 2000. **28** (6): 546-558.

[201] Hall M., *Vortex breakdown*. Annu. Rev. Fluid Mech., 1972. **4** (1): 195-218.

[202] Lucca-Negro O., and O'doherty T., *Vortex breakdown: a review*. Prog. Energy Combust. Sci., 2001. **27** (4): 431-481.

[203] Hu Y., Hariharan S. B., Qi H., Gollner M. J., and Oran E. S., *Conditions for formation of the blue whirl*. Combust. Flame, 2019. **205**: 147-153.

[204] Yuan T., Durox D., and Villermaux E., *An analogue study for flame flickering*. Experiments in fluids, 1994. **17** (5): 337-349.

[205] Buckmaster J., and Peters N., *The infinite candle and its stability—a paradigm for flickering diffusion flames*. Proceedings of the Combustion Institute, 1988. **21** (1): 1829-1836.

[206] Nagamine Y., Otaka K., Zuiki H., Miike H., and Osa A., *Mechanism of candle flame oscillation: Detection of descending flow above the candle flame*. Journal of the Physical Society of Japan, 2017. **86** (7): 074003.

[207] Williamson C., *Evolution of a single wake behind a pair of bluff bodies*. Journal of Fluid Mechanics, 1985. **159**: 1-18.

[208] Changchun L., Xinlei L., Hong G., Jun D., Shasha Z., Xueyao W., and Fangming C., *On the influence of distance between two jets on flickering diffusion flames*. Combustion and Flame, 2019. **201**: 23-30.

[209] Kármán T., *Aerodynamics* (Mcgraw-Hill Book Company, 1963).

[210] Roshko A., *On the drag and shedding frequency of two-dimensional bluff bodies*. 1954.

[211] Chakraborty P., Balachandar S., and Adrian R. J., *On the relationships between local vortex identification schemes*. Journal of Fluid Mechanics, 2005. **535**: 189-214.

[212] Dange S., Pawar S. A., Manoj K., and Sujith R. I., *Role of buoyancy-driven vortices in inducing different modes of coupled behaviour in candle-flame oscillators*. AIP Advances, 2019. **9**: 015119.

[213] Reddy D. R., Sen A., and Johnston G. L., *Time delay induced death in coupled limit cycle oscillators*. Physical Review Letters, 1998. **80** (23): 5109.

[214] Prasad A., Kurths J., Dana S. K., and Ramaswamy R., *Phase-flip bifurcation induced by time delay*. Physical Review E, 2006. **74** (3): 035204.

[215] Forrester D. M., *Arrays of coupled chemical oscillators*. Scientific Reports, 2015. **5**: 16994.

[216] Nakamura Y., Mochizuki, K., and Matsuoka, T, in *Proc. 27th International Symposium on Transport Phenomena* (Hawaii, 2016).

[217] Wan H., Ji J., Li K., Huang X., Sun J., and Zhang Y., *Effect of air entrainment on the height of buoyant turbulent diffusion flames for two fires in open space*. Proceedings of the Combustion Institute, 2017. **36** (2): 3003-3010.

[218] Hu L., Huang L., Wang Q., and Kuwana K., *Experimental study and analysis on the interaction between two slot-burner buoyant turbulent diffusion flames at various burner pitches*. Combustion and Flame, 2017. **186**: 105-113.

[219] Jeong J., and Hussain F., *On the identification of a vortex*. J. Fluid Mech., 1995. **285**: 69-94.

[220] Boulanger J., *Laminar round jet diffusion flame buoyant instabilities: Study on the disappearance of varicose structures at ultra-low Froude number*. Combustion and flame, 2010. **157** (4): 757-768.

[221] Kida S., and Takaoka M., *Vortex reconnection*. Annual Review of Fluid Mechanics, 1994. **26** (1): 169-177.

[222] Ashurst W. T., and Meiron D. I., *Numerical study of vortex reconnection*. Physical Review Letters, 1987. **58** (16): 1632.

[223] Hussain A. F., *Coherent structures—reality and myth*. Phys. Fluids, 1983. **26** (10): 2816-2850.

[224] Hussain A. F., *Coherent structures and turbulence*. Journal of Fluid Mechanics, 1986. **173**: 303-356.

[225] Hussain F., and Duraisamy K., *Mechanics of viscous vortex reconnection*. Physics of Fluids, 2011. **23** (2): 021701.

[226] Chi Y., Yang T., and Zhang P., *Dynamical Mode Recognition of Triple Flickering Buoyant Diffusion Flames: from Physical Space to Phase Space and to Wasserstein Space*. arXiv preprint arXiv:2201.01085, 2022.

[227] Guan Y., Moon K., Kim K. T., and Li L. K., *Synchronization and chimeras in a network of four ring-coupled thermoacoustic oscillators*. J. Fluid Mech., 2022. **938**.

[228] Ju X., Bunkwang A., Yamazaki T., Matsuoka T., and Nakamura Y., *Flame Flickering can Cease Under Normal Gravity and Atmospheric Pressure in a*

Horizontally Moving Dual Burner System. Physical Review Applied, 2023. **19** (1): 014060.

[229] Biju A. E., Srikanth S., Manoj K., Pawar S. A., and Sujith R., *Dynamics of minimal networks of limit cycle oscillators*. Nonlinear Dynamics, 2024. 1-20.

[230] Xu L., *Instability development of a viscous liquid drop impacting a smooth substrate*. Phys. Rev. E, 2010. **82** (2): 025303.

[231] Xu L., Barcos L., and Nagel S. R., *Splashing of liquids: Interplay of surface roughness with surrounding gas*. Phys. Rev. E, 2007. **76** (6): 066311.

[232] Yoon S. S., Jepsen R. A., James S. C., Liu J., and Aguilar G., *Are drop-impact phenomena described by Rayleigh-Taylor or Kelvin-Helmholtz theory?* Drying Technology, 2009. **27** (3): 316-321.

[233] Zhang L. V., Brunet P., Eggers J., and Deegan R. D., *Wavelength selection in the crown splash*. Phys. Fluids, 2010. **22** (12): 122105.

[234] Juarez G., Gastopoulos T., Zhang Y., Siegel M. L., and Arratia P. E., *Splash control of drop impacts with geometric targets*. Phys. Rev. E, 2012. **85** (2): 026319.

[235] Liu Z., Pan X., Ma Q., and Fang H., *Receding Dynamics of Droplet Deposition on a Smooth Surface from a Central Jet to Secondary Droplet Emission*. Langmuir, 2020. **36** (49): 15082-15093.

[236] Grishaev V., Iorio C. S., Dubois F., and Amirfazli A., *Complex drop impact morphology*. Langmuir, 2015. **31** (36): 9833-9844.

[237] Riboux G., and Gordillo J. M., *Experiments of drops impacting a smooth solid surface: A model of the critical impact speed for drop splashing*. Phys. Rev. Lett., 2014. **113** (2): 024507.

[238] Gordillo J. M., and Riboux G., *A note on the aerodynamic splashing of droplets*. J. Fluid Mech., 2019. **871** (R3).

[239] Stevens C. S., Latka A., and Nagel S. R., *Comparison of splashing in high-and low-viscosity liquids*. Phys. Rev. E, 2014. **89** (6): 063006.

[240] Xu L., *Liquid drop splashing on smooth, rough, and textured surfaces*. Phys. Rev. E, 2007. **75** (5): 056316.

[241] Liu J., Vu H., Yoon S. S., Jepsen R. A., and Aguilar G., *Splashing phenomena during liquid droplet impact*. At. Sprays, 2010. **20** (4): 297–310.

[242] Eggers J., Fontelos M. A., Josserand C., and Zaleski S., *Drop dynamics after impact on a solid wall: Theory and simulations*. Phys. Fluids, 2010. **22** (6): 062101.

[243] Engel O. G., *Waterdrop collisions with solid surfaces*. J. Res. Natl. Bur. Stand., 1955. **54** (5): 281-298.

[244] Agbaglah G., Josserand C., and Zaleski S., *Longitudinal instability of a liquid rim*. Phys. Fluids, 2013. **25** (2): 022103.

[245] Debrégeas G., Martin P., and Brochard-Wyart F., *Viscous bursting of suspended films*. Phys. Rev. Lett., 1995. **75** (21): 3886.

[246] Savva N., and Bush J. W., *Viscous sheet retraction*. J. Fluid Mech., 2009. **626**: 211–240.

[247] Murano M., and Okumura K., *Bursting dynamics of viscous film without circular symmetry: The effect of confinement*. Phys. Rev. Fluids, 2018. **3** (3): 031601.

[248] Mundo C., Sommerfeld M., and Tropea C., *Droplet-wall collisions: experimental studies of the deformation and breakup process*. Int. J. Multiph. Flow, 1995. **21** (2): 151-173.

[249] Palacios J., Hernández J., Gómez P., Zanzi C., and López J., *Experimental study of splashing patterns and the splashing/deposition threshold in drop impacts onto dry smooth solid surfaces*. Exp. Therm. Fluid Sci., 2013. **44**: 571-582.

[250] Liu Y., Tan P., and Xu L., *Kelvin–Helmholtz instability in an ultrathin air film causes drop splashing on smooth surfaces*. Proc. Natl. Acad. Sci. U.S.A., 2015. **112** (11): 3280-3284.

[251] Vander Wal R. L., Berger G. M., and Mozes S. D., *The splash/non-splash boundary upon a dry surface and thin fluid film*. Exp. Fluids, 2006. **40** (1): 53-59.

[252] Stevens C. S., *Scaling of the splash threshold for low-viscosity fluids*. EPL (Europhysics Letters), 2014. **106** (2): 24001.

[253] Almohammadi H., and Amirfazli A., *Droplet impact: Viscosity and wettability effects on splashing*. Journal of Colloid and Interface Science, 2019. **553**: 22-30.

[254] Zhang H., Zhang X., Yi X., He F., Niu F., and Hao P., *Reversed role of liquid viscosity on drop splash*. Phys. Fluids, 2021. **33** (5): 052103.

[255] Schmidt P., and Knauss G., *Prallzerstäubung von flüssigkeiten bei nichtbenetzung*. Chemie Ingenieur Technik, 1976. **48** (7): 659-659.

[256] De Goede T., Laan N., De Bruin K., and Bonn D., *Effect of wetting on drop splashing of Newtonian fluids and blood*. Langmuir, 2017. **34** (18): 5163-5168.

[257] Usawa M., Fujita Y., Tagawa Y., Riboux G., and Gordillo J. M., *Large impact velocities suppress the splashing of micron-sized droplets*. Phys. Rev. Fluids, 2021. **6** (2): 023605.

[258] Kong S. C., *Drop/wall interaction criteria and their applications in diesel spray modeling*. Atomization Sprays, 2007. **17** (6): 473-499.

[259] Shirota M., van Limbeek M. A., Sun C., Prosperetti A., and Lohse D., *Dynamic Leidenfrost Effect: Relevant Time and Length Scales*. Phys Rev Lett, 2016. **116** (6): 064501.

[260] Sreenivasan A., and Deivandren S., *Splashing of fuel drops impacting on heated solid surfaces*. Phys. Fluids, 2020. **32** (3): 032104.

[261] Xu L., *Instability development of a viscous liquid drop impacting a smooth substrate*. Physical review. E, 2010. **82**: 025303.

[262] Yang L., Li Z., Yang T., Chi Y., and Zhang P., *Experimental Study on Droplet Splash and Receding Breakup on a Smooth Surface at Atmospheric Pressure*. Langmuir, 2021. **37**: 10838–10848.

[263] Stow C. D., and Hadfield M. G., *An experimental investigation of fluid flow resulting from the impact of a water drop with an unyielding dry surface*. Proceedings of the Royal Society of London. A. Mathematical and Physical Sciences, 1981. **373** (1755): 419-441.

[264] Cossali G. E., Coghe A., and Marengo M., *The impact of a single drop on a wetted solid surface*. Exp. Fluids, 1997. **22** (6): 463-472.

[265] Range K., and Feuillebois F., *Influence of surface roughness on liquid drop impact*. Journal of colloid and interface science, 1998. **203** (1): 16-30.

[266] Riboux G., and Gordillo J. M., *Boundary-layer effects in droplet splashing*. Phys. Rev. E, 2017. **96** (1): 013105.

[267] Yarin A. L., Roisman I. V., and Tropea C., *Collision phenomena in liquids and solids* (Cambridge University Press, 2017).

[268] Driscoll M. M., Stevens C. S., and Nagel S. R., *Thin film formation during splashing of viscous liquids*. Phys. Rev. E, 2010. **82** (3): 036302.

[269] Vu H., Banks D., and Aguilar G., *Examining viscosity and surface wettability on lamella lift dynamics and droplet splashing*. At. Sprays, 2011. **21** (4).

[270] Snoeijer J. H., and Andreotti B., *Moving contact lines: scales, regimes, and dynamical transitions*. Annu. Rev. Fluid Mech., 2013. **45**: 269-292.

[271] Mandre S., Mani M., and Brenner M. P., *Precursors to splashing of liquid droplets on a solid surface*. Phys. Rev. Lett., 2009. **102** (13): 134502.

[272] Zhang L., Toole J., Fezzaa K., and Deegan R., *Splashing from drop impact into a deep pool: multiplicity of jets and the failure of conventional scaling*. J. Fluid Mech., 2012. **703**: 402-413.

[273] Gordillo J. M., and Riboux G., *A note on the aerodynamic splashing of droplets*. J. Fluid Mech., 2019. **871** (R3): 1–13.

[274] Schroll R. D., Josserand C., Zaleski S., and Zhang W. W., *Impact of a viscous liquid drop*. Phys. Rev. Lett., 2010. **104** (3): 034504.

[275] Jennings S., *The mean free path in air*. Journal of Aerosol Science, 1988. **19** (2): 159-166.

[276] Qin M., Tang C., Tong S., Zhang P., and Huang Z., *On the role of liquid viscosity in affecting droplet spreading on a smooth solid surface*. Int. J. Multiph. Flow, 2019. **117**: 53-63.

[277] Basso B. C., and Bostwick J. B., *Splashing on soft elastic substrates*. Langmuir, 2020. **36** (49): 15010-15017.

[278] Bernard R., Baumgartner D., Brenn G., Planchette C., Weigand B., and Lamanna G., *Miscibility and wettability: how interfacial tension influences droplet impact onto thin wall films*. J. Fluid Mech., 2021. **908**: A36.

[279] Zhang H., Zhang X., Yi X., He F., Niu F., and Hao P., *Effect of wettability on droplet impact: Spreading and splashing*. Experimental Thermal and Fluid Science, 2021. **124**: 110369.

[280] Sreenivasan A., and Deivandren S., *Splashing of fuel drops impacting on heated solid surfaces*. Phys. Fluids, 2020. **32** (3).

[281] Hao J., *Effect of surface roughness on droplet splashing*. Phys. Fluids, 2017. **29** (12): 122105.

[282] de Goede T., de Bruin K., Shahidzadeh N., and Bonn D., *Droplet splashing on rough surfaces*. Phys. Rev. Fluids, 2021. **6** (4): 043604.

[283] Howland C. J., Antkowiak A., Castrejón-Pita J. R., Howison S. D., Oliver J. M., Style R. W., and Castrejón-Pita A. A., *It's harder to splash on soft solids*. Phys. Rev. Lett., 2016. **117** (18): 184502.

[284] Pegg M., Purvis R., and Korobkin A., *Droplet impact onto an elastic plate: a new mechanism for splashing*. J. Fluid Mech., 2018. **839**: 561-593.

[285] Langley K. R., Castrejón-Pita A. A., and Thoroddsen S. T., *Droplet impacts onto soft solids entrap more air*. Soft Matter, 2020. **16** (24): 5702-5710.

[286] Hao J., Lu J., Lee L., Wu Z., Hu G., and Floryan J., *Droplet splashing on an inclined surface*. Phys. Rev. Lett., 2019. **122** (5): 054501.

[287] Liu Q., Lo J. H. Y., Li Y., Liu Y., Zhao J., and Xu L., *The role of drop shape in impact and splash*. Nat. Commun., 2021. **12** (1): 3068.

[288] Yun S., and Lim G., *Ellipsoidal drop impact on a solid surface for rebound suppression*. J. Fluid Mech., 2014. **752**: 266-281.

[289] Zhang X., Ji B., Liu X., Ding S., Wu X., and Min J., *Maximum spreading and energy analysis of ellipsoidal impact droplets*. Phys. Fluids, 2021. **33** (5).

[290] Yun S., *The role of oscillation in ellipsoidal drop impact on a solid surface*. J. Colloid Interface Sci., 2022. **605**: 592-601.

[291] Tang Q., Xiang S., Lin S., Jin Y., Antonini C., and Chen L., *Enhancing droplet rebound on superhydrophobic cones*. Phys. Fluids, 2023. **35** (5).

[292] Yang L., Liu X., Wang J., and Zhang P., *An Experimental Study on Complete Droplet Rebound from Soft Surfaces: Critical Weber Numbers, Maximum Spreading, and Contact Time*. Langmuir, 2024. **40** (4): 2165-2173.

[293] Hervieu E., Coutris N., and Boichon C., *Oscillations of a drop in aerodynamic levitation*. Nucl. Eng. Des., 2001. **204** (1-3): 167-175.

[294] Kistovich A., and Chashechkin Y. D., *Surface oscillations of a free-falling droplet of an ideal fluid*. Izv. - Atmos. Ocean. Phys., 2018. **54**: 182-188.

[295] Liao B., Zhang L., Yao L., Bu Y., and Chen S., *Oscillatory behavior of drops in an ambient liquid under an impact*. International Journal of Multiphase Flow, 2024. 104850.

[296] Lamb H., *Hydrodynamics* (University Press, 1932).

[297] Reid W. H., *The oscillations of a viscous liquid drop*. Q. Appl. Math., 1960. **18** (1): 86-89.

[298] Rayleigh L., *On the capillary phenomena of jets*. Proc. R. Soc. Lond., 1879. **29** (196-199): 71-97.

[299] Roisman I. V., Rioboo R., and Tropea C., *Normal impact of a liquid drop on a dry surface: model for spreading and receding*. Proc. R. Soc. Lond. A, 2002. **458** (2022): 1411-1430.

[300] Lee J. B., Derome D., Dolatabadi A., and Carmeliet J., *Energy budget of liquid drop impact at maximum spreading: Numerical simulations and experiments*. Langmuir, 2016. **32** (5): 1279-1288.

[301] Attané P., Girard F., and Morin V., *An energy balance approach of the dynamics of drop impact on a solid surface*. Phys. Fluids, 2007. **19** (1).